Multi-component Crystallisation in the Continuous Flow Environment

Wittering, Kate

Award date:
2016

Awarding institution:
University of Bath

Multi-component Crystallisation in the Continuous Flow Environment

Kate Elysse Wittering

Thesis submitted for the degree of Doctor of Philosophy

University of Bath
Department of Chemistry

October 2015

Supervisor: Professor Chick C. Wilson

Abstract

The research described in this thesis was carried out as part of the EPSRC National Centre in Continuous Manufacturing and Crystallisation (CMAC), whose vision is to accelerate the adoption of continuous manufacturing processes for the production of high-value chemical products. Results focus upon the crystallisation of multi-component molecular complexes (MMCs), in particular co-crystals, an important class of potential functional molecular materials. MMCs are commonly discovered through small scale batch solvent evaporation, a method that provides little control over the crystallisation process, often yields only small quantities of crystalline material which may not be phase pure and is not generally scalable. Methods have been developed to help translate traditional small scale batch co-crystallisation of MMCs to selective continuous co-crystallisation processes.

The co-crystal system urea-barbituric acid (UBA) has three polymorphs, previously identified in the literature and was selected as a candidate for transfer to continuous crystallisation as its polymorphism offers a development challenge in being able to achieve selectivity of solid products through by various crystallisation processes. Chapter 4 describes small scale crystallisation studies of UBA using evaporation, cooling and mechano-crystallisation techniques, demonstrating that UBAI is the more prevalent polymorph. Solid state and solubility analysis of the isolated UBA polymorphs are detailed; these data provide information on the energetic relationship between the polymorphs highlighting the similarity in energy of UBAI and UBAIII, and the metastable nature of elusive UBAII. In addition the polymorphic nature of the barbituric acid starting material has been investigated with samples from different suppliers proving to consist of different polymorphs. As well as being important in designing subsequent crystallisation processes, results from these studies corroborate work previously reported in the literature

Chapter 5 describes how these results have been used in development of continuous crystallisation experiments using Mixed-Suspension Mixed-Product Removal (MSMPR) with a cascade of three stirred tank reactors, while Chapter 6 investigates flow crystallisation of UBA using the Continuous Oscillatory Baffled Crystalliser (COBC) and the Kinetically Regulated Automated Input tubular flow Crystalliser (KRAIC). The KRAIC was designed and constructed as part of this research. The continuous crystallisation experiments presented in Chapters 5 and 6 demonstrate the selective continuous co-crystallisation of UBAI across all three continuous crystallisation platforms.

In Chapter 7 a range of novel co-crystalline MMCs is presented, with structural determinations, using single crystal X-ray diffraction, coupled with characterisation of properties and crystallisation characteristics; these studies emphasise the physical property advantages of MMCs and in some cases their potential for future translation to continuous crystallisation.

Acknowledgements

Firstly, thank you Chick for all your help, support and positivity throughout my PhD, for "ideas with wine" and for letting me subject you to endless monologues about my work.

Thanks go to the EPSRC and University of Bath for funding and to everyone in CMAC, especially to Professor Chris Rielly and Professor Zoltan Nagy for welcoming me into your group in Loughborough. Ali Saleemi, Keddon Powell and Giulia Bartollini, thank you all for your help with UBA crystallisation. Naomi Briggs, Vishal Raval, Thomas McGlone and Cameron Brown, thank you for your support with all things continuous and questions about the COBC, enjoy working in the TIC.

To my CMAC industrial mentors Amy Robertson, Helen Wheatcroft and Chris Price, thank you for your advice and support over the past four years. Particular thanks go to Amy, Helen and Alexandra Parker for providing me with the excellent opportunity to work in the Right Particle team at AstraZeneca and to Sophie Janbon for being a fantastic supervisor. Additionally, thank you Rachel Sullivan, Anna Jawor-Baczynska, David Wilson, Kirsty Millard, Stefan Taylor and Dean Murphy for your help and guidance whilst on placement.

Karen, thank you for reading through drafts of my thesis and for being my ideas soundboard, all the in-depth discussions about "slugs" etc. have proved invaluable. "Dr Dyanne" thanks for all the "fat chats", structural discussions, your patience and for not thinking I'm completely "cooked".

Thank you Lynne for all your support over the last five years (fortunately we didn't need to walk around the duck pond as much with this thesis) and for your help with I11 beam time. Which brings me nicely on to Claire Murray at Diamond, thank you for your help with the VT-PXRD experiments on I11and for showing me the wonders of filling a capillary with an electric toothbrush.

Thank you to all the Chicklets past and present. Louise "Oh my god trampoline!" thanks for being there through all the "crazy times". Big Al thanks for the "hoffing" and practical jokes, and Lauren thanks for always being happy to help and there for moral support. Anneke, Charl, Lucy and more recently, Alex, Jane, Pi-Ba and Ruth, it wouldn't have been half as fun without you all.

Wrapping up I would like to thank Mum, Dad and Paul for all your support and encouragement throughout my PhD and especially for taking me back (with all my furniture in tow) after eight years away.

Finally to Andrew, thank you for always being at the end of the phone and for putting up with me at the best of times and the worst of times. I'm looking forward to the future together.

Table of Contents

List of Figures

List of Tables

List of Symbols and Abbreviations

3DU…….	3-deazauracil
BP……	4,4’-bipyridine
4Cl35DNBA……...	4-chloro-3,5-dinitrobenzoic acid
5FCYT……	5-fluorocytosine
5OHU…….	5-hydroxyuracil (isobarbituric acid)
8AG……	8-azaguanine
AO…….	Acros Organics
API…….	Active pharmaceutical ingredient
AZ……..	AstraZeneca, Macclesfield
BA……..	Barbituric acid
BA-AO……..	Barbituric acid supplied by Acros Organics
BA-SA……...	Barbituric acid supplied by Sigma Aldrich
BA-TCI……..	Barbituric acid supplied by Tokyo Chemical Industry
BFDH…….	Bravais, Friedel, Donnay and Harker
BOBC…….	Batch Oscillatory Baffled Crystalliser
CA……..	Chloranilic acid
CCD……...	Charge coupled device
CFC……	Crystal Form Consortium
CMAC……	EPSRC Centre for Innovative Manufacturing in Continuous Manufacturing and Crystallisation
CNT……	Classical nucleation theory
COBC…….	Continuous Oscillatory Baffled Crystalliser
CRD……	Cambridge Reactor Design
CSD……	Cambridge Structural Database
CSTR……..	Cascade of stirred tank reactors
CYT……	cytosine
DoE…….	Design of experiments
DPI…….	Dry powder inhaler
DSC……	Differential scanning calorimetry
DVS……	Dynamic vapour sorption
FBRM…….	Focused beam reflectance measurement
FEN……	Fenamic acid
FLU……	Flufenamic acid
GV1……	Growth vessel 1
GV2……	Growth vessel 2
HBA……...	Hexamethylenbisacetamine
HME……...	Hot melt extrusion
HSM……...	Hot stage microscopy
IPA……....	Isopropyl alcohol
IR…….....	Infra-red
KRAIC……..	Kinetically regulated automated input crystalliser
LAG……...	Liquid assisted grinding
LU…….....	Loughborough University

MEF……..	Mefenamic acid
MO…….....	Mode of operation
MMCs……	Multi-component molecular complexes
MNT……..	Multi-step nucleation theory
MSMPR……	Mixed suspension mixed product removal
MSZ……..	Meta-stable zone
MSZW……	meta-stable zone width
NaCl……..	Sodium Chloride
NLO……..	Non-linear optical
NSAID……..	Non-steroidal anti-inflammatory drug
Nuc. ……..	Nucleator vessel
OXA……..	oxalic acid
PAT……...	Process analytical technologies
PFPE……	Perfluoropolyether
PMSMPR……..	Periodic mixed suspension mixed product removal
PSD……...	Particle size distribution
PTFE……	Polytetrafluoroethylene
PVM……..	Particle visualisation measurement
PXRD……	Powder X-ray diffraction
RBF……...	Round bottomed flask
RH…….....	Relative humidity
rpm…….....	Revolutions per minute
RT…….....	Room temperature (18 °C)
RT…….....	Residence time
RTD……..	Residence time distribution
SA…….....	Sigma Aldrich
SCO……..	State of controlled operation
SEM……..	Scanning electron microscopy
STR……...	Stirred tank reactor
SU…….....	Standard uncertainty
SXRD……	Single crystal X-ray diffraction
TCI…….....	Tokyo Chemical Industries
TGA……..	Thermogravimetric analysis
TOL……..	Tolfenamic acid
TRIM……	Trimesic acid
UBAI……	Urea-barbituric acid co-crystal – polymorph 1
UBAII……..	Urea-barbituric acid co-crystal – polymorph 2
UBAIII…….	Urea-barbituric acid co-crystal – polymorph 3
vdW……..	van der Waals
VTPXRD……..	Variable temperature powder X-ray diffraction

1 Introduction I – Multi-Component Materials

1.1 Crystal Engineering and Multi-component Crystallisation

Crystal engineering is a modern branch of chemistry considered to have originated around 40 years ago and was first documented in 1971 when Schmidt published a paper on solid state photochemical properties of cinnamic acids, in which he coined the phrase "crystal engineering"[1]. Crystal engineering involves design and facilitation of the solid state organised self-assembly of molecules using non-covalent interactions, in order to form a crystalline solid that displays a desirable property[2, 3].

In contrast to chemical synthesis where emphasis is placed upon the reactivity of a molecular species and the ability to form new covalent bonds, crystal engineering focuses on the geometry and functionality of a molecule to give an indication of the propensity to form intermolecular interactions that influence the molecular packing within a crystal[4].

In the infancy of crystal engineering Schmidt predicted that future progress in the field would '*be difficult if not impossible until we understand the intermolecular forces responsible for the stability of the crystalline lattice.*'[1] It is the desire to understand further these non-covalent intermolecular interactions that has driven the evolution of the crystal engineering field, which has swiftly evolved over the past 15 years[5].

A crystal engineering approach to the production of new molecular materials commonly involves studying the crystallisation of compounds related by a systematic variation in molecular structure. This enables variations in properties that appear upon analysis to be pinpointed to a specific detail in the crystal structure[6]. The choice of materials and their variation in crystal engineering is governed by an analysis of their likely intermolecular interactions, primarily the hydrogen bond but also with consideration of other possible significant intermolecular interactions.

This systematic variation is also used to produce multi-component molecular materials. A target material is combined with one or more additional materials (co-formers) to crystallise together in the same crystal lattice through intermolecular interactions, altering the packing arrangement of the target material and potentially inducing a favourable change in physical properties. This proved useful when studying molecular complexes involving chloranilic acid (CA) which are known to be brightly coloured, either red, orange or purple[7]. The structures of molecular complexes combining CA with one of a family of picolinic acid based co-formers showed structures in which proton transfer had occurred between CA and the co-former, altering the protonation state of the CA. From the structures each of the three colours could be assigned to one of the three protonation states of chloranilic acid, as previously proposed by Molcanov et al.[7]

In co-crystallisation studies by Aakeroy et al.[8] using hexamethylenbisacetamine (HBA), an API used for prevention of proliferation of lung cancer cells and as a treatment for leukaemia, HBA was crystallised with a variety of dicarboxylic acids with systematic variation in carbon chain lengths in an attempt to increase the aqueous solubility of the API. Complexes of the API and co-formers formed structures containing alternating chains of API and co-former. The co-crystal involving the shortest dicarboxylic acid, succinic acid, was found to improve aqueous solubility by a factor of 2.5. As the chain length increased, the aqueous solubility of the co-crystals produced was reduced, to the extent that their solubility was less than that of the API alone[8]. It is also possible to use co-crystallisation as a templating method to access a particular polymorphic form of a single component API, as found recently with paracetamol form II[9].

1.2 Classification of Multi-component materials

Multi-component molecular complexes (MMCs) can be classified into several sub groups, namely co-crystals, salts, solvates and hydrates, the nomenclature of which is highly debated[6, 10, 11]. However it is generally accepted that a salt is produced with a free acid and a basic salt former (or a free base and an acidic salt former) between which proton transfer occurs. This results in a single crystal lattice comprised of two or more oppositely charged species where the crystal remains neutral overall. Salt formation is commonly used in the pharmaceutical and agrichemical industries as a convenient method to isolate synthetic products and/or to improve physicochemical properties[12].

Similarly to salts, co-crystals are formed by two or more different compounds held together in the same crystal lattice through intermolecular interactions. However, the molecular species within a co-crystal remain neutral, i.e. as in molecular systems such as those studied here, there is no proton transfer. As for salts, co-crystals can be used in the industrial context as they can strongly influence physicochemical properties such as solubility, melting point and others, relevant to processing, delivery or bioavailability of materials.

Salts and co-crystals are not inclusive of hydrates or solvates where the second component is a water molecule or solvent molecule introduced by the solvent of crystallisation. Solvates and hydrates are occasionally referred to in the literature as pseudo-polymorphs[13, 14] or even classed as polymorphs by some authors, however in the context of this thesis they shall be termed solvates. Solvates and hydrates can be classified further into two subgroups – either as true solvates/hydrates where the solvent/water molecule is incorporated into the crystal lattice in a fully ordered manner through intermolecular interactions in a stoichiometric ratio, or as non-stoichiometric solvates/hydrates, i.e. those where water or solvent is trapped in pores or channels, often exhibiting disorder, and can be adsorbed or removed upon heating or with gas or solvent displacement[15].

It is important to note that in this work a multi-component product will be referred to as a molecular complex, encompassing both molecular salts and neutral complexes under this term. The term co-crystallisation is commonly accepted shorthand for multi-component crystallisation and the two can be used interchangeably[10].

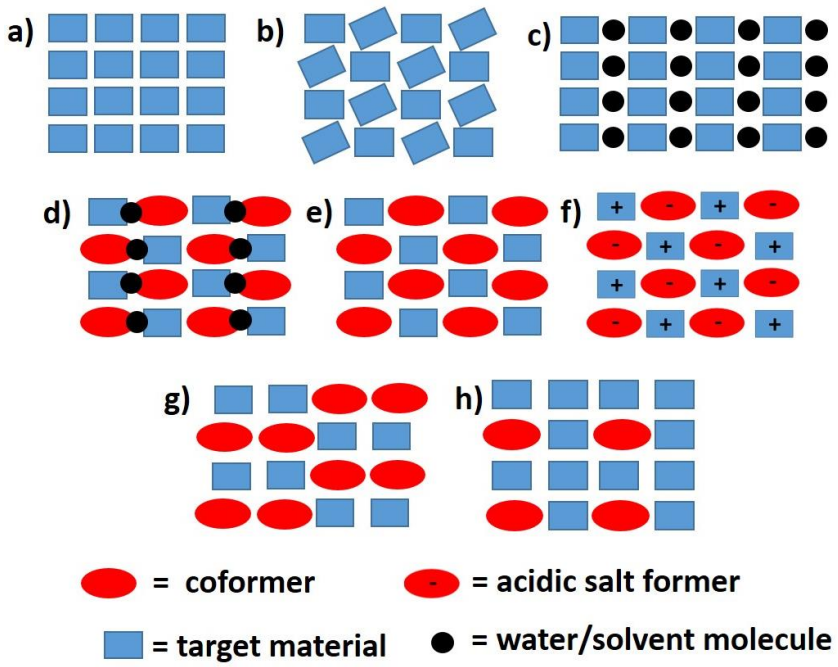

Figure 1.1 Schematic highlighting polymorphism and different types of multi-component molecular complexes (MMCs) showing (a) the target material, (b) polymorph (c) hydrate, (d) hydrated co-crystal, (e) 1:1 co-crystal, (f) salt, (g) 1:1 co-crystal polymorph and (h) 3:1 co-crystal.

1.3 Understanding Polymorphism in Crystalline Solids

Crystalline solids, including many important pharmaceutical and other functional molecular materials, can exhibit polymorphism; this is a common phenomenon in which crystalline solids containing identical molecular species can adopt different packing arrangements forming different crystalline forms or phases known as polymorphs. The discovery of polymorphism, in 1832 by Wohler and von Liebig's [16] study on benzamide, and its subsequent investigation, has been essential in many industries, not least in the pharmaceutical industry where polymorphism can affect physicochemical properties such as solubility, drug retention times and compression properties, not to mention implications in regulatory and patent documentation.[17, 18]

Although not widely known outside of the academic community, most people will have personally encountered polymorphism in products they use daily. One obvious example of contrasting physical

properties are the carbon polymorphs (allotropes) – soft graphite found in pencil lead and hard diamond used in jewellery [19]. Polymorphism is regularly found in any industry involved in the manufacture of crystalline products including washing detergents, pharmaceuticals, cosmetics and foodstuffs.

The orientation and packing of the molecular species within each polymorph are strongly reliant upon the intermolecular interactions between these species and this gives rise to variation in the relative stability and physicochemical properties between polymorphs. In structures comprising flexible molecular species, polymorphs can be formed *via* alterations in conformation about a single bond due to differing intermolecular interactions; this is commonly referred to as conformational polymorphism[2, 16, 20-22]. In essence, polymorphism is to crystal structures what isomerism is to discrete molecules and can present itself in single component materials and MMCs alike. It has been proposed that all crystalline solids are polymorphic, but in certain systems the conditions under which their polymorphic forms are obtainable have yet to be identified or cannot be achieved[23]. Compounds that have been studied in detail appear to display a higher degree of polymorphism than lesser studied compounds, likely to be due to increased knowledge, greater resources expended on exploring crystallisation conditions under which different polymorphs may be found, and an increased amount of experimental data[23, 24].

One medicinal molecule that exhibits significant polymorphism is 5-methyl-2-[(2nitrophenyl)amino]-3-thiophene carbonitrile, commonly known as ROY (for red-orange-yellow) (Figure 1.2).

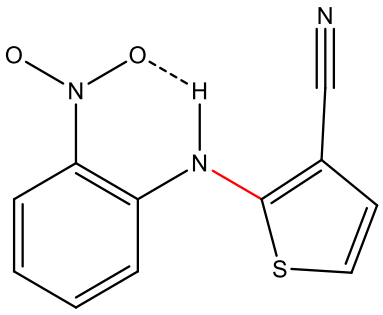

Figure 1.2 Molecular structure of ROY (conformational bond highlighted in red)

This flexible molecule, discovered accidentally by researchers at Eli Lilly in the early 90s[20], has ten known polymorphs to date, however that alone is not what caught the attention of crystal engineers. Each polymorph of ROY displays a different combination of crystal shape and colour ranging from red prisms to yellow needles, which is attributed to the conformational polymorphism of this molecule in the solid state. The alteration of torsion angles can affect the π-conjugation between the thiophene and phenyl rings which leads to a shift in the visible absorption spectra[19]. Earlier studies of coloured polymorphs were carried out on dimethyl-3,6-dichloro-2,5-dihydroxyterepthalate

(MCOHT) by Byrn et al. in 1972 [25]. This showed that MCOHT underwent a temperature induced transition between two different coloured polymorphs (Figure 1.3).

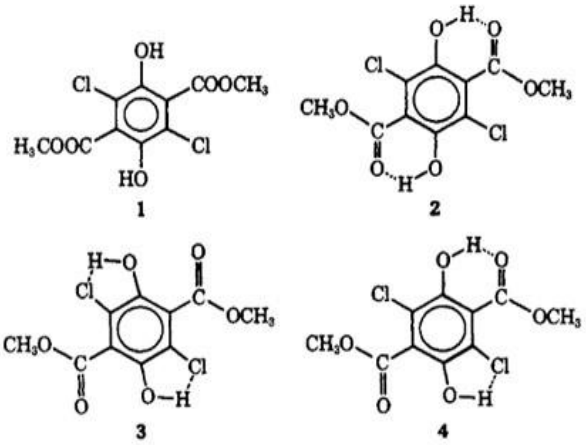

Figure 1.3 shows dimethyl-3,6-dichloro-2,5-dihydroxyterepthalate (1) the two polymorphs; yellow (2) and white (3) and their reactive intermediate (4)[25].

1.4 Thermodynamics of Polymorphism

As detailed in section 1.3 above, polymorphism is the phenomenon where the molecules of a material have the ability to crystallise in more than one arrangement to create different polymorphic phases which will have variation in thermodynamic stability due to the free energy of each form. In understanding the relative stabilities of polymorphs, and trying to control their formation, it is important to understand the underlying thermodynamics, while recognising that the formation of solid crystal forms is governed not only by thermodynamics but also by kinetics.

Properties governed by thermodynamics, relevant to the potentially different physical properties seen in different solid forms of a material, include the following:

- Melting points;
- Desolvation of adsorbed and bound solvents;
- Internal/structural energy, enthalpy, heat capacity, entropy, free energy, including surface free energy;
- Thermodynamic activity, including phase transitions (heats of transitions including melting and crystallisation, glass transitions for amorphous materials, polymorphic transitions);
- Vapour pressure;
- Solubility and hygroscopicity;
- Thermal expansion;
- Stability under processing conditions (including under different environments);
- Compatibility of materials (interactions between components).

All systems have an internal energy and it is possible to measure a change in the physical properties if they are accompanied by a change in this internal energy, by methods such as differential scanning calorimetry (DSC) (section 3.6). These changes can then be related to changes in the key thermodynamic parameters such as enthalpy and entropy. For example, transformation from a solid to a liquid (melting) results in a transfer of energy to the sample (endothermic process) in the form of heat. It is important to note that it is only possible to measure a difference in energy and not the absolute energy.

Thermodynamic properties can be classed as either extensive, whereby the value is dependent upon the mass of the sample present, or intensive when a value is independent of mass. For example the amount of heat required to melt 10 g of sodium chloride (NaCl) is an extensive value but if this value were divided by mass to give heat/g of NaCl this value will be true for any mass of substance, which is intrinsic to that material and is an intensive property. The difference in these properties across two systems can determine whether energy will be exchanged between the two systems and if so in which direction it will be exchanged. Temperature, for example, is a measure of the intensity of heat in a system (system A) and relative to the temperature of another system (system B) this will indicate how much heat will flow between system A and system B and which system will be the heat donor and which will be the heat acceptor. This is directly related to the Second Law of Thermodynamics, which states that no process is possible whose sole result is the transfer of heat from a colder to a hotter body (in the Clausius formulation), and is the basis for the definition of the thermodynamic quantity of entropy.

The First Law of Thermodynamics allows the energy differences to be quantified, as it states that "the total energy of a system and its surroundings must remain constant although it may be changed from one form to another". Critically, the First Law refers to both system and surroundings – there can be local changes in the energy of the system itself, which can be measured in experiments such as DSC.

The energy of a system is dependent upon the pressure, volume, temperature, mass and composition within that system, and since we measure differences in energy, we typically refer to quantities such as $\Delta E = E_{II} - E_{I}$, which would be the change in energy when transforming from one state to another (in this case as state I goes to state II).

Of the quantities that are commonly measured in looking at crystalline solid forms, their transformations and polymorphism, enthalpy is key. Enthalpy, H, is defined as U + PV, where U is the internal energy, and this shows that enthalpy is dependent upon the pressure and volume of a system. The quantity governing chemical transitions is the Gibbs free energy G.

G is defined as U – TS + PV = H – TS, and for a chemical process assumed to be isothermal (constant T), this leads to the common thermodynamic expression $\Delta G = \Delta H - T\Delta S$. The value of ΔG governs the thermodynamic spontaneity of chemical processes, the key condition for such spontaneity being that $\Delta G < 0$. However, since both ΔH and ΔS are dependent on temperature, and with T a primary parameter in the expression for ΔG, it follows that variation of temperature is one factor that can be used to control which chemical (or physical) state will be the most stable (minimising G). The same is true for pressure, but here we focus only on the variation in temperature.

As the temperature term is directly linked in this expression with entropy not enthalpy, then the term $T\Delta S$ will increase more rapidly than H leading to a more negative value of G with increasing temperature.

The free energy differs between polymorphs, the form with the lowest free energy being classed as the most thermodynamically stable, and due to the different thermodynamic characteristics of different solid forms, the relationship between the free energy and temperature also differs between polymorphs (Figure 1.4). This means that the free energy curves for different polymorphs (Forms I and II in the figure) may cross; at a given temperatures the two polymorphs may be isoenergetic in terms of free energy (shown by the point of interception in Figure 1.4), which would represent the phase transition temperature between the polymorphs.

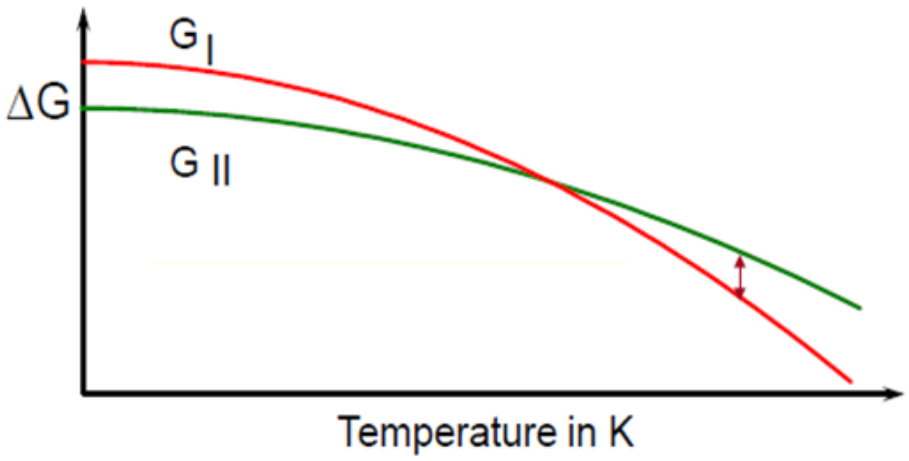

Figure 1.4 Schematic to highlight the variation in the relationship between free energy and temperature for different polymorphs

It is important to note that thermodynamics is not concerned with the rate of polymorph transformation (kinetics), but only the relative energies and stabilities of the polymorphs. Using the carbon allotropes diamond and graphite as an example, diamond is thermodynamically less stable than graphite, however it is the extremely slow kinetics of the transformation that allow diamond to persist in a metastable state.

1.4.1 *Solid-state Transitions Between Polymorphs: Enantiotropy and Monotropy*

Two polymorphs (termed A and B for this explanation) are defined as enantiotropic if the two phases can undergo a fully reversible solid state phase transition i.e. below the melting points of A and B there is a transition point ($T_{transition}$) at which the Gibbs free energies of A and B are equal (Figure 1.5, right). When $T < T_{transition}$, $G_A < G_B$ and thus polymorph A is more thermodynamically favourable however when $T > T_{transition}$, $G_B < G_A$ and so the stability is reversed with polymorph B now the most thermodynamically stable[24, 26].

On the other hand if polymorphs A and B are defined as monotropic they are related through an irreversible solid state phase transition where under all temperature conditions one form (A, for example) would remain the most thermodynamically stable and form B would always convert to form A, never the reverse (Figure 1.5, left).

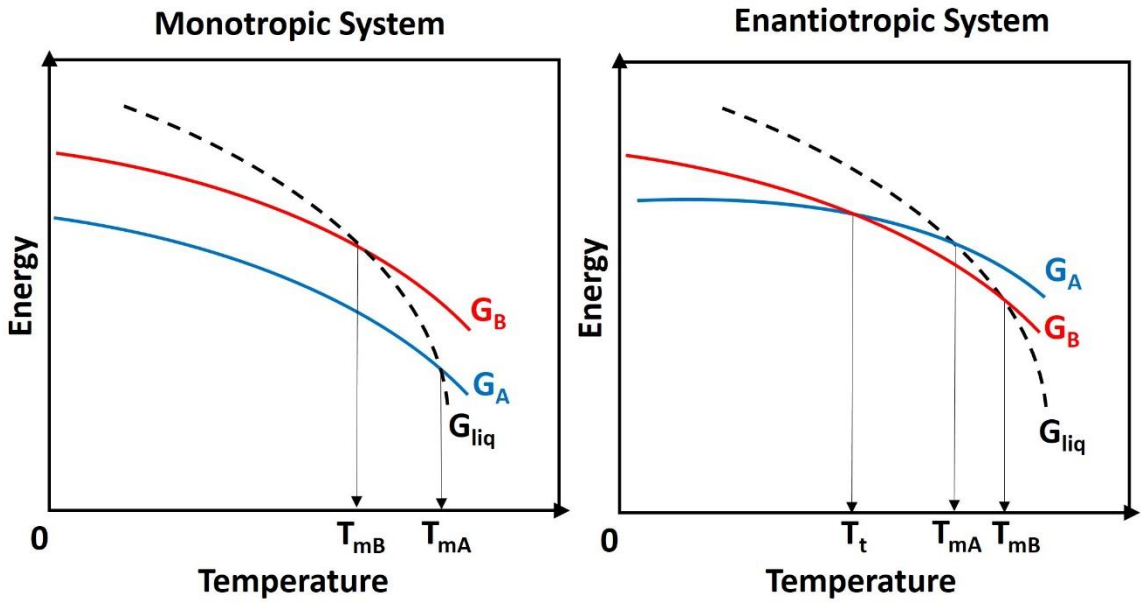

Figure 1.5 Plot showing relationship between energy and temperature for polymorph A (blue) and B (red) with a monotropic relationship and an enantiotropic relationship (where G_A, G_B and G_{liq} represent the free energy of polymorphs A and B and the liquid phase, T_{mA} and T_{mB} are the melting points of A and B and T_t is the temperature of the phase transition from A to B)

The stability ranges for a particular form (as a function of pressure, temperature and other variables such as composition) form the basis for the construction of phase diagrams, a key tool in using thermodynamics to guide studies of polymorphism and solid form control. Phase diagrams have not been determined during this work, and will not be discussed further here.

1.5 The Importance of Solid Form Control

Pharmaceutical manufacture and processing is heavily focused upon the control of the physical properties of the product (Table 1.1), including polymorphism. Physical properties can not only affect drug bioavailability and how the active pharmaceutical ingredient (API) interacts with the target in the body, but it also affects the manufacturing process itself[27]. Control is achieved by monitoring the physical properties using process analytical technologies (PAT) and tailoring the crystallisation conditions by using alternative solvents and additives, adjusting temperature and supersaturation or by changing the method of crystallisation altogether.

Table 1.1. Control of physical properties during manufacturing and potential effects on manufacturing, processing and the final product.

Physical property	Secondary effects
Crystal size	• Bulk powder flow • Rate of dissolution • Filtration
Crystal size distribution (CSD)	• Bulk powder flow • Filtration • Consistency of downstream processing
Crystal morphology	• Bulk powder flow • Agglomeration • Ease of downstream processing • Rate of dissolution
Surface properties	
Polymorphic form	• Bioavailability • Solubility • Melting point • Stability
Solvate formation	
Co-crystallisation	

It is important that polymorphs of the API and associated excipients can be isolated and controlled. This is achieved by using different crystallisation conditions, crystallisation techniques and/or additives. There is only one thermodynamically stable polymorph of a material; while there may be many metastable polymorphs, over time metastable forms will convert back to the most thermodynamically stable form. In order to prevent unwanted polymorphic conversion it is preferential to use the most thermodynamically stable form unless particular desired properties are exhibited in other less stable forms alone. Transformation can also occur in the presence of water or water vapour to form hydrates or can be in contact with solvent vapours in manufacturing processes to form undesirable solvates.

Control of the solid form is vital in drug delivery methods. For example, mannitol is used as a drug carrier molecule for APIs administered to the lungs using a dry powder inhaler (DPI). The efficiency of the API-carrier formulation is reliant upon the physical properties of not just the API but also the mannitol carrier crystals. Crystal size, morphology and properties of the crystal surface are influential on the success of mannitol as a drug carrier. Fine particles are required to reach lower areas of the lungs and the elongated rod morphology is useful in aiding deposition in the lungs. These properties are influenced by the crystallisation conditions in production, particularly the degree of supersaturation of the crystallisation solution [28].

Tableting of an API is also influenced by the solid form of the material; an example of this is the commonly used analgesic paracetamol. The most common polymorphic form of paracetamol is form I, however studies have shown that the more elusive polymorph, form II, is more readily compressed into tablet form due to its slip-layered structure especially in comparison to the interlocked concertina structure of form I (Figure 1.6) [9].

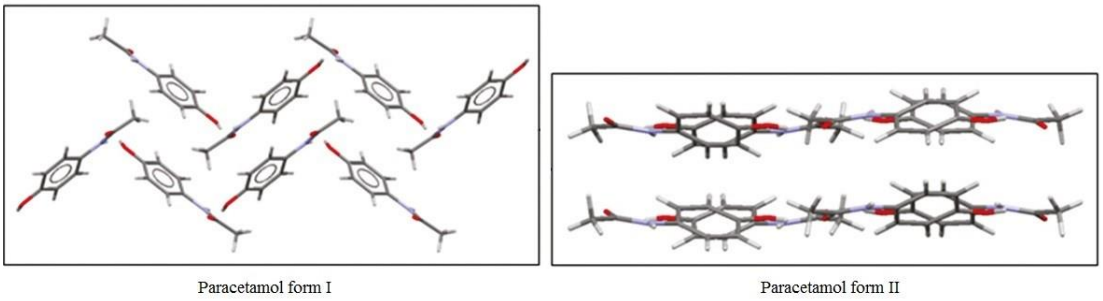

Figure 1.6 The interlocked concertina structure of paracetamol form I and the slip-layered structure of paracetamol form II[9].

Problems have been encountered in some cases due to a lack of polymorphic control. Norvir®, a brand of the protease inhibitor ritonavir, a part of an AIDS treatment preparation, was produced successfully for two years, prior to a new thermodynamically stable polymorph emerging in the manufacturing process. The presence of this more thermodynamically favourable form meant that the original polymorph could no longer be produced and the thermodynamically stable polymorph had reduced solubility and bioavailability in comparison. Re-formulation of the drug was required and in the interim the drug had to be removed from the market reducing profit to the manufacturer and, more importantly, reducing the availability of an important AIDS treatment[24, 27].

1.6 Functional Materials; Optimisation of Solid State Properties of Molecular Materials

Functional crystalline materials have a wide variety of applications, from food additives to explosives, each reliant on a specialist function that has been heavily influenced by its crystal structure (Table 1.2). Some applications have been discussed in more detail below.

Pharmaceuticals and Agrochemicals

An important property of many crystalline products is their aqueous solubility. In pharmaceuticals this is important in enabling an API to dissolve readily when administered orally and to ensure efficient and consistent uptake into the body. Similarly, the active agrochemical ingredient (AAI) in agrochemical products is usually hydrophilic and delivered to the crop in an aqueous solution, though in some cases it may be important to form a lipophilic crystal to enable the AAI or API to bind to animal tissues. Many APIs and AAIs initially have poor aqueous solubility, but through crystallisation with co-formers to form salts and co-crystal it is possible to increase their solubility (see section 7.5 for an example)[29, 30].

Energetic materials

Energetic materials including explosives and propellants are used as components in fireworks, munitions and for demolition. It is important to regulate the sensitivity of these materials to ensure that detonation occurs in a controlled manner and only when required. Polymer binders are often used to enclose crystals of the energetic material acting as a shock absorber, alternatively sensitivity can be reduced through co-crystallisation to alter the crystal structure of the material. Studies have produced 1:1 co-crystals of hexanitrohexaazaisowurtzitane (CL-20) and trinitrotoluene (TNT) which exhibits a reduction in sensitivity in comparison to its constituents whilst maintaining the same explosive intensity[31].

Pigments and Dyes

The colour of crystalline solids can be tuned by altering conjugation of systems and adjusting π-π stacking arrangements the crystal structure through polymorphism and co-crystallisation. This can induce intense colour in crystalline materials which proves particularly useful in pigment and dye manufacture. An example of this is a molecular complex formed between 4-cyanopyridine and squaric acid, both off-white in colour, which involves a 4-cyanopyridinium cation and a singly deprotonated squaric acid mono-anion and is red in colour. The colour is believed to be caused by a shift in a charge transfer band due to the layered structure of homodimers of the squarate anion[32].

Porous materials

In recent years metal organic frameworks (MOFs) have emerged as an important area of materials chemistry due to their porous nature which provides potential for gas storage, especially carbon dioxide and hydrogen gases. MOFs lend themselves to this function due to their stability and high surface area and their functionality can be readily modified through crystallisation to tailor them to adsorb particular molecules[33].

Table 1.2 Properties that can be controlled in functional materials.

Property type	Property	Examples of application domains
Chemical	Chemical and photochemical reactivity or bioavailability	Photography Pharmaceutical Agrochemicals Explosives Catalysts
Kinetic	Stability, kinetics of solid state reactions, rate of dissolution	Explosives Pharmaceuticals Agrochemicals Fast moving consumer goods
Physical and Thermodynamic	Thermal and electrical conductivity, Melting point, thermal stability, heat capacity, solubility, hygroscopicity, free energy and chemical potential, vapour pressure.	Electronic devices Pharmaceuticals Agrochemicals Fast moving consumer goods Dyes and pigments
Spectroscopic	Rotational, vibrational and electronic properties and spectral features in nuclear magnetic resonance.	Dyes and pigments Optically active materials
Mechanical	Hardness, compression and thermal expansion	Electronic devices Pharmaceuticals Gas storage Fast moving consumer goods Explosives
Surface	Crystal morphology, surface area, surface free energy, CSD.	Gas storage Catalysis Pharmaceuticals Agrochemicals Fast moving consumer goods

1.7 Intermolecular Interactions

As stated previously, intermolecular interactions are fundamental to formation of molecular crystalline solids whether they contain only a single molecule type or are multi-component molecular complexes. The interactions to be described in this section can also occur between non-bonded atoms within the same molecule, termed intramolecular interactions. Intramolecular interactions are not as common as intermolecular interactions but can alter the conformation of molecules within a crystal and can give rise to conformational polymorphism[2] (section 1.3).

1.7.1 Hydrogen Bonding

The first mention of the term "hydrogen bond" was made in 1930 by Pauling[34]. Though it goes against basic valence bond theory that a hydrogen atom should form more than one chemical bond, Pauling said that the hydrogen bond affected by two "parent" atoms and not just one could act like a bond between the two atoms, known as a hydrogen bond[35]. A hydrogen bond is comprised of a donor atom (D) bonded covalently to the hydrogen atom (H) attached to acceptor atom (A), where H is deficient in electron density as a result of the higher relative electronegativity of D. As a result of this difference in electronegativity the D-H bond contains an induced dipole which interacts with the concentrated electron density, e.g. a lone electron pair or other polarisable electrons, of the acceptor atom (A) (Figure 1.7(i))[34, 36, 37]. Though H is initially covalently bonded to D, in a hydrogen bond H can be located at position equidistant from D and A or in some cases it can even undergo proton transfer by which H moves to be located on A rather than D (Figure 1.7(ii)). It also possible that hydrogen bonds can form between one donor site and multiple acceptor sites. A hydrogen bond with two acceptor sites is known as a three-centre bond or more commonly as a bifurcated hydrogen bond[36] (Figure 1.7(iii)).

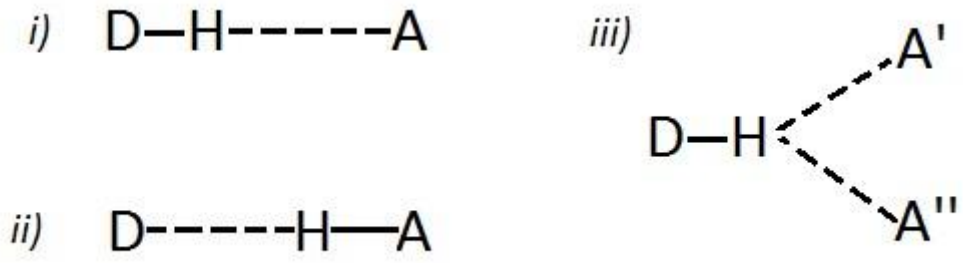

Figure 1.7 Different variations in hydrogen bonding between hydrogen donor atom D and hydrogen acceptor atom A. i) standard hydrogen bond, ii) hydrogen bond that has undergone proton transfer, iii) bifurcated or three-centred hydrogen bond.

Hydrogen bonding is the most versatile of intermolecular interactions, due to a wide range of possible donors and acceptors and varying bond strengths, and it is additionally valued for its directionality[38]. This diversity has made defining a hydrogen bond a challenge, which has led to a variety of definitions over the years. Steiner adjusted the definition previously proposed by Pimental and McLellan by stating that *'An X-H…A interaction is called a "hydrogen bond", if it constitutes as a local bond, and X-H acts as a proton donor"* rather than an electron donor[36, 39]. More recently, in 2011, IUPAC (the International Union of Pure and Applied Chemistry) defined the hydrogen bond as "*an attractive interaction between a hydrogen atom from a molecule or a molecular fragment X–H in which X is more electronegative than H, and an atom or a group of atoms in the same or a different molecule, in which there is evidence of bond formation.*"[40].

Hydrogen bonds vary widely in strength but can be loosely categorised through a system devised by Jeffrey (Table 1.3), in which the strength of a hydrogen bond is classified by the distance between the donor and the acceptor atoms. There are three ranges, corresponding to strong, moderate and weak hydrogen bonds. Hydrogen bonds of D···A distances of <2.5 Å are classed as strong and can resemble covalent bonding, while the weak bonds of D···A distances of 3.2 Å to 4 Å are electrostatic in character and are similar to van der Waals forces. The intermediate region between 2.5 Å and 3.2 Å is where the vast majority of interactions lie and these are classified moderate hydrogen bonds which are mostly electrostatic in nature[36, 39].

Table 1.3. Classification of hydrogen bonds into strong, moderate and weak categories[36].

	Strong	**Moderate**	**Weak**
A–H···B interaction	Mostly covalent	Mostly electrostatic	Electrostatic
Bond lengths	A–H ≈ H···B	A–H < H···B	A–H << H···B
H···B bond length (Å)	~1.2-1.5	~1.5-2.2	2.2-3.2
A···B bond length (Å)	2.2-2.5	2.5-3.2	3.2-4.0
Bond angles (º)	175-180	130-180	90-150
Bond energy (kcal mol^{-1})	14-40	4-15	<4

1.7.2 Van der Waals Interactions

Van der Waals (vdW) interactions are attractive or repulsive intramolecular or intermolecular interactions which are relatively weak in comparison to covalent bonds. vdW interactions can be subdivided into three categories due to variations in the polarisability of the interacting species (Table 1.4).

Table 1.4. Categorization of Van der Waals interactions.

Interaction type	Species 1	Species 2
Keesom forces	Permanent dipole	Permanent dipole
Debye forces	Permanent dipole	Induced dipole
London dispersion forces	Instantaneously induced dipole	Induced dipole

Keesom forces, more commonly referred to as dipole-dipole interactions[41], are highly dependent upon the orientation of the polarised molecules; they must be precisely aligned before they can interact and the strength of this interaction is also contingent of the distance between the interacting species. In comparison Debye forces are not as dependent upon orientation. The electrons of a non-polar molecule can readily respond to the presence of a polar molecule which induces polarity of the electron cloud of the initially non-polar molecule. London forces, also known as dispersion forces, occur between non polar uncharged molecules due to transient dipoles present due to instantaneous movement of the positions of their electrons, known as instantaneous dipoles. The presence of the instantaneous dipole can bring about a dipole in a neighbouring non-polar uncharged molecule generating an induced dipole which is attracted to the instantaneous dipole lowering the potential energy of the molecular pair[42].

1.7.3 π-π stacking Interactions

π-π stacking interactions are weak in comparison to hydrogen bonding interactions, but are also of importance. They can play a vital role in the packing of layered structures as the interactions occur between stacked aromatic rings. π-π stacking is fundamental in biological structures, for example acting between the aromatic rings of stacked nucleobases within DNA helping to stabilise the double helix conformation.

Mostly governed by London dispersion forces[43], π-π stacking interactions between aromatic rings involve polarisation of the delocalised π-electron clouds which induces a dipole moment allowing the two rings to interact[44]. The presence of electron donating or electron withdrawing groups on the aromatic rings can significantly affect the polarisation of the electron cloud and influences the orientation of the interaction. There are three prevalent orientations by which aromatic rings can assemble through π-π stacking interactions, T-shaped, off-centred and centred (Figure 1.8a, b and c). The orientation of the assembly and the presence of electron donating or withdrawing substituents on the ring has the potential to alter the intermolecular bonding capacity of the molecules. Off-centred and T-shaped configurations are more favourable than the centred configuration due to the reduction in π-electron overlap which reduces the repulsion between the rings.

The presence of electron withdrawing substituents on the aromatic ring can help to improve π-π stacking interactions when in the centred configuration (Figure 1.8d). It was found in studies by Mignon *et al*. that the off-centred parallel configuration improved the potential of a nucleobase for hydrogen bonding especially if there were electron donating substituent present on the aromatic ring[43].

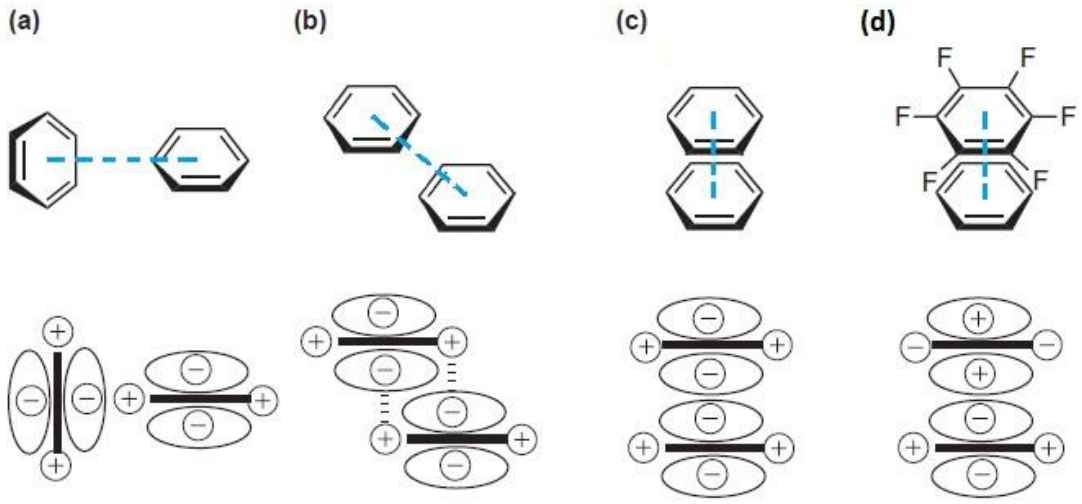

Figure 1.8. Prevalent orientation of aromatic rings through π-π stacking interactions. a) T-shaped, b) off-centred c) centred d) centred with electron withdrawing substituents[45].

2 Introduction II – Crystallisation

2.1 Supersaturation

A solution in thermal equilibrium with the solid phase (for a fixed temperature) is termed a saturated solution. If a hot saturated solution was cooled down in a controlled manner and without agitation it is possible for the solute to remain in solution. The solution would now contain more dissolved solid than is expected for a solution in thermal equilibrium at the new, lower temperature, a state known as supersaturation, which is an essential part of all crystallisation processes[46]. A solution in the supersaturated state can be subcategorised as either labile or metastable (Figure 2.1), the classification depending on whether crystals can nucleate (labile) or not (metastable); in both cases they can grow larger from seeds, if such are present. There is a higher precipitant concentration in the former (labile) than the latter (metastable) case, and crystallisation will not normally occur in the metastable situation, while it can occur in the labile case[47, 48].

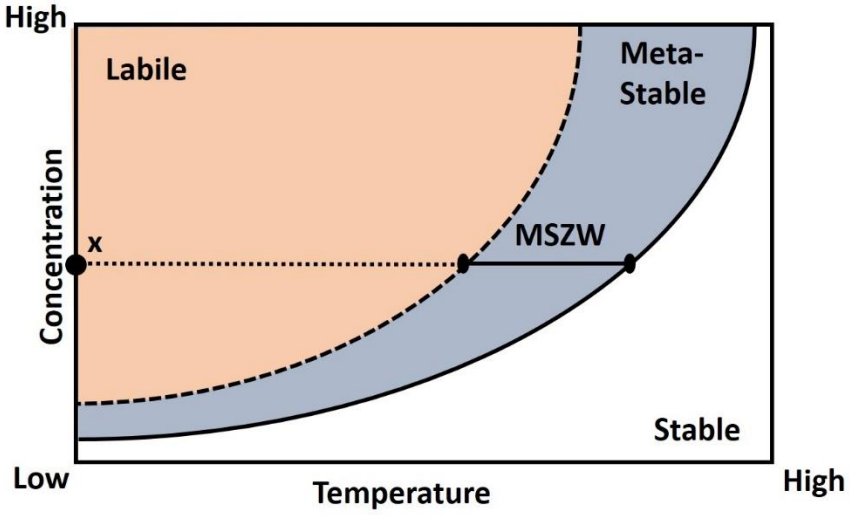

Figure 2.1 Schematic to show the solubility and supersolubility curves in relation to solution concentration and temperature and to illustrate the concept of metastable zone width (MSZW).

The solubility curve can be derived from measurements of the clear point (point of dissolution) of a solution at a range of solute concentrations. It is well defined for a single component, with little variation due to factors other than temperature or concentration. The supersolubility curve, obtained from the solution cloud point (point of recrystallisation) can be influenced by external factors such as the rate of supersaturation, e.g. the cooling rate and the agitation intensity. This externally dependent nature often means that the supersolubility curve is poorly defined; it can prove particularly challenging to define the supersolubility in multi-component or polymorphic materials[46]. During the dissolution process of a multi-component material it is likely that the two species will dissociate, and depending upon the stability of the two components, it may be more favourable for one or both of the species to recrystallise separately. In such a situation the supersolubility

measurement obtained is therefore of the single species rather than the multi-component material. A similar complication can occur in polymorphic materials, for example where an initial polymorph (polymorph A) is dissolved to obtain the solubility measurement, but when the material recrystallises it may transform to a second polymorph (B) and consequently the supersolubility measurement corresponds to polymorph B rather than polymorph A.

The metastable zone is the region between the solubility and supersolubility curves and the metastable zone width (MSZW) indicates the amount of undercooling that a solution can experience prior to nucleation commencing. As it is related to the position of the supersolubility curve the MSZW varies with a range of external factors as mentioned previously. As the variation of solubility with respect to temperature and concentration is not proportional to the variation of supersolubility with respect to temperature and concentration then it follows that the MSZW can vary with saturation temperature (Figure 2.1). It is therefore important when designing a crystallisation process to balance the temperature and concentration and also consider the size of the MSZW that corresponds to those conditions. The MSZW can be calculated using a range of different apparatus but this can only be used as a guide as the values are highly dependent upon the method of detecting the cloud and clear points, of which the most common are focussed beam reflectance measurements (FBRM), particle visualisation measurements (PVM), or visually by eye.

Supersaturation can be quantified using the concentration driving force (Δc) (Equation 1), the supersaturation ratio (S) (Equation 2) and the relative supersaturation (σ) (Equation 3) as highlighted below.

$$\Delta c = c - c^* \qquad \textbf{Equation 1}$$

$$S = c/c^* \qquad \textbf{Equation 2}$$

$$\sigma = \Delta c / c^* = S - 1 \qquad \textbf{Equation 3}$$

Where c is the solution concentration and c^* is the concentration at equilibrium saturation for a specified temperature. It should be noted that the fundamental driving force of crystallisation is the difference in chemical potential (μ) of the starting and ending states of a given material (i.e. $\mu_{solution} - \mu_{crystal}$).

2.2 Nucleation

Nucleation is the "*generation of a new solid phase from a supersaturated homogeneous mother phase*"[49]. The mechanism by which nucleation occurs is not completely understood. There are two types of nucleation (Figure 2.2); primary nucleation, in which nucleation occurs in a system which does not contain any previously formed crystalline matter, and secondary nucleation whereby nucleation occurs on or near to previously formed crystalline material[46].

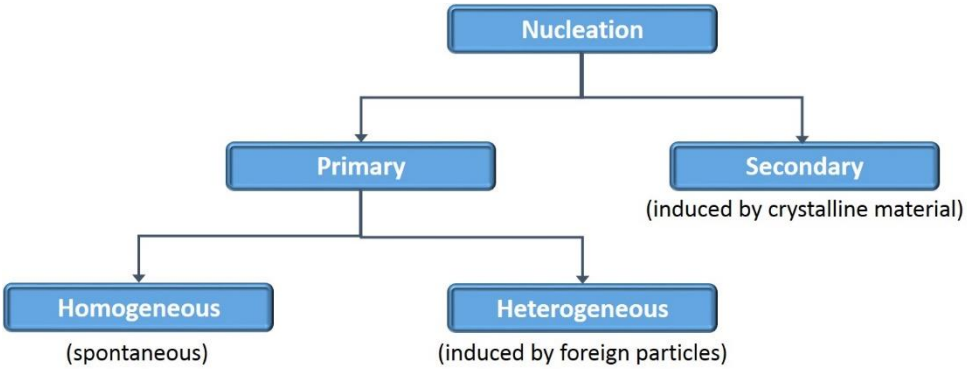

Figure 2.2 Schematic showing the classification of nucleation.

2.2.1 Primary Nucleation

Primary nucleation can be further divided into homogenous nucleation and heterogeneous nucleation. Homogeneous nucleation is the spontaneous nucleation of crystal from within a single phase, for example, a saturated homogeneous solution[46, 50, 51]. It is uncertain how the initial crystalline nuclei are formed, though it is unlikely that the molecules that make up a nucleus should collide with exactly the right force at precisely the right time to generate a periodic crystalline solid. Instead it has been proposed that it should arise from a consecutive chain of "bimolecular additions"[46] which build up to form a crystal cluster or nucleus until the nucleus reaches critical size. This theory was originally developed to understand the condensation of a vapour to a liquid but was later adapted to crystallisation and termed Classical Nucleation Theory (CNT). For each system there is a specific size of cluster that allows the nucleus to become self-sustaining and hence grow; this is termed the critical nucleus and its size is a function of various factors including the types of molecules involved and the degree of saturation of the solution. Upon subsequent addition to this critical nucleus the free energy barrier (ΔG^*) to nucleation would be overcome and nucleation would be induced (Figure 2.3)[52].

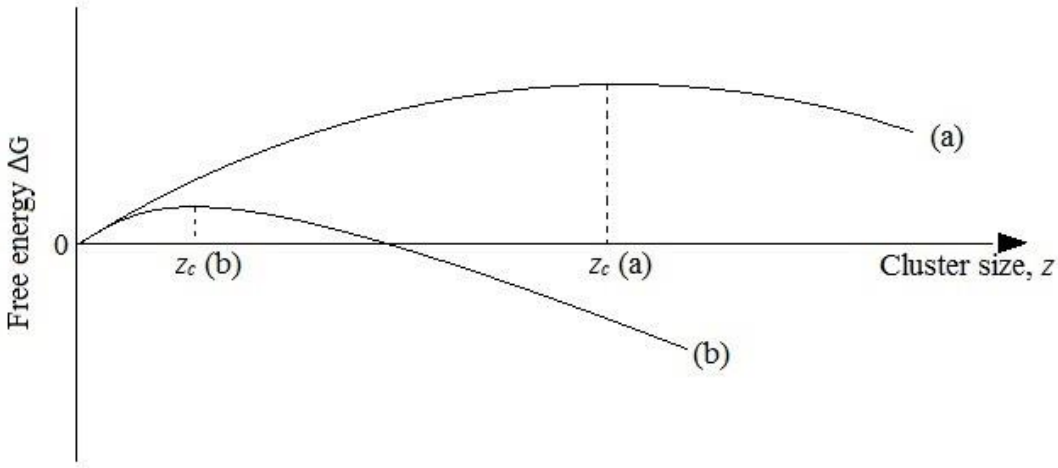

Figure 2.3. Illustration of the change in free energy as a function of supersaturation and crystal cluster size, where (a) depicts a system at low supersaturation, (b) depicts a system at high supersaturation and Z_c is the cluster size of the critical nucleus under the different conditions.

This process occurs rapidly at localised supersaturated areas within the system, however until the nuclei formed reach critical size they are deemed unstable and prone to dissolution back into the system[46]. The formation of numerous crystallites below critical size increases the free energy within the system which is thermodynamically unfavourable and so to counteract this they dissolve back into solution. If clusters grow larger than the critical size, they bring about a decrease in the free energy within the system and now the process of nucleation becomes thermodynamically favourable and spontaneous[52]. True homogeneous nucleation is rare, nucleation is often unknowingly induced by dust and particulates in the surrounding environment[46]. Therefore it should be classed as heterogeneous nucleation which refers to any nucleation induced by foreign surfaces or particles e.g. the impurities present in solution or a scratch on the surface of a crystallisation vessel[51].

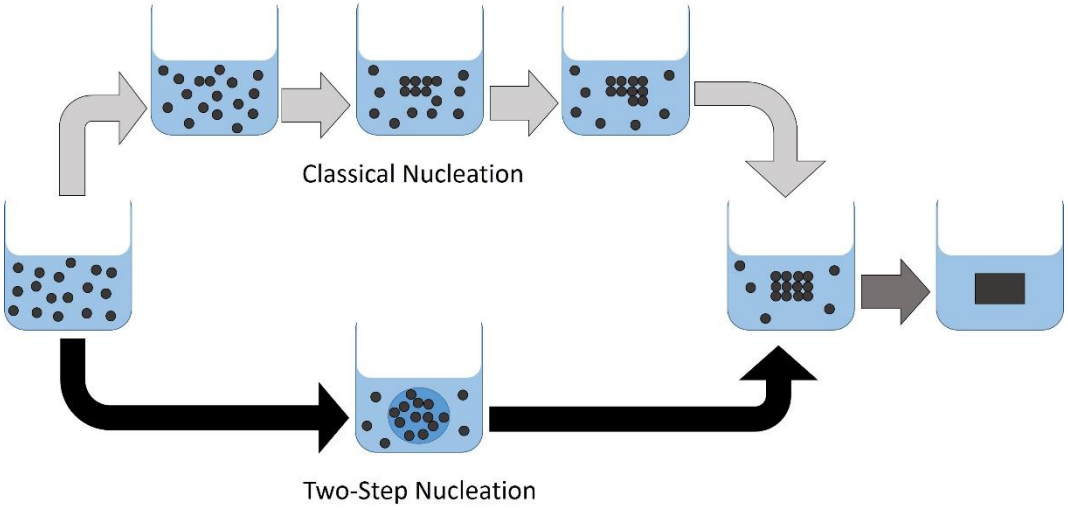

Figure 2.4 Schematic to show the nucleation process following Classical and Two-Step nucleation theories.

There are several assumptions used by CNT that in recent years computational and experimental investigations have called into question and suggested that the theory of nucleation needs to be reconsidered. One of the proposed theories is the two-step nucleation theory, also referred to as multi-step nucleation theory (MNT)[53, 54] whereby a dense liquid cluster of solute molecules is produced and once at a critical size the solute cluster reorganises to produce an organised crystalline nucleus within this droplet (Figure 2.4).

2.2.2 Secondary Nucleation

Secondary nucleation occurs in the presence of pre-formed solute crystals in a supersaturated solution, which facilitate nucleation allowing it to take place more readily at lower supersaturation values than those required for primary nucleation[46, 55]. The addition of a small quantity of seed crystals can give rise to a significant and unproportioned increase in the number of new nuclei created a process referred to as crystal breeding[53]. Numerous factors have been proposed to induce secondary nucleation processes (Table 2.1) but currently a definitive mechanism for secondary nucleation has not been adopted by the scientific community.

Table 2.1. Factors inducing different types of secondary nucleation

Type of Secondary Nucleation	**Cause**
Initial breeding	Seeded by dust or small crystallites present on the surface of parent crystals.
Needle breeding	Seeded by dendritic crystallites fractured from the parent crystals.
Polycrystalline breeding	Seeded from breakage of irregular polycrystalline agglomerates.
Shear nucleation	Fluid shear occurring at a growing crystal face can remove the loosely ordered boundary layer which then acts as a crystal nucleus.
Contact nucleation	Collision breeding from crystal to crystal contact or contact between crystal and crystalliser apparatus.

Three main processes control the rate of secondary nucleation: generation of secondary nuclei at or in close proximity to a solid phase; removal of generated clusters; and formation of a new solid phase from crystal growth. These processes are affected by the degree of supersaturation, the cooling rate, any agitation used and the presence of any impurities within solution[55].

2.3 Crystal Growth

As for nucleation, there is no single distinct model for crystal growth, instead there are numerous postulated theories; many of these are based around an understanding of the attachment of molecules onto crystal faces, and models of such attachments make distinctions between different modes of attachment, for example as represented by steps, kinks and flats in the Hartman and Perdock Classification (Figure 2.5).

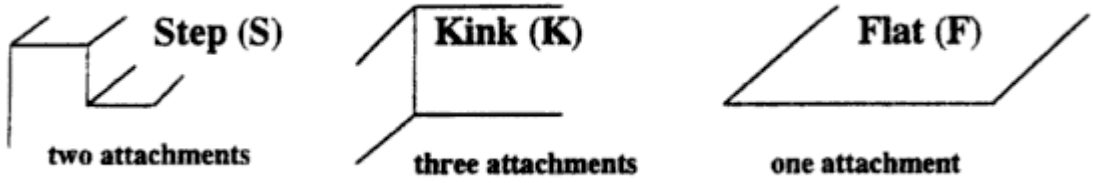

Figure 2.5 The Hartman and Perdock classification of crystal faces.[56]

Initial crystal growth mechanisms were based upon the presence of an adsorbed solute layer at the solid-liquid interface of crystal nuclei. The Gibbs-Volmer theory proposes that molecules of solute adsorb to the crystal surface but do not bind fully, enabling them to move across the surface of the crystal. The solute molecules migrate to active sites, e.g. to a site where another molecule is adsorbed to the surface, facilitating attractive interatomic or intramolecular forces to hold the molecules in place[46]. This builds to form a circular aggregation of solute molecules known as a two dimensional nucleus which can be described by two dimensional nucleation theory. Similarly to its three dimensional equivalent, classical nucleation theory, two dimensional nucleation theory is based upon the two dimensional nucleus reaching a critical size beyond which the Gibbs free energy favours the growth of the cluster. The monolayer of solute molecules spreads to cover the whole crystal face which has been described by three possible models; mononuclear growth, polynuclear growth and the birth and spread model (Figure 2.6)[55].

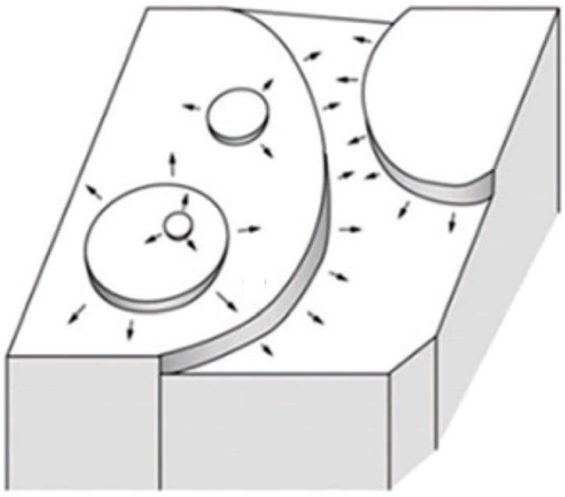

Figure 2.6 schematic to illustrate the Birth and spread model.[57]

A growing crystal surface can also be modelled as a series of stepped monolayers that appear to move continuously across the crystal surface due to solute adsorption, this is known as the Kossel model. Kinks present in the step edges are favoured adsorption sites for solute units. The kinks propagate along the edge of the step until the surface is completed. The likelihood of crystal growth occurring by this model is low as it would only be feasible at high supersaturation due to dependence upon surface nucleation and it also relies upon the presence of defects at the crystal surface which will reduce over time[46].

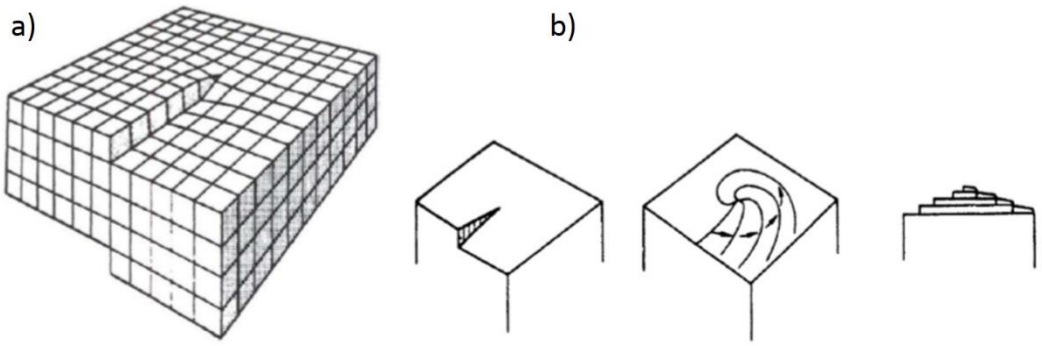

Figure 2.7 Showing a screw dislocation (a) and the self-perpetuating spiral (b) involved in spiral growth mechanisms[46].

Three dimensional theories that abandon the monolayer approach are available, including the Burton-Cabrera-Frank surface diffusion model and the Chernov bulk diffusion model that are both based upon a self-perpetuating growth spiral. The spiral is formed by the presence of steps formed by crystal dislocations (Figure 2.7 a), in particular a screw dislocation which allows the crystal face to grow continuously round in a spiral (Figure 2.7 b) as the screw dislocation acts as a kink site to which it is favourable for new solute molecules to adhere[46].

In addition to nucleation and growth the process of Ostwald ripening (also referred to as ripening or coarsening) can occur whereby smaller particles dissolve and larger particles increase in size. This process is thermodynamically driven by the minimisation of the surface energy of the system. Smaller particles have a higher surface area to volume ratio resulting in a higher surface energy making them less stable than the larger particles. The unstable small particles are thus more likely to dissolve into solution and, supersaturation levels permitting, in the Ostwald ripening model these molecules will tend to adhere to the more stable larger particles further minimising the surface energy (Figure 2.8). Over time this results in an overall increase in the mean particle size distribution[58, 59].

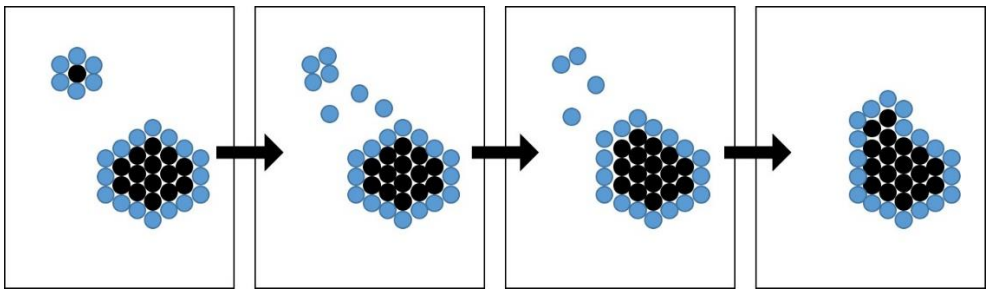

Figure 2.8 Schematic of Ostwald ripening of crystalline particles in solution (Stable bulk molecules and less stable surface molecules are shown in black and blue, respectively).

2.4 Methods of Multi-component Crystallisation

2.4.1 Evaporative Crystallisation

A principal technique used in discovery and crystallisation of multi-component crystalline materials, evaporative crystallisation generates a range of conditions which can yield mixtures of different crystal forms. This is particularly useful from a discovery perspective (production of new solid forms, for example of MMCs), however it can prove a challenge when aiming to implement selective control over a crystallisation process. As a result large scale evaporative crystallisation has not seen any substantial development within the pharmaceutical and fine chemical industries.

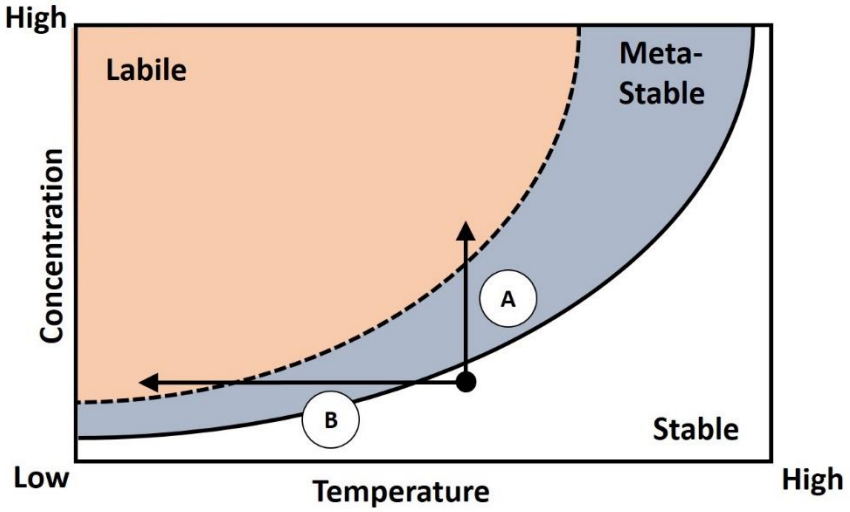

Figure 2.9 Inducing nucleation via supersaturation using evaporation (a) and cooling (b).

The evaporative crystallisation process involves dissolving one or more components in a chosen solvent or solvent mixture to generate an undersaturated solution. The solution is left open to the atmosphere at a fixed temperature and as the solvent evaporates the saturation increases reaching a state of supersaturation, inducing nucleation and crystal growth. At the point of nucleation the solution concentration momentarily decreases due to the removal of solute as solid, but returns to a supersaturated state due to the ongoing evaporation process (Figure 2.9, path A).

There are many variables in evaporative crystallisation including solvent of crystallisation, saturation temperature, concentration, temperature of evaporation, which all have significant effects upon the point of supersaturation and the rate of nucleation. The rate of evaporation, governed by the temperature and crystallisation vessel, has a considerable impact on the crystal size and crystal habit. The methods are often applied in parallel crystallisations covering a range of the possible variables using temperature controlled devices including hot plates fitted with DrySyn® holders (Figure 2.10).

Figure 2.10 Temperature controlled evaporative crystallisation carried out in 7 mL glass vials using custom designed DrySyn® holders (Asynt Ltd.) on hotplates at a range of temperatures, allowing the parallel exploration of a range of crystallisation variables.

2.4.2 Cooling Crystallisation

The principles of cooling crystallisation are similar to those of evaporative methods, but the method is in many senses complementary. In this case the supersaturation is generated by cooling the solution, thereby reducing the intrinsic solubility of the solute and hence reaching a state of supersaturation, inducing nucleation and crystal growth (Figure 2.9, path B). In comparison to evaporative crystallisation techniques it is possible to afford more control over the crystallisation process as the rate of cooling can be accurately controlled. If the MSZ is identified (by determining the solubility and supersolubility curves) it is possible to cool to the labile zone to induce nucleation and then control the cooling profile to remain within the meta-stable region which promotes crystal growth and reduces spontaneous primary nucleation and often leads to enhanced crystal attributes. For this reason cooling crystallisation has been the main technique used in industrial crystallisation, particularly in the pharmaceutical industry and many continuous crystallisation technologies have been developed with this in mind.

Figure 2.11 ReactArray Solo Microvate reaction block for temperature-controlled crystallisation.

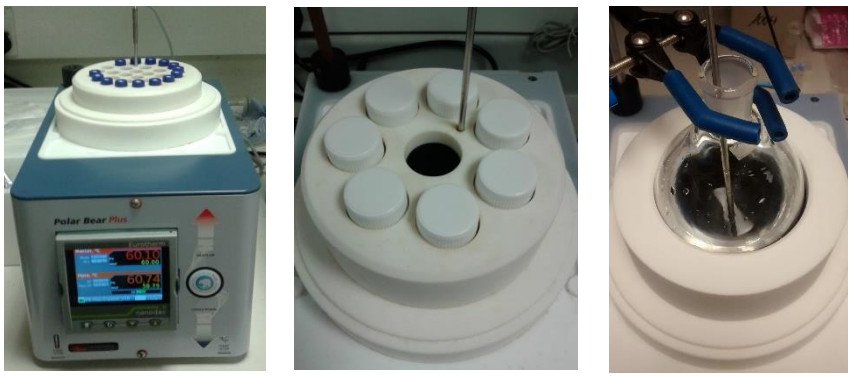

Figure 2.12 Cooling crystallisation using the Cambridge Reactor Design (CRD) Polar Bear Plus on a range of scales. (2 mL 20 mL and 100 mL)

Typical small scale cooling crystallisation apparatus (Figure 2.11 Figure 2.12) includes the Cambridge Reactor Design (CRD) Polar Bear Plus which, using interchangeable vessel holders, facilitate scale-up of cooling crystallisation from 2 mL up to 500 mL. These pieces of apparatus have helped to bridge the gap between small scale crystallisation required for materials discovery and industrial scale cooling crystallisation.

2.4.3 Anti-solvent Crystallisation

The final method of crystallisation to be described here is that of anti-solvent crystallisation. During such a process, the supersaturation required to induce nucleation is created by adding a second solvent to the system, in which the target is poorly soluble, known as an anti-solvent or non-solvent. The overall solubility of the solvent in the now-mixed solvent system is lower, hence again reaches a state of supersaturation, inducing nucleation and crystal growth (Figure 2.13, path C).

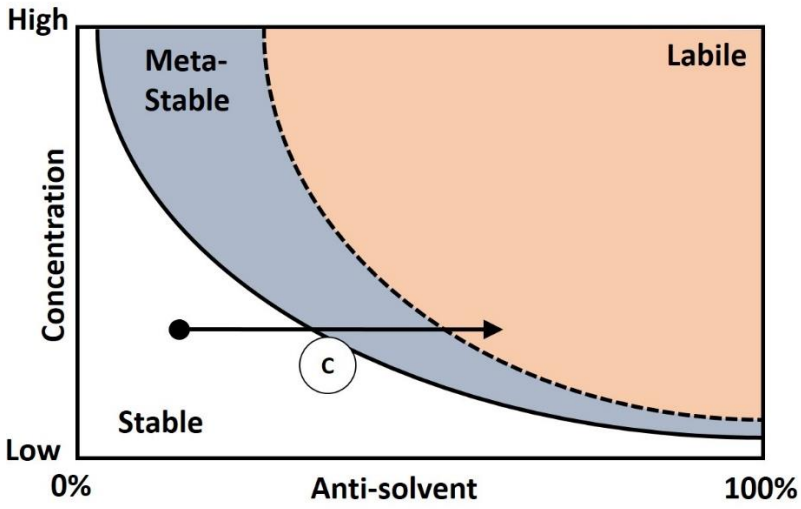

Figure 2.13 Inducing nucleation via supersaturation using anti-solvent addition (c).

Anti-solvent crystallisation is not as well studied as cooling crystallisation, but proves particularly useful in materials where there is little variation in solubility with temperature[60, 61]. It is also a favoured method for crystallisation of materials that are unstable at high temperatures. Industrially it is often used in combination with cooling[61] and has been used in a range of studies as a route to control of morphology, CSD[62] and in some cases as a route to polymorph control[63]. With inherently rapid nucleation kinetics, anti-solvent crystallisation can allow access to metastable polymorphs that can often be difficult to obtain using other crystallisation techniques[64-66]. Anti-solvent crystallisation can also be added as a final step to enhance the yield of the crystallisation process[67, 68].

2.4.4 Mechano-crystallisation

Mechano-crystallisation, which is commonly referred to as grinding or kneading, has proven to be a useful route to rapid screening for co-crystals[69, 70], as demonstrated by Caira *et al.* in a co-grinding study on sulfadimidine and a range of aromatic carboxylic acids[71]. The heat and pressure generated by these processes can enable intermolecular interactions in the original materials to be weakened affording freedom to the molecules which can orientate to form other more favourable intermolecular interactions. This can result in either a new polymorph of either of the starting components or formation of an MMC. It is important to note that mechano-crystallisation can allow access to solid forms that would have remained unidentified if only solution crystallisation techniques were used.

The crystallisation processes can take a matter of minutes or may take days of mechanical action. This can be facilitated by addition of a few drops of solvent which helps to solubilise some of the material, acting as a plasticiser, and is termed solvent-drop grinding or liquid assisted grinding (LAG). Apparatus for mechano-crystallisation (Figure 2.14) varies from a basic pestle and mortar to ball mills and single or twin screw extruders. The choice of milling equipment and the material from which it is made will have a significant effect on both the conversion and the rate at which it occurs.

Figure 2.14 Apparatus used for mechano-crystallisation.

The mechanism of mechano-crystallisation is still not well understood. Models for this mechanism are based upon the effect of mechanical work on the material; this has two effects: (i) disrupting the intermolecular interactions, breaking down the crystalline order and allowing for the generation of new intermolecular interactions, for example allowing molecular complex formation; and (ii) introducing localised hot-spots of increased heat and pressure. The material thus often becomes significantly less ordered, for example adopting an amorphous state, prior to recrystallisation. If an amorphous solid form is desired, which has become common in recent years, cryo-grinding can be used as the reduced temperature is said to help prevent recrystallisation and reordering of the material. In essence this represents the converse of LAG.

Research by Medina *et al.* demonstrated that it is possible to scale up mechanical grinding processes using twin screw extrusion techniques[72] Their studies focused on the caffeine oxalic acid co-crystal system previously produced through small scale grinding by Trask *et al.*[73] and the AMG-517 ascorbic acid salt produced by Amgen[74]. Heating can be coupled with extrusion to give a hot melt extrusion process (HME); the additional heat aids the co-crystallisation process as shown by Moradiya *et al*. in HME co-crystallisation experiments on the carbamazepine and *trans*-cinnamic acid system[75]. There are several benefits to using grinding techniques over more traditional solution based crystallisation, of which one of the key benefits is in the reduction of solvent used in the manufacturing process which is one of the main targets in approaches to sustainable chemistry[76].

Just as in crystallisation from solution, the choice of solvent in mechano-crystallisation can have a significant effect on the product of crystallisation. In LAG co-crystallisation studies of the 1:1 caffeine-glutaric acid co-crystal system[77], Trask and co-workers demonstrated that the polarity of the solvent used in LAG can have a significant effect on the polymorph produced (Table 2.2).

Table 2.2 Solvents used by Trask et al to produce each polymorph of the caffeine-glutaric acid co-crystal by liquid-assisted grinding.

Caffeine-glutaric acid (form I)	Caffeine-glutaric acid (form II)
• N-hexane • Cyclohexane • N-heptane	• Chloroform • Dichloromethane • Acetonitrile • Water

The solvent effects were rationalised by differences between the crystal packing of each polymorph. Of particular interest was a non-polar cleavage plane (200) observed in form I (but not form II), which presented a surface of exposed methyl and methylene groups with which polar solvents can interact, influencing growth of form I.

2.4.5 Seeding in Crystallisation

Seeding can be applied to all methods of crystallisation, in particular solution-based techniques. A small quantity of crystals, known as seeds, can be added to a crystallisation solution to promote nucleation and/or further growth of crystals around these seed centres and can allow greater control over the crystal properties including solid form and particularly particle size distribution (PSD). However, this is dependent upon the bulk properties of the seed crystals used.

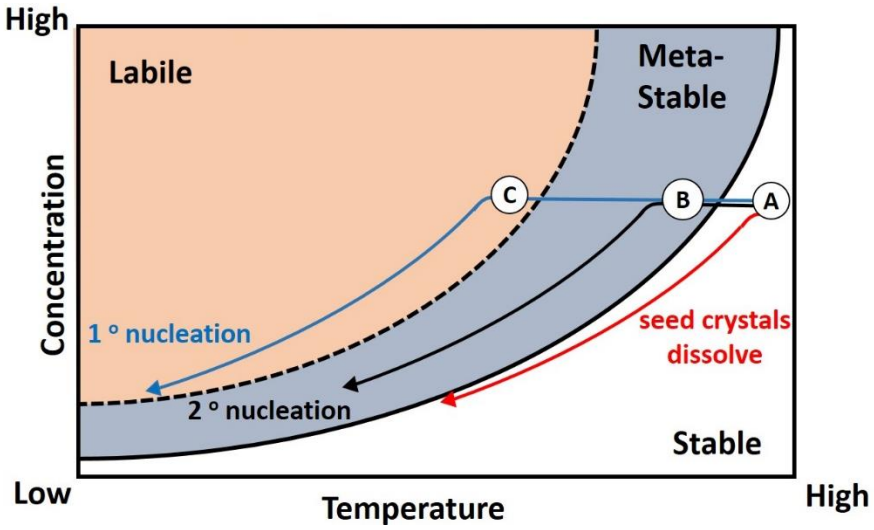

Figure 2.15 Diagram to highlight the importance of the point of seeding (A, B or C) combined with an appropriate cooling profile where either primary nucleation is dominant (blue), secondary nucleation is dominant or where nucleation doesn't occur and the seed crystals dissolve (red).

If the solution is metastable at the point of seed addition the seeds are able to form a suspension (Figure 2.15, B). Cooling the solution following the trajectory of the MSZ (Figure 2.15, black trajectory) maintains the conditions for crystal growth; secondary nucleation will dominate affording well controlled crystal attributes and avoiding uncontrolled primary nucleation, which occurs in the

labile regions. If the cooling is such that the solution enters the stable region where the solution is under-saturated the seed crystals added will dissolve (Figure 2.15, A) and will not act as sites for crystal growth (Figure 2.15 red trajectory). On the other hand if the supersaturation is too high and the solution enters the labile zone some secondary nucleation will occur, but once again unwanted primary nucleation will dominate (Figure 2.15, blue trajectory). Overall, seeding helps to reduce unwanted spontaneous and uncontrolled primary nucleation events, which often lead to heterogeneous crystal properties and promote secondary nucleation regulated by the bulk properties of the seed.

2.5 Current Practice in Industrial Crystallisation

2.5.1 Batch vs Continuous Crystallisation

Current pharmaceutical manufacture is predominantly carried out using batch processes but there is potential to transform the industry with the conversion to continuous manufacturing. Continuous crystallisation techniques will be highly beneficial to the pharmaceutical industry as continuous crystallisers require smaller footprints than large batch reactors and so can reduce overheads accrued from large production sites or enable manufacture of higher product volumes than batch processes at a site of an equivalent size. Due to a reduction in the mass of material and solvent used at any given time, less energy is required for heating and cooling in crystallisation cycles in continuous crystallisers than in batch crystallisers. Even though a smaller mass is used per residence time (total time spent within the crystalliser), overall the continuous process can have a much higher throughput, enabling increased productivity. Continuous manufacturing also promotes increased flexibility and product quality through the more targeted use of process analytical technologies (PAT) that can closely monitor the product *in situ* and allow for real-time process tuning. This has benefits over the use of PAT in batch processes, as in continuous crystallisation a small sample of the material is being monitored, all of which has experienced identical conditions; hence the required change in parameters calculated for the 'sampled' material will be directly relevant to the required treatment of the following material.

Benefits of Continuous Crystallisation

The drive towards developing platforms and processes for the continuous crystallisation of fine chemicals and pharmaceuticals stems from the benefits offered by the methodology over traditional batch manufacturing methods (Table 2.3). It should be noted that continuous manufacturing methods are well established in a range of sectors, but the work pursued here is part of the effort targeting its establishment in the chemical and pharmaceuticals sectors, where it is not yet widely used.

The general benefits of continuous over batch manufacturing include the general areas of sustainability (e.g. reduction of solvent use, recovery and recycling of solvent), footprint reduction of production plant; speed of scale-up of continuous platform technologies (which in many cases are more easily scalable than batch platforms) and improved control of the quality of crystals and particles that is possible in continuous processes, particularly with the potential for the integration of in-line process analytical technologies in continuous process design.

For pharmaceuticals and fine chemicals in particular, the methodology is well suited to the increasing trends in developing personalised medicines, by which adaptable, small volume production methods will become increasingly important. This concept also plays strongly into current, more general, trends towards localised and distributed manufacturing, which has the added element of such localised systems having the potential to have in-built re-configurability and adaptability. In the context of the present work (see Chapter 6 below), one example of this capability is the reconfiguring of the Continuous Oscillatory Baffled Crystalliser (COBC) at the University of Bath to a quarter of its original size over just one afternoon. Such re-configurability will become increasingly important in the development of more efficient and adaptable manufacturing processes.

Table 2.3 A comparison of batch and continuous processing for crystallisation of fine chemicals

Batch process (e.g. STR)		**Continuous process (e.g. COBC)**	
Non-linear scale up	• Difficult to transfer from lab to industry	**Linear scale up**	• Can transfer from lab to industry more easily.
Non-uniform mixing	• Unpredictable concentration and temperature gradients. • Non uniform products.	**Uniform mixing**	• Uniform temperature gradient. • More uniform products. • Allows in-line monitoring equipment to be used.
Large mass	• Lots of energy required to heat and cool crystallisation cycles • Long crystallisation cycle	**Small mass**	• More energy efficient
Low throughput	• Reduced efficiency	**High throughput**	• Enables high productivity, even with small masses
Large footprint	• High costs at production site	**Small footprint**	• Reduced costs at production site
Well established technology	• Large base of prior knowledge • Equipment is already installed	**Developing technology**	• High capital required to convert batch manufacturing sites • Technology not fully understood

Factors Limiting Adoption of Continuous Crystallisation in Industry

As mentioned in Table 2.3 above, continuous crystallisation processes are based upon developing technologies in comparison to the routine batch crystalliser technologies that have been tried and tested over decades. Consequently there is a lesser amount of technical knowledge around the developing continuous platforms although a lot of the theory can be modified from batch crystallisation processes and continuous processes in other areas of manufacturing and other industries and until the technology is established, this initially results in a higher risk to manufacturers who may look to adopt such processes.

In addition batch technology is heavily imprinted in industrial crystallisation; pharmaceutical and fine chemical manufacturers have a significant amount of capital invested in batch crystallisation equipment. Further investment would be required to move towards continuous processing and thus if the continuous crystallisation platforms can build upon or modify existing batch equipment or stand alongside existing batch equipment then the adoption of continuous crystallisation processes is likely to be more favourable.

It is also important to note that continuous crystallisation processes should not be considered as catch all approach. Many industrial crystallisation processes are efficient in batch e.g. industrial crystallisation of paracetamol which is very cheap to produce that it is often thought of as a commodity. In cases such as these, switching to a continuous crystallisation process offers very limited potential improvement.

2.5.2 Current Crystallisation Platforms

Any of the methods of crystallisation previously described in 2.4 can be utilised in a range of crystalliser technologies however crystallisation within the pharmaceutical industry has been dominated by cooling crystallisation and this has persisted in designs for newer crystallisers.

2.5.2.1 Batch Crystallisers

Development of batch crystallisation for industry started from the most basic tank crystalliser operates by allowing a saturated solution is left to cool in a large open tank allowing some of the mother liquor to evaporate after which excess liquor is drained and the resulting crystals harvested. This approach amounts essentially to large scale uncontrolled evaporative crystallisation. In the development of industrial crystallisation, this was then modified with agitation, most commonly through stirring using an impeller, and by introducing control of the cooling process by jacketing the vessel walls and circulating temperature-regulated fluid. These developments produced the workhorse of pharmaceutical crystallisation, the batch stirred tank reactor (STR). Batch crystallisers have developed over the years, some using evaporation and adiabatic cooling, such as the Swenson-Draft Tubed baffled crystalliser, and some cooling crystallisation, for example in the case of

classified suspension crystallisers (Oslo crystallisers)[78]. These crystallisers are more commonly used in the petrochemical, mining and bulk chemical industries and so from a pharmaceutical context are beyond the scope of this report.

2.5.2.2 Continuous Crystallisers

Continuous crystallisation technologies include a cascade of STRs (cSTRs) of which a particular subset include the continuous mixed-suspension mixed-product removal (MSMPR)[79] systems that have been utilised in this work, continuous Couette-Taylor crystallisers[80], the COBC, microfluidic crystallisers[81] and other custom designed tubular crystallisers[82], including the Kinetically-Regulated Automated Input Crystalliser (KRAIC) which was designed at the University of Bath and is used in this work. The details of these crystallisers (shown in Figure 2.16) are discussed below.

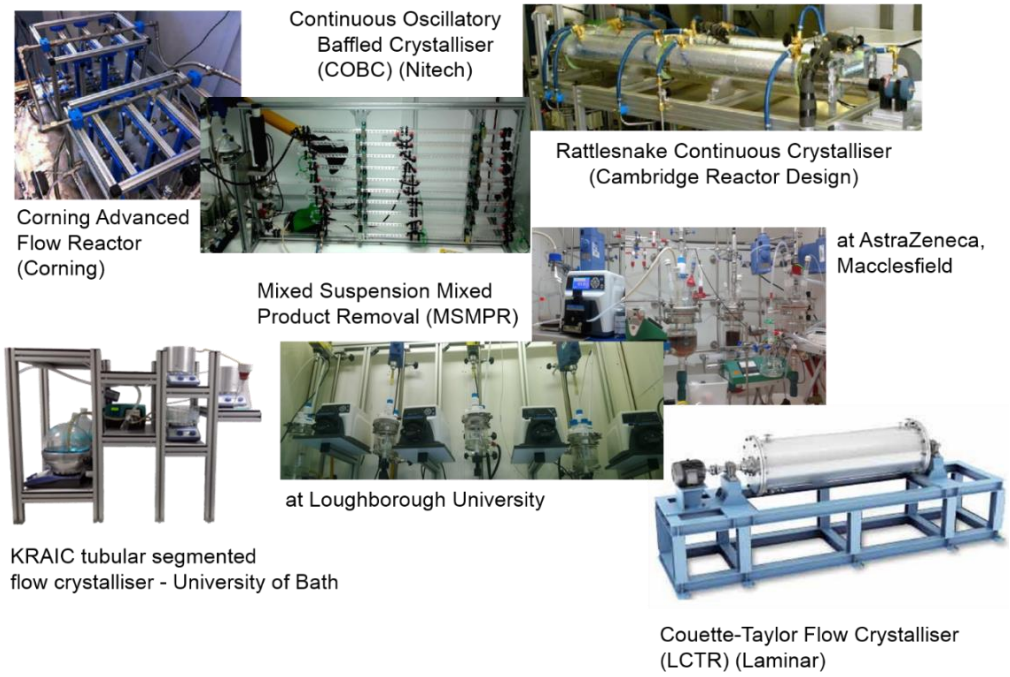

Figure 2.16 Images of continuous crystallisers technologies, some commercially available and others developed in academia.

Mixed-Suspension Mixed-Product Removal (MSMPR): Conventional (batch) STRs can be modified to form a cascade of STRs (cSTR) in which the reaction solution is transferred from tank to tank by a range of means. Of particular relevance here is the variant of cSTR known as MSMPR which applies to crystalline solids in suspension rather than reactive solutions. The mode of operation of cSTR or MSMPR can be continuous, i.e. as fluid (or suspension) enters the vessel it is continuously withdrawn from the vessel at the same rate. Alternatively it can be operated in a periodic mode (PMSMPR), in which case (see Chapter 5.2), the operation is arranged such that there is a significant dwell time of the crystallisation solution in each STR, prior to pumping the suspension to the next STR whilst simultaneously replenishing the solution in the current STR with feedstock. Each STR is normally set to different temperatures, thus executing a cooling crystallisation regime as the solution passes through the MSMPR cascade.

Couette-Taylor crystallisers are based on the principles of Taylor-Couette flow, generated within a fluid contained between two rotating cylinders. Depending on the parameters of the device and the fluid, the flow can be of two types – azimuthal (circular Couette flow) or, when the angular velocity of the inner cylinder is increased, various types of vortex flow, initially toroidal Taylor vortex flow but eventually breaking up into the regime of turbulence. The various types of flow offer possibilities for the control of crystallisation processes.

Continuous Oscillatory Baffled Crystalliser (COBC): The COBC is a tubular crystalliser which couples the generation of oscillatory flow (generated by a periodic piston operating through a bellows arrangement) with the inclusion of baffles (annular constrictions) at regular intervals along the tubular pathway. By combining the baffled cylindrical with fluid oscillation, eddies are generated when fluid flow passes through the baffles, enabling significant radial motions where events at the wall are of the same magnitude as these at the centre. These eddies create uniform mixing in each baffled cell, collectively along the reactor. As each baffled cell acts as a continuous stirred tank reactor, with a number of baffled cells in the reactor/crystalliser, COBC plug flow conditions are achieved under laminar flow. The COBC offers the opportunity to vary flow and oscillation rates to control the eddies formed and hence the mixing characteristics and residence times in each segment of the crystalliser. Cooling regimes imposed along the tubular pathway give the cooling conditions required for crystallisation to occur. The COBC used in this work is the NiTech DN15 (ID 15mm).

Corning Advanced Flow Reactor: One of the earliest continuous reactors that allowed scale-up of continuous flow processing into production, the Corning Advanced Flow Reactor allows for continuous process production capacity of up to hundreds of kilograms per hour for pharmaceuticals and fine chemicals. One critical design feature of the Corning Advanced Flow Reactor is the incorporation of various mixing devices that allow for efficient mixing of multiple input streams, which affords a high degree of flexibility on either flow chemical reaction or crystallisation processes. The flexibility is enhanced by the use of corrosion-resistant glass and/or ceramic fluidic modules with integrated piping connecting these modules with the feeding and mixing sources.

KRAIC and other segmented flow devices: The KRAIC (Kinetically-Regulated Automated Input Crystalliser) flow reactor/crystalliser developed at the University of Bath combines the ideas of optimised pre-mixing from multiple feed vessels (as implemented, for example, in the Corning Advanced Flow Reactor) with the exploitation of segmented flow (in which air or liquid volumes are incorporated in the reactant flow along the crystalliser, breaking this into regular segments (or slugs), each of which effectively acts as an independent reactor offering a stable environment with internal vortex circulation (see Figure 6.1) in which crystallisation can occur as the fluid moves along the reactor pathway. As with other crystallisers discussed here, the flow passes through a series of temperature-controllable regimes, offering the potential for controlled cooling crystallisation to be implemented. The KRAIC is representative of a variety of technologies exploiting segmented flow, and is described in detail in Chapter 6.

CRD Rattlesnake: The Rattlesnake continuous crystalliser from Cambridge Reactor Design offers a new platform for scalable crystallisations. Recently developed, the Rattlesnake combines various features alluded to above, including uniform mixing and precise temperature control over the entire reactor volume, incorporation of multiple ports and windows for monitoring and analysis (for example using process analytical technologies), various features to minimize encrustation and a range of construction materials options. The Rattlesnake has been deployed in various crystallisation campaigns within CMAC, but has not been exploited in the present work.

It is important to select the most suitable continuous crystallisation platform for the individual crystallisation process, taking into account the solvent system, solid loading and crystallisation kinetics, as each platform offers access to different mixing dynamics, residence times and cooling rates.

3 Theory of Analytical Methods

3.1 Optical Microscopy

Crystalline samples were assessed for suitability for single crystal X-ray diffraction using an optical microscope fitted with a polarising lens. When viewed under non-polarised conditions the crystal shape can be checked. Crystals are rejected if deformities can be seen, such as cracks, fractures and/or passenger crystals. The crystal morphology can also indicate if a crystal is starting material, if the morphology of the starting material is distinct and has already been determined. If the selected crystals are able to transmit polarised light, when viewed under such light and slowly rotated on the microscope stage the crystal should sharply extinguish, i.e. turn dark, at 90^{o} intervals. A crystal may not extinguish fully or not at all, indicating that it is not a single crystal but possibly several smaller aggregated crystals, and that it is therefore unsuitable for single crystal X-ray diffraction.

3.2 Scanning Electron Microscopy

In scanning electron microscopy (SEM), a focused beam of high-energy electrons (typical energies up to 40 keV) interacts with the sample, resulting in a decrease in kinetic energy of the incident electrons as they decelerate as a result of a range of processes. Detecting the signals resulting from these deceleration processes gives information about the sample, specifically the surface structure and composition of solid specimens. For the SEM images obtained in this work, the relevant signals are those from secondary electrons, which show the morphology of samples (at typical resolution of 10 to 100 nm). Backscattered electrons are also frequently used in studies of crystalline samples, as they allow the determination of composition, and thus examination of difference in composition in multiphase samples, which can be explored point by point across the sample. To generate an SEM image, SEM data are collected over a selected area of the sample (the area can be in a wide range between 1 cm and 5 μm linear dimension), and a 2-dimensional image is generated.

3.3 X-ray Diffraction

X-rays have a wavelength in the region of 0.5 Å to 3 Å which is comparable to the interatomic distances within molecules or ions in a crystal. As a result X-rays are an ideal tool for probing the atomic structure of crystalline materials[83, 84]. A coherent X-ray beam directed through a crystal, brings about interactions between the electric field of the X-ray beam and the vibrating electrons present within atoms of the crystalline solid. The interference with individual electrons induces emission of secondary X-ray radiation scattering the incident X-ray beam, termed Thomson scattering. The electromagnetic waves scattered from electrons within an atom can interact

constructively or destructively. Constructive interference occurs when the interacting scattered waves are in phase; this has an additive effect, increasing wave amplitude. In contrast, destructive interference occurs if the scattered waves interact out of phase with each other decreasing the overall wave amplitude. A diffracted beam is only observed at a point of constructive interference. This only occurs if a particular reflection condition is upheld for a family of lattice planes [83].

This is often analysed in terms of the Laue Equations (Equation 4); all three equations must be satisfied for constructive interference to occur which results in the presence of a single diffraction spot in the diffraction pattern. This is equivalent to noting that for two waves to interact constructively they must be in phase with one another, i.e. the path length between the waves must be an integer number of wavelengths.

$$a\,(\cos\alpha - \cos\alpha_0) = h\lambda$$
$$b\,(\cos\beta - \cos\beta_0) = k\lambda$$
$$c\,(\cos\gamma - \cos\gamma_0) = l\lambda \qquad \textbf{Equation 4}$$

The diffracted waves are collected using an area detector, such as a charge coupled device (CCD) or an image plate, where the presence of each beam is recorded as an individual spot forming part of a two dimensional diffraction pattern. This is an image comprising a series of spots arranged in a geometrical configuration which reflects the symmetry and geometry present in the crystal.

3.3.1 Bragg's Law

In 1912 W. L. Bragg (1890-1971) reported a proof for calculating the angle (θ) at which the reflection conditions, involving the originally developed Laue equations describing diffraction geometry, are satisfied, and in the subsequent year published his findings in the paper *The Diffraction of Short Electromagnetic Waves by a Crystal*[85].

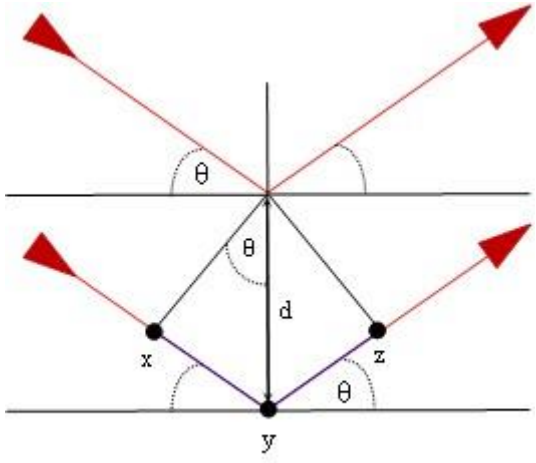

Figure 3.1. Diffraction of X-rays from a parallel set of lattice planes (in red) with their corresponding path difference (in purple).

An X-ray is diffracted from a family of parallel lattice planes that have a constant inter-planar spacing, d, and each family can be represented by a Miller Index (hkl) (Figure 3.1). The Miller indices are related to the reciprocals of the intersects of the lattice plane with the unit cell edges, and are also used to denote the coordinates of an equivalent point in the reciprocal lattice (see below). The angle of the incident X-ray beam (θ) is equivalent to the angle of the diffracted beam and can be calculated using the path difference between an X-ray diffracted by one plane and an X-ray diffracted by the neighbouring plane within the family (Equation 5). The path difference must be an integral number of wavelengths in order to ensure constructive interference.

$$2d\sin\theta = n\lambda \quad (n= 1, 2, 3\ldots) \qquad \textbf{Equation 5}$$

Where θ represents the scattering angle, commonly referred to as the Bragg angle, λ represents the X-ray wavelength and *d* corresponds to the spacing between neighbouring parallel lattice planes. It is common practice that the integer term *n* is assumed to be unity.

The amplitude of X-ray scattering is dependent on the number of electrons present in the atom (Z) and also on the scattering angle θ, which both contribute to the atomic scattering factor (f_j). The scattered X-rays from an individual atom interfere constructively in phase when the scattering angle is equivalent to zero degrees i.e. directed straight forward. At zero degrees f_j is equivalent to the atomic number of the scattering atom. As the X-rays are scattered at increasing angles (greater than zero) destructive interference occurs leading to a reduction in scattered X-ray intensity and hence a smaller value of f_j . The intensity falls off as a function of (sinθ)/λ (Figure 3.2). It should be noted that the X-ray scattering amplitudes for hydrogen atoms are low, as Z = 1, and this makes it more difficult to assign the positions of hydrogen atoms within a unit cell from X-ray data.

3.3.2 Reciprocal Lattice and Ewald Sphere

The reciprocal lattice is a useful tool in crystallography helping to interpret the workings of X-ray diffraction. The reciprocal lattice is the polar reciprocal transform of the direct lattice whereby the base vectors of the direct lattice (a, b and c) and the volume of the unit cell can be used to generate the base vectors of the reciprocal lattice (a*, b* and c*) (Equation 6)

$$\underline{a}^* = \underline{b} \times \underline{c} / V \qquad \underline{b}^* = \underline{a} \times \underline{c} / V \qquad \underline{c}^* = \underline{a} \times \underline{b} / V \qquad \textbf{Equation 6}$$

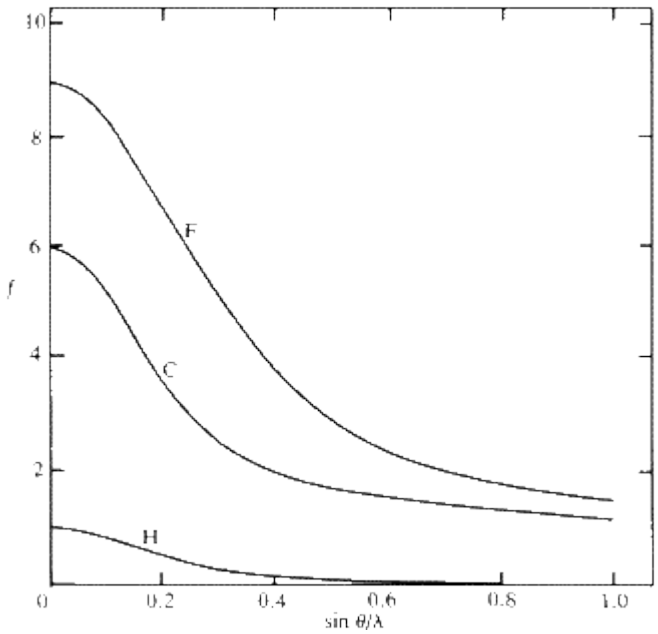

Figure 3.2. X-ray atomic scattering factors for hydrogen, carbon and fluorine[86]

The reciprocal lattice can be generated in geometrical terms that illustrate its close link to the concept of (real space) lattice planes. The reciprocal lattice point (r.l.p.) corresponding to the lattice plane *hkl* is produced by dropping a perpendicular from the (*hkl*) lattice plane to the unit cell origin. This gives the direction of the r.l.p., and its distance from the origin of reciprocal space is given by $1/d_{hkl}$ where d_{hkl} is the real space separation of the (*hkl*) lattice planes. Thus each r.l.p. is related to a particular lattice plane; since diffraction measurements (which are effectively made in reciprocal space) capture the scattered intensity at each r.l.p. they can be thought of, loosely, as measuring the scattering from that lattice plane.

3.3.3 Structure Solution

Each diffraction spot within a diffraction pattern has a specific intensity (I_{hkl}), which is related to the electron density at positions x, y, z within the unit cell *via* Fourier transformation (FT) (Equation 7 to Equation 9) and can be used to form an electron density map from which atom positions within the unit cell can be identified[84].

$$\rho_{xyz} = \frac{1}{V}\sum_{hkl}\left|F_{hkl}\right| \cdot \exp\left[i\varphi_{hkl}\right] \cdot exp\left[-2\pi i\left(hx+ky+lz\right)\right] \qquad \textbf{Equation 7}$$

The intensities, I_{hkl}, of the diffraction spots are proportional to the square of the structure factor (F_{hkl}) (Equation 8). The structure factor F_{hkl} has amplitude and a phase (Equation 9), but it is only possible to determine the amplitude from the measured I_{hkl} values as the squared term in the relationship

between F_{hkl} and I_{hkl} removes the phases. This lack of phase determination is more commonly referred to as "the Phase Problem", which is commonly solved by the use of Patterson or, more frequently, Direct Methods (see below).

$$I_{hkl} \propto \left| F_{hkl}^{\,2} \right| \qquad \textbf{Equation 8}$$

$$F_{hkl} = \left| F_{hkl} \right| \cdot \exp\left[i\varphi_{hkl} \right] \qquad \textbf{Equation 9}$$

The structure factor contains information about all the types of atoms present in the unit cell along with their corresponding atomic positions as shown by the atomic scattering factor term f_j and the atomic fractional coordinates, respectively, in the structure factor equation (Equation 10)

$$F_{hkl} = \sum_{j=1}^{N} f_j \exp\left[2\pi i\left(hx_j + ky_j + lz_j \right) \right] \qquad \textbf{Equation 10}$$

In this work, Direct Methods and charge flipping have been used to solve the crystal structures of materials obtained in multi-component materials screening studies. These methods are therefore outlined briefly here.

3.3.3.1 Direct Methods

Direct methods have become one of the most popular methods of structure solution after the computing-intensive aspects of the methods became more tenable – and now very rapid and routine – with the advancement of CPUs. Direct methods can be used to solve a diverse range of structure types and are especially useful for solving organic structures comprised of small molecules[84].

The structure factors and phases of reflections are related through the electron density present which is in turn the Fourier transform of the structure factor, as discussed above. Direct methods try to overcome the phase problem by attempting to derive the phases of the structure factors by probabilistic means. Approximations of the phases are obtained from the measured structure factor intensities combined with knowledge about the properties of electron density that can be written as a series of mathematical constraints on the function $\rho_{(xyz)}$. These properties include that electron density is confined to concentrated areas and it cannot be negative, only positive or zero[87]. An initial estimate of phases of some of the strongest reflections are developed through statistical relationships between the phase of the stronger reflections in the diffraction pattern, leading to sets of possible solutions (sets of phases assigned to the initial set of reflections) that can be used to calculate preliminary electron density maps. The approximated phases and known structure factor amplitudes are used to calculate the values of $\rho_{(xyz)}$ and obtain an approximate electron density map.

The phases determined from the approximate electron density map undergo further iterative mathematical treatment to determine several converging sets of new phase values which is subsequently repeated many times. Each set of new phase values is analysed for its acceptability using several mathematical phase functions known as the figures of merit. A final electron density map is calculated using the most appropriate sets of phase values which upon interpretation can yield the atomic positions within the unit cell by using knowledge of a predicted molecular structure, common structural features and known stereochemical principles[84].

3.3.3.2 Charge Flipping

Charge flipping (CF) is an iterative method for structure solution which is particularly useful for solution of periodic, incommensurate and quasi-crystalline crystal structures but can also be used for more common crystal structure solution. A computationally intensive technique, CF has proved more popular in recent years due to advancements in computer processing power[88]. Like classical direct methods CF applies constraints to the diffraction data in reciprocal space, however as it is a dual-space method it also uses constraints on real space (electron density) [89]. Similar to direct methods, the two most significant constraints applied to the data are that the electron density must be positive and that the unit cell consists of individual atoms. One of the advantages of CF over direct methods is that it does not require any information on the chemical composition or the symmetry of the material to reconstruct the electron density. It is important to note that using CF all electron density is treated using P1 symmetry.

Outlined here is the stepwise procedure of the simplest CF algorithm adapted from the clear and concise description by Oszlányi *et al.*[89] The process of structure solution using the CF algorithm is an iterative cycle which starts by assigning random phases to experimental (observed) amplitudes generating a trial set of structure factors[88-90].

1. Using an inverse FT on the trial set (of experimental amplitudes and assigned phases) it is possible to calculate the electron density.
2. The calculated electron density is then modified using charge flipping. A positivity threshold value (δ) is assigned where all points on the grid with an electron density below δ are charge flipped by multiplying by -1 and any values that remain below zero are removed to comply with the positivity constraint.
3. FT of the modified electron density calculates a set of temporary structure factors, which have associated calculated phases.
4. The phase of the temporary structure factors are then combined with the experimental amplitudes to give a new trial set of structure factors which can be input into the subsequent iteration cycle (repeating from step 1).

The process is repeated until certain convergence criteria are met. Weak reflections can pose a problem. In SUPERFLIP[90], a program used for structure solution using CF, the CF algorithm has been modified in the way weak reflections are handled, to help the convergence of the algorithm. In SUPERFLIP, if a reflection is weak then the calculated amplitude of the temporary calculated structure factor is retained instead of pairing it with the experimental amplitude and the phase is shifted by $\pi/2$. This has been found to improve the function of the algorithm[90].

After convergence the symmetry information obtained from the symmetry in the diffraction pattern can be input into the solution. Due to the nature of the CF algorithm used in SUPERFLIP there may be a risk that the electron density has been shifted and so it may be necessary to redefine the space group origin[90].

3.3.4 Structure Refinement

Least squares structural refinements are carried out to improve the model determined during structure solution, and to highlight other atoms remaining unidentified by initial structure determination. The parameters that can be refined during a structural refinement process include atomic positions and thermal displacement parameters for each of the atoms in the structure, occupancies of atomic sites (for potentially disordered structures) and a range of others. These parameters (typically several hundred in number) are refined using least squares methods, against the data set of observed reflection intensities (of which there are usually several thousand). Using the trial structure obtained in a refinement cycle, a calculated diffraction pattern can be obtained *via* forward Fourier transformation (equation 2) which is formed on the basis of the trial structure. This calculation generates a series of calculated structure factors (F^{calc}) each with amplitude ($|F^{calc}|$), and unlike the observed structure factors (F^{obs}) they each have an associated phase (φ^{calc}). The calculated structure factors are compared to the experimentally obtained observed structure factor amplitudes (Equation 11) to give a residual factor (R-factor).

$$R = \frac{\sum_{hkl} \left\| F_{obs} \right| - \left| F_{calc} \right\|}{\sum_{hkl} \left| F_{obs} \right|} \qquad \textbf{Equation 11}$$

As the calculated structure converges towards the observed structure, the R-factor lowers until it reaches a typical value of around 0.02-0.06.

Weighting factors can be applied to the reflection intensities. A common weighted residual factor wR_2 (Equation 12) multiplies the difference between corresponding F_{obs} and F_{calc} values by its own

weight (w) assigned based upon the (reciprocal of the) standard uncertainties (S.U.) of the observed value. This provides a more realistic assessment as it takes into account the "relative reliability" of each individual measurement.

$$wR_2 = \sqrt{\frac{\sum_{hkl} w\left(F_{obs}^2 - F_{calc}^2\right)^2}{\sum_{hkl} w\left(F_{obs}^2\right)^2}} \qquad \textbf{Equation 12}$$

Once the structure is completed the goodness of fit (S) (Equation 13) should tend towards unity when calculated for n data and p refined parameters.

$$S = \sqrt{\frac{\sum_{hkl} w\left(F_{obs}^2 - F_{calc}^2\right)^2}{n - p}} \qquad \textbf{Equation 13}$$

3.3.5 Powder X-ray Diffraction

PXRD uses a polycrystalline sample in which the crystallites and the lattice planes within will be arranged in a wide range of orientations (for an ideal powder all possible orientations will be present and with an equal distribution). PXRD is measured using a powder diffractometer which typically operates in "θ-2θ" geometry: the detector scans through the (Bragg) scattering angle 2θ, while the sample scans θ (Figure 3.3, left), thus bring successive reflections (with distinct d_{hkl} values) into the diffracting position according to Bragg's Law. At higher 2θ values, smaller d_{hkl} values are accessed.

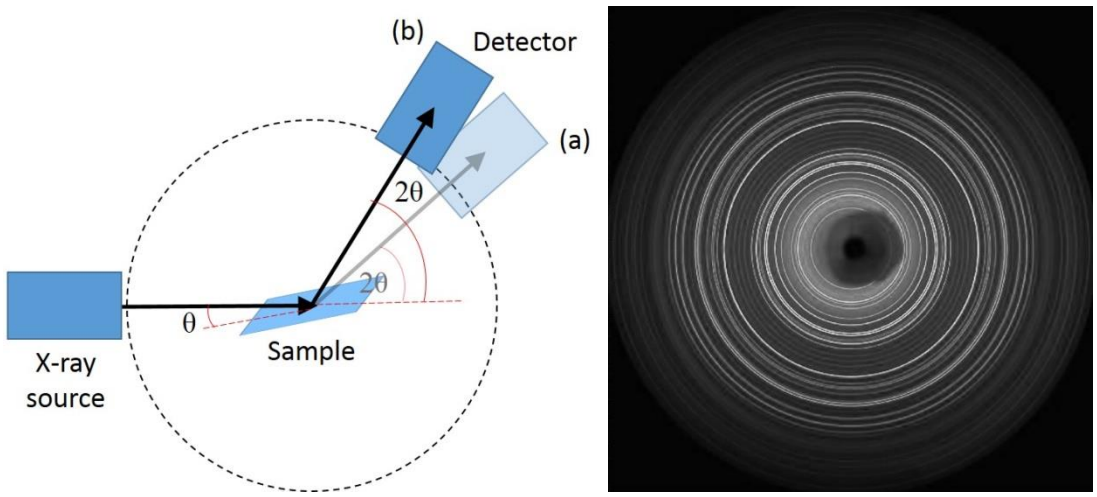

Figure 3.3 Schematic of a powder diffractometer with detector moving through 2θ angle from position (a) to (b) and an example of a powder X-ray diffraction image showing the Debye-Scherrer rings around the incident X-ray beam.

As the detector moves through the 2θ angle, a number of crystallites will have lattice points in the appropriate orientation to satisfy the Bragg equation for the refection (or reflections) with a corresponding d-spacing; these will constructively diffract the incident beam creating a series of diffraction spots some of which will overlap. Each crystallite produces its own set of Bragg reflections which overlay to form Debye-Scherrer rings which appear as a set of concentric circles with the incident beam positioned at the centre as 0° θ (Figure 3.3, right).

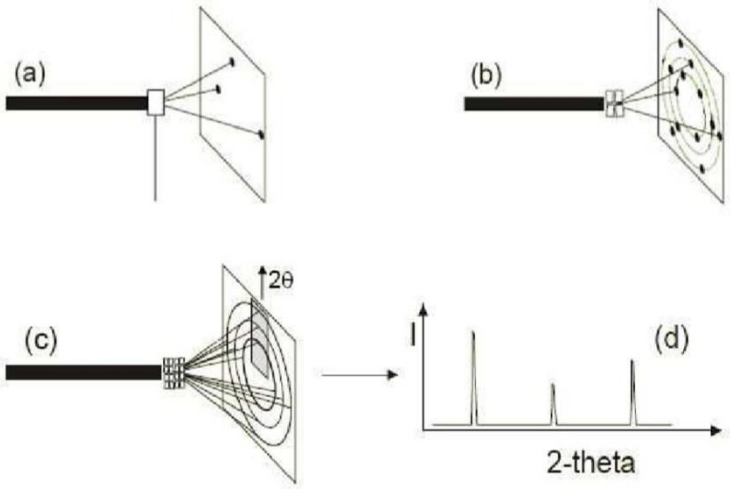

Figure 3.4 Schematic showing diffraction from (a) a single crystal, (b) four single crystals of different orientations, (c) a polycrystalline material (with multiple orientations) from which the intensities can be extracted and plotted against the angle 2θ to give a diffraction pattern (d).[84]

A PXRD pattern, essentially a cross section through the Debye-Scherrer rings, can be produced by plotting the intensity of each ring against the measured 2θ angle (Figure 3.4 d).

SXRD uses a single crystal that is preferentially selected using optical microscopy, as noted above, which increases the chance that it may not represent the bulk sample. This may not be as important for initial materials discovery but at large scale in industry this can be vitally important. This is why the bulk technique of powder X-ray diffraction is such a useful tool as it can be used to verify the homogeneity of the sample, complementing the structural data obtained through SXRD. This is carried out by generating a PXRD pattern from the crystal structure determined from the SXRD data and comparing this to the PXRD pattern from the bulk sample; for a single phase product (i.e. only comprising the material for which the SXRD has been obtained), all peak positons will match between the observed and calculated PXRD patterns. The intensities should also match, but these are susceptible to effects such as preferred orientation and the position-matching is usually taken as the primary indicator for this "fingerprinting" approach.

Through a combination of instrumentation improvements, with high resolution instruments available both in the laboratory and at synchrotron sources, and computational advances, PXRD has also become a valuable tool in determining a complete crystal structure for polycrystalline samples. In

the past it was difficult to obtain a full structural solution from PXRD data, from which the available techniques often were only capable of structure refinement, primarily using the Rietveld method which uses the full powder profile to aid the refinement process. In trying to use PXRD for structure solution, difficulties arise due to problems with peak overlap, as the 3D information in a single crystal pattern is reduced to 1D in PXRD. As in SXRD structure solution methods, traditional PXRD methods for structure solution analysed individual reflections to provide a series of I_{hkl} values which could then be used in Direct or Patterson methods for structure solution, but these techniques cannot resolve peak overlap inherent in PXRD. Instead direct space approaches have been devised where multiple theoretical crystal structures are created independently of the diffraction data (for example using simulated annealing techniques) and a PXRD pattern generated for each theoretical structure. The fit of these synthesised patterns are measured against the experimental diffraction pattern using a weighted profile R factor (R_{wp}) analogous to that of Rietveld refinement. Both Rietveld-based refinement and structure solution from powder data based on model-generation and testing, focus on the overall shape of the PXRD pattern, not the individual peak intensities, thus overlapped peaks do not hinder structural solution so severely[83, 91].

3.4 Mid-IR, Infrared Spectroscopy

Infrared spectroscopy (IR) results from the absorption of electromagnetic radiation by molecules at characteristic resonant frequencies that are directly related to the bond vibrations in the molecule and hence are characteristic of functional groups. The absorption process relies on the vibration resulting in a change in dipole moment of the molecule and is sensitive to bond strength, the masses of the atoms that are bonded, and the local molecular environment including, for some vibrations, the intermolecular interactions. Many functional groups can thus be identified by their vibrational frequencies observed as absorption peaks in an IR spectrum. Characteristic peaks corresponding to vibrations within the molecules (normal modes) are observed in the infrared region (typically $400cm^{-1}$ to $4000cm^{-1}$). The samples required for IR need not be crystalline (or even solid).

Fourier transform IR (FTIR) can increase the sensitivity of IR measurements by employing an interferometry approach in which the interference pattern generated by recombination with the reference beam can be Fourier transformed to produce the IR spectrum. FTIR has the benefit of decreasing the required sample size and allowing more rapid collection of the spectrum, and is adopted as standard in modern IR spectrometers such as those used in this project.

Hydrogen bonding effects are observed within an IR spectrum by analysis of the O–H or N–H bands which characteristically appear at the high frequency end of the spectrum as a result of the low mass of the hydrogen atom. The strength of a hydrogen bond may be observed by analysis of the frequency

of these bands; a stronger hydrogen bond will increase the covalent O–H or N–H bond length, lowering the vibration frequency and leading to a broader absorption band.

3.5 Raman Spectroscopy

Raman spectroscopy is a complementary technique to infrared spectroscopy, which again probes the vibrational modes of that molecule (though it can also examine molecular rotations). In this case, however, instead of the vibrational mode having to result in a change in dipole moment to allow absorption, it for Raman signals it must involve a change in the molecular polarisability. Raman typically uses incident visible or UV radiation, produced by a laser source. This high energy incident radiation excites the electronic state of a molecule from a ground state to a higher energy (virtual) state. Upon relaxation, a small number of the photons are re-emitted at a different energy, thus exhibiting a change in frequency. If the system returns to a more energetic state than that of the original state, a photon of a lower frequency will be emitted from the sample. This is termed a Stokes shift, and the shift corresponds to the absorbing process (a molecular vibration in this case). If it is less energetic, the frequency of the emitted photon will be higher, causing an anti-Stokes shift to be observed, the shift again corresponding to the molecular vibration.

Similarly to X-ray powder diffraction, Raman scattering provides fingerprint information on small samples by analysing peak positions and comparing them to pure references. It is a very powerful tool for determining the presence of small changes between samples, for example between two polymorphs of the same material (in which there will be changes in the intermolecular frequencies and hydrogen bonding within the structure).

3.6 Differential Scanning Calorimetry (DSC)

Differential Scanning Calorimetry (DSC) is a thermal technique that can be used to gain information about the crystalline behaviour of a material highlighting any desolvation events and polymorph transitions as well as the melting point and eutectic behaviour. The technique focuses on how temperature affects the heat capacity of a material, the amount of heat energy required to raise the temperature of one unit mass of material by one degree. Changes in the heat capacity are measured as changes in heat flow which are affected by events such as melting and recrystallisation which are endothermic and exothermic processes, respectively.

A DSC instrument comprises a single furnace with an empty reference pan and sample pan containing a few milligrams of material (Figure 3.5). The two pans are connected and the DSC experiment measures the temperature variation between the sample and reference, known as the heat flux, as the temperature of the reference pan is increased at a specified rate. Heat flux can be

converted to heat flow using calibration data from a known reference (commonly indium or sapphire). The differential heat flow required to ensure that sample and reference temperatures increase at the same rate is derived and applied during the DSC measurement. Data are plotted as heat flow as a function of the sample temperature; the energy of any thermal events that occur can be calculated through integration of the area under the curves. For example, the area of the characteristic endotherm of melting gives the heat of fusion, a key parameter in many computational calculations. It is also possible to use DSC to gain some information about the kinetics as well as the thermodynamics of the process, while the shape of the DSC peaks gives information about sample purity.

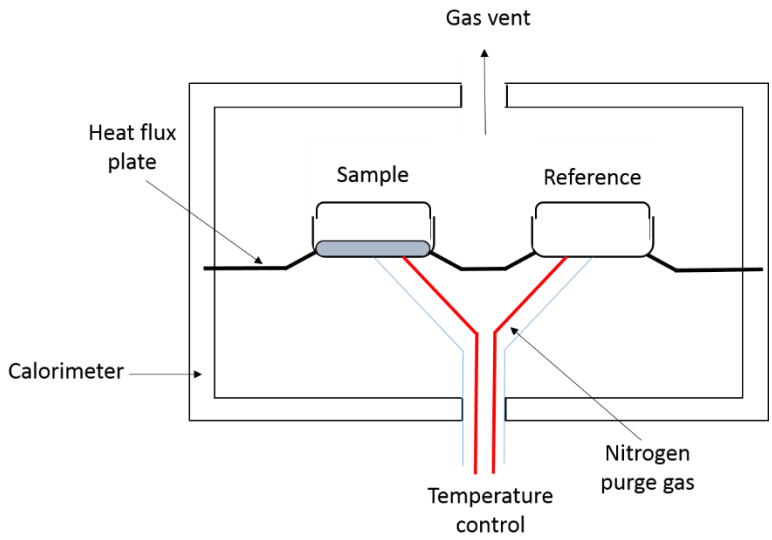

Figure 3.5. Schematic of a differential scanning calorimeter

As a sample is heated, say from room temperature to its decomposition temperature, peaks with positive and negative ΔdH/dt may be recorded. Each peak corresponds to a heat effect associated with a specific process, e.g. crystallisation or melting. The information obtainable from a DSC curve includes:

- Temperature at which a certain process occurs, for example, the melting point of a material;
- Temperature at which a reaction, such as decomposition, starts (peak position corresponds to T of max reaction rate);
- Phase transition temperatures, and whether these are endothermic or exothermic;
- Glass transition temperatures, T_g (important in polymers, for example);
- Enthalpies of transitions;
- Changes in heat capacity;
- Phase purity of the material being studied.

Even though it may be simple to identify if thermally induced phase transitions are present in a DSC pattern it can often prove much more challenging to directly assign these transitions as the thermally induced phases may only be short lived (metastable) adding challenges to structural characterisation[92].

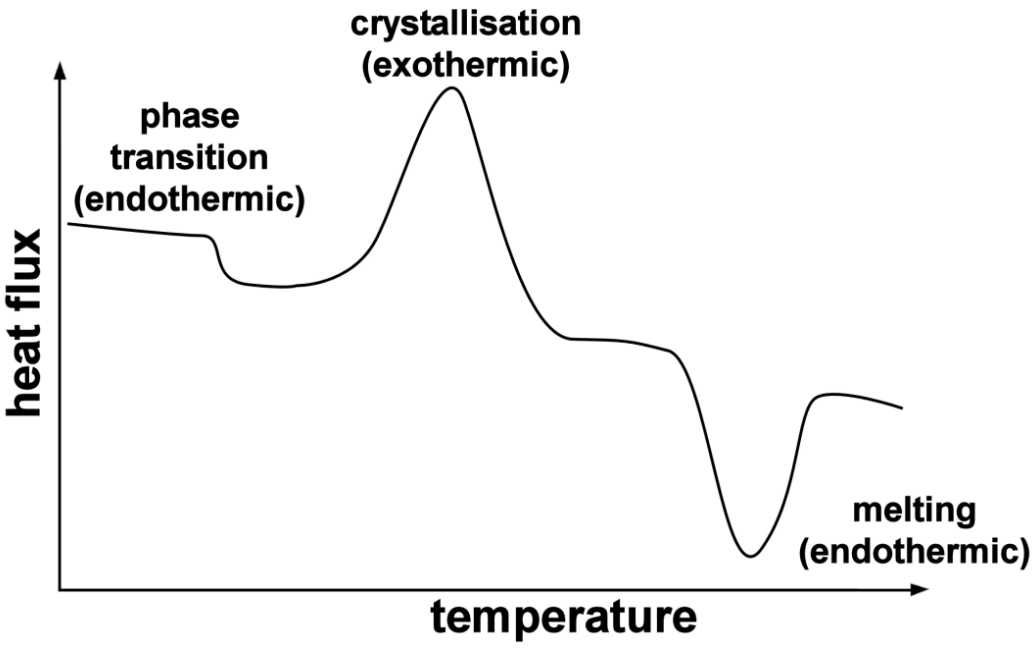

Figure 3.6. Schematic of a differential scanning calorimetry (DSC) trace, showing some of the characteristic thermal events that can be identified (Image used with permission).[51]

The types of events that are commonly observed in a DSC trace (Figure 3.6) include:

- Endothermic events: melting, sublimation, (some) solid-solid transitions, desolvation, (some) chemical reactions;
- Exothermic events: crystallisation, (some) solid-solid transitions, decomposition, (some) chemical reactions;
- Baseline shifts: glass transitions in polymers or amorphous materials.

3.7 Thermogravimetric Analysis (TGA)

Thermogravimetric analysis (TGA) measures the change in mass of a specimen with respect to temperature whilst the specimen is subjected to a controlled heating programme[93]. A mass loss will occur when a volatile component is lost in processes such as desolvation, dehydration and decomposition, which are shown as a sigmoidal step in a plot of mass against temperature (Figure 3.7). The weight loss as a percentage can provide useful information about the stoichiometry of

hydrates, solvates or decomposition products. Volatile components may not be evolved from all materials that undergo some form of reaction or transformation with respect to temperature and it is therefore important to perform complementary Differential Scanning Calorimetry experiments[94]. TGA can also be coupled with mass spectrometry (TG-MS) to confirm the type of material evolved and can aid characterisation of unknown volatile decomposition products.

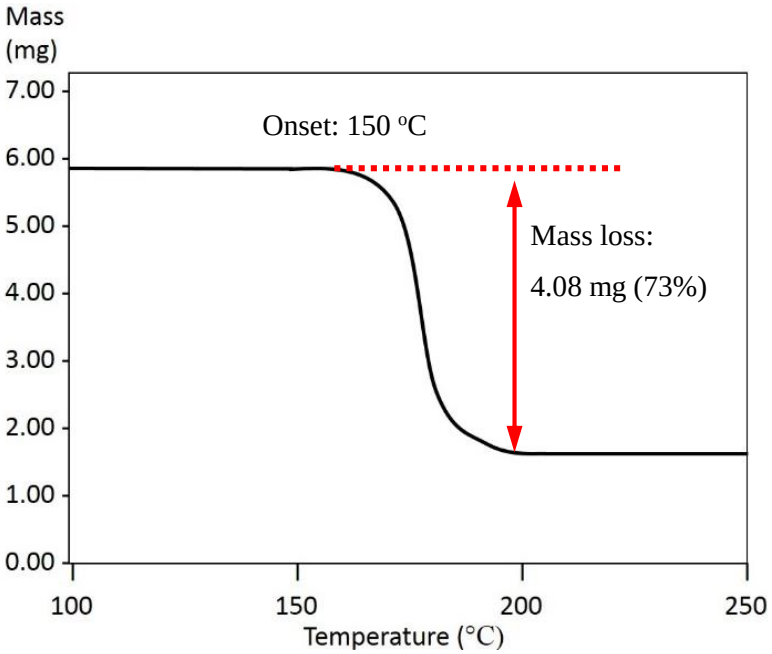

Figure 3.7 Example of a TGA plot

3.8 Dynamic Vapour Sorption (DVS)

Dynamic vapour sorption is useful in measuring the stability of crystalline materials and their ability to form hydrates and solvates. A sample is exposed to a series of stepped humidity conditions by varying the vapour concentration around the sample and the change in sample mass is measured as a function of time. It is important that the sample reaches gravimetric equilibrium before adjusting to the next humidity level. A sorption isotherm is created using the equilibrium mass values at each humidity level. A recording microbalance monitors the mass of the sample as the vapour concentration of the environment is changed. This is achieved by a flowing gas system whereby a constant stream of carrier gas (N_2 or air) is passed over the sample. The stream of gas is saturated to different solvent vapour pressures (relative humidity in the case of water vapour) and is constantly delivered to the sample. The different vapour concentrations are created by using mass flow controllers to mix a dry and a saturated gas stream. A mass increase indicates a sorption process; either absorption or adsorption and a mass loss is indicative of desorption. Square hysteresis in the sorption and desorption isotherms indicates the formation of stoichiometric hydrates or solvates

whose composition can be calculated from the change in mass relative to that of the non-solvated material. A typical DVS system, as used in this work, is shown below in Figure 3.8.

Figure 3.8 DVS Advantage dynamic vapour sorption apparatus

4 Crystallisation & Properties of Polymorphic Solid Forms of Urea Barbituric Acid

Barbituric acid is not an API itself but is used as a precursor for 5-5-substituted barbiturate drugs including amopental, barbitone and phenobarbital[95], used in the past as analgesics and more recently as general anaesthetics, anticonvulsants in epilepsy treatment and in treatment for anxiety[96]. Due to their pharmaceutical relevance and due to the geometric positioning of the hydrogen bond donating and accepting groups barbituric acid and its derivatives have been the subject of a range of crystal engineering studies.

The polymorphic urea-barbituric acid co-crystal system (UBA) was first documented by Gryl *et al.* in 2008[14]. UBA was originally studied to investigate potential non-linear optical (NLO) properties as previously studied in the barbituric acid melamine (cyanuric acid) co-crystal system by Zerkowski and Whitestides[97-99]. Three polymorphs of the 1:1 co-crystal were produced using evaporative crystallisation under different crystallisation conditions (Table 4.1).

Table 4.1. Crystallographic details and crystallisation conditions used by Gryl *et al.* to obtain each of the UBA polymorphs[14]

UBA polymorph	I	II	III
Crystallographic information			
Crystal habit	plate	block	block
Crystal colour	"yellowish"	colourless	colourless
Collection temp. (K)	293	293	293
Space group	$P2_1/c$	Cc	$P\bar{1}$
a (Å)	6.962	5.098	8.159
b (Å)	7.886	8.369	9.112
c (Å)	14.428	10.553	10.927
α (°)	98.03	109.55	100.25
β (°)	90.00	90.00	91.52
γ (°)	90.00	107.73	99.19
Volume ($Å^3$)	784.356	401.546	787.821
Z	4	4	4
Z'	1	1	2
R Factor (%)	4.29	3.25	5.34
CSD Ref Code	EFOZAB	EFOZAB01	EFOZAB02
Crystallisation conditions			
Solvent	Methanol	Ethanol	Methanol
Ratio of U:BA	1:2 or 1:3	2:1	2:1
Dissolution temp. (°C)	50	50	50
Evaporation temp.	Room temperature	Room temperature	Room temperature

All three polymorphs are stable between 100 K and 295 K as indicated during single crystal X-ray diffraction experiments. Gryl *et al.* noted that over time samples of UBAI and UBAII converted to UBAIII and concluded that UBAIII was the most thermodynamically stable form under ambient conditions.

This polymorphic nature makes the UBA system an ideal candidate for investigating control of polymorphism in co-crystals. The main purpose of this study is to scale-up from evaporative crystallisation to laboratory scale cooling crystallisation and develop strategies for producing specific polymorphic forms consistently via cooling crystallisation. The starting materials urea and BA are safe, cheap and readily available which is important when moving into larger scales and working in academic environments. Even though urea and BA are small molecules which do not necessarily represent the large floppy molecules typical of APIs, the complexity of the system with polymorphic starting materials, formation of hydrates and polymorphic co-crystal products is representative of the multifarious nature of pharmaceutical crystal systems.

4.1 Characterisation of Barbituric Acid: polymorphic starting material

As fine chemical manufacturers are not usually concerned with the polymorph of the material obtained, only the chemical identity, purity and yield, it is common to obtain previously unidentified polymorphs of starting materials from suppliers; an example of this was found with 4-Cl-3,5-dinitrobenzoic acid (section 7.4.5) in which Wittering *et al.* thought that they had discovered a previously unreported polymorph through cooling crystallisation experiments, but in fact the new polymorph could be traced back to the commercial starting material[100]. It is well known in the pharmaceutical industry that the physical properties of starting materials used for manufacturing drug substances can have a large impact upon the outcome of the synthesis including effects on yield, purity and solid form. The same starting component may show variation between suppliers and even between batches from the same supplier. It is therefore very important to monitor the properties of the starting materials used, to enable any changes in the product to be attributed to, or discounted from, variations in the starting material and allow the physical properties to be monitored and controlled accordingly to control the synthesis.

The same is true for crystallisation processes and is particularly important when using polymorphic starting materials such as barbituric acid and urea. Urea is known to have one polymorph at ambient pressure and temperature[101], however there are several phases that have been identified under high pressure[102, 103] and non-ambient temperature conditions. Although in standard solution-based crystallisation processes these conditions will not be met the material may encounter high pressure environments especially in down-stream processes such as granulation and tabletting.

Barbituric acid (BA) can display a significant degree of tautomerism (Figure 4.1) and is polymorphic with four identified forms. BAI [104] and BAII [105] are both stable under ambient conditions, the latter determined to be more stable in lattice energy calculations carried out by Braga *et al.*[106] The full structures of forms III and IV have been characterised using solid state NMR studies [107, 108] but have not been characterised using SXRD to date and therefore are not present in the CSD. Additionally BA can form a dihydrate [109, 110] when exposed to water or humid conditions; as noted in the Introduction above, identification and prevention of hydrate formation is a key objective in industrial crystallisation processes, and this is clearly also important here, in delivering anhydrous BA reliably into the co-crystallisation experiments to ensure process consistency.

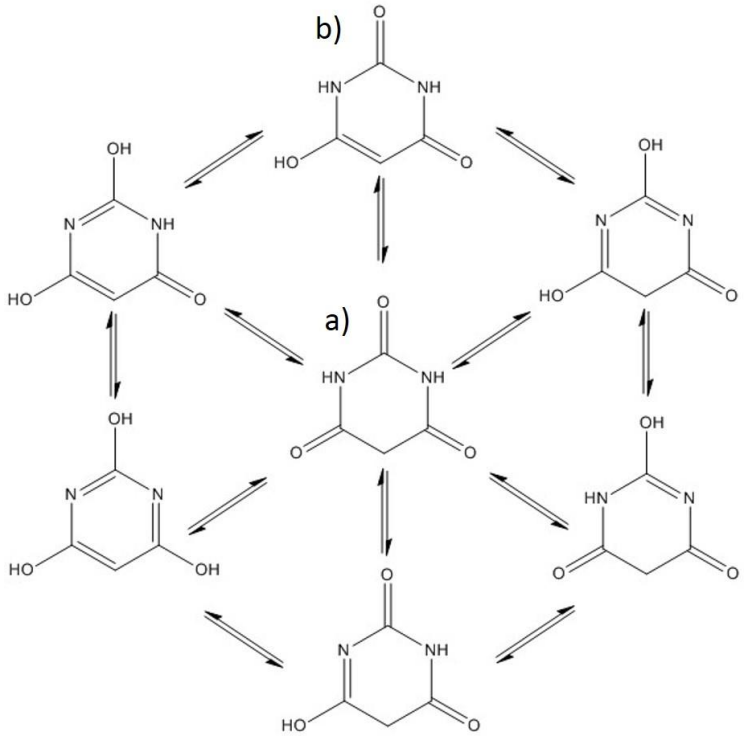

Figure 4.1 Several potential tautomers of barbituric acid. The keto-tautomer a) features in BAI and BAII and the enol-tautomer b) is present in BAIV.

All three commercial samples of BA starting material were characterised using a range of solid state techniques with the aim of polymorph identification in these candidate starting materials.

4.1.1 Powder X-ray Diffraction

Powder X-ray diffraction data were collected in flat plate mode on a Bruker D8 Advance equipped with monochromated Cu Kα radiation (λ=1.54056 Å) in reflection geometry at 298 K.

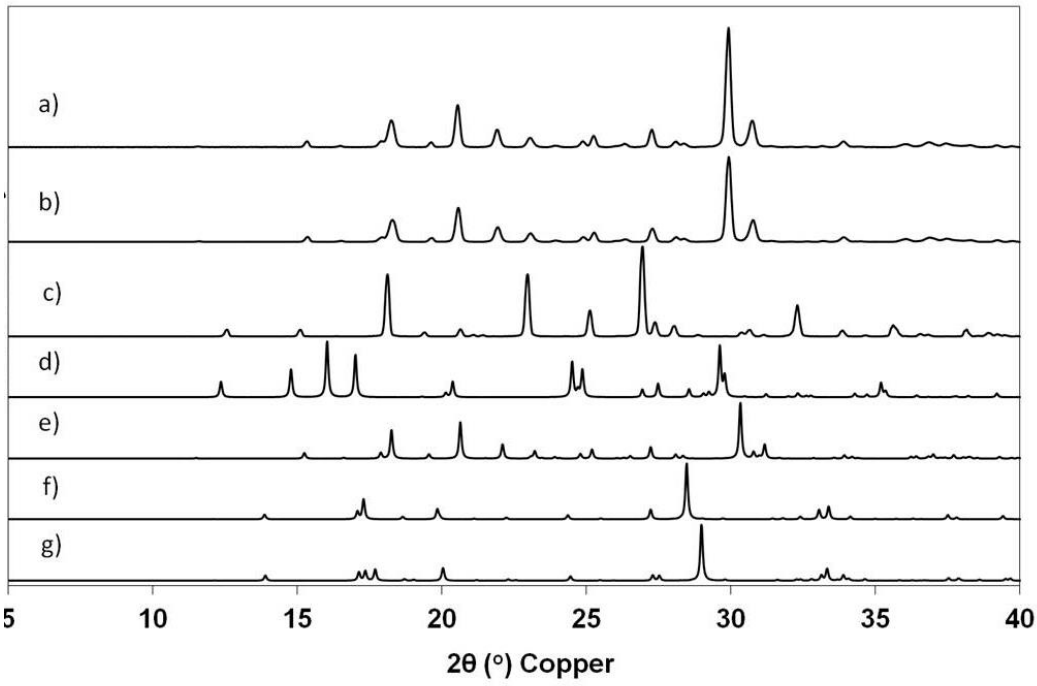

Figure 4.2 For comparison PXRD patterns of BA starting material obtained from a) Acros Organics, b) Sigma Aldrich and c) Tokyo Chemical Industries are displayed alongside patterns calculated from SXRD data for BA I (d), BA II (e), BA dihydrate I (f) and BA dihydrate II (g). (Note BA II and BA dihydrate II were calculated from data at 150 K)

All three commercial starting materials could be co-crystallised with urea to form UBA co-crystals however there were some significant differences observed in the physical properties of these starting materials. PXRD was used to identify which polymorph of BA was produced by each supplier (Figure 4.2). BA-AO and BA-SA were identified as BAII [105], however the PXRD pattern of BA-TCI did not correspond to BAI, BAII or BA dihydrate.

This may be a new polymorphic form of BA; indeed, studies by Chierotti *et al.*[108] to investigate induction of solid state phase transformations in BA by grinding BAII (about 200 mg) with 3-4 drops of absolute ethanol using a ball mill for 24 hours and identified an unknown phase which displays different X-ray diffraction behaviour to BAI and BAII and through solid state NMR, which could represent previous occurrence of one of the uncharacterised solid forms of BA.

BAIII, the enol tautomer, was identified in a later study by Schmidt *et al.* through slurry experiments of BAII. In this study the material was characterised using solid state NMR, DSC and PXRD,

however no SXRD data was collected and therefore a PXRD pattern cannot be calculated from the data for comparison with the PXRD pattern of BA-TCI. Instead the PXRD patterns obtained in the study by Schmidt *et al.* are shown below for comparison (Figure 4.3).

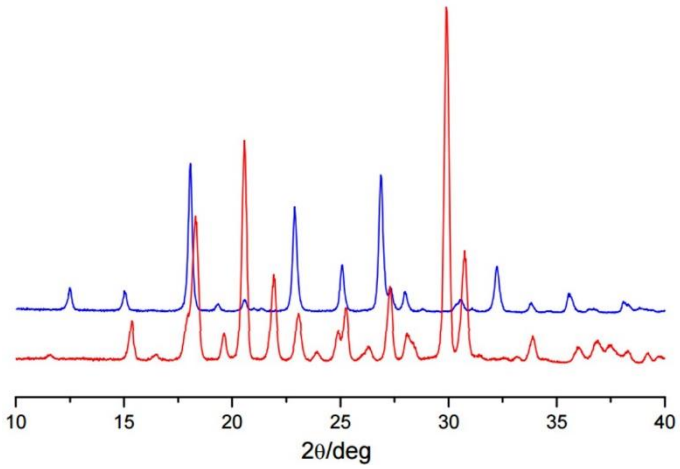

Figure 4.3 PXRD patterns of BAII (red) and BAIII (blue) obtained in the discovery of BAIII by Schmidt *et al* [107]

The PXRD pattern of BAIII (Figure 4.3, blue) clearly matches the PXRD pattern of BA-TCI (Figure 4.2 c) indicating that the BA-TCI starting material is BAIII. The industrial process used by TCI to manufacture BA may by chance have the optimum conditions to produce BAIII.

4.1.2 Scanning Electron Microscopy

Whilst on placement at AstraZeneca Macclesfield samples of crystalline materials were analysed using a Hitachi TM-1000 table-top scanning electron microscope. Samples were gold coated prior to examination, using a Quorum EMS 150R gold sputter coater, to prevent charge build up on the surface of the samples.

Although different polymorphs of a material may exhibit different crystal morphologies, the environment in which a material is crystallised tends to have such a large influence upon the morphology and size distribution that these cannot generally be used as a definitive way of distinguishing between polymorphs.

Interestingly from SEM imaging the crystals of BA-SA and BA-AO appear to have similar shape and size (Figure 4.4 a to d) but BA-TCI looks much more cube like and appears to be more regular (Figure 4.4 e and f). These differences may be due to the polymorphic form or, more likely, indicate that the manufacturing processes for BA used by TCI are very different to those used by SA and OS, in turn having an effect on the solid form.

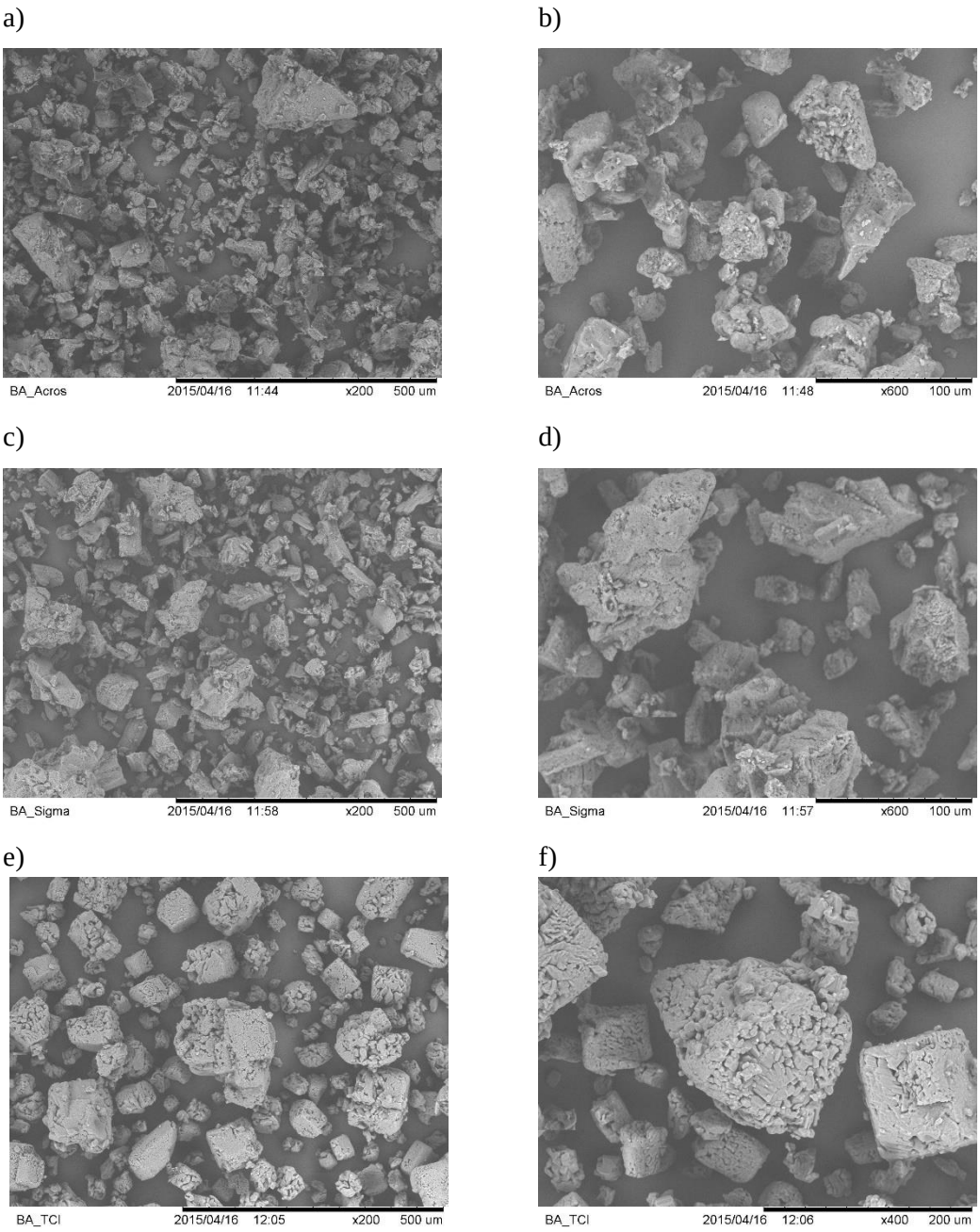

Figure 4.4 SEM images showing the morphology of BA-SA (a and b), BA-AO (c and d) and BA-TCI (e and f)

4.1.3 IR and Raman Spectroscopy

Samples were analysed using a Thermoscientific Nicolet 6700 FT-IR with ATR head. A resolution of 4 cm^{-1} was used with 32 scans collected (Figure 4.5) over a scan range of 3600-600 cm^{-1}. Raman analysis was carried out using a Thermofisher Scientific DXR Raman microscope equipped with 780 nm laser (Figure 4.5). Data were analysed with OMNIC software v8.1.210 (© 1992-2009 Thermo Fisher Scientific Inc.).

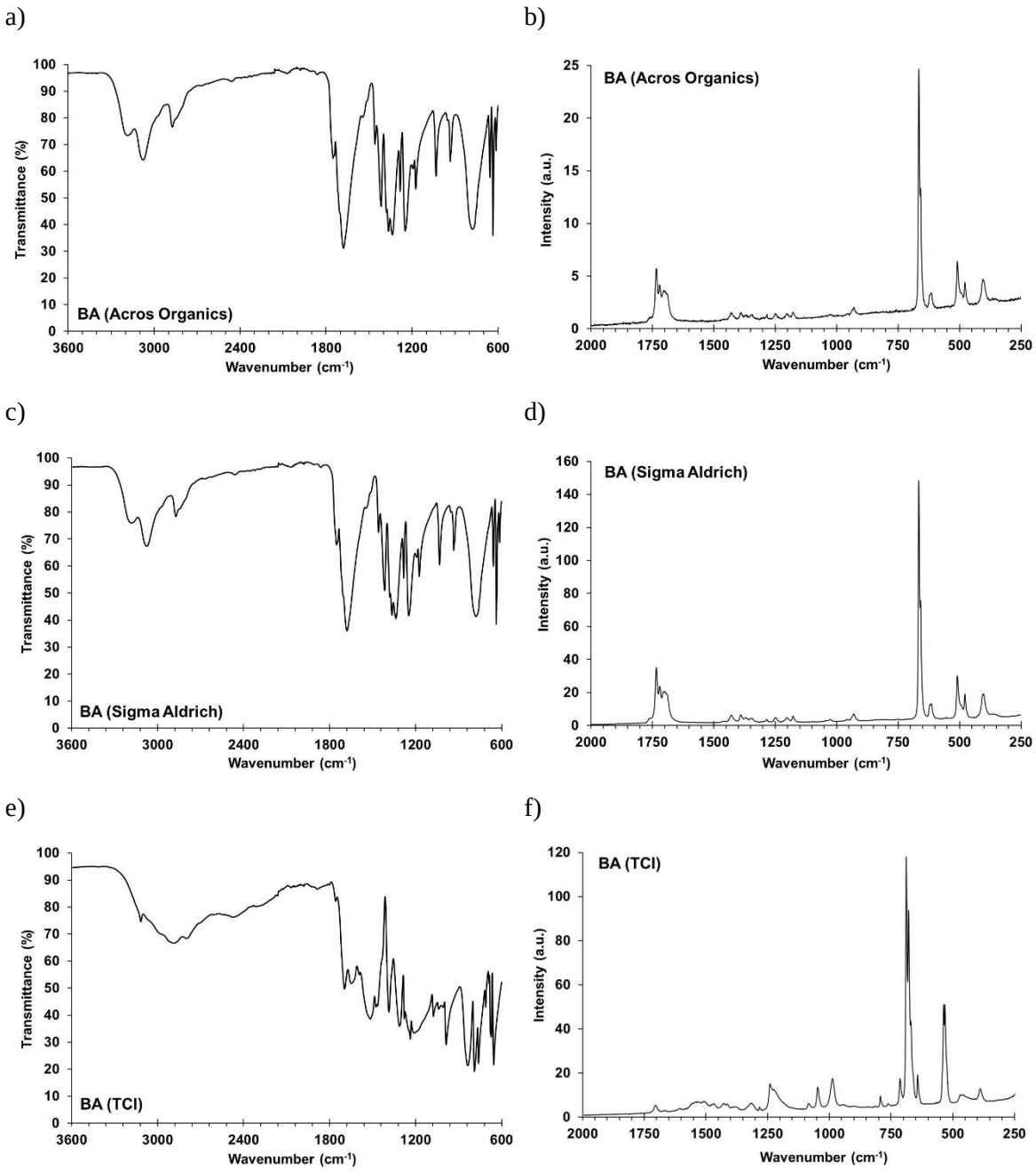

Figure 4.5 IR and Raman spectra of BA-AO (a and b), BA-SA (c and d) and BA-TCI (e and f)

As observed using other methods of analysis the IR and Raman spectra of BA-AO and BA-SA are identical however the spectra from BA-TCI are significantly different indicating a different form of BA starting material. BAIII was fully characterised in a study by Schmidt *et al* [107]; the FTIR spectra of BAII and BAIII from this study are shown below (Figure 4.6).

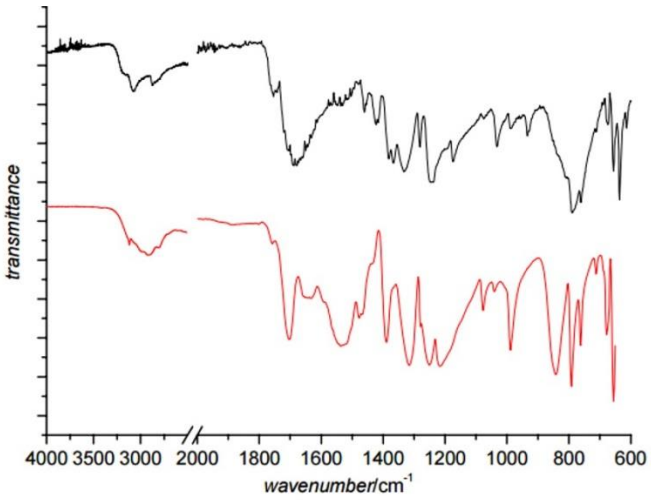

Figure 4.6 FTIR spectra of BAII (black) and BAIII (red) obtained in the discovery of BAIII by Schmidt *et al* [107]

On comparison with the FTIR spectrum obtained in this study on the BA starting materials it is clear that BA-AO (Figure 4.5 a) and BA-SA (Figure 4.5 c) match with BAII (Figure 4.6, black) and BA-TCI (Figure 4.5 e) corresponds to BAIII (Figure 4.6, red) as characterised by Schmidt *et al*.

4.1.4 Differential Scanning Calorimetry

DSC on BA starting materials obtained from Sigma Aldrich, Acros Organics and TCI was carried out using a Thermal Advantage Q20 DSC from TA Instruments, equipped with Thermal Advantage Cooling System 90 and operated with a dry nitrogen purge gas at a flow rate of 18 cm^3 min^{-1}. The samples were placed in sealed Tzero aluminium pans and a heating/cooling rates of 2 to 10 K min^{-1} were used. Data were collected using the software Advantage for Qseries.

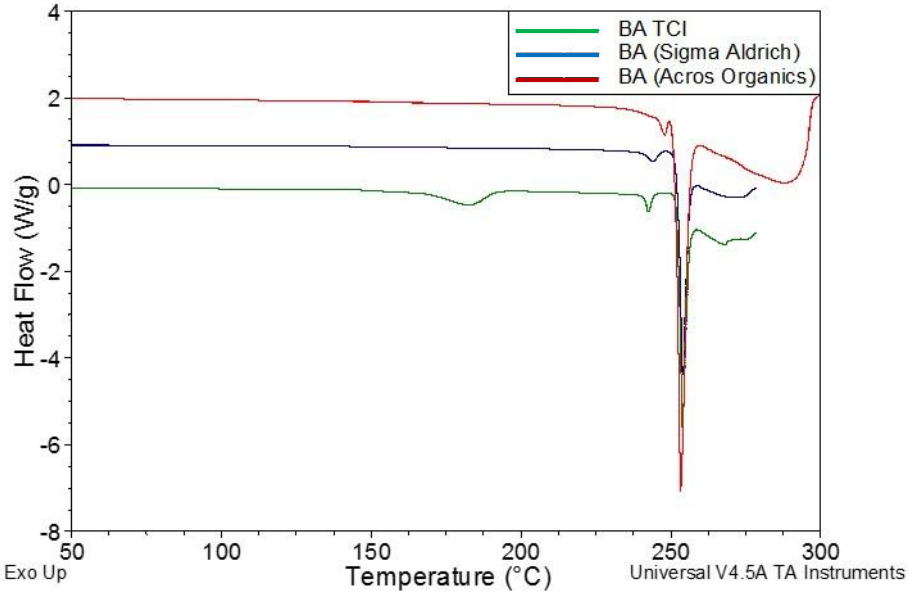

Figure 4.7 DSC of BA starting materials, BA-TCI, BA-SA and BA-AO

Table 4.2 Temperatures of thermal events in DSC traces of the BA starting materials for comparison with temperatures for BAII (reported by Roux *et al.*) and BAIII (reported by Schmidt *et al.*)

Thermal event	Onset temperature of event for each material (°C)				
	BA-SA	BA-AO	BA-TCI	BAII [111]	BAIII [107]
Phase transition BA III → BA II	-	-	170	-	172
High temperature phase	245	241	241	243	243
Melt and decomposition	251	253	252	253	251

The endothermic event in the DSC trace of BA-TCI (T_{onset} = 170 °C) (Figure 4.7, green) is indicative of a phase transition characteristic of BAIII, which was confirmed to be a phase transition between BAIII and BAII by Schmidt *et al.* Both BA-SA and BA-AO (Figure 4.7 blue and red, respectively) display two endothermic events. The first event (at 245 °C and 241 °C for BA-SA and BA-AO) corresponds to a phase transition to an unknown high temperature phase of BA and the second event (at 251 °C and 253 °C for BA-SA and BA-AO) corresponds to the melting and decomposition of this phase[107, 111]. This analysis agrees with the identification of BA-SA and BA-AO as BAII and BA-TCI as BAIII.

4.1.5 Dynamic Vapour Sorption

Dynamic vapour sorption was carried out on BAII (BA-SA). Using a Surface Measurement Systems DVS Intrinsic, approximately 20-30 mg of material was weighed into an aluminium sample pan. The relative humidity (RH) was taken from a starting humidity of 0% RH up to 90% RH in 10% steps then decreased down to 0% RH in 10% steps at a constant temperature of 25 °C. This relative humidity cycle was repeated. Equilibration at each humidity step was set such that the rate of change of weight with time (min) was less than 0.0005%/min. for 5 minutes before moving on to the next humidity step.

BAII (BA-SA and BA-AO) readily forms BA dihydrate (CSD ref BARBAD) [109, 110, 112] upon exposure to moisture, and this is clearly demonstrated by the hysteresis in the DVS plot (Figure 4.8). The mass increase at 80% RH corresponds to the mass of two mole equivalents of water (relative to the number of moles of BA in sample), consistent with the formation of BA dihydrate. The dihydrate persists in DVS experiments down to 40% R.H. below which the original BA starting material is produced, indicating that once formed the BA dihydrate is stable under ambient humidity conditions (usually around 60% RH). Interestingly on the second cycle the onset of hydrate formation occurred at 70% RH. Access to DVS equipment was not readily available and as a result BAIII (BA-TCI) was

not analysed using DVS. It would be interesting to see if BAIII formed BA dihydrate and if so under what humidity conditions; this is therefore proposed as future work.

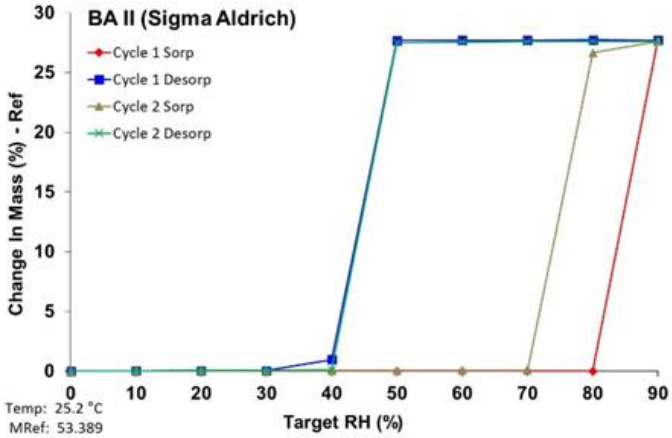

Figure 4.8 Dynamic vapour sorption experiment on BAII (BA-SA) showing reversible hydration to BA dihydrate

4.1.6 Humidity studies

Access to DVS equipment was available during a three month secondment at AstraZeneca, Macclesfield. For studies carried out at the University of Bath, samples were subjected to humidity testing using a sealed container filled with 200 g sodium chloride mixed with approx. 10 mL deionised water and fitted with a humidity sensor suspended upon a plastic shelf inserted into the container (Figure 4.9). The container was placed in an oven set at 50 °C and the conditions allowed to equilibrate for 24 hours. The humidity stabilised at 78% RH at a temperature of 45 °C. The samples that were subjected to RH ageing were monitored on a weekly basis using PXRD (Figure 4.10 - Figure 4.12).

Figure 4.9 Rudimentary set-up for long term humidity exposure testing comprising airtight container, sodium chloride and water mixture, plastic shelf to hold materials and a humidity sensor

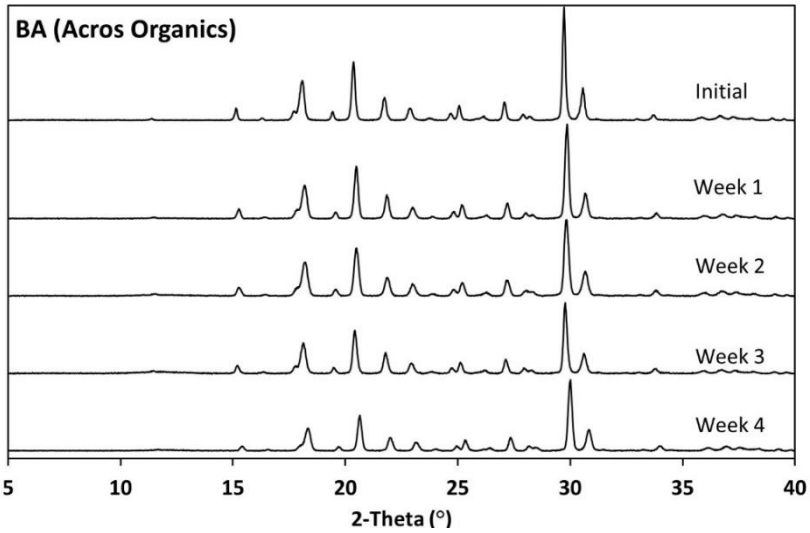

Figure 4.10 Weekly PXRD analysis of BA-AO subjected to 78% RH at 45 °C for four weeks.

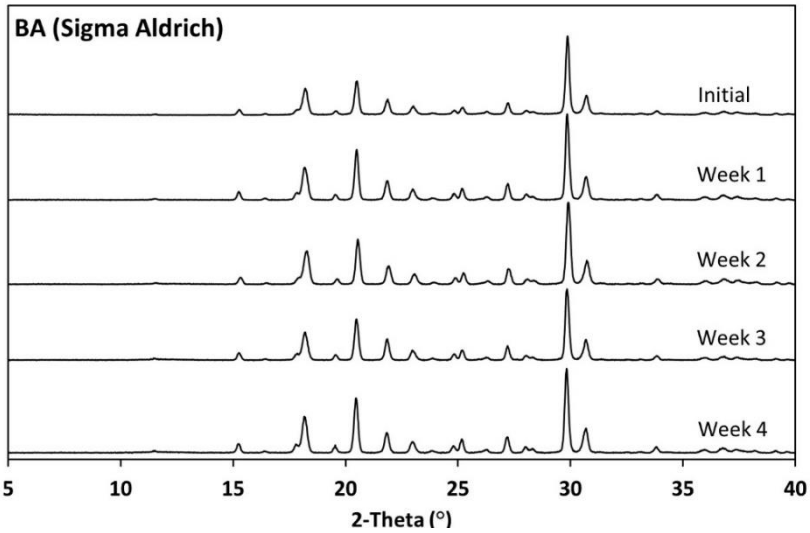

Figure 4.11 Weekly PXRD analysis of BA-SA subjected to 78% RH at 45 °C for four weeks

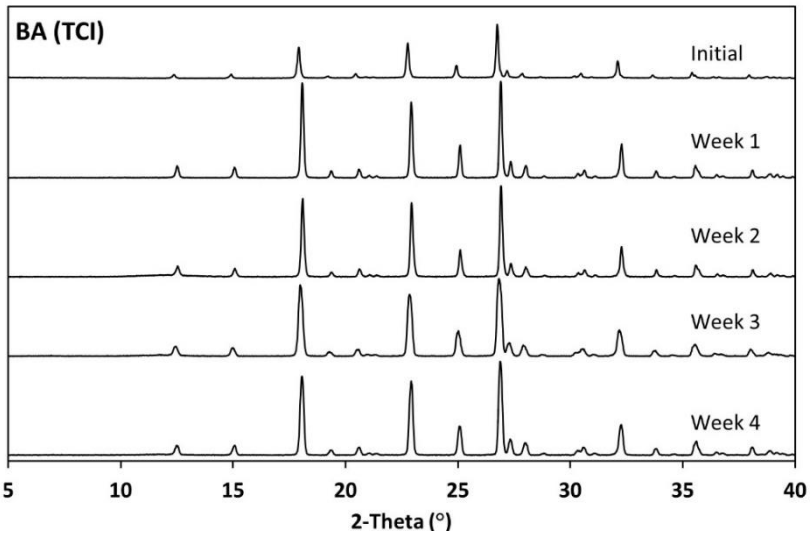

Figure 4.12 Weekly PXRD analysis of BA-TCI subjected to 78% RH at 45 °C for four weeks

All three commercially available BA starting materials remained unchanged after four weeks at 45 °C and 78% RH. Conversion between BAIII (BA-TCI) and BAII (BA-SA and BA-AO) under these environmental conditions is not expected as the phase transition occurs at much higher temperatures (170 °C). There is no indication of BA hydrate formation within the PXRD patterns however DVS analysis of BAII (Figure 4.8) shows that the hydration of BAII is a reversible process and as the PXRD experiments are not carried out under humidity controlled conditions then it would be expected that any BA dihydrate produced would dehydrate under ambient conditions. Investigations using variable humidity PXRD have been carried out previously on BAII by Zencirci *et al.*[96] and in future data could be collected for BAIII to complement this.

4.1.7 Conclusions

Analysis was conducted of commercially available BA obtained from three suppliers; Sigma Aldrich (BA-SA), Acros Organics (BA-AO) and TCI (BA-TCI). None of the suppliers identified which polymorphs of BA was provided. The range of solid state characterisation confirms that BA-SA and BA-AO are BAII and BA-TCI is the BAIII polymorph. BAIII and BAIV are not deposited in the CSD, often a crystal engineer's first port of call for information about the polymorphic behaviour of a material and initially they were overlooked until the wealth of information was discovered in the ESI of the paper published by Schmidt *et al*. which lead to confirmation that BA-TCI was BAIII. Further analysis of the solubility of BAIII is required to compare to solubility data obtained for BAII as this may affect the dissolution behaviour of the BA starting material during cooling crystallisation which will have implications upon the crystallisation conditions required.

4.2 Evaporative Crystallisation of UBA

The discovery / initial production of solid forms of the UBA system was carried out in the present work by small scale evaporation, using the conditions detailed in Table 4.1 (above)[14]. As the previous studies carried out by Gryl *et al.* did not investigate the bulk properties from their evaporative crystallisation experiments it is difficult to know if the single crystals used for structure solution in that work were representative of the bulk. The evaporative crystallisation experiments were replicated and built upon here in order to ascertain if different evaporative conditions could be designed that were able to isolate the individual UBA polymorphs.

4.2.1 Materials

Urea (98% bio-reagent grade) was purchased from Sigma Life Science and BAII (98% reagent grade) was purchased from Sigma Aldrich. All reagents were used without further purification. Laboratory reagent grade solvents purchased from Sigma Aldrich were used for all crystallisations.

4.2.2 Method

Urea and barbituric acid, weighed out into a 7 mL glass vial, in either a 1:1 ratio (23 mg urea and 50 mg BA) or a 2:1 ratio (47 mg urea and 50 mg BA) were dissolved in approximately 5 mL of either methanol or ethanol. The vials were capped with a pierced plastic lid and left to evaporate at a fixed temperature (RT, 30°C or 50°C) until dry (24 to 48 hour on average). The conditions of each crystallisation are detailed in Table 4.3.

The entire content of each vial was removed and gently kneaded in a pestle and mortar for 10 s, long enough to ensure that the samples are uniform and to reduce preferred orientation in PXRD analysis, but short enough to prevent any mechano-chemical transformations. All samples were analysed using PXRD.

4.2.3 Results and Discussion

A summary of the qualitative results obtained from PXRD analysis are detailed in Table 4.3 and the PXRD patterns are shown in Figure 4.13.

Table 4.3 Summary of crystallisation conditions and results obtained from PXRD analysis of UBA evaporative crystallisation experiments

No.	Solvent	Temp. of evap. (°C)	Ratio U: BA	Product (from PXRD analysis)					
				UBAI	UBAII	UBAIII	BAI	BA (H_2O)	U
1	Methanol	RT	1:2	X		X		X	
2	Methanol	30	1:2			X	X		
3	Methanol	50	1:2		X	X	X		
4	Methanol	RT	2:1			X	X		X
5	Methanol	30	2:1	X		X			X
6	Methanol	50	2:1	X		X	X		X
7	Ethanol	RT	2:1	X		X			X
8	Ethanol	30	2:1	X					X
9	Ethanol	50	2:1	X		X			X
10	Ethanol	RT	1:2	X				X	
11	Ethanol	30	1:2	X			X		
12	Ethanol	50	1:2	X		X	X		

RT = 18°C in a temperature controlled laboratory
X = positive identification in PXRD pattern

Crystallisation trials from neither the methanol nor ethanol solvent selectively produced a single UBA polymorph. However, in all experiments using methanol UBAIII was always present, whilst when using ethanol UBAI was always present in the mixture. This is particularly clear in experiments 2 and 4 (from methanol) and experiments 8 and 10 (from ethanol). It may be that the change in solvent could have a templating effect on the UBA polymorph, but this is unlikely due to the similarity in functionality of ethanol and methanol, and the differing tendency for dominant polymorph production in these trials is more likely to be due to differences in solubility of UBA in the different solvents or the difference in volatility of the solvents.

In summarising the above trials, all experiments produced mixtures of the UBA polymorphs in which residual urea and BA starting materials were also present, as qualitatively identified through PXRD. If further work were to pursue selectivity and yield in such evaporative crystallisation approaches in a quantitative way, the proportions of each solid form present in the mixtures could be quantified using multi-phase Rietveld analysis of the PXRD patterns.

4.2.4 Conclusion

The systematic evaporative co-crystallisations carried out on the UBA system have shown that it is possible to produce each of the UBA polymorphs. The more stable pair of polymorphs (UBAI UBAIII) are produced under a range of conditions, while the most metastable polymorph UBAII is only produced in one of the trials carried out; this is in keeping with its metastable nature, and its known status as an elusive solid. Although all forms of UBA have been produced, and on some of

the trials only one solid form of UBA is found, it should be noted that UBAI and UBAIII frequently co-exist, while in all cases the final product includes evidence of residual starting material.

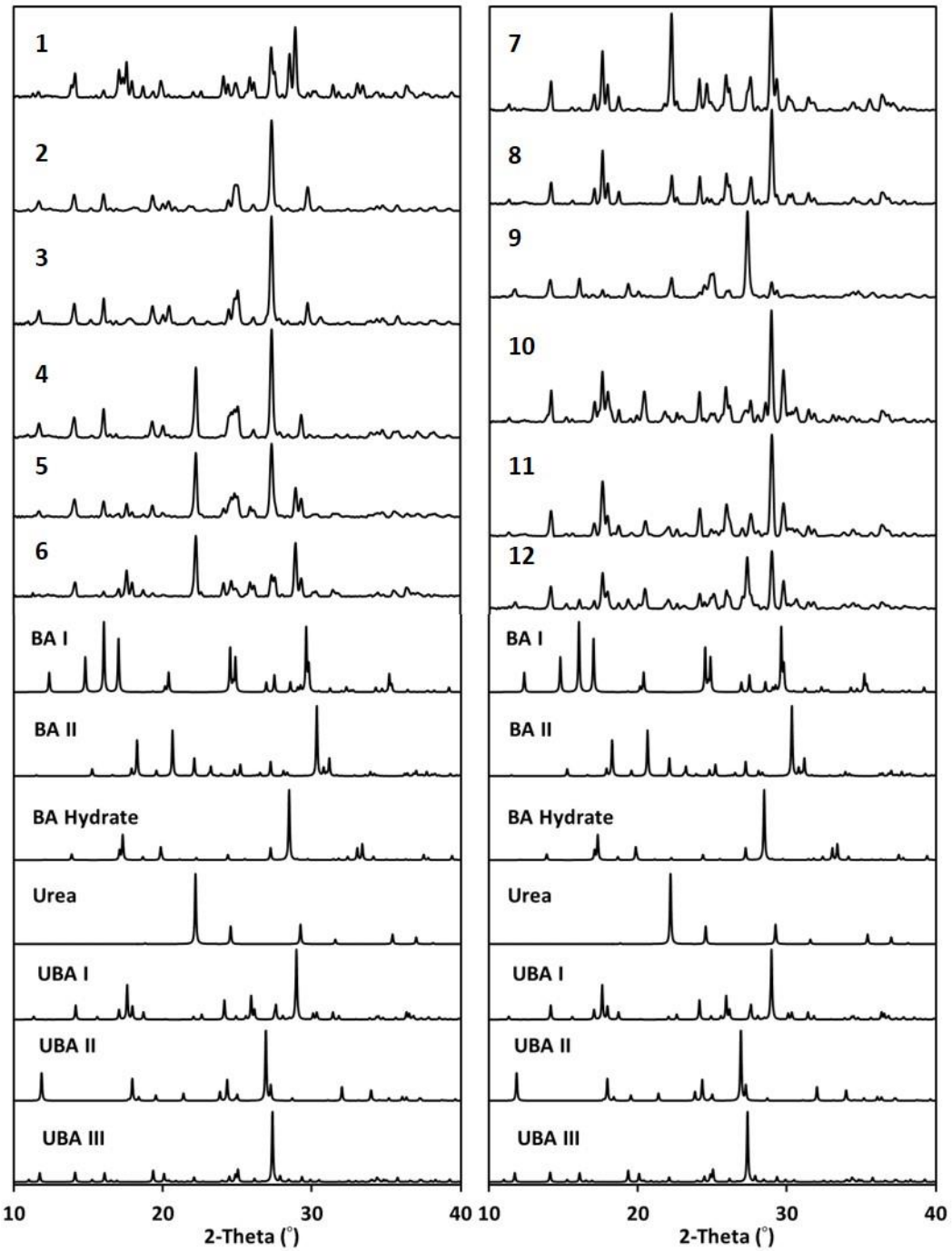

Figure 4.13 PXRD patterns of evaporative crystallisation experiments 1-12 for comparison with urea and BA starting materials and the UBA polymorphs

4.3 Small Scale Mechano-crystallisation of UBA

As discussed in section 2.4.4 mechano-crystallisation can be a useful route to producing MMCs and has particular environmental benefits over solution based crystallisation. Small scale evaporative crystallisation was the only technique reported by Gryl *et al.* for producing UBA co-crystals now complemented by the successful cooling crystallisation of UBA is detailed in section 4.2 above. The aim of this study is to explore whether it is possible to co-crystallise urea and BA by mechano-crystallisation and if so which polymorphs of UBA are produced. This will allow access to questions such as whether it is possible to access different UBA polymorphs, or different selectivity amongst the known polymorphs, using this different crystallisation method. Successful production of UBA using mechano-crystallisation would be particularly useful for the generation of seeds especially if it is possible to isolate a single UBA polymorph.

4.3.1 Materials

Urea (98% bio-reagent grade) was purchased from Sigma Life Science and BA (98% reagent grade) was purchased from Sigma Aldrich. All reagents were used without further purification. Laboratory reagent grade solvents purchased from Sigma Aldrich were used for all crystallisations.

4.3.2 Method

Urea and barbituric acid in either a 1:1 ratio (23 mg urea and 50 mg BA) or a 2:1 ratio (47 mg urea and 50 mg BA) were combined in a pestle and mortar, kneading for 15 minutes. This was carried out using both dry and solvent assisted grinding. Solvent assisted experiments involved dropwise addition of either water, methanol, ethanol or isopropyl alcohol to produce and maintain a paste texture. The solvent readily evaporated from the end sample prior to PXRD analysis. Three control samples, a 1:1 mixture, a 2:1 mixture and a 1:2 mixture (U:BA) of urea and BA, that were simply mixed with a spatula for a few seconds (i.e. without compression) were produced and analysed using PXRD as a control for comparison to the kneaded samples.

4.3.3 Results and Discussion

A summary of experimental conditions and the qualitative results obtained from PXRD analysis are detailed in Table 4.4 and the PXRD patterns for the samples are shown in Figure 4.15 to Figure 4.17.

The control experiments highlight that without the mechanical work from grinding the urea and BA do not interact to form co-crystals (Figure 4.14). When the materials are exposed to heat and pressure from grinding in the absence of any solvent UBAI is produced. As all UBA co-crystals are of a 1:1

stoichiometry when a 2:1 ratio of urea:BA is used an excess of urea is present in the final product as would be expected. One would anticipate that if a 1:1 ratio of urea:BA is used complete conversion can be achieved. However in practice in addition to UBAI there is also BA II starting material present in the product and no indication of urea in the PXRD pattern. One suggestion could be that some of the urea has become amorphous and will not be detected explicitly in the PXRD pattern.

Table 4.4 Summary of crystallisation conditions and results obtained from PXRD analysis of UBA mechano-crystallisation experiments

No.	Solvent	Ratio U: BA	Product (from PXRD analysis)					
			UBAI	UBAII	UBAIII	BA	BA (H_2O)	U
-	CONTROL	1:1				X		X
-	CONTROL	2:1				X		X
-	CONTROL	1:2				X		X
1	N/A	1:1	X			X		
2	N/A	2:1	X					X
3	N/A	1:2	X			X		
4	Water	1:1	X				X	
5	Water	2:1	X					X
6	Water	1:2	X				X	
7	Methanol	1:1	X					
8	Methanol	2:1	X *					
9	Methanol	1:2	X				X	
10	Ethanol	1:1	X					
11	Ethanol	2:1	X *					
12	Ethanol	1:2	X				X	
13	IPA	1:1	X					
14	IPA	2:1	X *					
15	IPA	1:2	X			X	X	

X = positive identification in PXRD pattern
*Additional peaks are present that do not match UBA polymorphs, starting materials or hydrates.

LAG experiments with water produced UBAI using a 1:1, 2:1 and 1:2 ratio of starting materials. As observed for solvent free experiments an excess of urea was present from the 2:1 ratio and the 1:1 ratio, but BA dihydrate was present in the final product rather than BAII starting material. For all other LAG experiments (using methanol, ethanol or IPA) UBAI was produced exclusively when using a 1:1 ratio of starting materials. When a 2:1 ratio of urea:BA was used UBAI was also produced although additional peaks present in the PXRD patterns (Figure 4.16) that do not correspond to any of the UBA polymorphs, the starting materials or hydrates, suggest there may be an additional unknown phase or phases present, which are unidentified at this time.

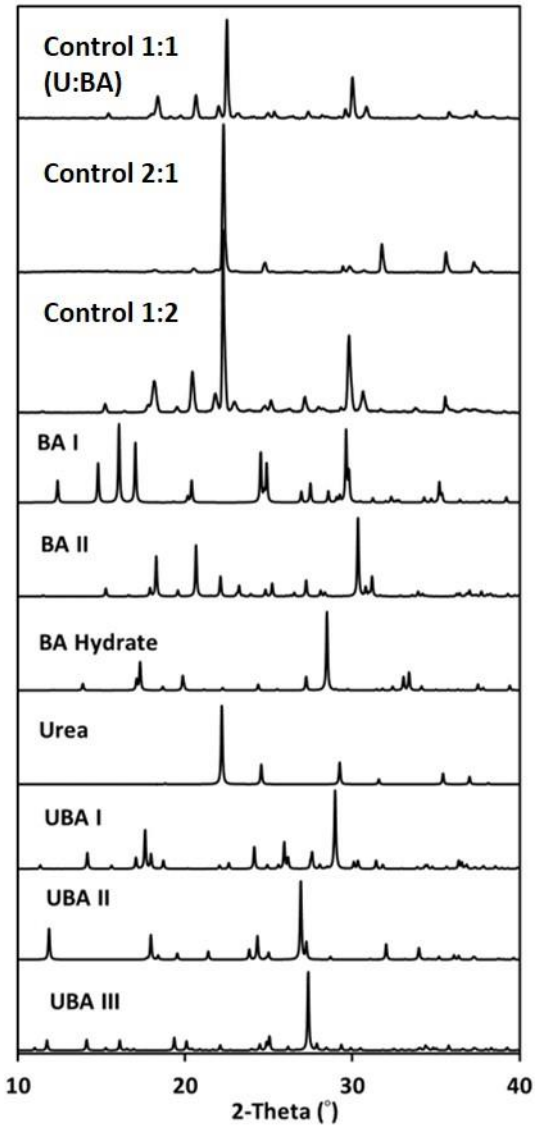

Figure 4.14 Control mixtures of urea and BA in a 1:1, 2:1 and 1:2 ratio (urea:BA)

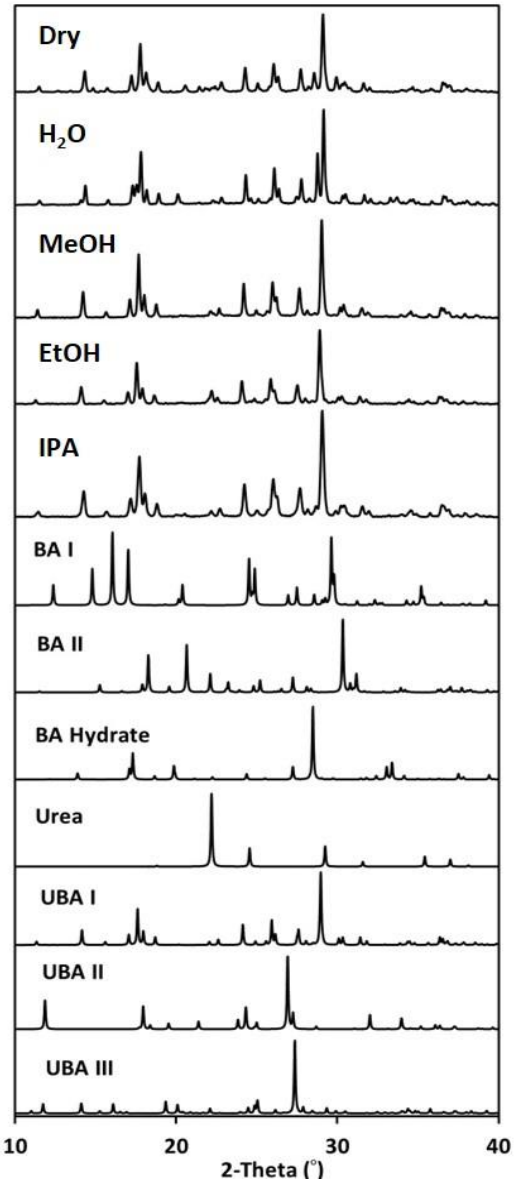

Figure 4.15 PXRD analysis of mechano-chemical experiments using 1:1 ratio (urea:BA) and a range of solvents

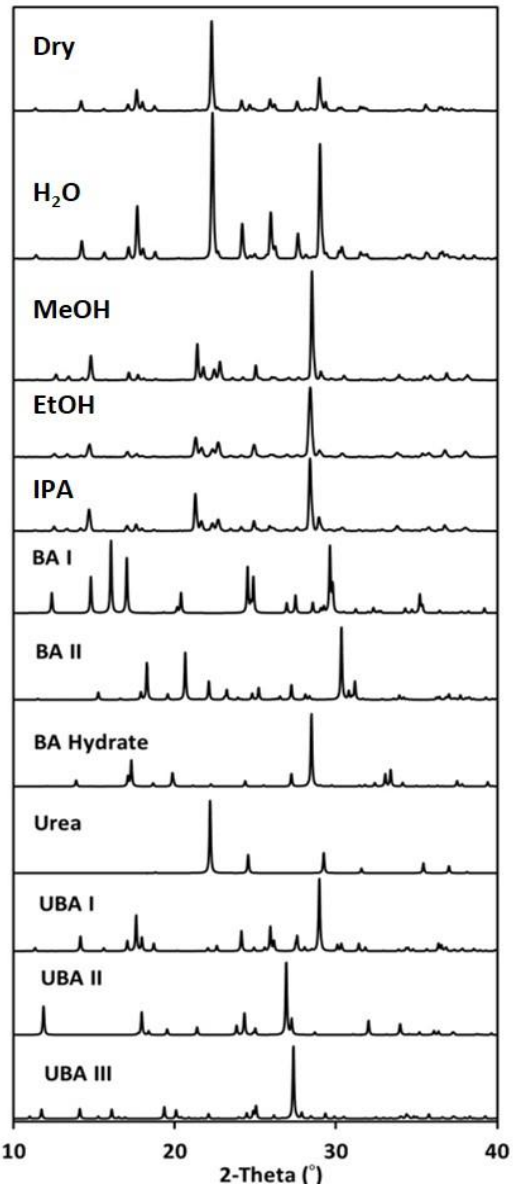

Figure 4.16 PXRD analysis of mechano-chemical experiments using 2:1 ratio (urea:BA) and a range of solvents

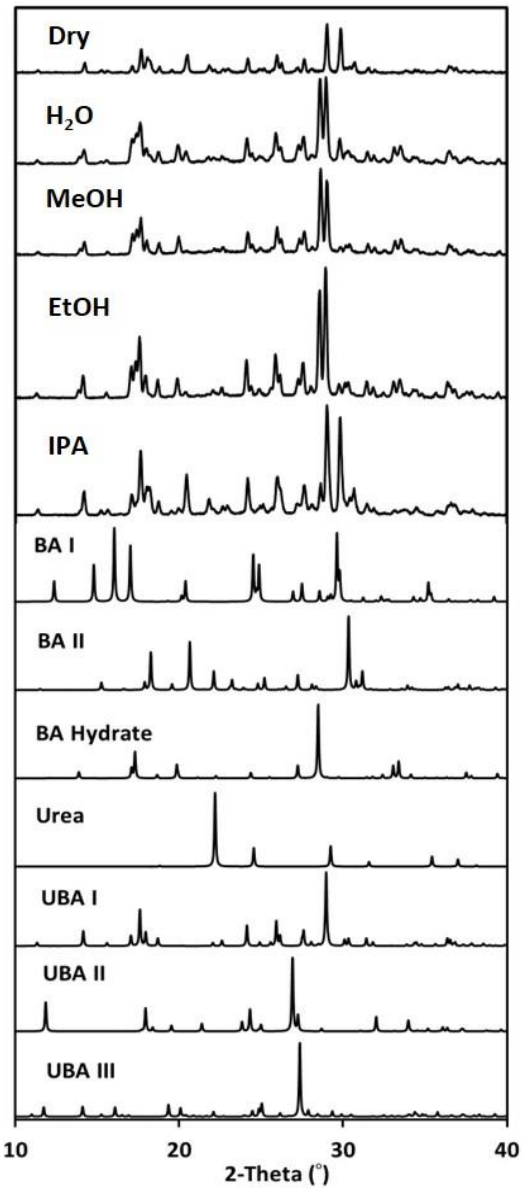

Figure 4.17 PXRD analysis of mechano-chemical experiments using 1:2 ratio (urea:BA) and a range of solvents

4.3.4 Conclusion

The mechano-crystallisation experiments give access exclusively to UBAI, and in 1:1 LAG experiments using either methanol, ethanol or water UBAI is formed as the sole product. Thus mechano-crystallisation, although accessing only one polymorph, does so selectively in a way that was not possible with the evaporative approaches trialled. This facile and selective route to UBAI that can be exploited as a method for UBAI seed production to be used in future UBAI selective crystallisation experiments.

4.4 Small Scale Cooling Crystallisation of UBA – Design of Experiments (DoE)

Design of experiments (DoE) is a statistical method that is used to sample the entire problem space in a systematic and even manner. In an experiment, one or more process variables (or factors) are normally changed, in order to observe the effect the changes have on one or more response variables. DoE is an efficient procedure for planning experiments so that the data obtained can be analysed to yield valid and objective conclusions.

DoE begins with determining the objectives of an experiment and selecting the process factors for the study. An Experimental Design is the laying out of a detailed experimental plan in advance of doing the experiment. Well-chosen experimental designs maximize the amount of "information" that can be obtained for a given amount of experimental effort. DoE is a far more effective method of exploring process variables as it uses a computer-enhanced, systematic approach to experimentation that considers all factors simultaneously. DoE provides information about the interaction of factors and how the total system works, while also showing how interconnected factors respond over a wide range of values, without requiring the testing of all possible values directly.

DoE fits (multi-dimensional) response data from the experiments carried out to mathematical equations. Collectively, these equations serve as models to predict what will happen for any given combination of values once the model has been deduced from the discrete, systematically sampled experiments. With these models, it is possible to optimize critical responses and find the best combination of values to produce a particular response (which can be a property, process variable, etc). The most commonly adopted method for sampling the parameter space is that of full factorial design, in which every setting of every factor appears with every setting of every other factor. A common experimental design is one with all input factors set at two levels each; these levels are called `high' and `low' or `+1' and `-1', respectively. A full factorial design for such a system, with N factors, would require 2^N experiments for a full factorial design (i.e. for four factors, 16 experiments, for five factors, 32 experiments, etc). Other designs are possible and are usually implemented for N=5 or more. One common method used is to run only a fraction of the full factorial design which, while less than optimal, is more feasible experimentally as it reduces the number of experiments required. The so-called fractional factorial design effectively reduces the number of factors by relating some of these to functional combinations of others; these “constraints” reduce the dimensionality of the problem[113].

DoE here was applied to the optimisation of the crystallisation of UBA. Seven factors (Table 4.5) were identified as potentially influential in UBA crystallisation (based on the available studies on UBA). These were used to form a DoE matrix with a 2^4 fractional factorial design involving 16 experiments and four control points (see Table 4.5 below), with the aim to decide which of the

experimental variables is most influential in controlling UBA crystallisation. A fractional factorial design was chosen over a full factorial design as with seven factors (2^7 design) 128 experiments would be required to map the design space as opposed to 20 in the 2^4 fractional factorial design significantly reducing the experimental time required to understand the experimental space. This is where the fractional factorial design becomes really helpful.

4.4.1 Materials

Laboratory reagent grade methanol (99.8% Sigma Aldrich), urea, 98% bio-reagent grade from Sigma Life Science and either BAIII from TCI Europe (98% pure) or BAII from Sigma Aldrich, were used for all crystallisations.

4.4.2 Methods

Each experiment was prepared using 100 ml methanol which was heated to 50 °C in a 250 ml round bottomed flask using the CRD Polar Bear Plus followed by addition of the urea and BA starting materials (quantities specified in Table 4.5). The solution was then heated to 60 °C and held for either 10, 35 or 60 minutes with stirring from a 2.5 cm magnetic stirrer bar at either 200, 400 or 600 rpm.

4.4.3 Results and Discussion

PXRD analysis (Figure 4.18) shows that of the 24 experiments (16 standard experiments, four control experiments and four extra experiments), six produced some UBA III (Experiments 2, 8, 10, 16, 21 and 23 Table 4.6), one of which was pure UBAIII (Experiment 10). UBAII was not present in any of these experiments. However UBAII was subsequently obtained from batch cooling crystallisation using a two-step cooling profile (section 5.1) as opposed to the linear cooling profiles used to obtain UBA I and UBAIII and in the DoE protocols investigated here.

All the experiments that produced UBAIII were not carried out in a consecutive order showing that there was no seeding of UBAIII from previous experiments. UBAIII was produced in experiments that used BAIII (from TCI) however it does not follow that all experiments using UBAIII starting material produce UBAIII (as shown by results from experiments 3, 5, 11, 13, 16, 19 and 20).

Table 4.5 Conditions used to carry out a 2^4 fractional factorial design of experiments for UBA cooling crystallisation on 100ml scale using CRD Polar Bear Plus

expt. no.	run order	concentration (g/g wrt BA)	Ratio BA:U	Stirring speed (rpm)	Cooling Rate (°C min^{-1})	Final Temp (°C)	Addition	BA polymorph	Initial dwell time (mins)
1	10	0.0125	2:3	200	0.1	5.0	U then BA	BAII	10
2	14	0.0168	2:3	200	0.1	5.0	BA then U	BAIII	60
3	16	0.0125	1:2	200	0.1	25.0	U then BA	BAIII	60
4	19	0.0168	2:3	200	0.1	25.0	BA then U	BAII	10
5	22	0.0125	2:3	600	0.1	25.0	BA then U	BAIII	10
6	13	0.0168	2:3	600	0.1	25.0	U then BA	BAII	60
7	11	0.0125	1:2	600	0.1	5.0	BA then U	BAII	60
8	8	0.0168	1:2	600	0.1	5.0	U then BA	BAIII	10
9	4	0.0125	2:3	200	2.0	25.0	BA then U	BAII	60
10	6	0.0168	2:3	200	2.0	25.0	U then BA	BAIII	10
11	21	0.0125	1:2	200	2.0	5.0	BA then U	BAIII	10
12	24	0.0168	1:2	200	2.0	5.0	U then BA	BAII	60
13	5	0.0125	2:3	600	2.0	5.0	U then BA	BAIII	60
14	12	0.0168	2:3	600	2.0	5.0	BA then U	BAII	10
15	18	0.0125	1:2	600	2.0	25.0	U then BA	BAII	10
16	7	0.0168	1:2	600	2.0	25.0	BA then U	BAIII	60
Control 17	20	0.0147	4:7	400	1.0	15.0	Mixture	BAII	35
Control 18	17	0.0147	4:7	400	1.0	15.0	Mixture	BAII	35
Control 19	15	0.0147	4:7	400	1.0	15.0	Mixture	BAIII	35
Control 20	23	0.0147	4:7	400	1.0	15.0	Mixture	BAIII	35
Extra 21	1	0.0110	2:3	600	2.0	5.0	U then BA	BAIII	60
Extra 22	2	0.0110	2:3	200	2.0	14.0	BA then U	BAII	60
Extra 23	3	0.0125	2:3	200	2.0	25.0	BA then U	BAIII	60
Extra 24	9	0.0168	1:2	600	2.0	5.0	U then BA	BAII	60

All experiments that produced a yield over 55% (total solids) were carried out using high concentration (0.0168 M wrt. BA) and a low final temperature (5 °C). Experiments 12 and 24 have identical crystallisation conditions except for stirring rates, which are 200 rpm and 600 rpm, respectively. The yield for these experiments is identical which suggests that stirring rate does not have an effect on the yield of these crystallisation trials. This conclusion may be more widely applicable for the UBA system but this was not investigated systematically.

Table 4.6 Yield and Polymorphic form of UBA crystals obtained from experiments in DoE set-up.

expt. no.	Yield (%)	Dominant Polymorph (from PXRD analysis)
1	39.2	UBAI
2	58.1	UBAI and UBAIII
3	23.9	UBAI
4	45.5	UBAI
5	8.0	UBAI
6	38.9	UBAI
7	52.0	UBAI
8	57.6	UBAI and UBAIII
9	9.0	UBAI
10	37.4	UBAIII
11	47.3	UBAI
12	59.1	UBAI
13	40.7	UBAI
14	55.0	UBAI
15	24.5	UBAI
16	43.7	UBAIII and UBAI
Control 17	44.2	UBAI
Control 18	39.0	UBAI
Control 19	40.9	UBAI
Control 20	40.1	UBAI
Extra 21	39.3	UBAIII and UBAI
Extra 22	17.8	UBA I
Extra 23	18.1	UBAIII and UBAI
Extra 24	59.1	UBA I

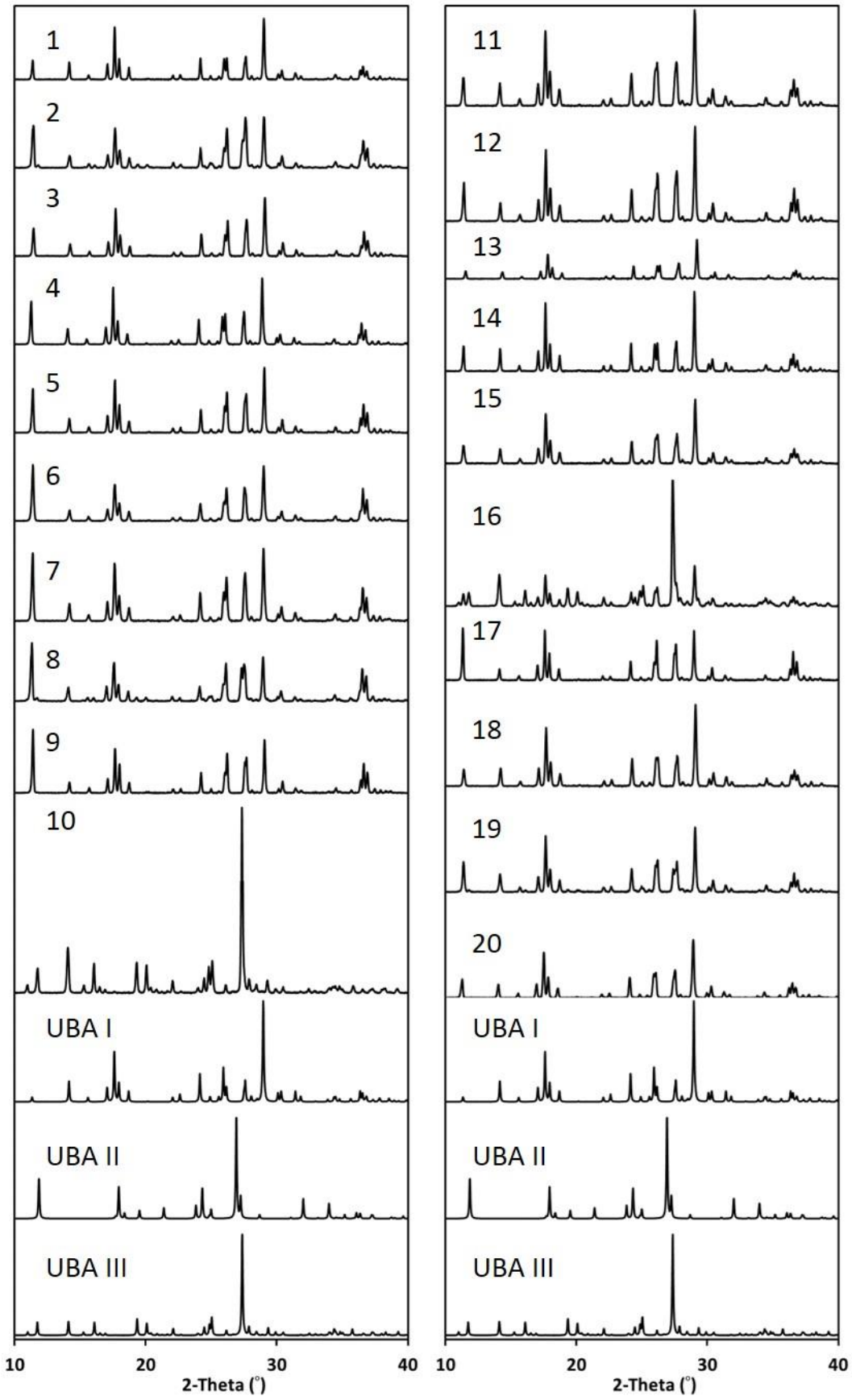

Figure 4.18 PXRD patterns of 100 mL scale cooling crystallisation experiments 1-20 in UBA DoE for comparison with the UBA polymorphs.

4.4.4 Conclusions

DoE highlights that within the experimental space investigated UBAI was the dominant polymorph. And as observed in evaporative and mechano-chemical co-crystallisation experiments UBAII proved elusive. There is very little correlation between the conditions observed and the polymorphic outcome. This may be due to the fact that polymorphs UBAI and UBAIII have very similar physicochemical properties (section 4.5) and the design space may not be broad enough to discover UBAII.

This DoE study is in its early stages. Further analysis using software for multivariate analysis on the results collected can be used in future to carry out regression analysis and create regression models based upon the raw data will be able to help to map out the conditions required to produce a specific UBA polymorph. This is an approach that is being taken within the Wilson group (A. J. P. Cousen, *CMAC PhD project, University of Bath*) as a result of this work.

Quantitative analysis of the PXRD patterns using software such as PolySNAP-3[114] (a cluster analysis software programme) may be of benefit to identify which crystallisation conditions yielded the highest amounts of each polymorph. This may not prove representative due to potential issues with preferred orientation owing to the nature of the sample preparation for PXRD analysis.

4.5 Analysis and Characterisation of the UBA Co-crystal System

The crystal structures of UBAI, UBAII and UBAIII were determined in 2008 by Gryl *et al*. and the packing arrangements within these structures have been described focusing on the hydrogen bonding interactions and graph set notation to distinguish the three polymorphs. As the work by Gryl *et al.* focused on discovery of NLO active materials particular attention was paid to the resonance forms of the BA molecules within each polymorph with an emphasis on charge density studies.

The purpose of the work detailed here is significantly different, attempting to reproducibly isolate each of the UBA polymorphs in bulk; a task in which the relative stability of each UBA polymorph is critical. One observation reported by Gryl *et al.* regarding UBA stability was that when crystals of UBAI and UBAII were left in their mother liquor at 293 K over a period of several weeks the crystals transformed to UBAIII. From this finding Gryl deduced that UBAIII is the most stable UBA polymorph under ambient conditions.

4.5.1 Structural Comparison of Three Polymorphs of UBA

In this section elements of the UBA crystal structures are discussed, and in later sections correlated with experimental characterisation in attempts to rationalise the polymorphic stability within the UBA co-crystal system.

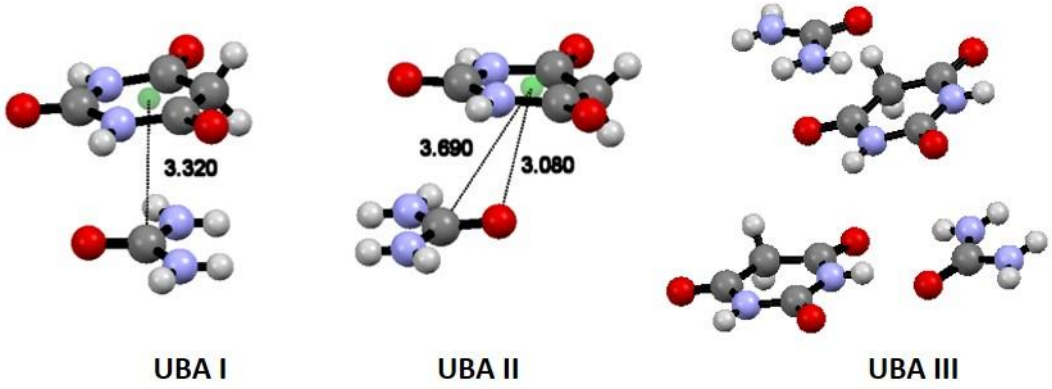

Figure 4.19 The asymmetric unit for UBA polymorphs I, II and III

4.5.1.1 UBAI

Urea and BA can crystallise in the space group $P2_1/c$ forming a 1:1 co-crystal with the unit cell parameters, known as UBAI. The asymmetric unit comprises of one urea and one BA molecule which are positioned such that the carbonyl group of urea and the cyclic amide carbonyl of BA are orientated in the same direction (Figure 4.19). Urea and BA interact to form a heterodimer between BA and urea through N3-H5···O1 and N2-H3···O4 hydrogen bonds (Figure 4.20 a and b, respectively) which form a tetramer unit through two identical N2-H4···O2 hydrogen bonds (Figure 4.20 c).

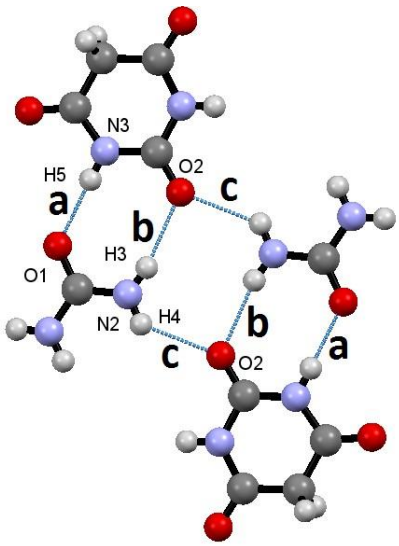

Figure 4.20 Hydrogen bonded tetramer unit present in UBAI

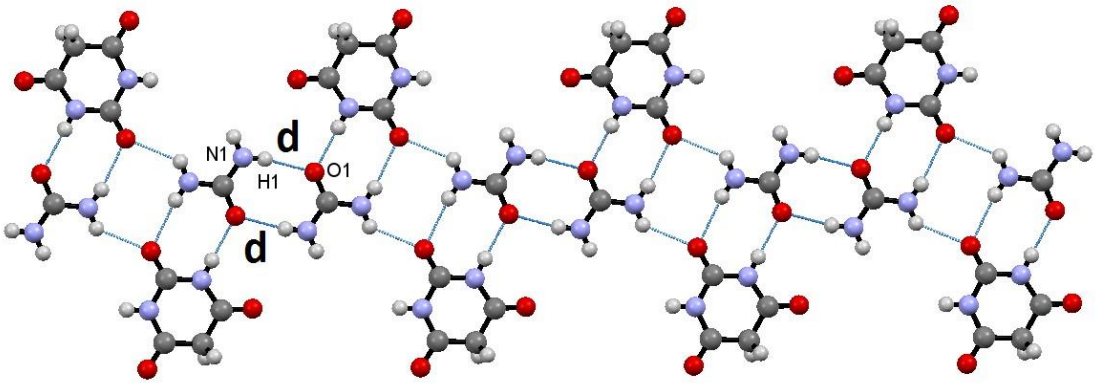

Figure 4.21 UBAI tape comprising tetramers hydrogen bonded through a urea-urea $R_2^2(8)$ motif

Both urea molecules in the tetramer interact with urea in two neighbouring tetramers *via* two symmetry related hydrogen bonds N1-H1···O1 (Figure 4.21 d). This forms a tape of tetramers connected through $R_2^2(8)$ motifs (Figure 4.21). The remaining four hydrogen bond donors (primary amine group in urea and secondary amine in BA) and four hydrogen bond acceptors (two carbonyl groups on each BA molecule) on each tetramer are involved in hydrogen bonding to a further four tetramers units each of which is involved in a separate UBA tape[102]; (Figure 4.22). These connections are formed through DD-A bifurcated hydrogen bonds, comprising N1-H2···O3 and N4-H6···O3 (Figure 4.22 e and f, respectively), between a urea and BA molecule from one tape and a BA molecule from a neighbouring tape.

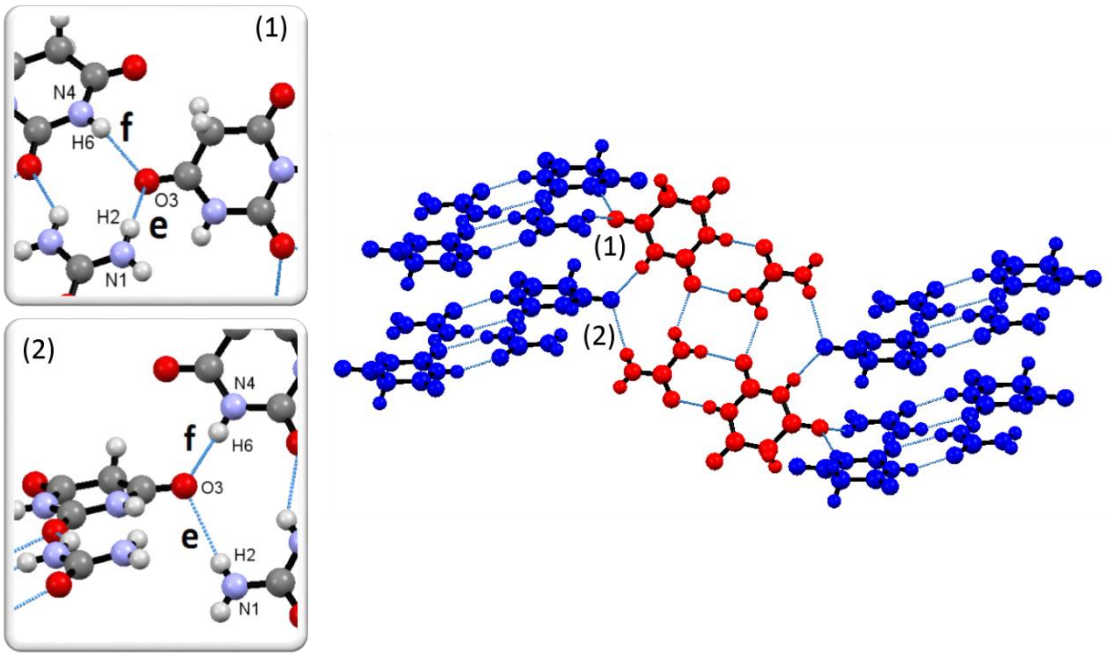

Figure 4.22 Each tetramer bonds to another four tetramers through bifurcated hydrogen bonds (e and f). (1) BA (in red) interacts with BA and urea (in blue) of a neighbouring tape and (2) BA and Urea (red) interact with BA (blue) in another neighbouring chain

The chains stack up on top of one another interacting though π-π interactions between urea and BA in neighbouring layers (3.320 Å carbon to BA centroid distance) and form layers of chains with alternating orientations (Figure 4.23). The full interaction map (FIM) is shown in Figure 4.24; this type of map highlights the similarity in the location of the proposed donor and acceptor sites within molecular components in a crystal structure. In this case the observed spatial relationship between hydrogen bond donors and acceptors within the UBAI structure is shown to be highly probable and favourable, due to the arrangement of the components in the packing of the complex.

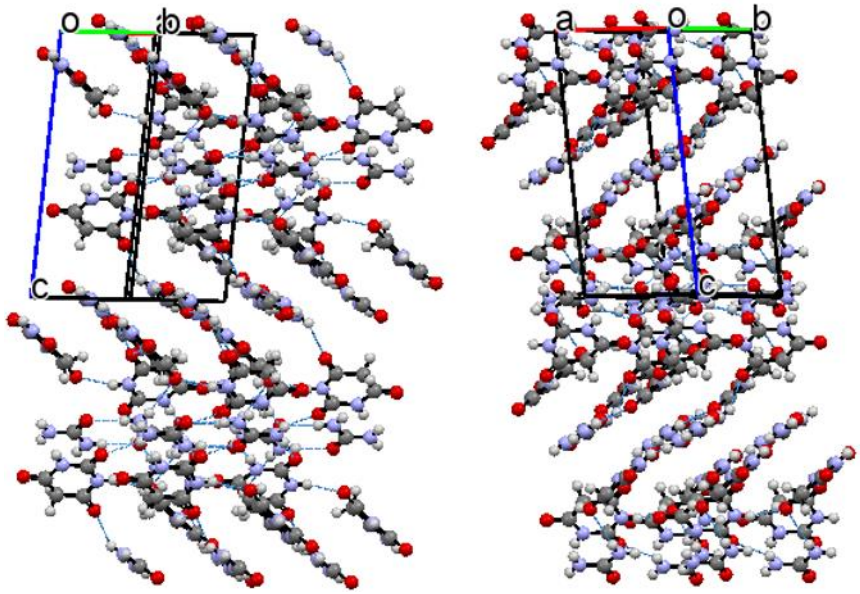

Figure 4.23 Alternating layers of tapes in UBA I highlighted in the shift in orientation when rotated through 90° about the c-axis (left)

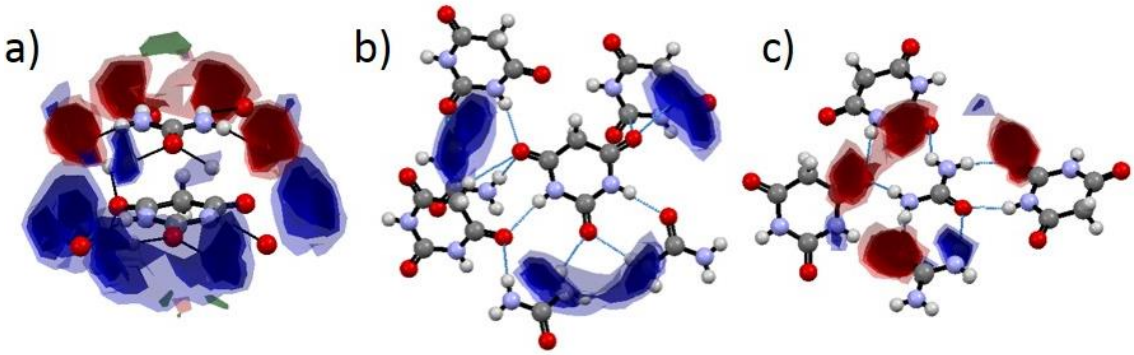

Figure 4.24 Full interaction map (FIM) of UBAI, calculated using Mercury Solid Form Tools showing a) both urea and BA in asymmetric unit, b) proposed hydrogen bond donor sites for BA in the asymmetric unit and c) proposed hydrogen bond donor and acceptor sites for urea in the asymmetric unit (potential donor sites shown in blue, potential acceptor sites shown in red and potential π-π interactions shown in green)

4.5.1.2 UBAII

UBAII crystallises in the space group *Cc*, in a 1:1 ratio of urea to BA, with an asymmetric unit comprising one molecule of urea and one molecule of BA as observed in UBAI. However unlike UBAI, the urea carbonyl group and the BA cyclic amide carbonyl are orientated opposing one another (Figure 4.19). As in UBAI urea and BA from a homodimer unit through two N-H···O hydrogen bonds (N2-H3···O2 and N3-H5···O1, Figure 4.25 a and b, respectively).

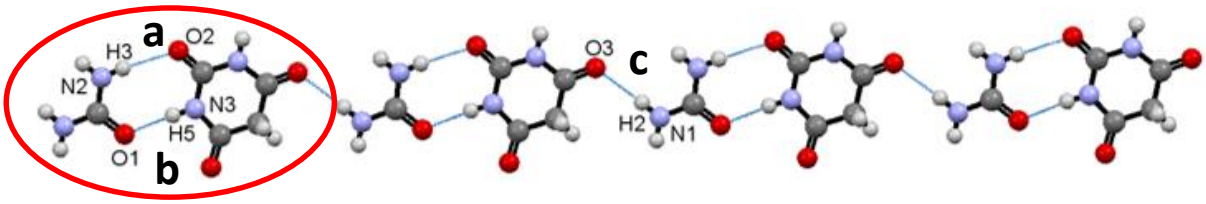

Figure 4.25 Within the UBA II structure urea-BA homodimer units (circled in red) interlink to form a UBA chain

The urea-BA homodimers form a UBA chain through N1-H2···O3 hydrogen bonds between the BA carbonyl and free primary amine in urea within neighbouring homodimers (Figure 4.25 c).

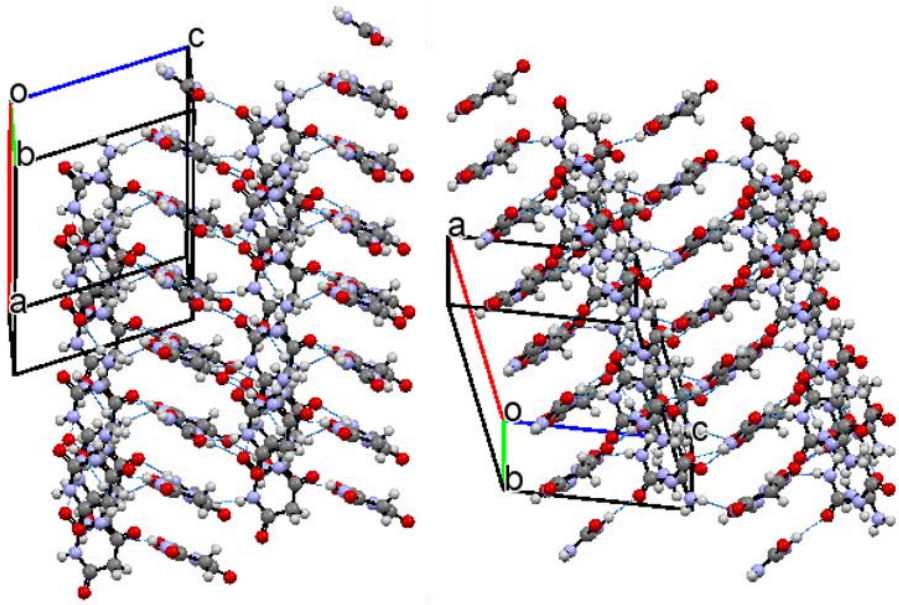

Figure 4.26 Alternating layers of chains in UBAII highlighted in the shift in orientation when rotated through 90° about the c-axis (left)

As in UBAI, the most obvious π-π stacking is in this case between the carbonyl on a urea molecule and a BA molecule, but in this case is significantly offset (Figure 4.19).[14]

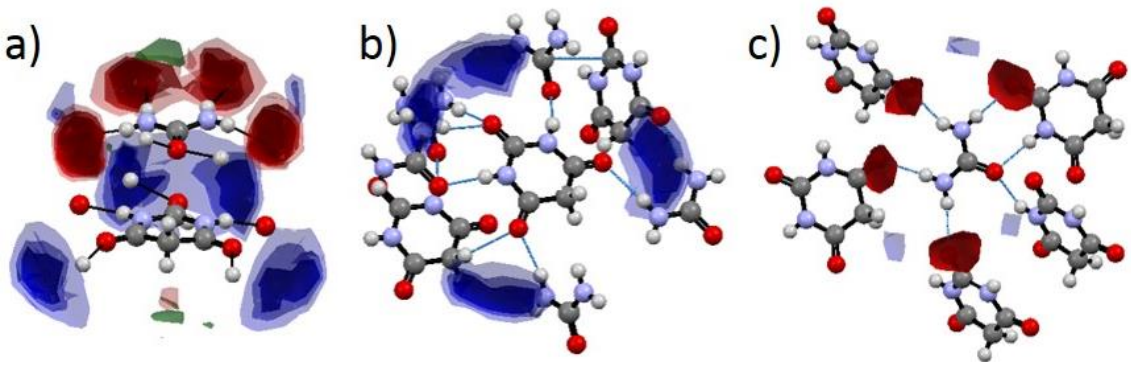

Figure 4.27 Full interaction map (FIM) of UBAII, calculated using Mercury Solid Form Tools showing a) both urea and BA in asymmetric unit, b) proposed hydrogen bond donor sites for BA in the asymmetric unit and c) proposed hydrogen bond donor and acceptor sites for urea in the asymmetric unit (potential donor sites shown in blue, potential acceptor sites shown in red and potential π-π interactions shown in green)

4.5.1.3 UBAIII

UBA III crystallises in the space group $P\bar{1}$ Unlike the previous two polymorphs UBAIII has two molecules of urea and two molecules of BA in the asymmetric unit (Figure 4.19), but it is still a 1:1 co-crystal as is UBAI and UBAII.

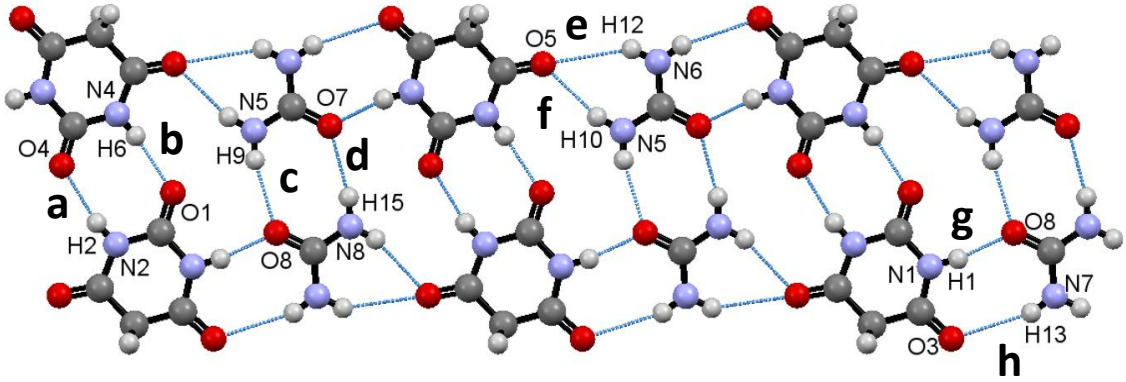

Figure 4.28 Hydrogen bonded UBA chain within the UBA III structure

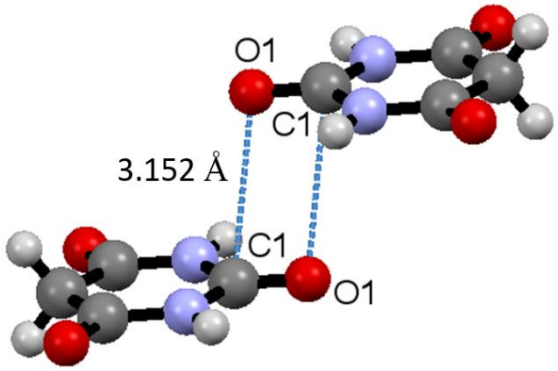

Figure 4.29 π-π stacking between BA molecules within UBAIII

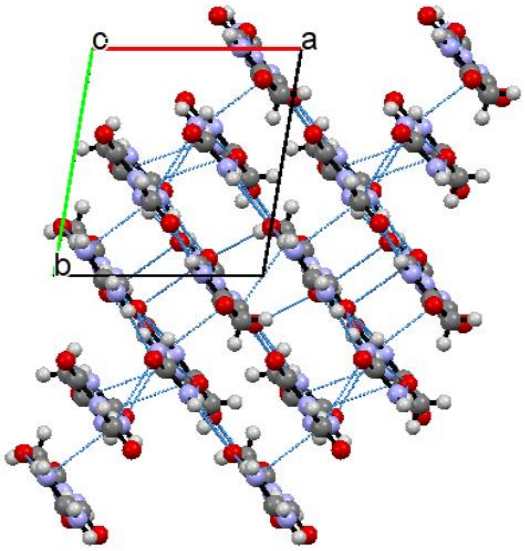

Figure 4.30 Layered structure of UBA III when viewed down the c-axis

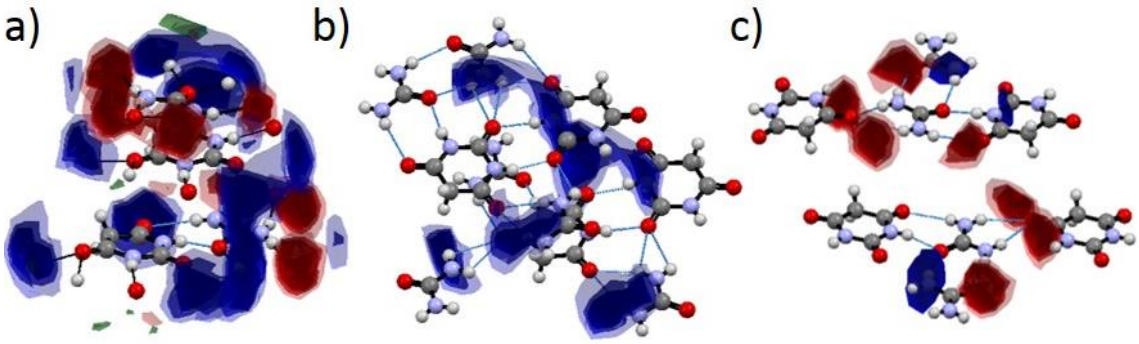

Figure 4.31 Full interaction map (FIM) of UBAIII, calculated using Mercury Solid Form Tools showing a) both urea and BA in asymmetric unit, b) proposed hydrogen bond donor sites for BA in the asymmetric unit and c) proposed hydrogen bond donor and acceptor sites for urea in the asymmetric unit (potential donor sites shown in blue, potential acceptor sites shown in red and potential π-π interactions shown in green)

4.5.1.4 Density Rule for Polymorph Stability

The densities of UBAI, UBAII and UBAIII are 1.593, 1.556 and 1.586 mg m^{-3}, respectively, as reported by Gryl *et al.* from calculations using single crystal data collected at room temperature[14].

The density rule for polymorphs stability proposes that based upon the principle of closest packing the most stable polymorph will have the highest density (at absolute zero). Kitaigorodskii identifies that for hydrogen bonded systems this principle becomes far more complex and cannot be accurately predicted although it can be used to get a rough estimation[115].

The densities presented here are calculated for the hydrogen bonded UBA system from data collected at room temperature (293 K) and so are certainly not a perfect representation. However, the density

of UBAI and UBAIII are very similar and UBAII is significantly less dense indicating that UBAII is the least stable polymorph, which complements results from other characterisation techniques discussed later in this chapter.

4.5.2 Evaluating Hydrogen Bonding Propensity Within the UBA Co-crystal System Using Mercury CFC Tools

CCDC launched the Crystal Form Consortium, a collaborative project between software, database and research experts at the CCDC, and industrialists specialising in solid state science from over 14 different organisations (predominantly from the pharmaceutical and agrochemical sectors), in 2008. The objective was to provide routes to solid form design using tools based upon structural informatics harnessed from the wealth of structural data held within the CSD. The software, which is under continual development, is capable of providing information on the stability of materials, the risk of polymorphism and on hydrogen bond propensity in single component and multi-component systems, information particularly helpful for crystal engineering studies.

As mentioned previously, UBAI and UBAII both have Z' = 1; the asymmetric unit comprises one urea molecule and one barbituric acid molecule, within which there is a total of five and six defined hydrogen bonds, respectively. UBAIII, on the other hand, has Z' = 2; the asymmetric unit comprises two urea molecules and two barbituric acid molecules, thus having an increased number of defined hydrogen bonds, twelve in total. The interactions for UBAIII can be classified into four groups, $Urea_1$-BA_1 (four hydrogen bond interactions), $Urea_2$-BA_2 (four hydrogen bond interactions), $Urea_1$-BA_2 (two hydrogen bond interactions) and $Urea_2$-BA_1 (two hydrogen bond interactions).

Using a statistical model the likelihood for hydrogen bond pairings to form in the target system are calculated, built using relevant structures from within the CSD. The model [116-118] utilises information on the environments of the functional groups, tailoring the prediction to the target system. The functional groups have been defined for the UBA system, three model groups in total, as shown in Figure 4.32.

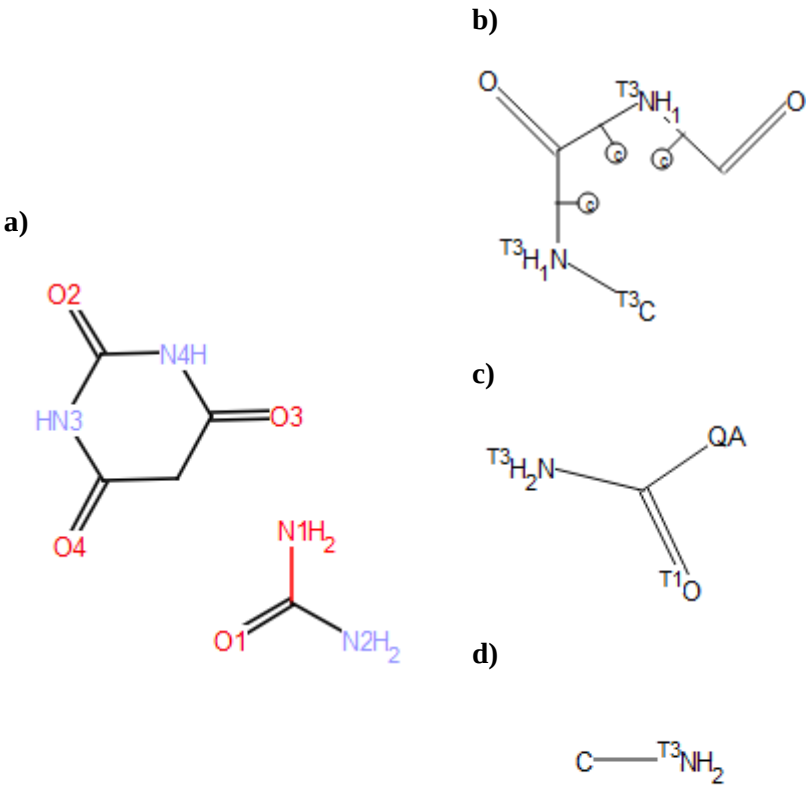

Figure 4.32 Target selection for UBA interactions, in which H-bond donor and acceptor sites are identified (a) and functional group are defined; (b) cyclic amide, (c) urea and (d) amino group

Hydrogen bonding descriptors are extracted from the structures within this training dataset upon which the regression model is based. The hydrogen bonding analysis process identifies any data relating to rare cases of donors or acceptors that may skew the outcome and give a poor fit to the model. These can be removed if present.

The H-bonding model is then fit using a range of different variables including the donor and acceptor atom type, the competition and the aromaticity of the donors and acceptors. Regression analysis identifies the goodness of fit of the data. This model can then be used to calculate the hydrogen bond propensities for each of the UBA polymorphs to allow for comparison of these and investigate whether the H-bond propensities affect the structure and properties of the UBA solid forms.

A range of potential alternative polymorphic forms can be produced computationally by combining the hydrogen bonding propensities with information about the frequency of hydrogen bond participation for each functional group essentially a map of the he resultant view of the solid state landscape addresses questions such as: how likely is polymorphism, and is there the possibility of a more stable form?

Table 4.7 Summary of the donor and acceptor combinations observed in the structures of UBAI, UBAII and UBAIII and their corresponding hydrogen bond propensities (urea-urea interactions in yellow, urea-BA interactions in red and blue and BA-BA interactions in green)

Donor	Acceptor	UBAI Hydrogen bond Propensity
N1 urea	O1 urea	0.93
N1 urea	O3 BA	0.88
N3 BA	O1 urea	0.85
N2 urea	O2 BA	0.78
N4 BA	O3 BA	0.75

Donor	Acceptor	UBAII Hydrogen bond Propensity
N1 urea	O3 BA	0.88
N2 urea	O4 BA	0.88
N3 BA	O1 urea	0.85
N4 BA	O1 urea	0.85
N1 urea	O2 BA	0.78
N2 urea	O2 BA	0.78

Donor	Acceptor	UBAIII Hydrogen bond Propensity
N5 urea1	O8 urea2	0.90
N8 urea2	O7 urea1	0.90
N5 urea1	O5 BA2	0.86
N6 urea1	O5 BA2	0.86
N6 urea1	O6 BA2	0.86
N7 urea2	O2 BA1	0.86
N7 urea2	O3 BA1	0.86
N8 urea2	O2 BA1	0.86
N1 BA1	O8 urea2	0.82
N3 BA2	O7 urea1	0.82
N2 BA1	O4 BA2	0.58
N4 BA2	O1 BA1	0.58

UBAI and UBAII both have one molecule of urea and one molecule of BA in the asymmetric unit with a potential to form 16 hydrogen bonds. UBAI forms five hydrogen bonds in total three of moderate propensity between urea and BA molecules, one high propensity bond between urea molecules and another lower propensity bond between BA molecules. UBAII forms six moderate propensity hydrogen bonds all occurring between urea and BA molecules.

As UBAIII has four molecules in the asymmetric unit (two urea molecules and two BA molecules) it has the potential to form 64 hydrogen bonds, of which 12 of these are observed in the crystal structure. Two high propensity hydrogen bonds are formed between urea1 and urea2 similar to those observed in UBAI. There are eight moderate propensity hydrogen bonds observed between urea and BA (four between urea1 and BA1, and four between urea2 and BA2). Note that no interactions are observed between urea1 and BA2, and urea2 and BA1. Additionally there are two low propensity hydrogen bonds observed between BA1 and BA2.

The presence of the favourable urea-urea hydrogen bonding interactions which are prevalent in structures within the CSD and occur in UBAI and UBAIII may provide added stability to the crystal structures which are not present in UBAII which appears to be less prevalent as shown by results from small scale crystallisations discussed previously. However in order to identify if there is any other correlation between the likelihood of the hydrogen bonds present in each UBA polymorph and their physical properties further investigation is required.

4.5.3 Solubility Measurement

Solubility measurements of UBAI, UBAII, UBAIII and BAII were obtained in both water and methanol solvent systems using a Crystal16 parallel crystalliser (Figure 4.33) from Technobis Crystallization Systems BV (formerly Avantium Pharmatech BV). Vials were cycled through temperature ranges from 20 °C to 75 °C in water and from 20 °C to 55 °C in methanol using a heating rate of 0.5 °C min^{-1} and stirring at 800 rpm using standard (4 mm) magnetic stirrer bars. Data were analysed using CrystalClear software to obtain the temperature of each clear points to construct each solubility curve. Due to the complexity of the UBA system cloud points were not considered accurate representations of the supersolubility and therefore the MSZW has not been determined.

Figure 4.33 The Crystal16 parallel crystalliser from Technobis Crystallization Systems BV (formerly Avantium Pharmatech BV)

Figure 4.34 and Figure 4.35 show the solubility of each UBA polymorph and the BAII starting material for comparison. Each UBA polymorph displays increased solubility in comparison to the BA starting material. UBAI and UBAIII have very similar solubility in both water and methanol further highlighting their similarity in lattice energy and stability. UBAII is the most soluble of the three UBA polymorphs in water (with respect to BA content within the co-crystal), in comparison to BA which would indicate that this is the meta-stable polymorph which supports the evidence from small scale evaporative, mechano-chemical and cooling crystallisations in which UBAI was obtained readily as well as UBAIII, however there was very little evidence of UBAII.

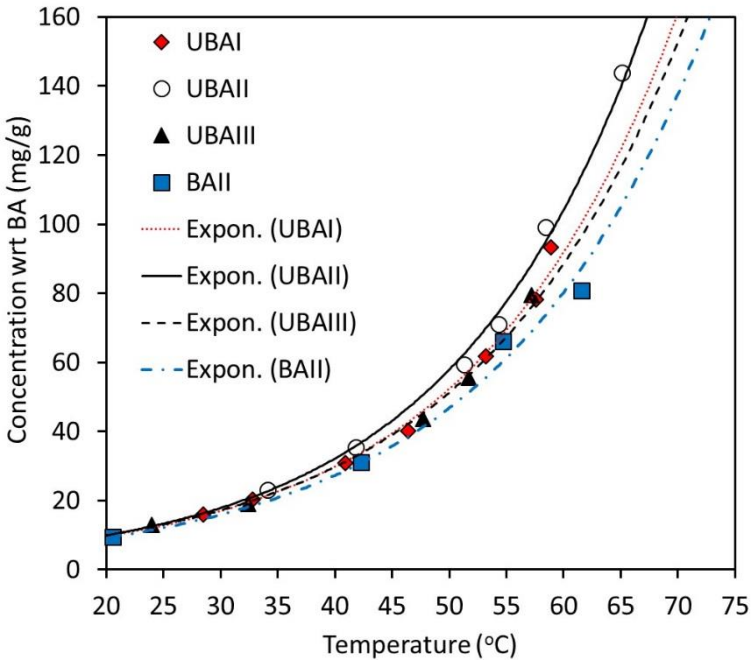

Figure 4.34 Solubility of UBAI, UBAII, UBAIII and BA starting material in water obtained using the Crystal16

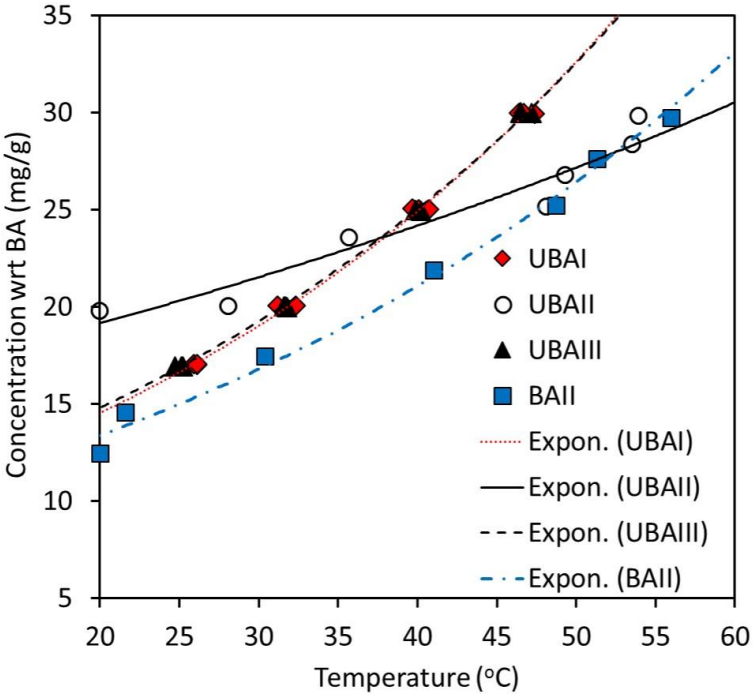

Figure 4.35 Solubility of UBAI, UBAII, UBAIII and BA starting material in methanol obtained using the Crystal16

In methanol UBAI and UBAIII again have very similar solubilities, however the relationship with UBAII solubility is very different to that found in water. UBAII remains more soluble than UBA I and UBAIII in water between 20 °C and 70 °C, but in methanol at temperatures above 37 °C the solubility of UBAII drops below that of UBAI and UBAIII. If UBAI and UBA III are more soluble

at higher temperatures, under cooling crystallisation conditions UBAII may be produced first, however once lower temperatures are reached the formation of UBAI and UBAIII become more prevalent and UBAII converts to UBAI or UBAIII. Similarly the increase in solubility at high temperatures may be due to potential conversion in solution as UBAII has been shown to be less stable than the other polymorphs. Further investigation using sampling and off-line PXRD analysis or potentially using a non-invasive Raman probe may be able to provide more clarity on this.

From a crystal engineering perspective co-crystallisation of urea with BA leads to an enhancement of BA solubility, although from an industrial perspective this increase is not considered significant and would not be reason enough alone to warrant adoption of multi-component crystallisation. However if coupled with other physical property enhancements it would strengthen the case.

If the solubility of each polymorph is known it is possible to use the data to maintain cooling crystallisation conditions within the MSZ close to the solubility curve of each polymorph, a process known as supersaturation control. This has been used in other systems to selectively produce a chosen polymorph.[63] For the UBA system it is very difficult to implement this process especially to select between UBAI and UBAIII which have very similar physical properties including solubility. Supersaturation control for the UBA system is doubly hindered not only by the polymorphic nature but also the multi-component nature of the system. It is particularly challenging to obtain supersolubility curves in order to determine the MSZW of a polymorphic material as there may be polymorphic transformation in solution and for multi-component materials the target and co-former are likely to dissociate in solution so upon cooling it may be either a different polymorph or one of the starting materials that crystallises first.

4.5.4 Morphology

SEM measurements were carried out on small crystals of each of the UBA forms (Figure 4.36), selected from preparations in which representative samples of each could be located. The samples were prepared by vacuum filtration and subsequent drying at room temperature. A Quorum QT Chrome Coater (UK) with a film thickness of 5 nm was used to coat the samples. The images were then obtained via use of a Hitachi TM-1000 table-top scanning electron microscope.

The SEM analysis of UBA shows that the UBA polymorphs have very different morphology. UBAI is very plate-like (Figure 4.36 a and b), UBAII has a crescent prism morphology and UBAIII displays a bipyramidal form. Agglomeration was common to all three samples analysed, in particular UBAIII which displays very uniform agglomerates (Figure 4.36 e).

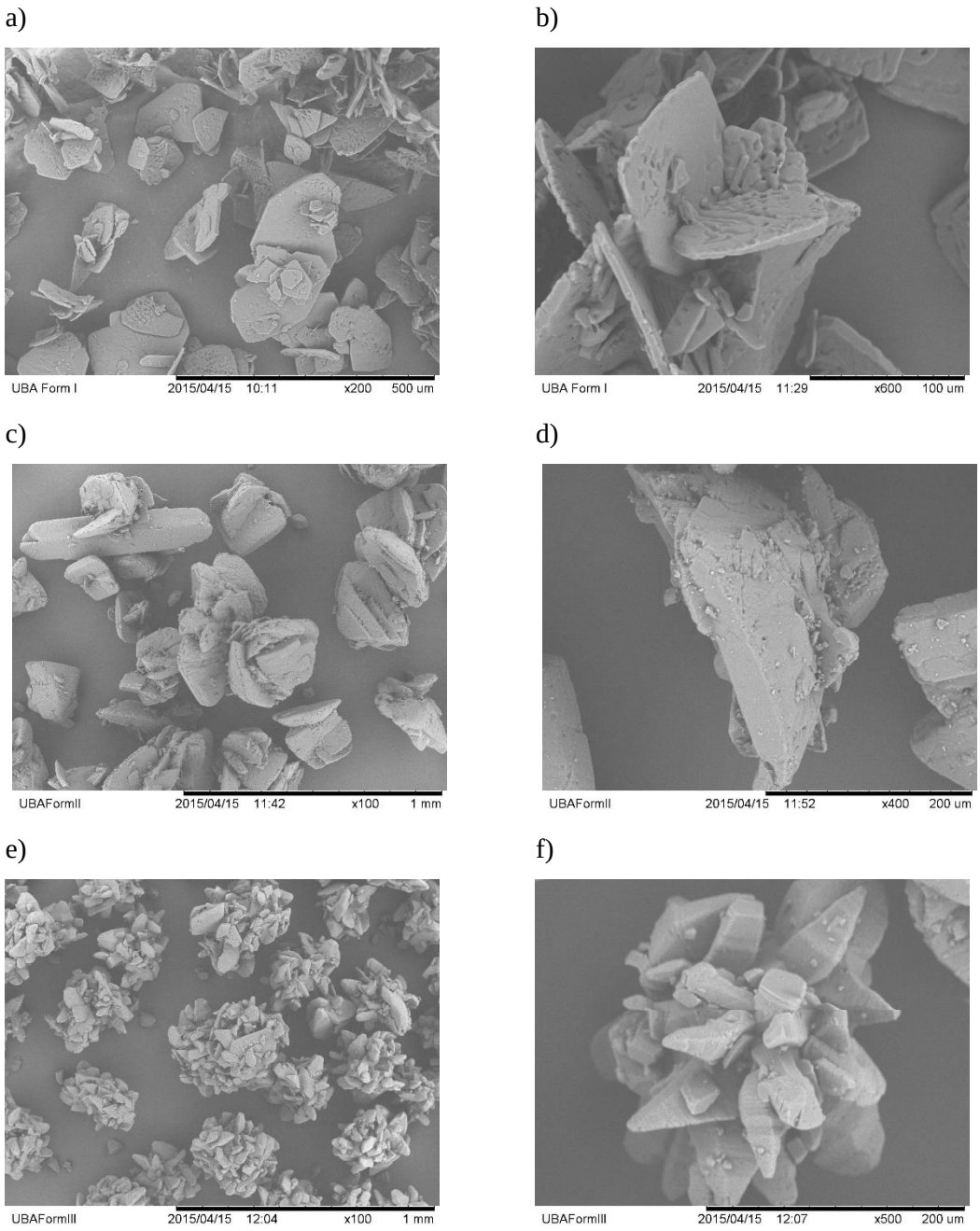

Figure 4.36 SEM images showing the morphology of UBAI (a and b), UBAII (c and d) and UBAIII (e and f).

The BFDH morphology tool in Mercury can be used to predict the morphology of a crystal structure based upon the Bravais, Friedel, Donnay and Harker (BFDH) approximation. The BFDH model is based on an original proposition by Bravais that the largest face of a crystal should be that corresponding to the largest (lowest index) interplanar spacing. This is equivalent to stating that the speed at which a face grows is inversely proportion to its interplanar spacing, as the area of a plane in the growing crystal is inversely proportional to its linear growth velocity. Originally verified as a legitimate approximation by Friedel, the model was extended by Donnay and Harker to include the

effects of lattice centring, screw axes and glide planes (which effectively reduce the interplanar spacings), to produce the BFDH model[119].

The BFDH model can make a first estimate of the crystal morphology on the basis of these simple rules. However this model assumes that the crystals were grown in water and it is well documented that solvent interactions can affect the crystal morphology. Additionally this model does not take into account the effects of hydrogen bonding which play a significant role in the hydrogen bonded networks of the UBA co-crystals. For these reasons, the morphologies observed differ significantly from those predicted using the BFDH morphology tool (Figure 4.37).

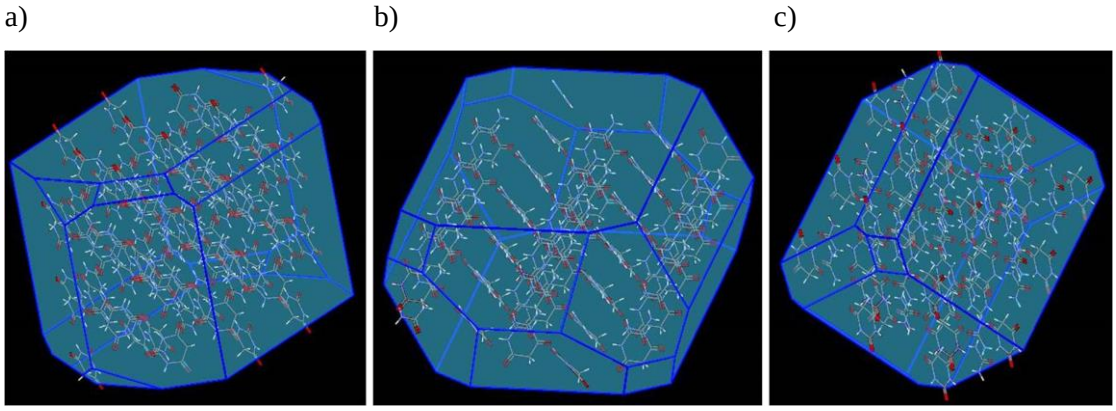

Figure 4.37 Crystal morphology prediction of UBAI (a), UBAII (b) and UBAIII (c) using the BFDH morphology tool in Mercury.

4.5.5 IR and Raman Spectroscopy

IR-spectroscopy was conducted by loading a small amount of each of the UBA polymorphs onto a Thermoscientific Universal ATR Sampling Accessory mounted on a Thermoscientific Nicolet 6700 FT-IR A resolution of 4 cm^{-1} was used with 32 scans collected (Figure 4.5) over a scan range of 3600-600 cm^{-1}.

A ThermoFisher Scientific DXR Raman microscope equipped with 780 nm laser was used as a supporting tool for polymorph characterization by both spectral acquisition and imaging. Raman spectra measurements were made of the three UBA polymorphs (Figure 4.38)

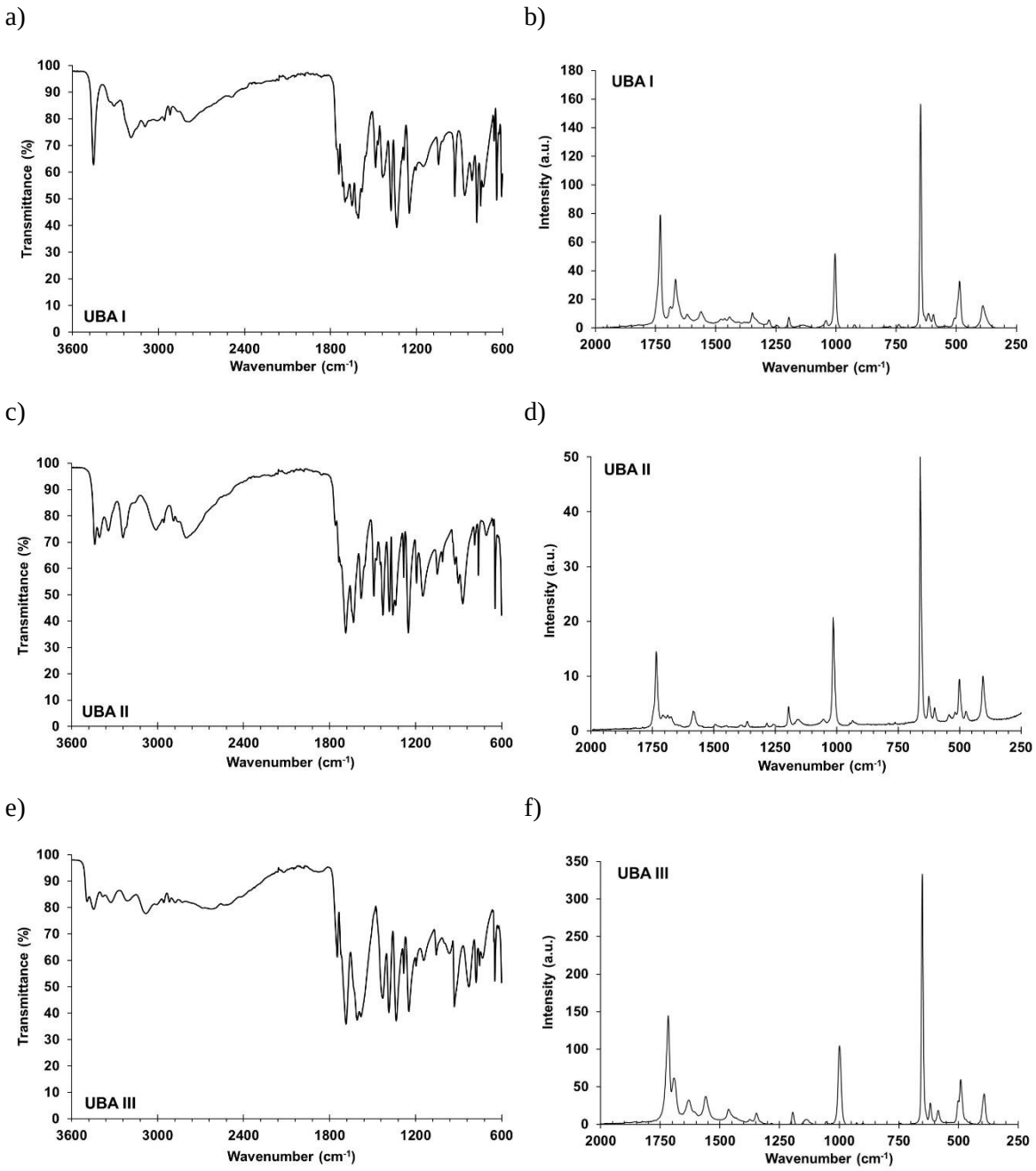

Figure 4.38 IR and Raman spectra of UBAI (a and b), UBAII (c and d) and UBAIII (e and f).

Comparing the IR and Raman spectra for the three UBA polymorphs shows that there are significant differences between these for both types of spectra. The IR spectra show particular differences in the hydrogen bonding region above ~3000 cm^{-1}, as might be expected, together with differences in the region around 1700 cm^{-1}, the C=O stretch region. In the Raman spectra, the latter region shows particularly pronounced changes, both confirming the IR findings and demonstrating the value of Raman in offering a very clear characteristic fingerprint for the different UBA polymorphs. This emphasises one of the reasons that Raman probes are often the spectroscopic method of choice in PAT development and exploitation.

4.5.6 Phase Transformations and Polymorph Stability of UBA Polymorphs

In order to gain a better understanding of the relationships between the polymorphs of the UBA system each of the polymorphs were investigated using a range of solid state and solution state stability techniques.

4.5.6.1 DSC of UBAI, UBAII and UBAIII

About 3mg of each UBA polymorph was weighed into a Tzero aluminium pan fitted with a lid. The pan was heated over the temperature range 50 °C to 300 °C at a constant heating rate of 10 °C per minute using a TA Instruments Q2000 DSC under a constant nitrogen purge. The melting points of the urea and BA starting materials are 133 °C and 251 °C, respectively (note BA transitions to a high temperature phase at 245 °C) (section 4.1.4). All temperatures and enthalpies of the thermal events for UBAI, UBAII and UBAIII are summarised in Table 4.8 below.

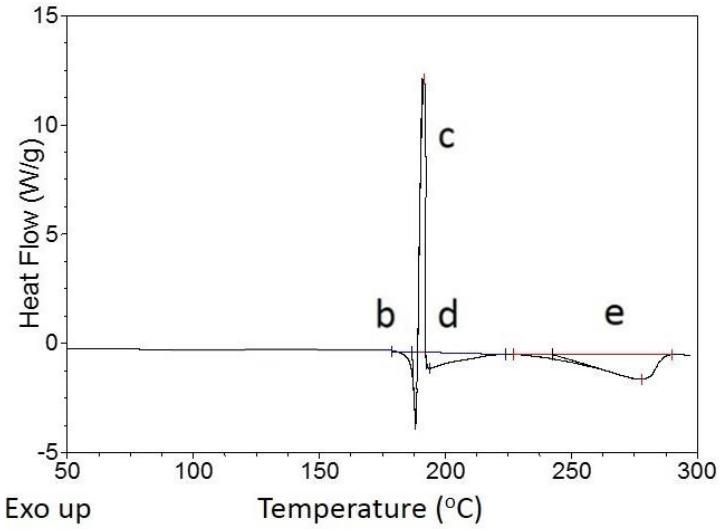

Figure 4.39 DSC of UBAI from 50 °C to 300 °C at 10 °Cmin^{-1}

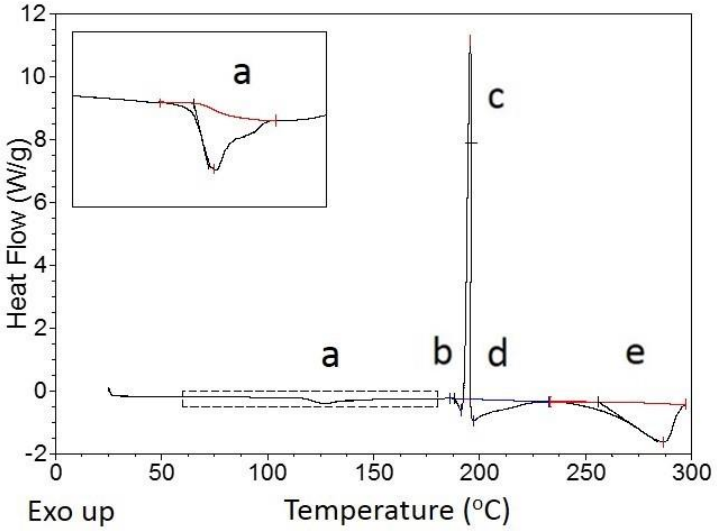

Figure 4.40 DSC of UBAII from 50 °C to 300 °C at 10 °Cmin^{-1}

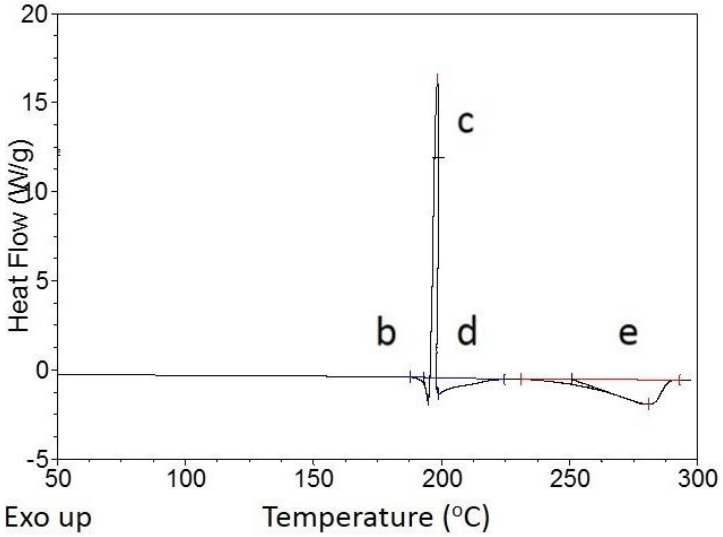

Figure 4.41 DSC of UBAIII from 50 °C to 300 °C at 10 °Cmin^{-1}

Table 4.8 Comparison of temperature and energy of thermal events observed in DSC of UBAI, UBAII and UBAIII

Thermal event	Onset temperature (°C) / ΔH (J/g) of event		
	UBAI	UBAII	UBAIII
a	-	117 / 18	-
b	187 / 40	188 / 5	193 / 16
c	189 / 100	196 / 93	198 / 57
d	192 / 59	197 / 57	199 / 57
e	243 / 188	256 / 182	251 / 202

The DSC trace of UBAII displays a low energy endothermic event (18 J/g) at 117 °C (Figure 4.40 a), which is believed to represent a phase transition of UBAII to UBAIII (as observed in VT-PXRD analysis, section 4.5.6.2 below). This is not present in either UBAI or UBAIII.

All three polymorphs of UBA display four other thermal events when heated from 50 °C to 300 °C (denoted as b to e in Figure 4.39 to Figure 4.41). The small endothermic event, b, is indicative of a melt prior to the large exothermic recrystallisation peak (c) that occurs at 189, 196 and 198 °C for UBAI, UBAII and UBAIII, respectively. This is thought to be a high temperature form of UBA to which all three polymorphs convert.

The endothermic events d and e may correspond to further high temperature phase transitions or a decomposition event which is shown by TGA to occur at 203 °C correlating with event d (section 4.5.6.3 below)

It should be noted that as with the solubility analysis the events within the DSC traces of UBAI and UBAIII occur at very similar temperatures, again highlighting the similarities in stability of these two polymorphs.

4.5.6.2 Variable Temperature (VT) PXRD of UBA on beamline I11 at Diamond Light Source

As a result of the complex DSC results it was thought to be beneficial to investigate the UBA polymorphic material using VT-PXRD and the opportunity arose to run VT experiments on the high resolution diffraction beamline (I11)[120] at the Diamond Light Source, UK (Figure 4.42) via which attempts were made to understand the phase transitions within the UBA system and to identify the unknown high temperature phase observed within the DSC traces.

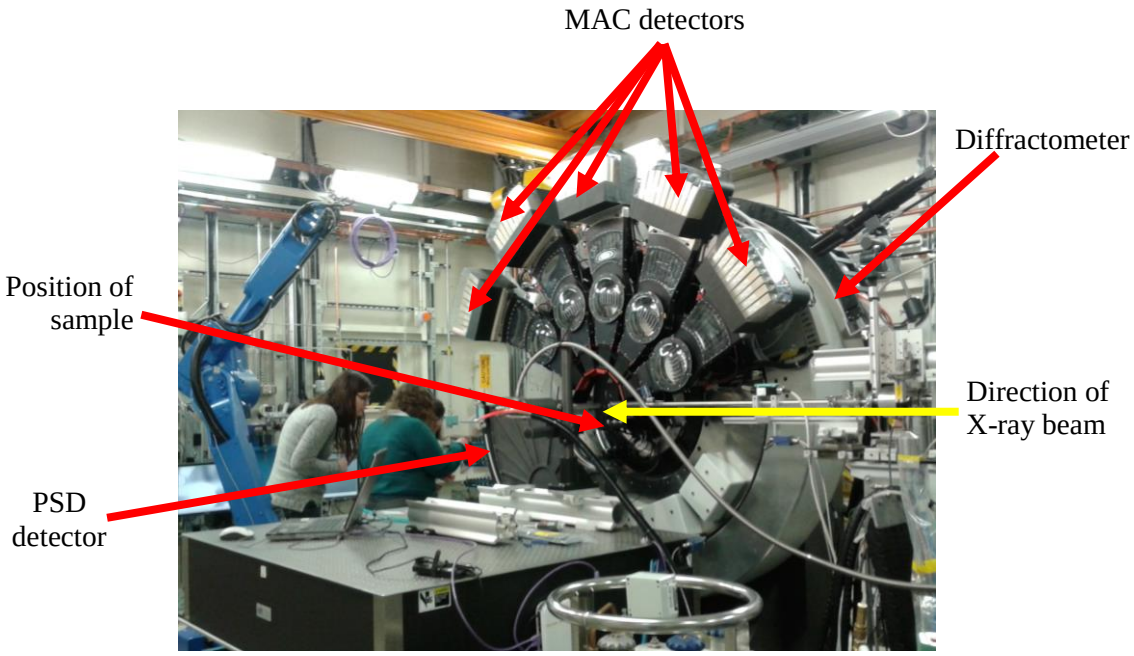

Figure 4.42 Photo of experimental hutch on beamline I11 at Diamond Light Source

PSD Experiments

Samples of each of the UBA polymorphs were prepared in 0.5 mm borosilicate capillaries and data were collected over a range of temperatures on the high resolution diffraction beamline (I11) (λ = 0.825698(2) Å and 2θ zero point = -0.003209). In order to gain an overview of the thermal transitions present in each of the UBA polymorphs fast experiments were carried out using the PSD detector with a 30 second exposure at each temperature point. The temperature range of 22-202 °C was selected for based upon the previous DSC results, detailed above.

MAC Detector Experiments

The transitions in UBAI and UBAII samples were investigated in more detail in experiments using MAC detectors (Figure 4.43 and Figure 4.44, respectively). Particular attention was paid to temperature ranges where variation in the PXRD patterns were observed (160-195 °C for UBAI, and 127-147 °C then 160-195 °C for UBAII) Once again the samples were mounted in 0.5 mm borosilicate capillaries and every 5 °C a 30 minute scan was taken. Due to the increased exposure time and the high intensity of synchrotron radiation the capillary was moved into the X-ray beam in increments of 2 mm every hour to reduce any degradation effects.

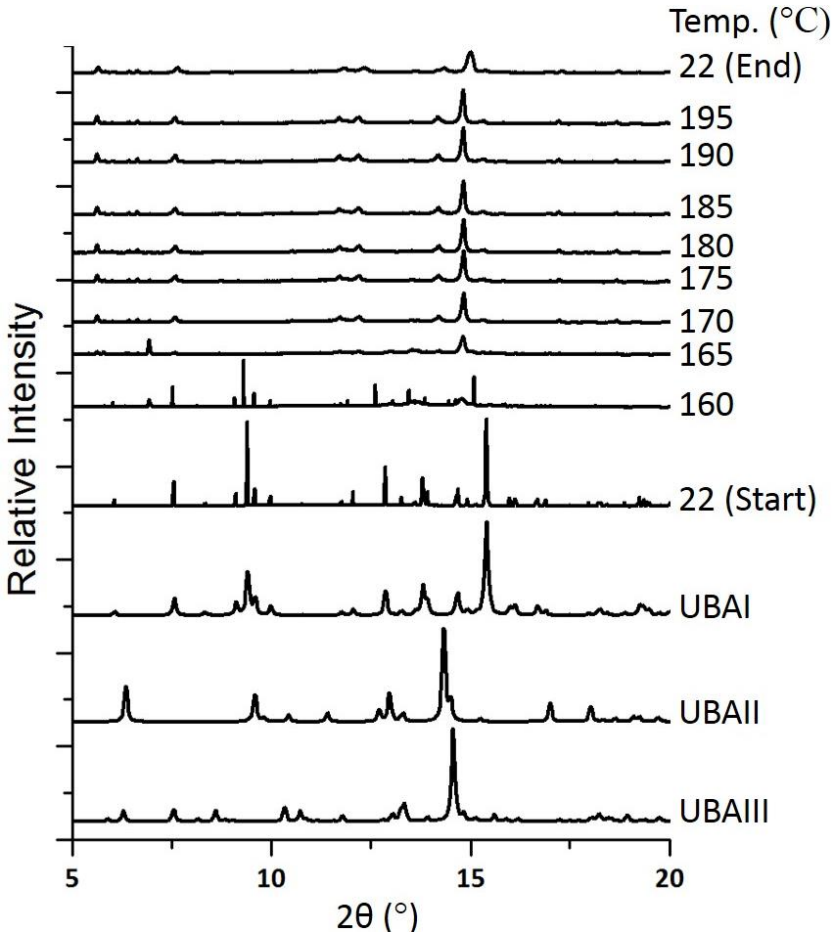

Figure 4.43 VT-PXRD MAC experiment heating UBAI from 160 °C to 195 °C in 5 °C increments (the sample was analysed at 22 °C before and after heating)

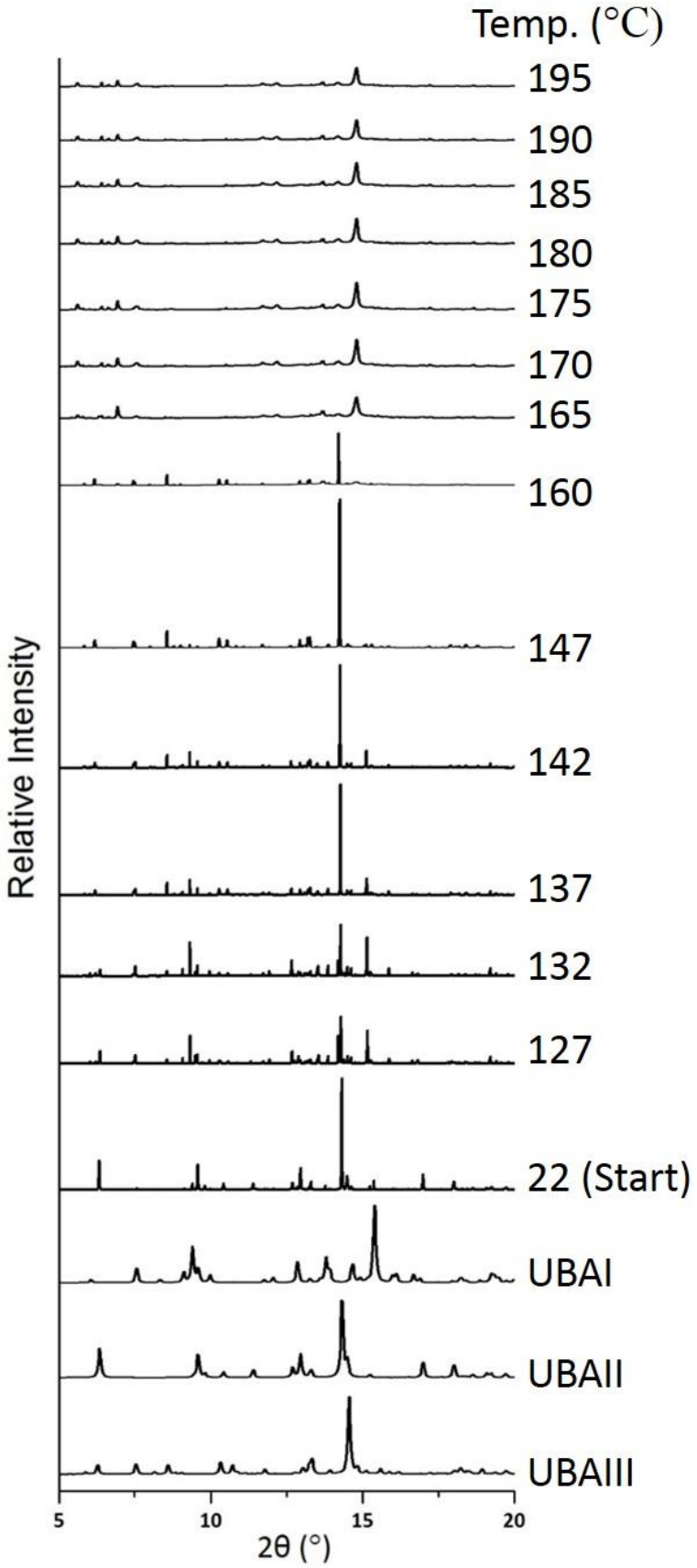

Figure 4.44 VT-PXRD MAC experiment heating UBAII from 127 °C to 147 °C and from 160 °C to 195 °C in 5 ° increments (the sample was analysed at 22 °C before heating)

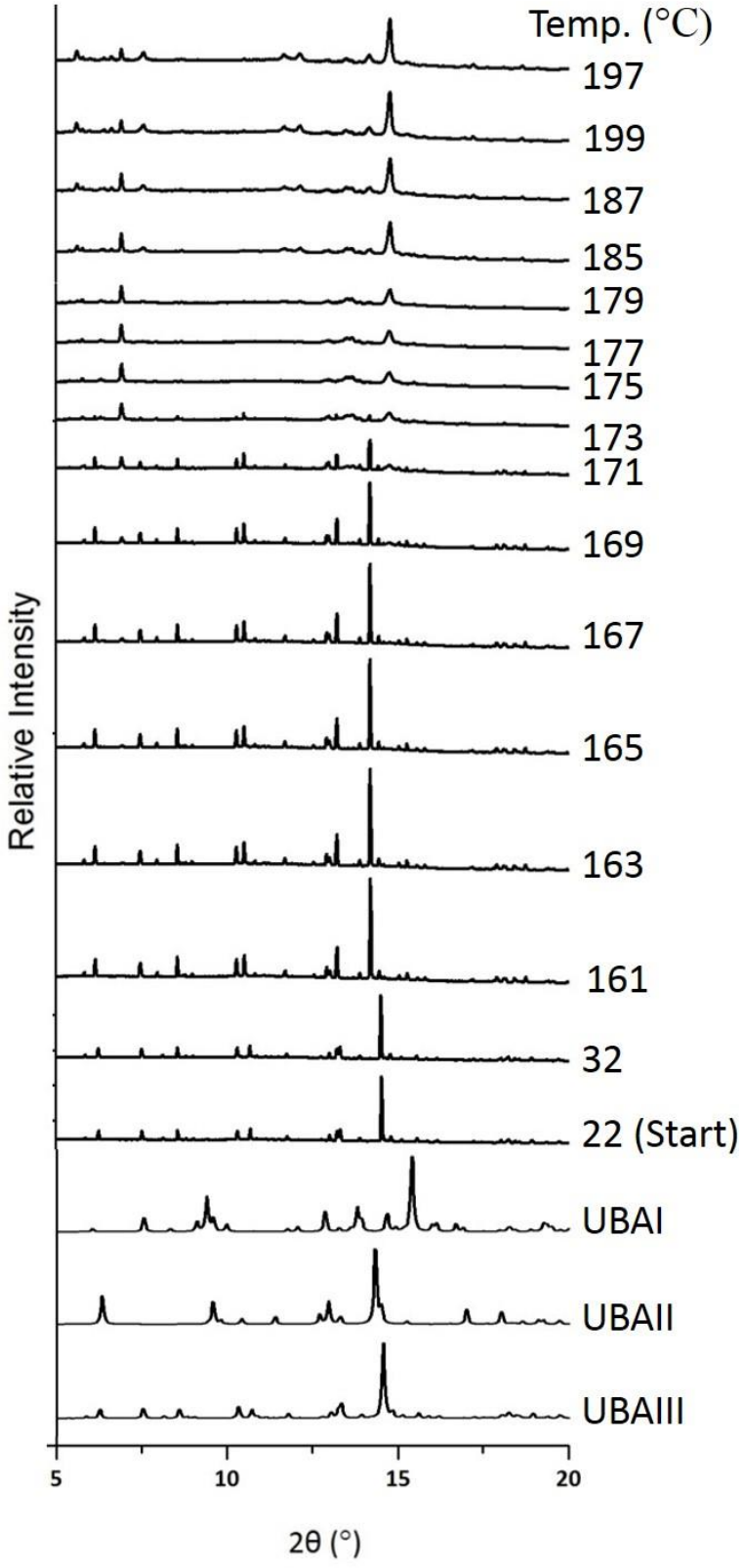

Figure 4.45 VT-PXRD PSD experiment heating UBAIII from 22 °C to 152 °C and from 160 °C to 195 °C in 10 ° and 2 ° increments, respectively (note that due to no changes between 22 °C and 161 °C some patterns have been omitted)

The temperatures of the phase transitions observed in the VT-PXRD data is summarised in Table 4.9 below. Both UBAI and UBAIII when heated convert to an unknown high temperature phase of UBA between 160 and 175 °C and this phase persists when the sample is cooled back down to room temperature (Figure 4.44 and Figure 4.45). Due to the loss of crystallinity at high temperature it proved particularly challenging to solve the unknown phase from the PXRD data collected. Further investigation into this will form part of the future work. UBAII when heated between 142 and 160 °C undergoes a phase transition to UBAIII prior to conversion to the same high temperature phase of UBA above 160 °C.

Table 4.9 Comparison of temperatures of phase transitions observed in VT-PXRD of UBAI, UBAII and UBAIII

Phase transition	Temperature at which the phase transition is complete (°C)		
	UBAI	UBAII	UBAIII
UBAII → UBAI	-	127 *	-
UBAI → UBAIII	165	160 *	-
UBAIII → HT form	170	170	175

*mixture of both phases are present at this temperature, transition occurred before this but no data was recorded.

When comparing the results from DSC to those from VT-PXRD the trends of the phase transitions are found to be the same; UBAII displays a clear transition to UBAI and all samples convert to UBAIII prior to transformation to the uncharacterised high temperature form. However, the temperatures of transitions observed in DSC data are significantly higher than those observed using VT-PXRD (approx. 20 °C). This effect has previously been noted in the literature; it is not uncommon to observe significant temperature variation between DSC and VT-PXRD data[121, 122] as it is difficult to replicate exactly the same experimental conditions across two different instruments. DSC uses continuous variation in temperature whereas the VT-PXRD usually uses a quasi-isothermal method with (in this case) a 30 minute isothermal step prior to each PXRD scan. This allows more time for the phase transitions to occur at each temperature and would result in an apparently lower transition temperature being determined using VT-PXRD; this agrees with the trend found in the UBA experiments. In addition the geometry of the sample holders in each instrument are different (metal pan *vs.* borosilicate capillary) which will affect the heat transfer through the sample. This is a well know issue, and in many cases the indications from the different types of data are used primarily to confirm assignment of phase transitions. However, in light of variation observed between DSC and VT-PXRD results Rigaku have developed a combined DSC-XRD instrument which allows both techniques to be used simultaneously on the same sample[123].

These findings further support the UBA polymorph relationships proposed based upon DSC analysis and solubility studies indicating that UBAI and UBAIII are very similar in stability and UBAII is the most metastable form.

4.5.6.3 TGA of UBA

TGA measurements were carried out for each of the three UBA solid forms, with scans from room temperature to 300 °C for each. The TGA plots of UBAI, UBAII and UBAIII were all very similar showing two mass losses of 7-10%, with onset temperatures of approximately 150 °C and 200 °C, as shown in the TGA of UBAI (Figure 4.46). In previous studies of the thermal decomposition of urea such as those carried out by Schaber *et al.*[124], events have been observed at 152-190 °C and 190-250 °C which can be attributed to decomposition of urea and its thermal decomposition product biuret, respectively. As urea decomposes, ammonia (NH_3) is evolved. With an RMM of 17.03 $gmol^{-1}$ ammonia would equate to 9% of the mass of UBA (RMM of 188.12 $gmol^{-1}$) which is consistent with the percentage mass loss observed in the TGA plots. The second starting component BA starts to decompose at around 180 °C (Figure 4.47), but the mass loss is far more significant than those observed in the TGA of UBA, and can be discounted in the interpretation of Figure 4.46.

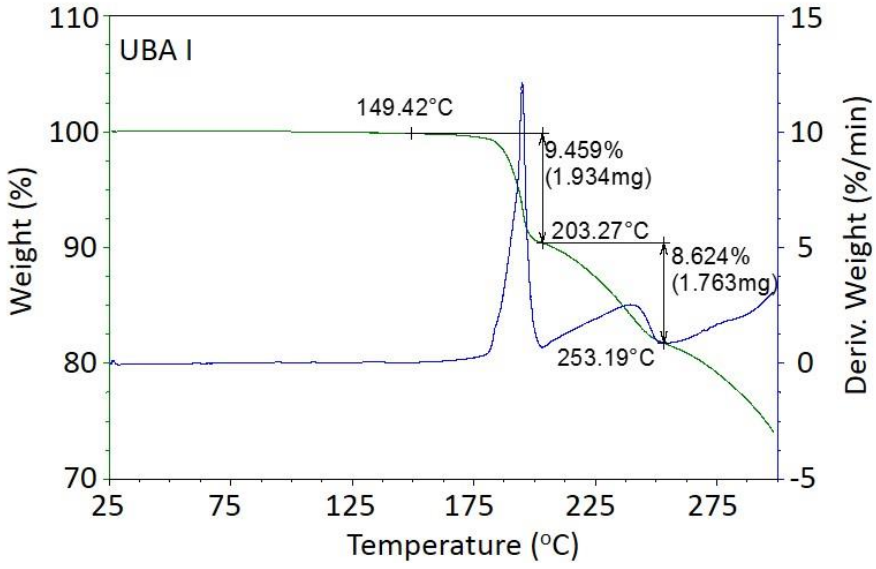

Figure 4.46 TGA of UBAI (from 25 – 300 °C at 10 °Cmin^{-1}) showing two mass loss events at 149 °C and 203 °C

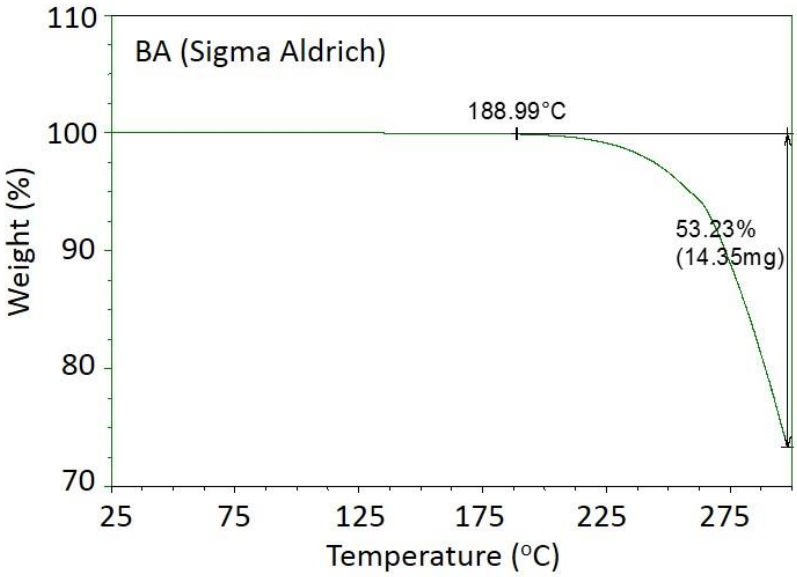

Figure 4.47 TGA of BAII starting material (from 25 – 300 °C at 10 °Cmin-1) showing a significant but incomplete decomposition event with an onset temperature of 189 °C

Following the TGA scans, the samples that had been heated to 300 °C were analysed by PXRD (Figure 4.48). These confirm the interpretation of the TGA plots, with no correlation of the PXRD peaks in the post-TGA experiments with those of any of the starting materials or UBA polymorphs; the samples have decomposed.

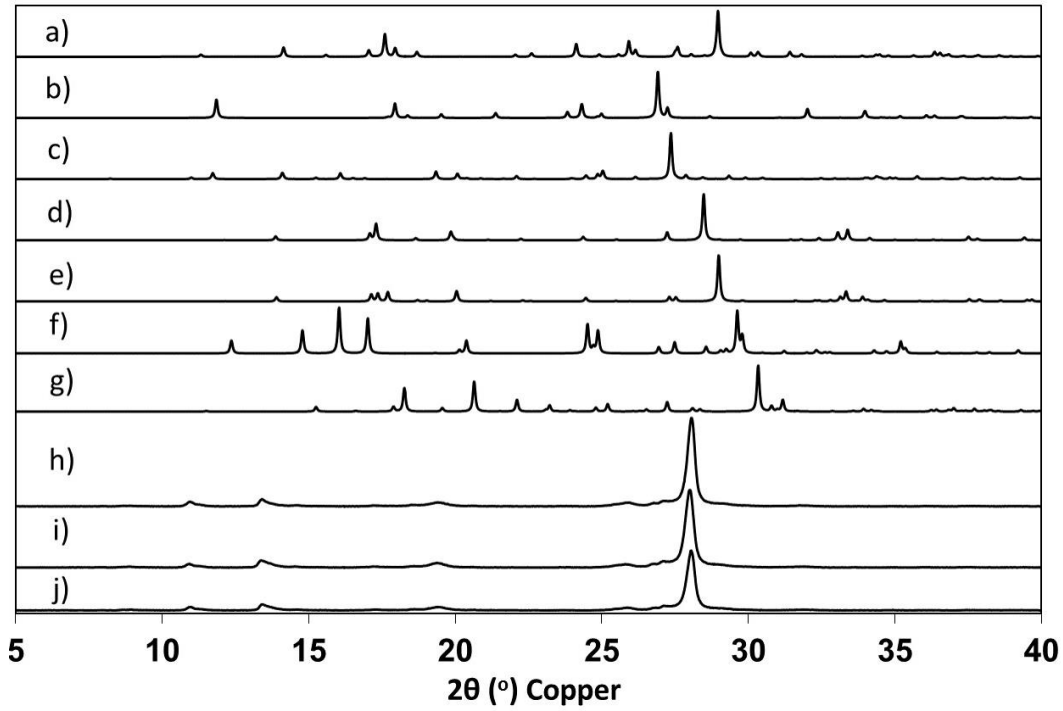

Figure 4.48 PXRD Patterns of UBAI, UBAII and UBAIII after TGA to 300°C (patterns h to j, respectively) for comparison with a) UBA I, b) UBA II, c) UBAIII, d) BA dihydrate I , e) BA dihydrate II, f) BAI and g) BAII

Further analysis of the material using thermogravimetric mass spectrometry (TG-MS) would allow the gases evolved to be analysed, and confirm the interpretation that urea decomposition is being observed (with the loss of ammonia), or if other unidentified decomposition products are present. In future work on this system, more information could be gained about the chemical identity and stoichiometry of the high temperature crystalline material indicated in the VT-PXRD above ~175 °C, using NMR or elemental analysis, for example, which may also aid in the identification of the decomposition products. Importantly, the TGA has confirmed that the decomposition of UBA does not commence until 140 °C, a temperature significantly higher than would normally be required for the stability of a pharmaceutical compound.

4.5.6.4 Stability of UBA Polymorphs in Solution

In order to ascertain the relative stabilities of the three UBA polymorphs in water and methanol, slurries comprising 40 mg of UBA (either polymorph I, II or III) and 1 g of solvent (methanol or water) were prepared in 2 mL glass vials and stirred continuously using a 7 mm magnetic stirrer in the Crystal16 with temperature regulated at 20 °C. Samples were left for 96 hours and subsequently analysed using PXRD to identify if any changes had occurred in the solid form.

Competition slurry experiments were also set up using 1:1 mixtures of UBAI with UBAII, UBAII with UBAIII and UBAI with UBAIII, all in methanol, to explore the relative stability of the UBA polymorphs during the crystallisation process. The mixtures were again analysed using PXRD, both before and after the slurry process. A summary of the results is given in Table 4.10 below.

Table 4.10 Experimental conditions and products obtained from UBA stability and competition slurry experiments using the Crystal16

Starting material	Solvent	Product (results obtained from PXRD analysis)
UBA I	Water	BA dihydrate
UBA II		BA dihydrate
UBA III		BA dihydrate
UBA I	Methanol	UBAI
UBA II		UBAI
UBA III		UBAIII
UBA I and UBA II	Methanol	UBAI (some residual UBAII)
UBA I and UBA III		UBAI
UBA II and UBA III		UBAIII

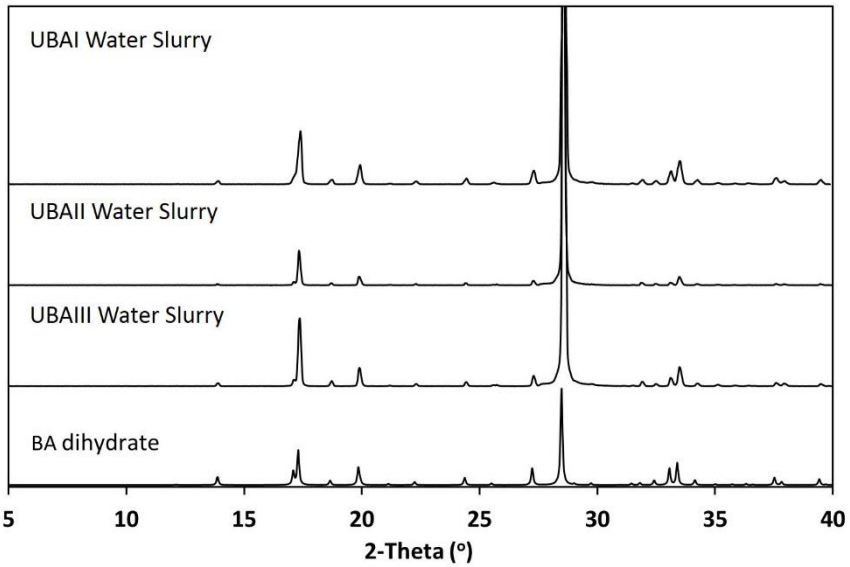

Figure 4.49 PXRD patterns of UBAI, UBAII and UBAIII after slurrying in water at 20 °C for 96 hours

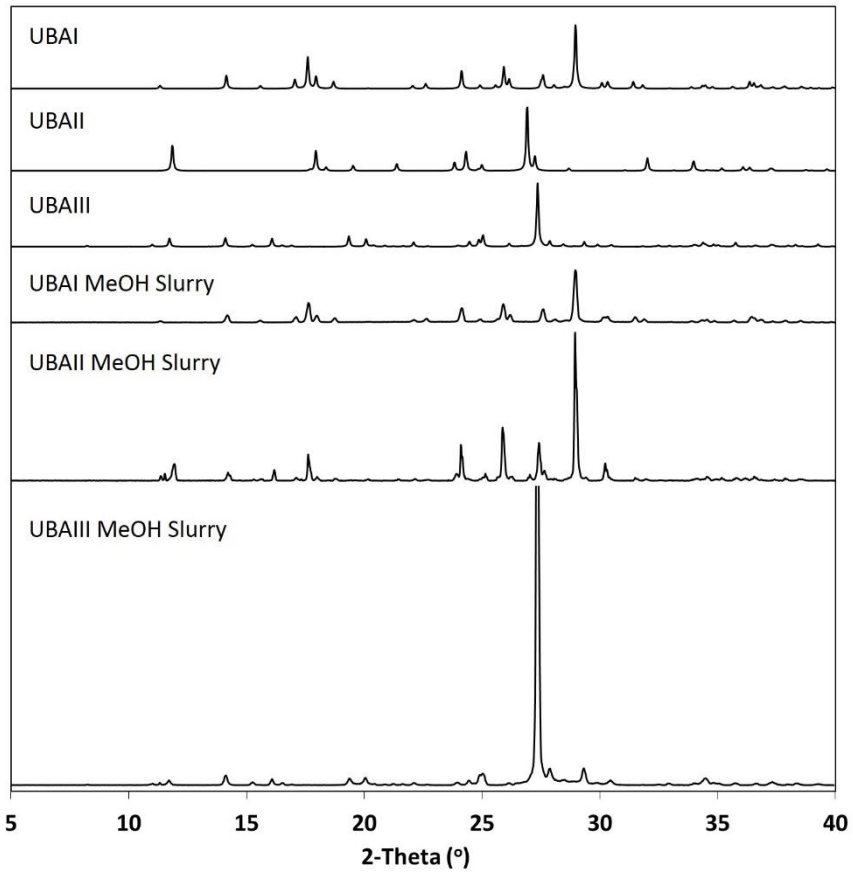

Figure 4.50 PXRD patterns of UBAI, UBAII and UBAIII after slurrying in methanol at 20 °C for 96 hours

a)

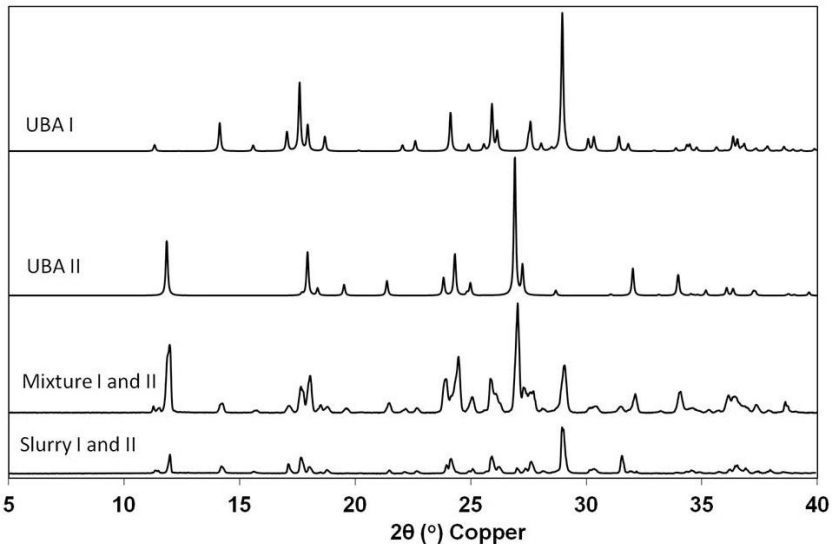

b)

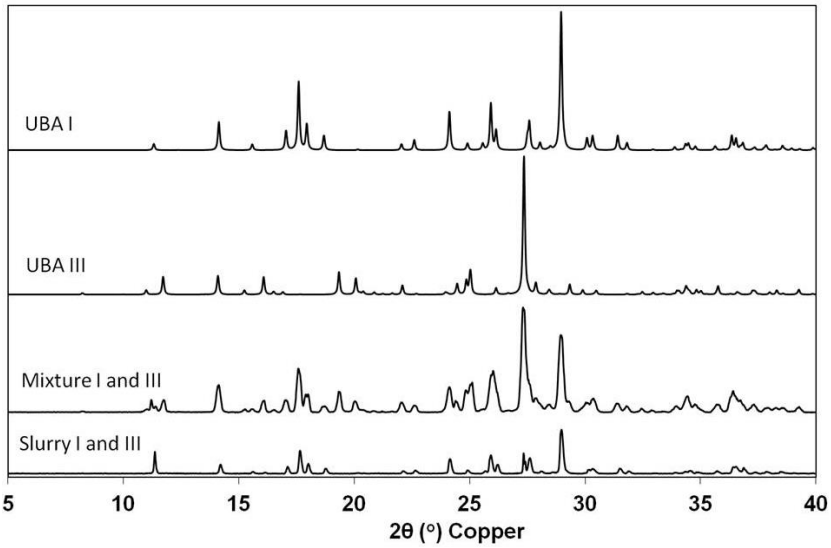

c)

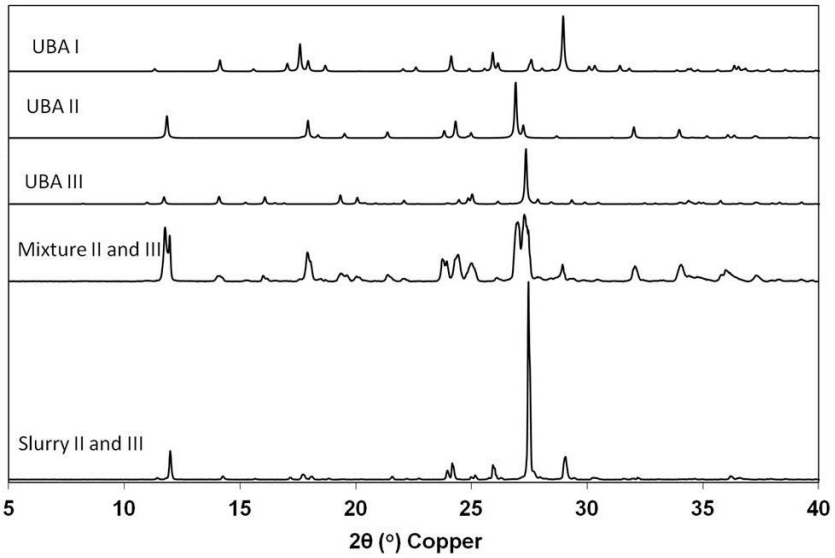

Figure 4.51 PXRD patterns showing results from 1:1 competition slurries in methanol for a) UBAI and UBAII, b) UBAI and UBAIII and c) UBAII and UBAIII

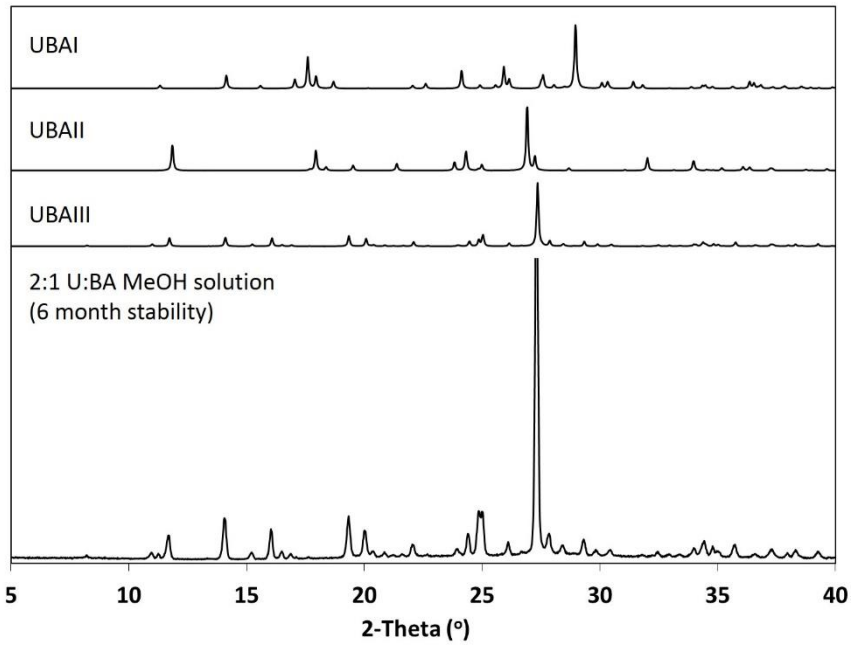

Figure 4.52 PXRD pattern of a solution 2:1 U:BA in methanol maintained in a sealed quiescent beaker at 20 °C for six months

Upon slurrying each UBA polymorph in water at 20 °C for 96 hours both UBAI, UBAII and UBAIII dissociated in solution and converted to BA dihydrate (Figure 4.49). When the experiment was repeated in methanol no BA dihydrate was produced instead UBAI remained as UBAI, UBAII converted to UBAI and UBAIII remained as UBA III. This indicates that at room temperature for a period of 96 hours Both UBAI and UBAIII are stable in methanol and the most metastable polymorph UBAII converts to UBAI. This corresponds with the data collected in solubility analysis, although the solution state transformation of UBAII → UBAI does not follow the solid state transition observed in the DSC analysis of UBAII which showed conversion to UBAIII.

When a 1:1 mixture of UBAI and UBAII were stirred in methanol, again for 96 hours UBAII appeared to convert to UBAI (Figure 4.51 a) as observed previously in the individual polymorph experiments. In the mixture of UBAII and UBAIII PXRD analysis showed conversion to UBAIII (Figure 4.51 c), which also substantiates that both UBAI and UBAIII are more stable than UBAII.

The most important experiment was for the mixture of UBAI and UBAIII as these polymorphs are particularly close in stability. PXRD analysis (Figure 4.51 b) showed that UBAI was dominant in the sample but there was still some UBAIII present. Perhaps if the experiment was allowed to continue for longer complete conversion to UBAI would be achieved.

Interestingly, U:BA in a 2:1 ratio was added to methanol and left to stand at room temperature in a quiescent beaker for six months. PXRD analysis of the filtered sample (Figure 4.52) indicates that

the starting materials have converted to UBAIII, as was observed by Gryl *et al.* Unlike the previous experiments this experiment was carried out without any stirring and so at room temperature it would be plausible to propose that UBAIII is the most thermodynamically stable and UBAI is the most kinetically stable with UBAII existing as a highly metastable polymorph.

Future work will involve solution stability experiments at a range of temperatures and different rations of UBA starting materials in order to build up a ternary phase diagram of the UBA system in methanol or another chosen solvent system (A.J.P. Cousen, *CMAC PhD project, University of Bath*).

4.5.6.5 Solid state kneading of UBA Polymorphs

To investigate the stability of UBA solid forms with respect to pressures typical of those encountered in some industrial processing routes, phase pure samples of each UBA polymorph were kneaded with a pestle and mortar over a period of 15 minutes with the sample periodically analysed using PXRD to identify if and at what point a phase transition may occur.

The sample of UBAII remained unchanged after fifteen minutes of kneading, however the peaks were not as sharp, indicating a loss of crystallinity (Figure 4.53a). It is important to note that due to the elusive nature of UBAII the initial sample used appeared to contain traces of UBAI, these remained throughout the experiment but did not increase suggesting that UBAII $\rightarrow$ UBAI conversion as observed in the solution state was not favourable under this form of processing.

UBAIII however, converted to UBAI with a characteristic cluster of peaks at 17.5° 2θ and a strong peak at 29° 2θ appearing after 2 minutes of kneading which continue to increase in intensity over time (Figure 4.53b). The relationship between the most intense peaks of UBAIII (27.4 °2θ) and UBAI (28.9 °2θ) changes over the duration of the kneading experiment with the UBAI peak growing in throughout the kneading process. Further investigation would be required to ascertain if complete conversion can be achieved. This is earmarked as a future experiment on the UBA system, to be carried out using the more regulated mechano-chemical environment provided in a ball mill device (A.J.P. Cousen, *CMAC PhD project, University of Bath*).

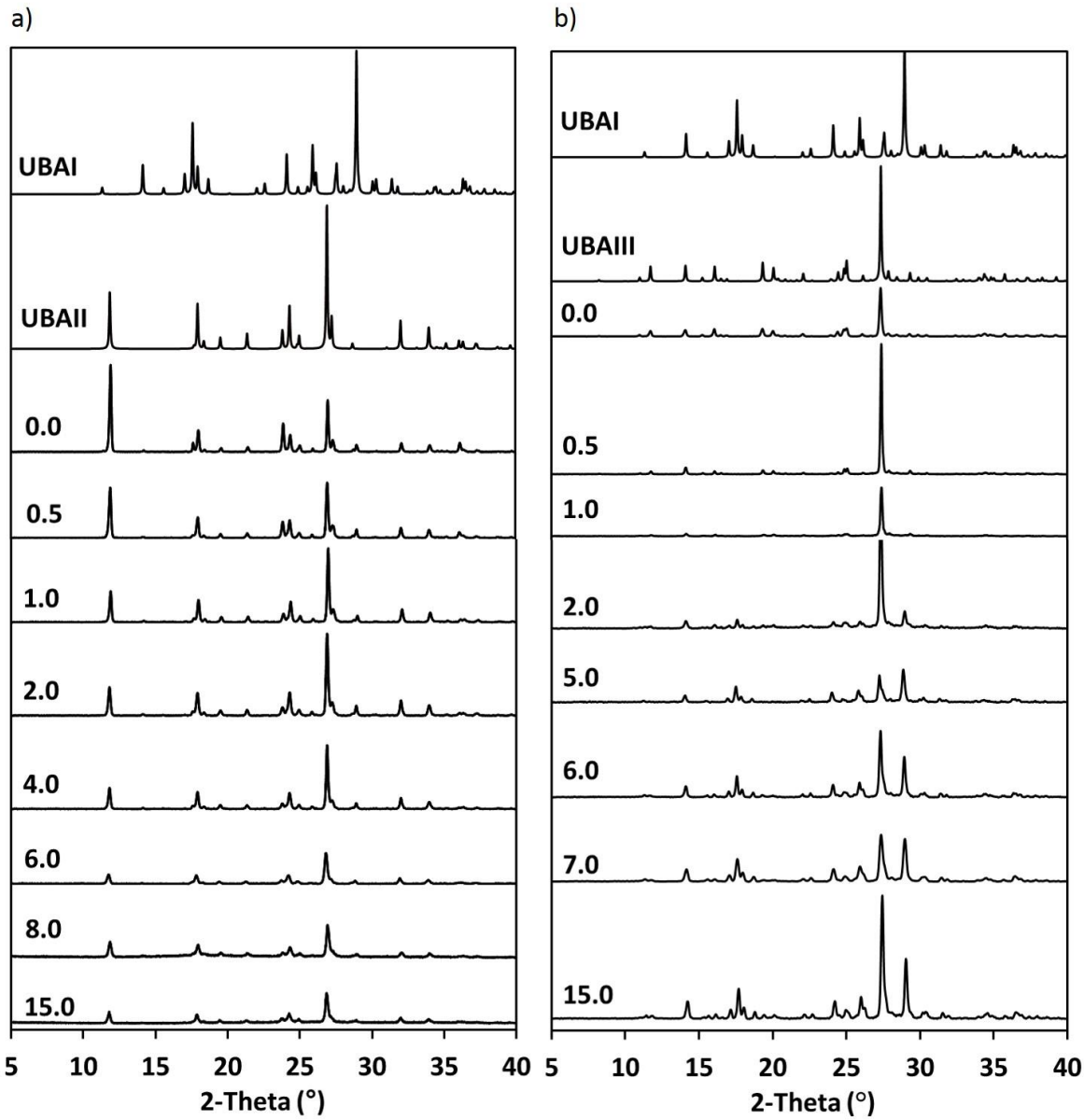

Figure 4.53 Experiments to test mechanical stability of UBA co-crystals. Graphs show PXRD analysis at intervals (time in minutes) throughout the kneading process for (a) UBAII and (b) UBAIII.

4.5.6.6 DVS of the UBA System

In order to identify the most suitable phase of an API or API-containing material for pharmaceutical development it is important to understand the behaviour of the material when exposed to moisture, as this may be encountered during the manufacturing process and during transportation and storage. If not properly managed or understood, phase transformations such as hydrate formation may occur; these can affect the behaviour of the material in downstream manufacturing processes and, more crucially, in the efficacy of the drug product for the patient.

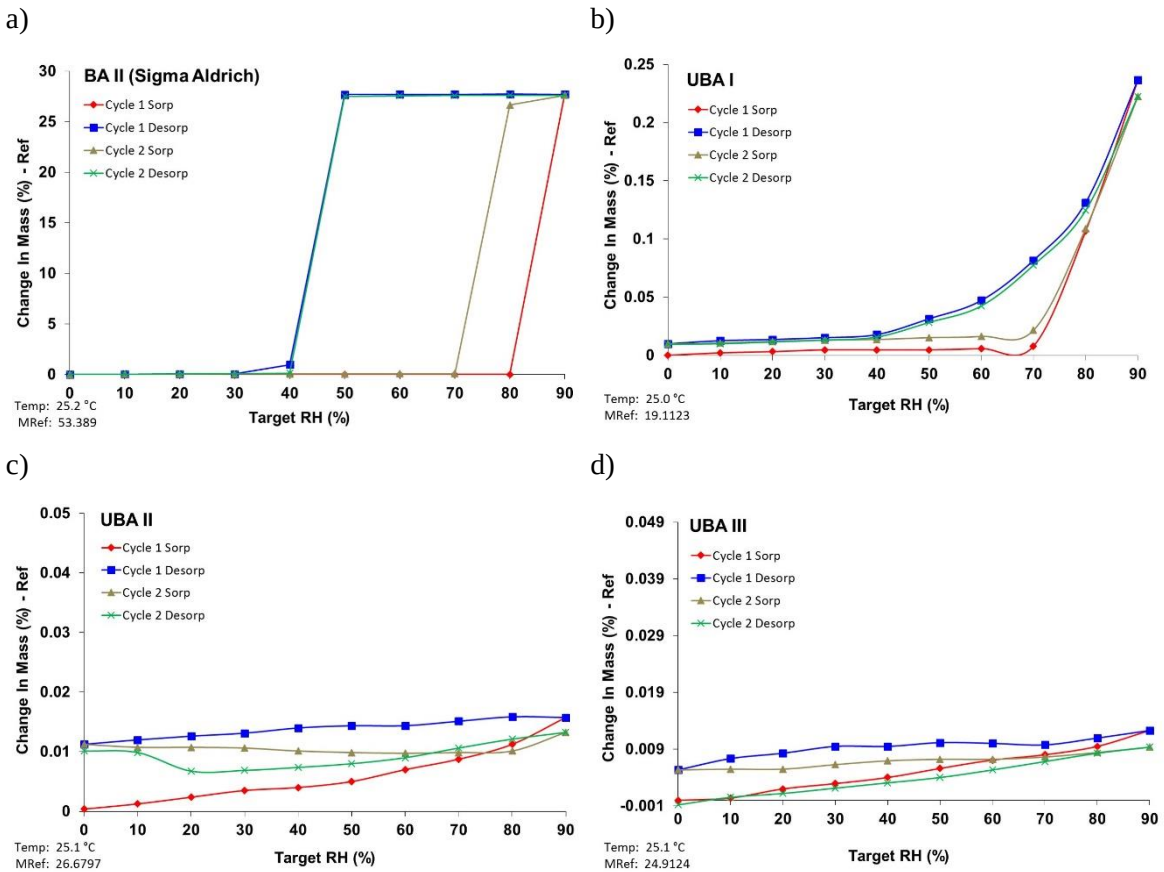

Figure 4.54 DVS profile BAII starting material for comparison with sorption characteristics of UBAI, UBAII and UBAIII.

DVS analysis of the UBA co-crystals, on the other hand, shows that none of the three polymorphs form hydrates, nor are they hygroscopic. The mass increase observed in the DVS experiments was minimal, less than 0.5% for all polymorphs, and is probably due to surface interactions (Figure 4.54 b, c and d). This indicates that through co-crystallisation of BA with urea it is possible to improve the humidity stability of the pharmaceutically-relevant BA component, removing the risk of hydrate formation during processing.

4.5.6.7 Humidity – "Ageing" Stability of UBA Solid Forms

Samples of all three UBA polymorphs were subjected to high humidity conditions (75% RH at 45 °C) for a period of four weeks (see Section 4.1.6 for experimental conditions), with weekly analysis of the materials using PXRD, in order to ascertain if there are any long term phase transformations that occur.

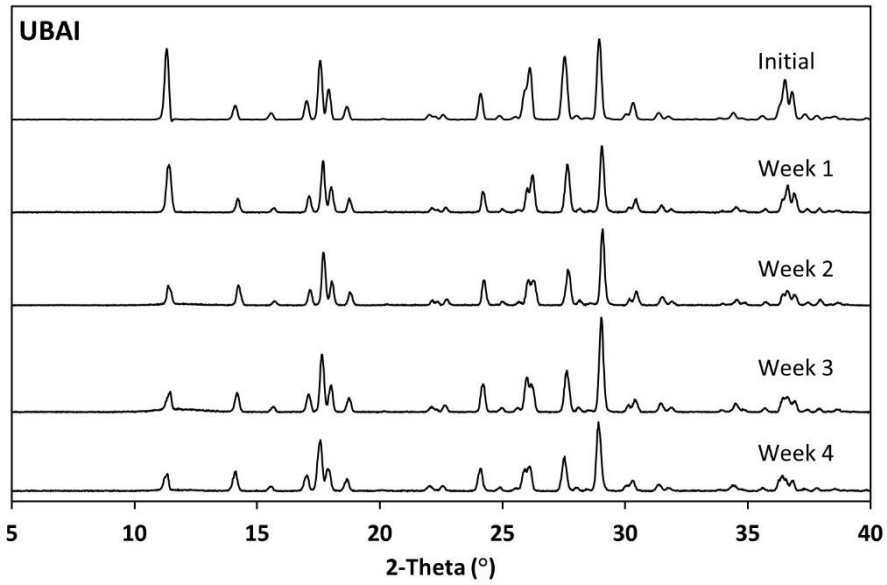

Figure 4.55 Weekly PXRD analysis of UBAI subjected to 75% RH at 45 °C for four weeks.

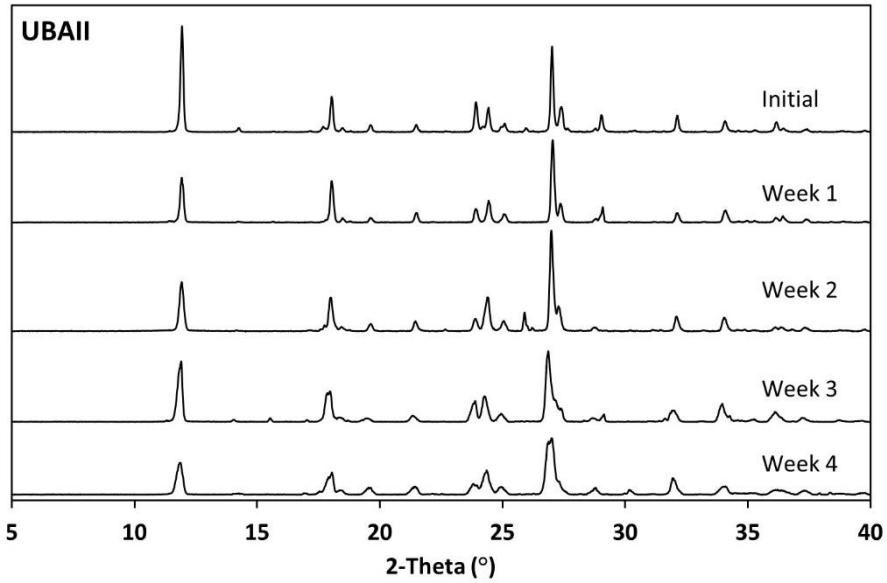

Figure 4.56 Weekly PXRD analysis of UBAII subjected to 75% RH at 45 °C for four weeks.

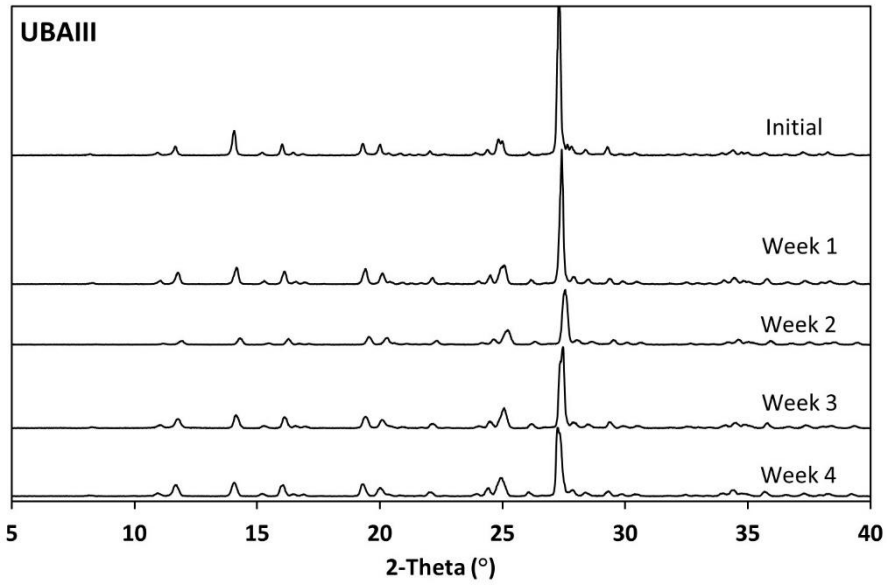

Figure 4.57 Weekly PXRD analysis of UBAIII subjected to 75% RH at 45 °C for four weeks.

PXRD analysis shows that over a period of four weeks under high humidity conditions the polymorphic form of UBAI, UBAII and UBAIII is maintained, with no growth of new peaks or disappearance of peaks present in the initial sample (Figure 4.55 to Figure 4.57). In all samples there is a noticeable loss of crystallinity especially in UBAII and UBAIII where peak broadening and loss of peak definition can be observed.

4.6 Conclusions – U-BA-UBA Phase Relationships

This chapter has explored the variation in UBA solid form produced through a range of batch crystallisation methods, and has also investigated the factors that can influence the solid forms adopted. Among these, experiments were undertaken to investigate if the initial polymorph of BA (a known polymorphic material) used had any impact upon the polymorph of UBA produced. The solid form of BA from three different suppliers were analysed prior to crystallisation experiments and solid state analysis identified that BA from two suppliers (Sigma Aldrich and Acros Organics) adopted the BAII polymorph, while that supplied by TCI was found to be BAIII. Both BAII from Sigma Aldrich and BAIII from TCI were subsequently used as starting materials in the small scale cooling crystallisation DoE investigation. Results from the DoE indicated that there was no correlation between the polymorph of BA used and the UBA polymorph produced.

Evaporative crystallisation experiments used to replicate those carried out by Gryl et al produced a mixture of UBA polymorphs and residual starting material. There appeared to be some indication of a possible relationship between the solvent used (either ethanol or methanol) and the prevalence of the UBA polymorph produced, with crystallisation from ethanol producing predominantly UBAI, while from methanol predominantly UBAIII resulted. The elusive metastable UBAII polymorph was only identified in one experiment (*via* evaporation from methanol of a 1:2 ratio of U:BA at 50 °C). The use of different solvents will affect evaporation not only through differing solubility and supersaturation, but also the rate of supersaturation due to the differences in solvent volatility. While methanol was chosen as the solvent to be used to investigate the cooling crystallisation of UBA in this research, future work using different solvents would allow investigation into whether cooling crystallisation from ethanol or other solvents may favour crystallisation of alternative UBA polymorphs.

A range of other crystallisation methods were also used to investigate further the potential for selectivity in generating UBA polymorphs, and in helping to design processes that could be transferred into continuous crystallisation. Mechano-crystallisation of UBA using dry and liquid assisted techniques with a range of solvents yielded mixtures of UBAI with residual starting materials. The studies found that mechano-crystallisation in the presence of water produced UBAI with additional unwanted BA hydrate. To reduce the likelihood of this hydrate, the addition of methanol, ethanol or IPA was investigated; using a 1:1 ratio of U:BA combined with a few drops of any of these solvents produced pure UBAI. This represents a facile route to formation of phase pure UBAI on the small scale which could be used in future to produce seeds for UBAI-selective seeded cooling crystallisation. In addition it may be possible to investigate mechano-crystallisation of UBA in continuous operation using equipment such as a twin screw extruder.

DoE (with a 2^4 fractional factorial design) of batch cooling crystallisation using the CRD Polar Bear Plus highlighted that within the design space investigated there was little correlation between the experimental conditions investigated and the polymorphic form of UBA isolated. The conditions varied included solution concentration, ratio of urea to BA starting materials, BA starting material polymorphic form, order of addition of starting materials, stirring speed and cooling regime. Of the 24 experiments, the majority produced UBAI under a variety of experimental conditions. Pure UBAIII was isolated in a single experiment which was not reproducible and five experiments produced mixtures of UBAI and UBAIII, within which the only similarity was that BAIII starting material was used, but this was not exclusive to these experiments. UBAII was not observed under the conditions explored. Future investigations to be carried out in the Bath CMAC research group will use a modified design space to see if UBAII and UBAIII can be obtained reproducibly.

All small scale crystallisation experiments highlighted that formation of UBAI was generally dominant but was often produced in a mixture with UBAIII. UBAII has proved elusive through all crystallisation methods, produced only in one evaporative crystallisation experiment; this supports the conclusion that this form is metastable or suggests that that there is a high energy barrier for conversion to UBAII from both UBAI and UBAIII. Fortunately UBAII was isolated later through cooling crystallisation (under conditions detailed in Chapter 5) allowing solid state analysis and polymorph stability testing to be performed.

The preparation of the UBA polymorphs was augmented by characterisation of their physical properties and phase transition behaviour. Turbidimetric solubility measurements of each UBA polymorph (in both water and methanol) indicated that all three polymorphs exhibited improved solubility (when calculated in terms of the concentration of BA delivered into solution) in comparison to the BA starting material although it would not be sufficiently significant to warrant the use of UBA over BA from a pharmaceutical perspective. The solubility measurements highlighted that in methanol and in water UBAI and UBAIII exhibit nearly identical solubility, supporting their similarity in energy, while in water UBAII is more soluble than UBAI and UBAIII; this substantiates the hypothesis that UBAII is metastable and difficult to isolate. Interestingly, unlike in water, the solubility of UBAII in methanol falls below that of UBAI and UBAIII at temperatures above 40 °C. This may be as a result of dissociation of urea and BA at higher temperatures, resulting in precipitation of less soluble BA; the turbidimetric methods employed do not allow for discrimination of the precipitate.

DSC and VT-PXRD indicate a phase transition from UBAII to UBAI between 140-170 °C and this conversion is also seen in solution in slurries of UBAII and mixtures of UBAI and UBAII in methanol. VT-PXRD studies of UBAI show mixtures of UBAI and UBAIII to be present at around

160-165 °C prior to conversion to an uncharacterised high temperature phase at 170-190 °C; the presence of UBAII at 160-165 °C would indicate that there is conversion from UBAI to UBAIII. UBAI is not present in the VT-PXRD patterns determined on heating UBAIII, which remain consistently representative of UBAIII until conversion to the same uncharacterised high temperature form occurs at 170-190 °C. The conversion from UBAI to UBAIII is only observed in solid state thermal studies such as VT-PXRD and not in solution state slurry experiments or mechanical stability testing where the converse is observed with transitions from UBAIII to UBAI. The thermally induced UBAI to UBAIII transition requires further investigation using DSC with temperature cycling combined with PXRD or analysis using a coupled XRD-DSC instrument to fully characterise this transition. In addition UBAIII was produced when U and BA were initially slurried in methanol and were subsequently left to rest in a quiescent beaker for over six months.

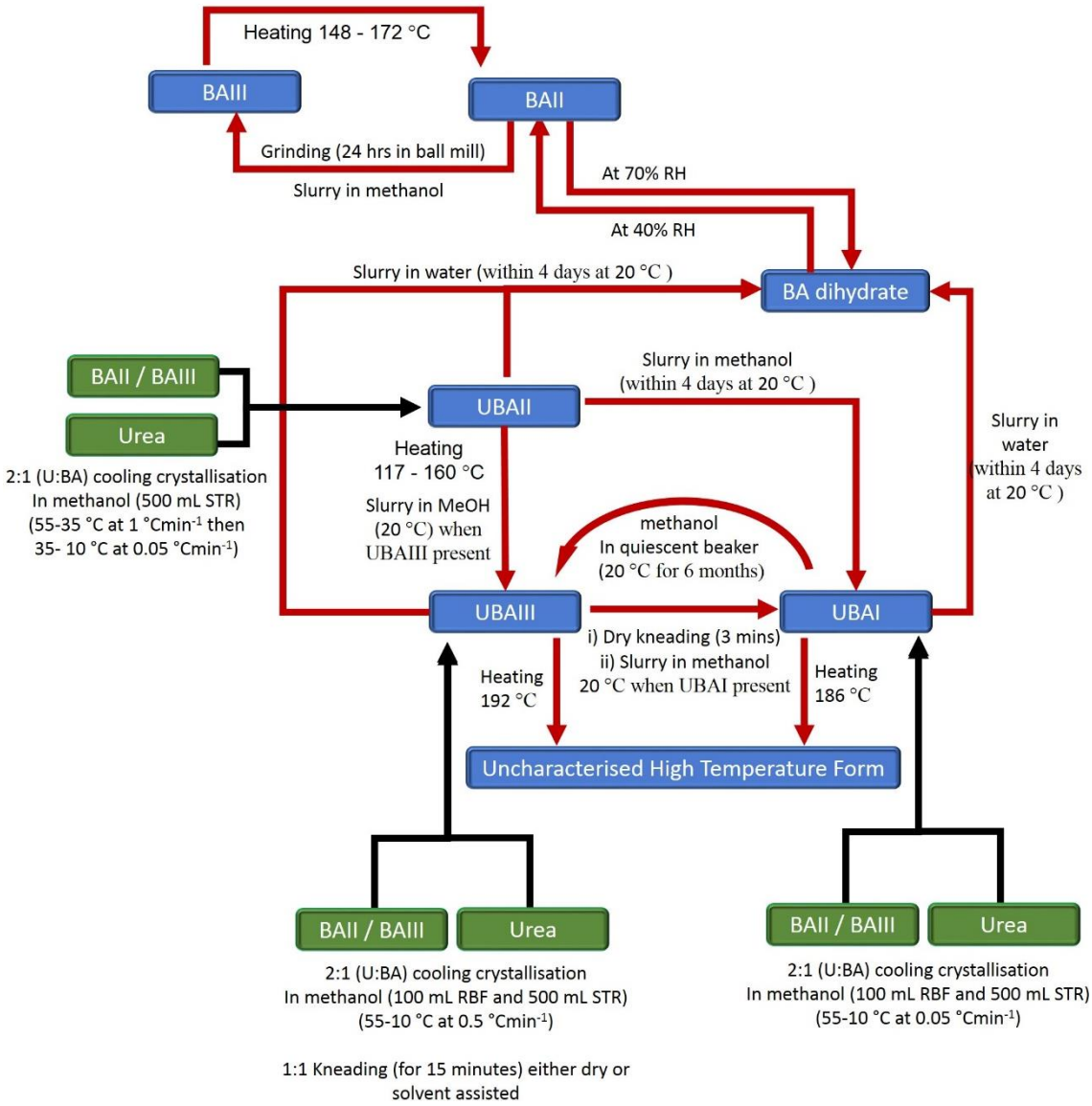

Figure 4.58 Schematic of crystallisation of UBAI, UBAII and UBAIII and the relationship between the UBA polymorphs and with the BA starting material.

Figure 4.58 summarises the relationships between the polymorphs of UBA discussed above, together with their relation to the solid forms of the BA starting material that were discovered from literature sources and from characterisation experiments detailed in this chapter. This diagram also includes the conditions under which each phase is formed, or under which the phase transformations occur.

It can be concluded is that UBAII is the least stable polymorph, although once obtained it remains stable against conversion at ambient conditions (as illustrated in Figure 4.59 a and b). The interconversion from UBAI to UBAIII and UBAIII to UBAI under different conditions and the difficulties encountered in separating these polymorphs *via* selective crystallisation makes it challenging to conclude which of UBAI and UBAIII is most stable (Figure 4.59 c).

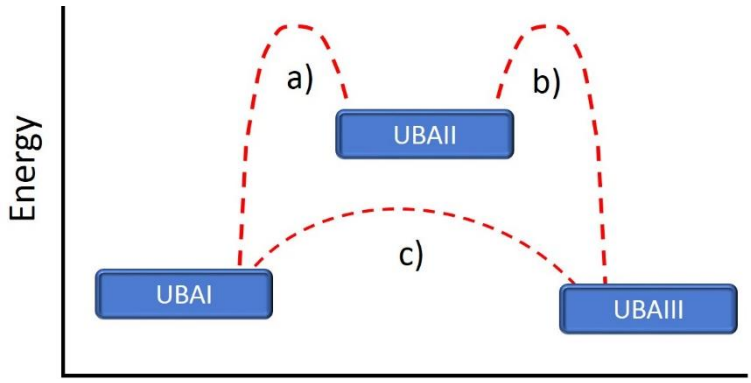

Figure 4.59 Schematic highlighting the energetic relationship between the UBA polymorphs deduced from the work carried out here, showing the similarity in energies between UBAI and UBAII, the highly metastable nature of UBAII, and the barriers to conversion that are evident between the polymorphs.

UBAI is the most prevalent polymorph under the solution state conditions encountered in cooling crystallisation; UBAI was thus chosen as the initial target polymorph in scale up to continuous crystallisation described below, in Chapters 5 and 6.

5 Scaling-up Batch Cooling Crystallisation of UBA and Transfer to MSMPR

5.1 Batch Cooling Crystallisation on a 500 mL Scale

5.1.1 Introduction

In order to transfer UBA crystallisation into the continuous platform offered by the mixed-suspension mixed-product removal (MSMPR) set-up at Loughborough, it is necessary to establish a cooling crystallisation route and to ensure that this scales to the volumes used in the MSPMR device. These experiments were carried out at Loughborough, where access to appropriately scaled batch vessels (STR) was readily available. This section notes the successful establishment of UBA cooling crystallisation at volumes up to 500 mL, with analysis of the range of solid forms produced in these.

5.1.2 Aim

As the majority of continuous crystallisation platforms operate *via* cooling crystallisation it is necessary to translate the evaporative crystallisation of UBA into a cooling crystallisation environment as a first step to developing a continuous process for this system. This was first carried out on the small scale (100 mL) to investigate the effect of the stoichiometry of the starting materials on yield of co-crystals of (1:1) UBA, and the effect of cooling rates on the selectivity for different UBA solid forms. The scale of these experiments was then increased within the context of the first stage 500 mL STR within the MSMPR platform.

5.1.3 Materials

BA starting material was obtained from three suppliers; BA 98% pure Tokyo Chemical Industries (TCI), BA 98% pure Sigma Aldrich (SA) and BA 98% pure Acros Organics (AO) (linked to Fisher Scientific). The BA polymorphic form in the commercial materials was not indicated by the suppliers.

5.1.4 Method

Two different methods of batch crystallisation were used; the first where both the urea and BA components were dissolved together in the 2:1 molar ratio (U: BA) and then subjected to the respective cooling profile and the second in which one molar equivalent of BA was dissolved completely in 500 mL methanol at 43 °C to which two molar equivalents of urea solids were added directly. The urea was allowed to dissolve and the solution was cooled and held at several temperatures (40, 30, 25 and 5 °C).

5.1.5 *Results and Discussion*

Experiments carried out using method 1 were initially monitored using a thermocouple, an FBRM probe and a Raman Probe, Method 2 was monitored using a Raman Probe. The FBRM counts and temperature profiles of experiments using method 1 are shown below in Figure 5.1 indicating the detectable onset of crystallisation. The *in-situ* Raman measurements were later shown to be unreliable in identifying the polymorphic state of crystals in suspension due to fouling on the Raman probes and so were only used as a qualitative indicator of solid form production (Figure 5.2). PXRD used as the prime method for identification of the solid forms produced in each experiment.

Method 1:

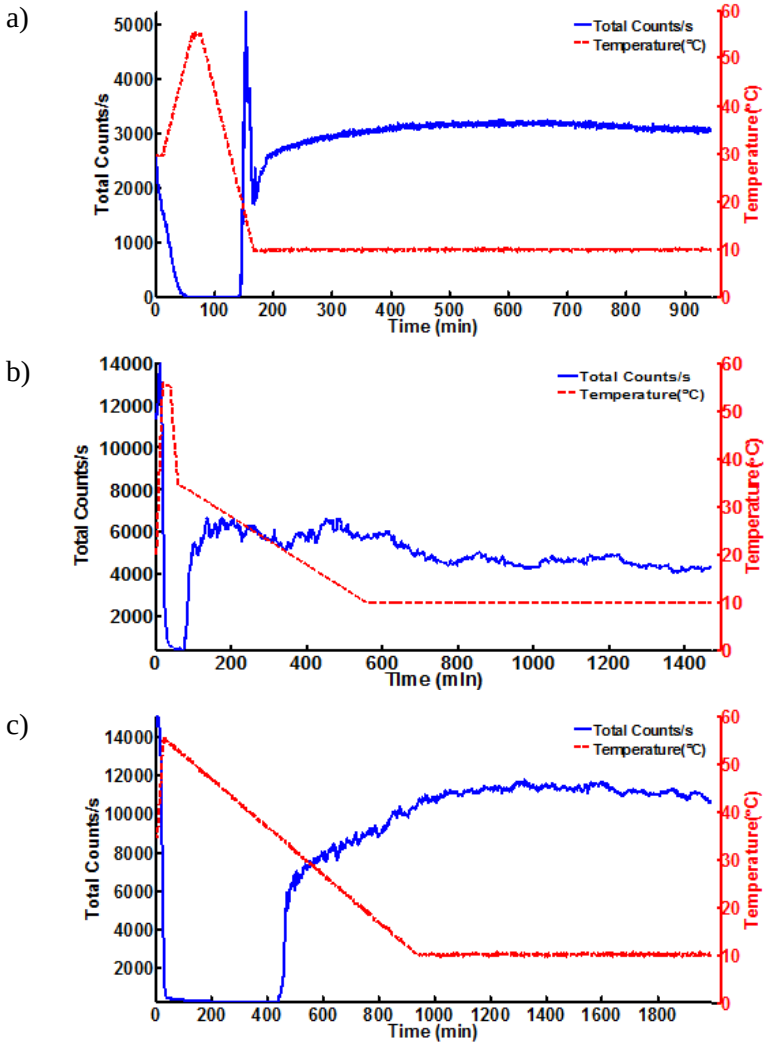

Figure 5.1 Temperature profiles (in red) used to obtain different polymorphic forms of UBA (a) UBAI, 0.5 °Cmin-1 (b) UBAII, 1 °Cmin-1 to 35 °C then 0.05 °Cmin-1 to 10 °C (c) UBAIII, 0.05 °Cmin-1. Total particle counts (in blue) were monitored using an FBRM probe.

It was discovered that within the STR environment cooling rates of 1-2 °Cmin^{-1} could be used to obtain UBAI, but to obtain UBAIII a much slower cooling rate of 0.05 °Cmin^{-1} was required (see Figure 5.1). This would indicate that UBAIII is the most thermodynamically stable form which agrees with original theories proposed by Gryl *et al*. However, under certain kinetic conditions it is possible to favour production of UBAI. The metastable form UBAII, on the other hand, proved elusive and very difficult to isolate. Only a single experiment in the STR, using a two-step cooling profile of 43 °C to to 35 °C at 1 °Cmin^{-1} followed by slow cooling to 10 °C at 0.05 °Cmin^{-1}, produced UBAII. Some traces of UBAI were also present.

Method 2: When using the separate dissolution method, in which urea is added after the dissolution of BA, all crystallisations yielded UBAI. Across the trials conducted using this method, the only significant variation was in the induction times for crystallisation, which ranged from over 9 hours when the solutions were held at 40 °C to under a minute when the solution was cooled to 5 °C.

***In-situ* Analysis**

IR analysis was ruled out for in-line PAT due to the strong signal from the methanol solvent. Raman analysis was used to test the possibility of identifying the UBA polymorphic form produced from solution. The signals from experiments used to produce each of the UBA polymorphs did show significantly different Raman signals (Figure 5.2). Further evaluation of the signals using Principal Component Analysis (PCA), performed by Dr A. Saleemi (University of Loughborough, now at GSK, Stevenage), identified three key clusters which correspond to each of the UBA polymorphs (Figure 5.3). As a result *in situ* Raman spectroscopy was considered a useful technique in monitoring cooling crystallisation of the UBA system. However, it was later discovered that these signals were attributable to solid state signals from fouling of UBA crystals on the optical window of the Raman probe.

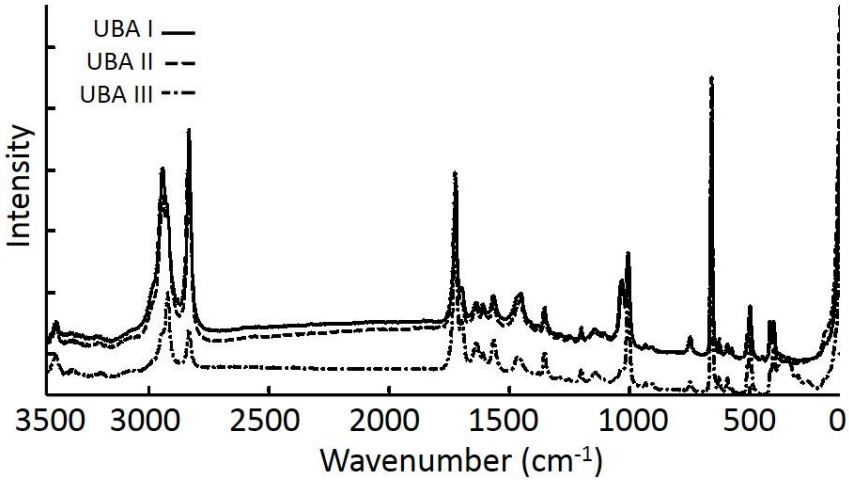

Figure 5.2 Raman spectra of UBAI, UBAII and UBAIII obtained *in situ* during three different experiments in which the respective polymorphs were isolated. These are qualitative measurements showing the formation of the three UBA solid forms; the signals were later found to be hampered by fouling of the respective polymorphs on the probe.

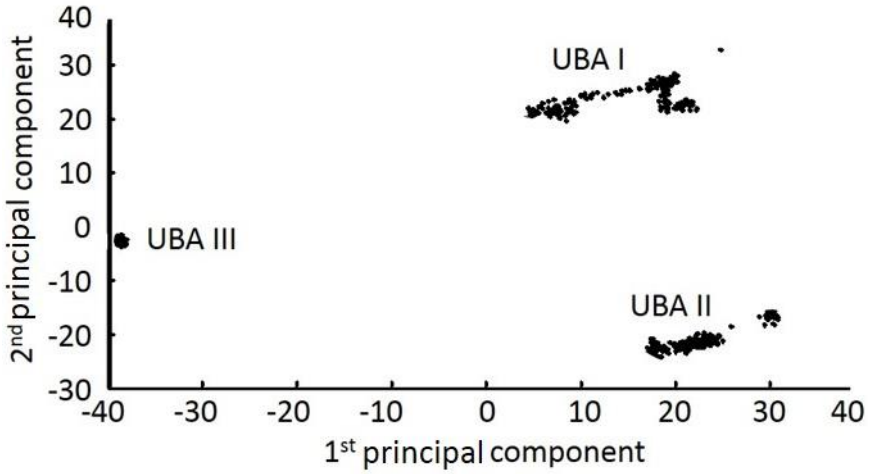

Figure 5.3 Three clusters identified in a first and second principal component plot from *in-situ* Raman spectra (qualitatively, this confirmed the production of all three UBA forms, but later these measurements were found to suffer from fouling of the probe)

5.2 UBA Crystallisation Through MSMPR

5.2.1 Introduction

This study is a collaborative effort within CMAC, building upon the knowledge obtained on the BA co-crystal system in the Department of Chemistry at the University of Bath (Chapter 4) and the understanding of MSMPR and the mode of continuous periodic operation as developed by Powell and co-workers in the Department of Chemical Engineering at Loughborough University (LU)[125].

Continuous mixed suspension mixed product removal (CMSMPR), as termed by Randolph *et al.* in 1988 [126, 127], is a form of continuous crystallisation that involves a continuous input of reactants to a single STR and a constant withdrawal of product, balancing the flow rates to maintain the working volume of the STR. The objective is to achieve a steady state which will be reached after a short period of operation, and which will help to attain regular crystal properties such as CSD and polymorphic form.[128]

This definition focuses upon a single STR, however several STRs can be connected in series adding more flexibility to the continuous crystallisation through which cooling profiles can be introduced. There are several studies in the literature that use two or more STRs in conventional CMSMPR crystallisation.[79, 129-134]

As an alternative approach, the work presented here introduces the unorthodox method of continuous *periodic* operation of MSMPR (PMSMPR)[127, 135]. PMSMPR, as with the more traditional continuous

MSMPR methods, couples the addition and withdrawal processes to maintain a constant working volume, but it operates at much higher flow rates which are cyclically interrupted by regular hold periods. This offers a range of operational advantages in that the higher flow rates help to prevent sedimentation and encrustation within the transfer lines[136], and PMSMPR offers access to longer residence times, particularly useful for slow growing systems or when trying to isolate a thermodynamic polymorph.

Key to the operation of PMSMPR is the concept of a "state of controlled operation" (SCO), which has been introduced as a means of characterisation of continuous periodic operation. In contrast to the established theory of "steady-state operation", SCO describes a system that experiences perturbations in its conditions due to controlled periodic operation yet still sustains a stable state of operation within a range of operation limits i.e. an oscillating steady state[125]. The PMSMPR crystalliser employed here was configured and operated as a three-stage cascade in order to allow the selective isolations of the polymorphic forms of the UBA co-crystal system.

The work presented here also examines the application of an integrated PAT array based on Raman and ATR-UV/vis, used to track changes in the solution phase, and FBRM and PVM, used to track the changes in solid phase. An in-house (CMAC-LU) developed commercial crystallisation process informatics system software tool, CryPRINS[137], was also used for real-time monitoring and implementation of the temperature control policy during the periodic flow crystallisation of UBA in a PMSMPR.

The results discussed below provide evidence that the proposed PMSMPR cascade system, with a suitably designed dissolution stage, can provide a platform for the consistent production of the desired polymorphic form of the model UBA co-crystal system, significantly decreasing product variability compared to the batch operation.

Following this work, the production of UBA solid forms was also carried out using a second MSMPR platform, made available to the author while on secondment to AstraZeneca, Macclesfield (AZ). These results are also presented below.

The value of this study, and of the development of the MSMPR-based approaches for continuous crystallisation, is very relevant to the key interest of the pharmaceuticals and fine chemicals industries in moving from batch to continuous. One of the great benefits of this type of crystallisation platform is that in many ways it is a hybrid between batch and continuous approaches. The STR elements of the MSMPR platforms use current industrial crystallizer technology, potentially

lowering the barrier to their adoption as continuous manufacturing systems in comparison to plug flow crystallisers.

Partly as a consequence of their being rooted in STR technology, there has been a significant increase in the use of MSMPR cascades over the past few years[79, 129, 131, 134]. The hybrid nature of the continuous MSMPR cascade means that it has two different types of mixing. Within the STR there is mixing with a wide residence time distribution, while within the transfer tubes the system delivers mixing with a narrow residence time distribution, as in a plug flow reactor[130].

However, in spite of these analogies, the de-supersaturation within an MSMPR cascade is very different to that of either a batch STR or a plug flow crystalliser (PFC); this has the advantage of potentially offering access to otherwise unattainable polymorphs (Figure 5.4). With respect to this element of polymorph selectivity, it has been noted that within MSMPR cascades the kinetic factors play an increased role in the polymorphic outcome[130].

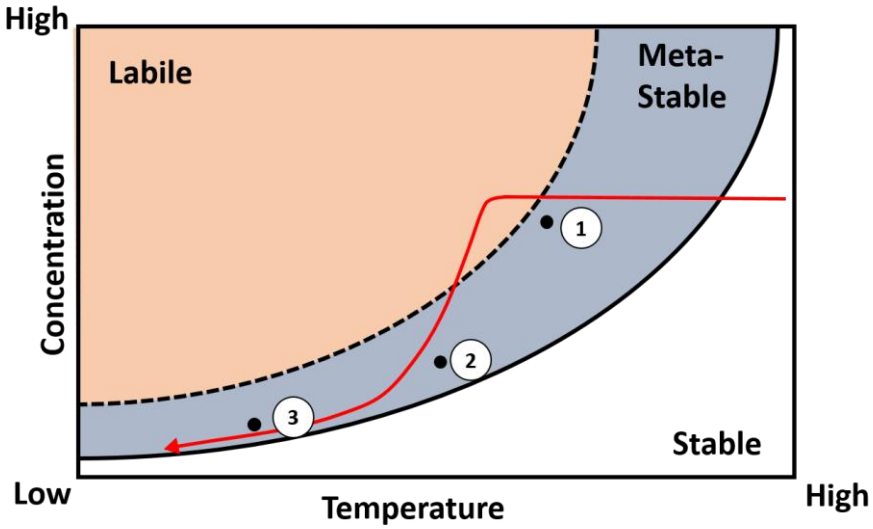

Figure 5.4 Desupersaturation in a PFC or batch cooled crystalliser (shown in red) and in an MSMPR system (discrete points).

5.2.2 Aim

This work explores multi-component crystallisation of UBA within the MSMPR crystalliser. The aim is to investigate what effect the continuous and periodic operation of the MSMPR apparatus has upon the polymorph of the UBA co-crystals produced and if there is a method by which a single UBA polymorph can be preferentially produced. The main focus is to isolate either UBAI or UBAIII; this is a challenge as they are very similar in energy and display very similar solubility profiles (section 4.5.2). This has been tested in two different MSMPR set-ups, one with peristaltic transfer (at LU) and the other with vacuum line transfer (at AZ).

5.2.3 Three-stage Continuous MSMPR with Peristaltic Pump Transfer

5.2.3.1 Materials

All cooling co-crystallisation experiments using MSMPR with peristaltic pump transfer were carried out using urea (99% pure), purchased from Sigma Aldrich UK, BA II (99% pure, purchased from Fisher Scientific UK; sourced from Acros Organics), and methanol solvent (analytical reagent grade, 99.97% purchased from Fisher Scientific UK).

5.2.3.2 Method

The three-stage continuous PMSMPR (Figure 5.5, Figure 5.6, Figure 5.7) comprises three 500 mL jacketed STRs (one nucleator (Nuc), two growth (GV) vessels), each fitted with a PTFE lid and a PTFE four-pitched blade impeller with overhead motor. All STRs are temperature controlled using separate thermofluid bath circulators regulated using a feedback control mechanism operated through the CryPRINS software[137]. In order to maintain a good suspension each STR was operated at a stirring speed of 450 rpm which was identified in preliminary experiments as striking a good balance between the best mixing conditions for effective crystal suspension and preventing formation of bubbles. To transfer the suspension from the Nuc to growth vessel 1 (GV1) two, glass dip-tubes (5 mm ID) were fitted into each vessel with the openings positioned a few centimetres clear of the impeller to ensure the transferred suspension is optimally dispersed. This was repeated for transfer between GV1 and GV2. The dip-tubes in neighbouring vessels were connected using Masterflex® L/S 16 platinum cured silicone tubing (3.1 mm ID), with each transfer line fitted to a Masterflex® L/S digital peristaltic pump (with EasyLoad head) set to operate in time dispense mode. The final transfer line exiting GV2 was pumped directly into a Buchner vacuum filter where the solid was washed, dried and removed.

Figure 5.5 Photograph of the MSMPR set-up (from left-feed vessel, nucleator and growth vessels 1 and 2) used in experiments carried out within CMAC at Loughborough University (LU).

The apparatus was set up with one of two different feed configurations (combined and separate). The only difference between the combined and separate configurations is the way in which the starting materials are introduced into the cascade of STRs. The combined configuration (Figure 5.6) features a single feed vessel (6 L jacketed STR) with urea and BA starting materials dissolved together prior to pumping into the nucleator vessel. The separate configuration (Figure 5.7) contains separate urea and BA feed vessels (a 1 L jacketed STR and a 6 L jacketed STR, respectively), the contents of which are first introduced together in the Nuc.

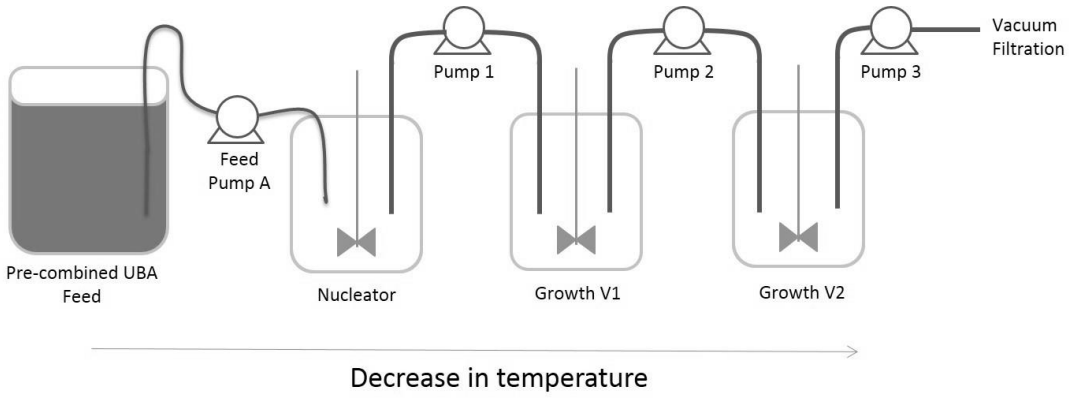

Figure 5.6 Schematic showing combined UBA feed configuration of MSMPR set-up at LU.

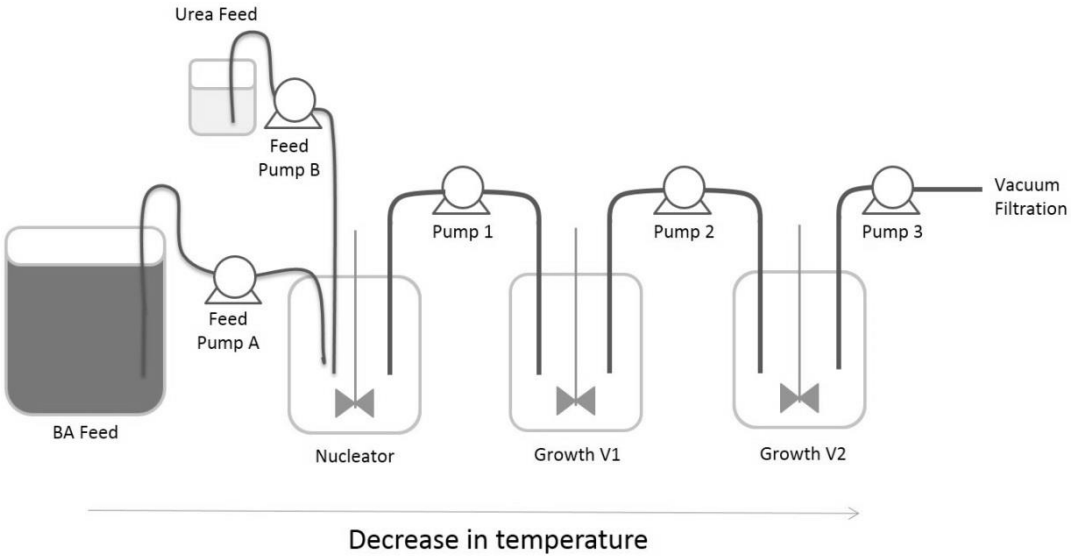

Figure 5.7 Schematic showing separate U and BA feed configuration of MSMPR set-up at LU.

Four methods of operation (MOs) were used for MSMPR experiments with peristaltic transfer (Table 5.1). MO1 uses the combined urea and BA feed configuration, while MO2 uses simultaneous urea and BA addition from separate feeds. MO3 also uses simultaneous urea and BA addition but decouples the first addition of urea and BA; for the first addition the full volume of BA is primed into the Nuc and the full volume of urea (74 mL of 0.078 g urea/ g methanol) is added in one quantity

directly from a beaker, which when added to the BA solution that has pumped into the nucleator produces a 2:1 urea: BA solution. Finally, MO4 is a continuously operated version of MO2.

For all experiments a fixed working volume of 400 mL was used and the peristaltic pumps were operated in time dispense mode whereby a fixed volume of solution is pumped across in a set time period. For Methods 1-3 400 mL of 2:1 urea: BA feed solution was transferred into the Nuc using pump 1 at 52.72 g/min taking 7.4 minutes. For MO1, MO2 and MO3 the solution was held subsequently in the nucleator (Nuc.) for 12.6 minutes prior to transfer to GV1 using pump 2 at 52.72 g/min. Pump 1 restarts at the same time as pump 2 to replenish the UBA solution in the Nuc as it is transferred into GV1. Efficient mixing is required in each vessel to ensure that the solution pumped from each vessel is representative of the bulk. The residence time of each particle will not be exactly the same within the PMSMPR as it is not guaranteed that an older particle will be withdrawn and transferred to the next vessel before a younger particle. This is known as residence time distribution (RTD) and the theory is to keep the RTD as narrow as possible to regulate the physical attributes of the particles.

Once 400 mL has been transferred, pumps 1 and 2 then stop simultaneously for 12.6 minutes to allow the solution environment to equilibrate. Pump 3 is coupled with the operation of pumps 1 and 2 and begins to transfer solution into GV2 whilst GV1 is replenished from the Nuc which in turn is replenished from the feed vessel. After another hold period of 12.6 minutes in all three vessels, pump 4 can begin to pump from GV2 into a filtration unit where the UBA solid is isolated. The process described here represents one residence time of the PMSMPR; this can be repeated continuously as required. It often takes several residence times before a continuous system reaches a steady state of operation, or in the case of periodic MSMPR mode, a state of controlled operation.

In MO4 the system is operated continuously rather than periodically the conditions remain the same except that the 12.6 minute hold periods are removed, reducing the total time in each vessel from 20 minutes down to 7.4 minutes and the residence time for the whole crystalliser reduces from 60 minutes to 22.2 minutes.

Table 5.1 Experimental conditions used for each method of operation (MO) (U = urea; BA = barbituric acid)

MO	Mode	Feed Config.	Feed conditions	Feed conc: (g/g $_{MeOH}$); V_{MeOH} (mL)		Feed Temp (°C)		Feed flow rate (g min^{-1})	
1	Periodic	Combined	N/A	U: 0.014; BA: 0.015; 5300		43		52.7	
2	Periodic	Separate	Simultaneous addition	U 0.078; 1300	BA 0.018 5300	U 20	BA 20	U 10.0	BA 42.7
3	Periodic	Separate	Rapid urea addition						
4	Continuous	Separate	Simultaneous addition						

The temperatures of the cascade of vessels used in the PMSMPR experiments were altered aiming to obtain either pure UBAI or UBAIII, based on the preliminary results from batch and semi-batch UBA co-crystallisation reported above. The experimental conditions used in each of the nine UBA PMSMPR crystallisations with peristaltic transfer are given in Table 5.2.

Experiments LU6 to LU9 were seeded with either UBAI or UBA II obtained from previous batch cooling crystallisation experiments; seeds were introduced prior to delivery of the combined solution (method 1) into the Nuc. The UBA concentration of the feed solutions used in seeded experiments was kept the same as in previous unseeded experiments. The solutions were prepared at 55 °C and cooled to 43 °C before seeding with the desired UBA co-crystal (10% of the theoretical mass of UBA (1:1 ratio of U:BA) present in solution). The UBA seed suspension was left to mature at the saturation temperature (43 °C) for 30 min before commencing the periodic operation. Subsequently the seed suspension was pumped to the Nuc vessel of the PMSMPR at a rate of 52.7 $gmin^{-1}$ for all experiments, except for LU6. LU6 used a flow rate of 41.7 $gmin^{-1}$, but upon visual inspection particle settling was observed in the transfer lines at this lower flow rate. All subsequent experiments were thus carried out with the higher flow rate of 52.7 $gmin^{-1}$ which helped to overcome this issue.

Table 5.2 Experimental conditions for crystallisation of UBA through PMSMPR using peristaltic transfer

Expt.	MO	Seed	Temperature (°C)		
			Nuc.	GV1	GV2
LU1	1	N/A	20	30	10
LU2	2	N/A	20	30	20
LU3	3	N/A	20	30	20
LU4	3	N/A	15	10	5
LU5	4	N/A	20	30	20
LU6	1	UBAI	27	17	10
LU7	1	UBAI	33	23	10
LU8	1	UBAIII	20	20	10
LU9	1	UBAIII	35	30	25

5.2.3.3 In-line Analysis – Process Analytical Technologies (PAT)

FBRM

In-situ focused beam reflectance measurement (FBRM), using Mettler Toledo model D600, was used for nucleation and dissolution detection and for monitoring the PSD in solution.

Raman

An RXN1 Raman system from Kaiser Optical Inc. (785 nm laser) with immersion probe was used in attempts to implement *in-situ* polymorphism monitoring.

ATR-UV/vis

UV/vis measurements were collected using a Hellma 661.822 ATR probe connected to a Carl Zeiss MCS621 UV/vis spectrometer.

Video-microscopy

Images of the crystals in solution were captured using Metler Toledo Process and Vison Measurement (PVM) probe.

All PAT probes and thermocouples were inserted just a few centimetres above the impeller in each vessel to ensure optimum process monitoring and temperature control.

5.2.3.4 Off-line Analysis

Particle Size Measurement

A Malvern MasterSizer® 2000 instrument fitted with Hydro SM dispersion unit was used for particle size analysis by laser diffraction. Filtered and dried crystalline samples were dispersed in IPA (pre-cooled to 0 °C) and introduced into the flow cell of the Mastersizer® unit via a circulation system for measurement. Three representative measurements of each sample were performed and the average value reported.

Raman Spectroscopy

A Thermofisher Scientific DXR Raman microscope equipped with 780 nm laser was used as a supporting tool for polymorph characterisation by both spectral acquisition and imaging. The Raman microscope was fitted with an Olympus TH4-200 optical component which was used for image analysis.

Methanol has particularly significant Raman activity (Figure 5.8 a) and this coupled with a particularly low UBA concentration owing to the poor solubility of BA in methanol, meant that it proved challenging to detect UBA in solution (Figure 5.8 c). Shortly after nucleation occurred there was a significant increase in the intensity of the Raman signal which upon further inspection was as a result of fouling on the Raman probe (Figure 5.8 d and e). The signal reverted to the normal solution signal (Figure 5.8 c) as soon as the probe was cleaned and re-submersed.

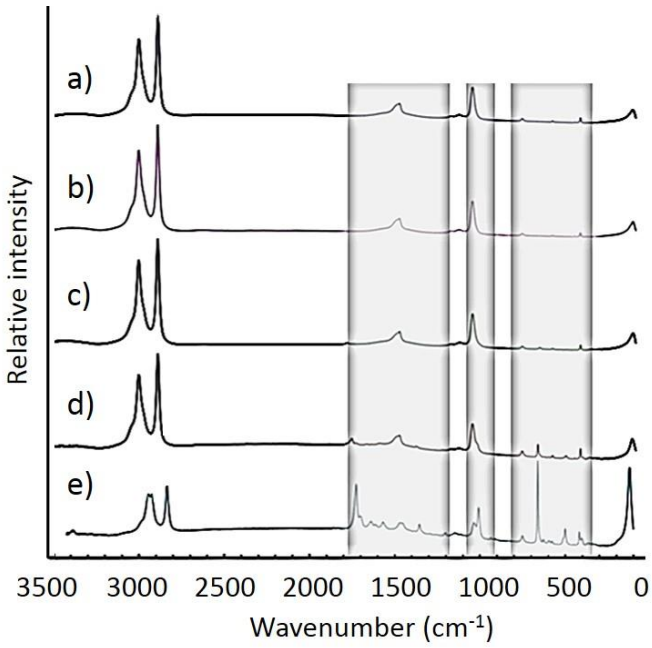

Figure 5.8 Signals from *in situ* Raman probes in a) methanol, b) urea in methanol, c) urea and BA in methanol for comparison with signals obtained d) 5 minutes and e) 8 minutes after UBA nucleation was detected.

PXRD

Solid products from all MSMPR runs were analysed by PXRD using a Bruker D8 Advance equipped with monochromated Cu Kα radiation (λ=1.54056 Å) at 298 K in flat plate mode in reflection geometry. The samples were pressed onto a 1 cm square glass slide which was mounted on a magnetically held rotating sample holder.

5.2.3.5 Results

The XRPD patterns of the dried, filtered products of runs LU1-LU5 are given in Figure 5.9-Figure 5.13, with the corresponding Raman spectra on samples extracted from GV2 given in Figure 5.14. For runs LU6-LU9, the PXRD patterns are in Figure 5.15-Figure 5.18, with the Raman spectra in Figure 5.19.

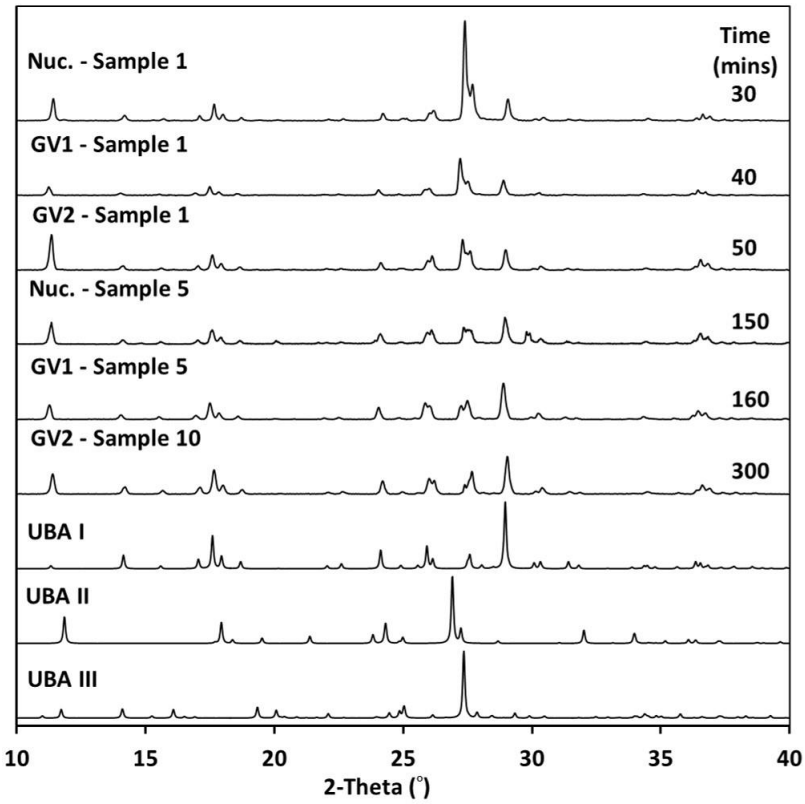

Figure 5.9 PXRD analysis of samples from Experiment LU1 of UBA continuous crystallisation using peristaltic transfer.

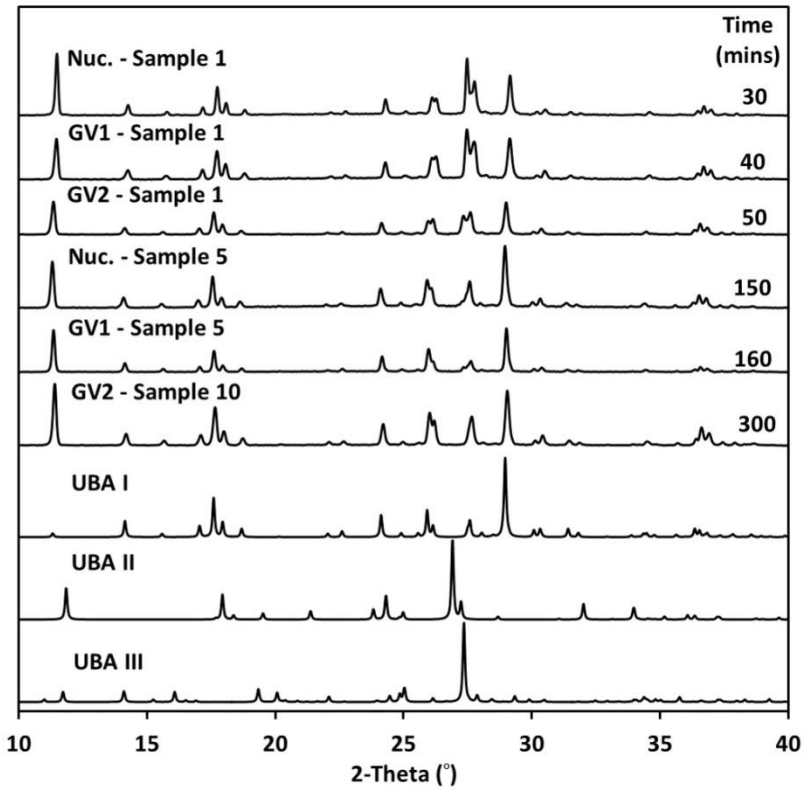

Figure 5.10 PXRD analysis of samples from Experiment LU2 of UBA continuous crystallisation using peristaltic transfer.

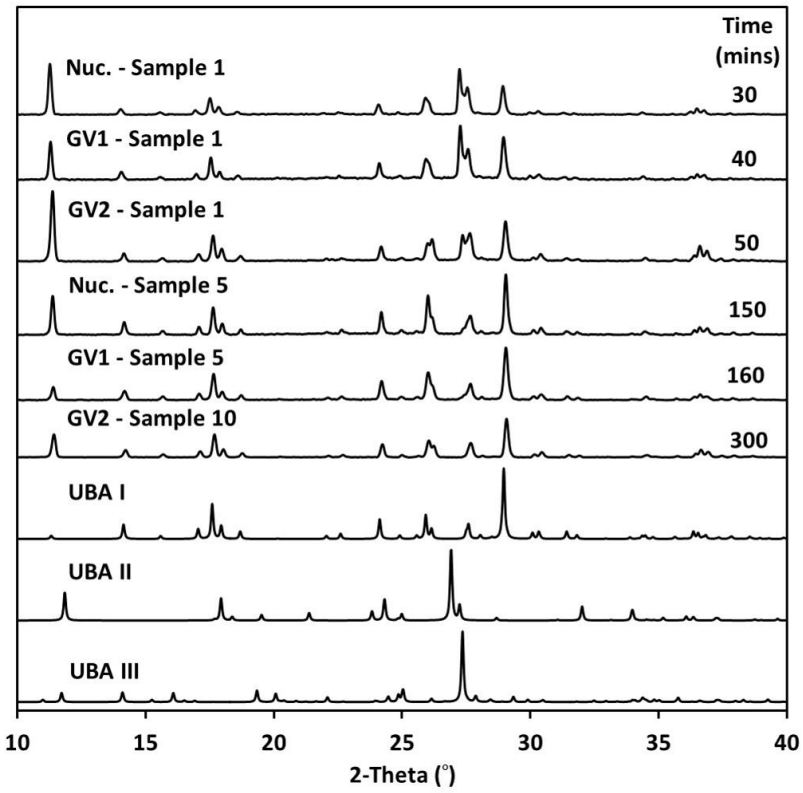

Figure 5.11 PXRD analysis of samples from Experiment LU3 of UBA continuous crystallisation using peristaltic transfer

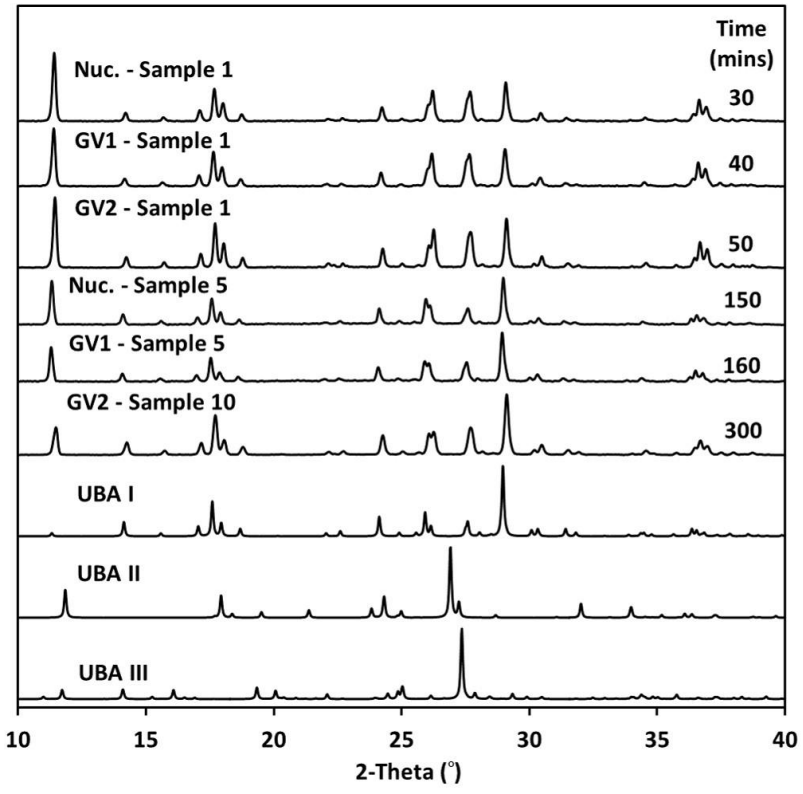

Figure 5.12 PXRD analysis of samples from Experiment LU4 of UBA continuous crystallisation using peristaltic transfer

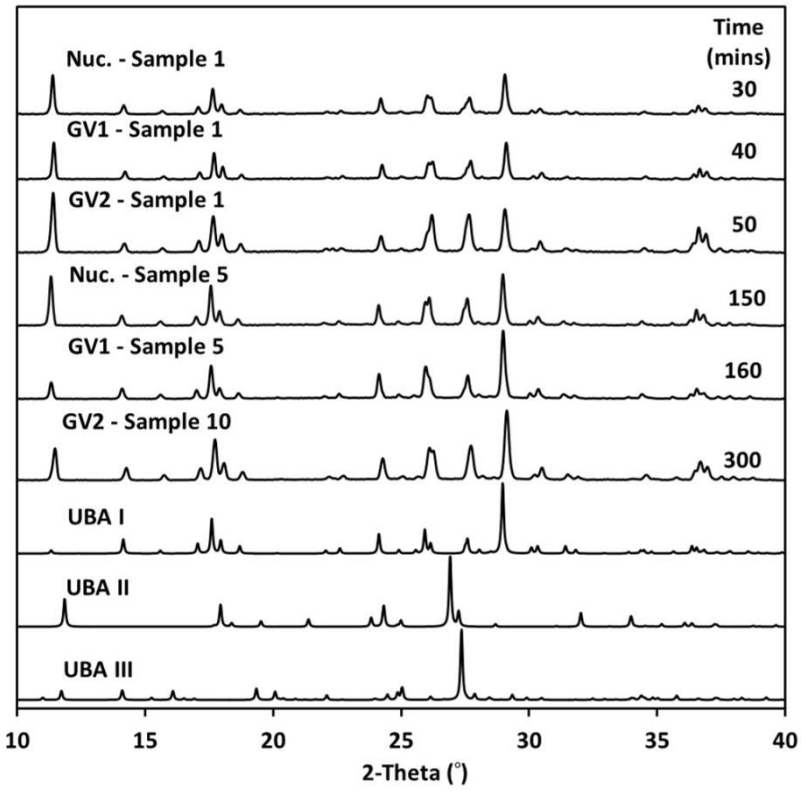

Figure 5.13 PXRD analysis of samples from Experiment LU5 of UBA continuous crystallisation using peristaltic transfer

The presence of UBAI and UBAIII in a sample can be identified by two characteristic peaks present at 27° and 29° 2θ, which are unique peaks in the patterns of UBAIII and UBAI, respectively. The PXRD patterns indicate clearly the polymorphic composition in each stage of the PMSMPR and highlight the changes in polymorphic composition over time. In experiments LU1 and LU2 a mixture of UBAI and UBAIII is initially produced (Figure 5.9 and Figure 5.10). As the PMSMPR run progresses the peak at 27° 2θ reduces in intensity indicating a reduction in UBAIII and in LU3 the peak disappears completely with only UBA I in NUC sample 5 taken at 150 minutes into operation (Figure 5.11). PXRD analysis of samples from LU4 and LU5 indicates that there is no UBAIII present throughout these experiments, preferentially producing UBAI (Figure 5.12 and Figure 5.13). Raman spectroscopy of samples 1 and 10 from GV2 for each experiment indicates conversion from a mixture of UBAI and UBAIII to UBAI (Figure 5.14).

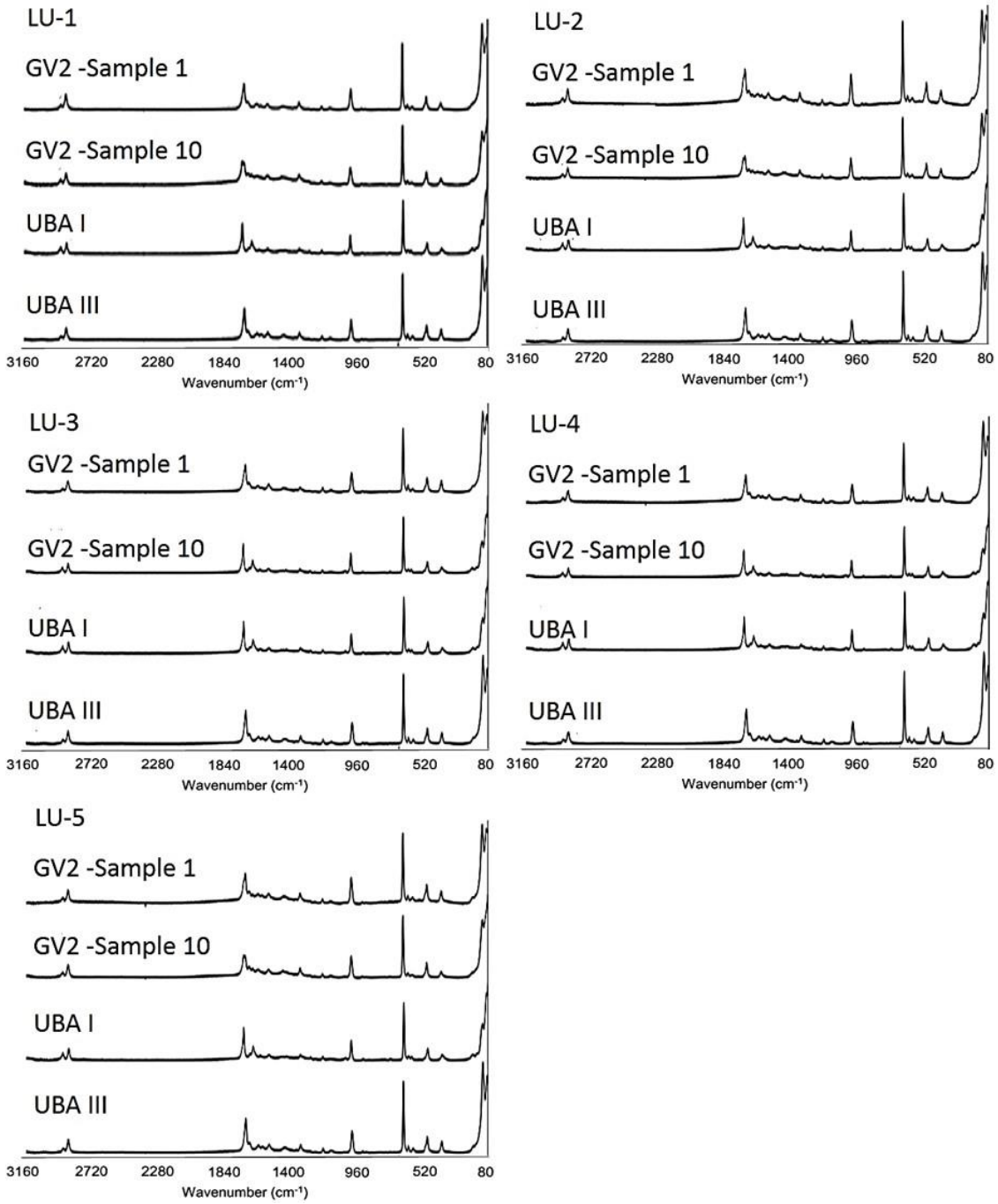

Figure 5.14 Raman spectra of sample 1 and 10 taken from GV2 for experiments LU1 to LU5 for comparison with the Raman spectra for UBAI and UBAIII

Experiments LU6 and LU7 were seeded with UBAI. PXRD and Raman analysis of samples 1 and 10 from GV2 of experiments LU6 and LU7 indicate that UBAI was preferentially produced throughout the crystallisation process (Figure 5.15, Figure 5.16 and Figure 5.19). On the other hand experiments LU8 an LU9 were seeded with UBAIII. Products from LU8 and LU9 are dominated by UBAIII as would be expected when seeding with UBAIII however there is some indication of UBAI in the PXRD patterns of samples 1 and 10 (Figure 5.17 and Figure 5.18) although Raman analysis indicates sample 1 and 10 of LU8 are both UBAIII and that LU9 converts to UBAI (Figure 5.19).

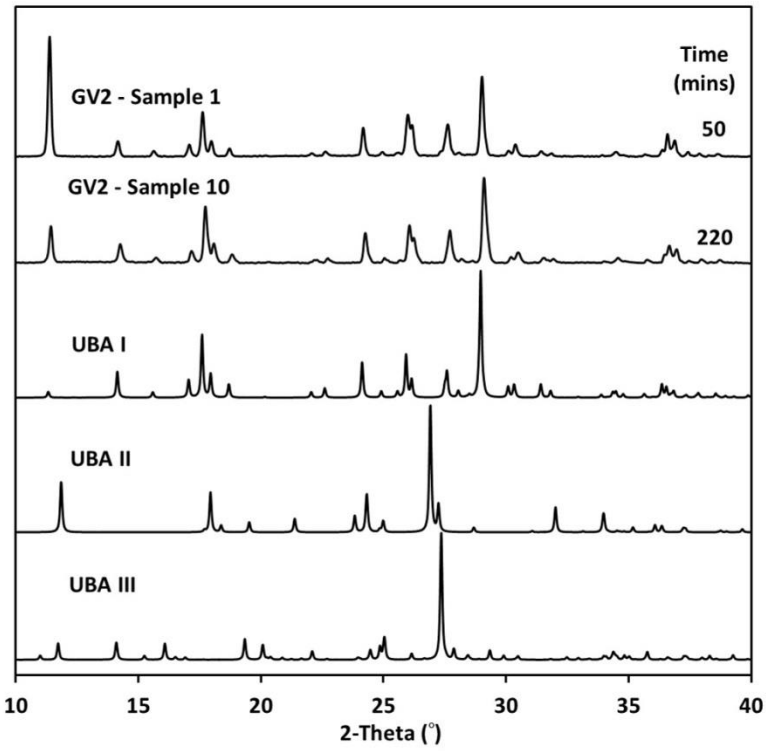

Figure 5.15 PXRD analysis of samples from Experiment LU6 of UBA continuous crystallisation using peristaltic transfer.

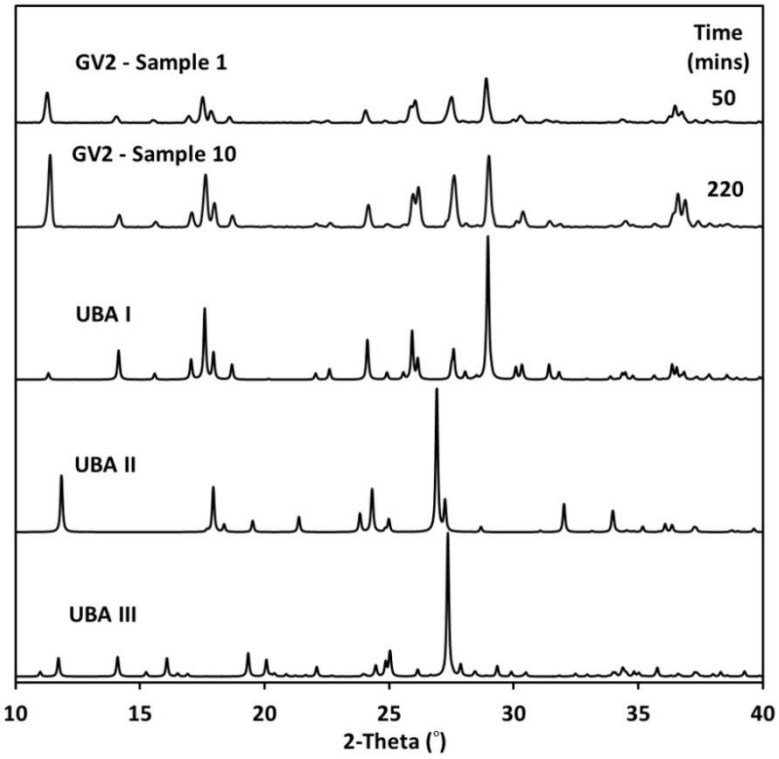

Figure 5.16 PXRD analysis of samples from Experiment LU7 of UBA continuous crystallisation using peristaltic transfer.

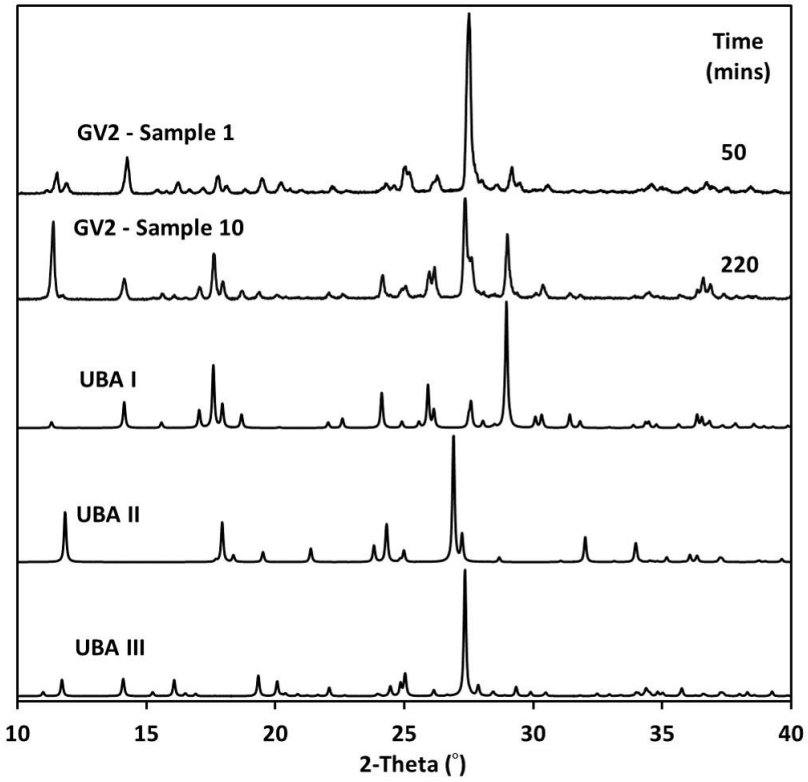

Figure 5.17 PXRD analysis of samples from Experiment LU8 of UBA continuous crystallisation using peristaltic transfer.

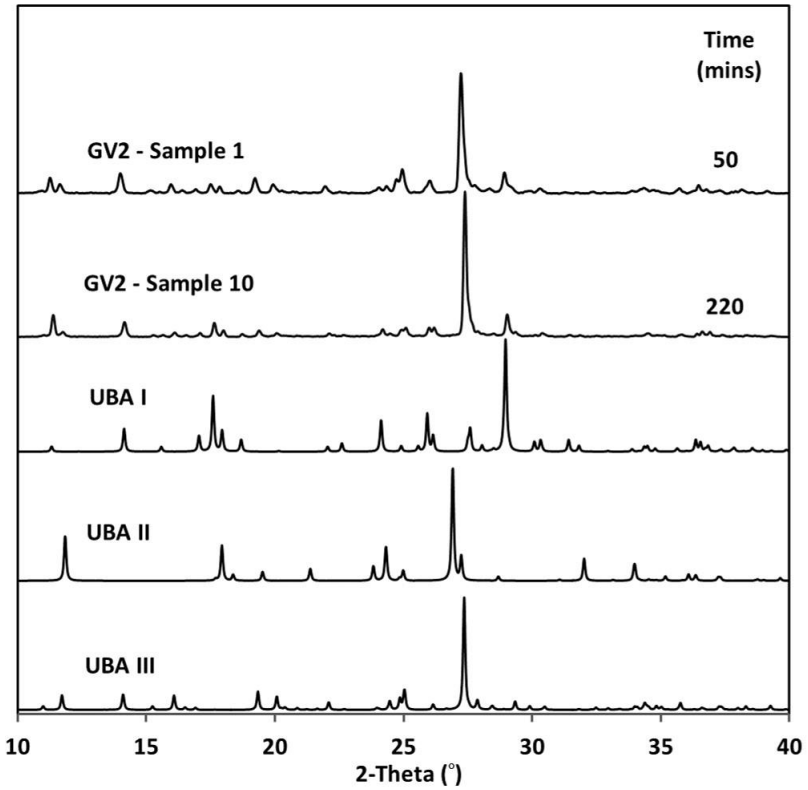

Figure 5.18 PXRD analysis of samples from Experiment LU9 of UBA continuous crystallisation using peristaltic transfer.

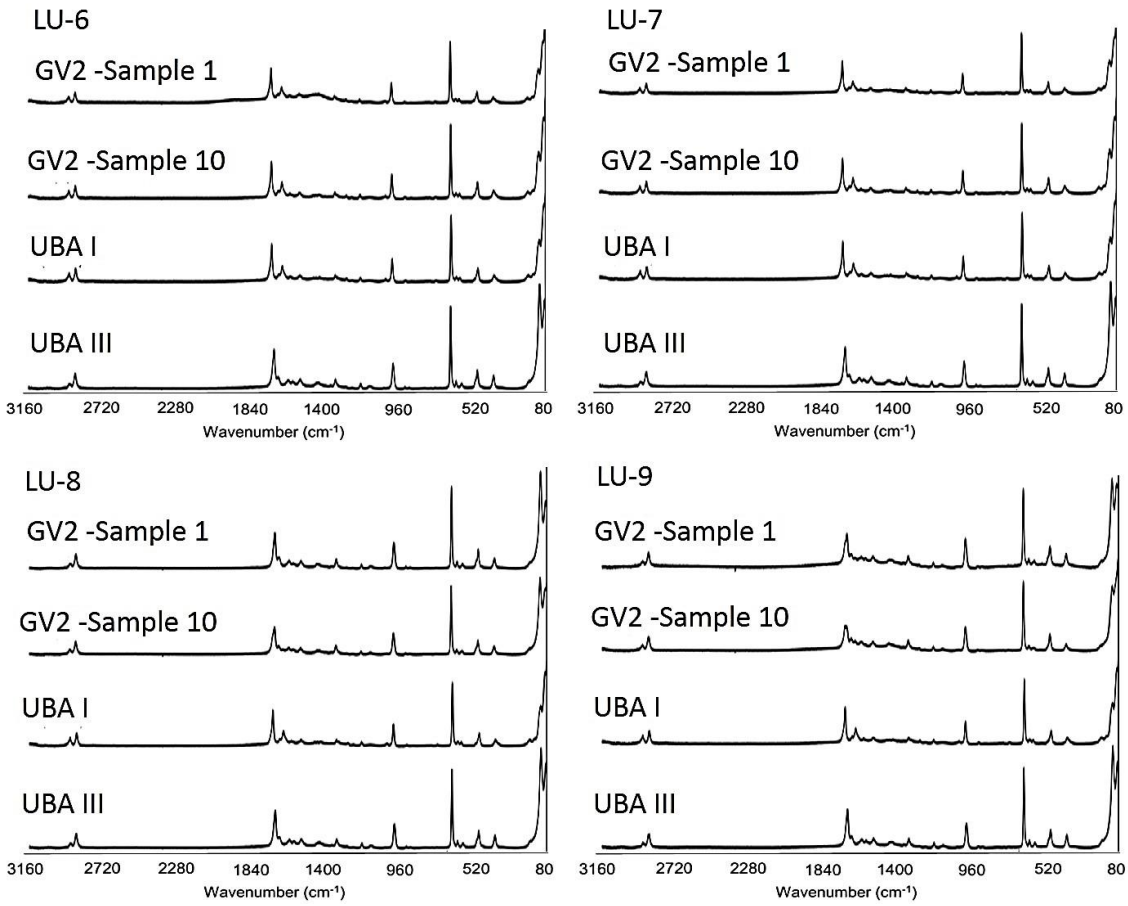

Figure 5.19 Raman spectra of sample 1 and 10 taken from GV2 for experiments LU6 to LU9 for comparison with the Raman spectra for UBAI and UBAIII.

A summary of the crystallisation conditions and the results from Raman and PXRD analysis are given in Table 5.3.

Table 5.3 Summary of UBA polymorphs identified using PXRD and Raman microscopy for MSMPR experiments LU1 to LU9

Expt.	MO	Seed	Temp. (°C)	Product (PXRD)	Product (Raman)
LU1	1	N/A	20/30/10	UBAI & UBAIII	UBAI & UBAIII
LU2	2	N/A	20/30/20	UBAI & UBAIII	UBAI & UBAIII
LU3	3	N/A	20/30/20	UBAI	UBAI & UBAIII
LU4	3	N/A	15/10/5	UBAI	UBAI & UBAIII
LU5	4	N/A	20/30/20	UBAI	UBAI & UBAIII
LU6	1	UBAI	27/17/10	UBAI	UBAI
LU7	1	UBAI	33/23/10	UBAI	UBAI
LU8	1	UBAIII	20/20/10	UBAIII & UBAI	UBAIII
LU9	1	UBAIII	35/30/25	UBAIII & UBAI	UBAIII & UBAI

5.2.3.6 Conclusion

In this study at LU, pure UBAI was successfully isolated using seeded PMSMPR (LU6 and LU7), but isolation of pure UBAIII remained elusive (even with seeding) and there was no evidence of the highly metastable UBAII. The periodic flow PMSMPR process shows potential as operating strategy for polymorphs selective industrial crystallisation as it provides a different operating trajectory through the phase diagram compared to batch and continuous processes. The PMSMPR is particularly useful for slower-growing systems such as UBA that require long mean residence times to produce large crystals. The increased residence time in each vessel can also be used to alleviate common problems such as fouling, encrustation and blockage that are often observed in conventional continuous MSMPR operations normally due to lower velocities in transfer lines.

5.2.4 Three-stage Continuous MSMPR with Vacuum Line Transfer

5.2.4.1 Materials

In all cooling co-crystallisation experiments using MSMPR with vacuum line transfer the materials were urea (99% pure), purchased from Sigma Aldrich UK, BA (form II) was sourced from Sigma Aldrich (99% pure) and methanol (Laboratory reagent grade) purchase from Fisher were used.

5.2.4.2 Method

In contrast to the peristaltic pump operated transfer used in the PMSMPR set-up at LU the continuous MSMPR set-up used at AZ (Macclesfield) was operated using vacuum transfer (Figure 5.21).

Figure 5.20 Photograph showing the set-up of vessels used in UBA MSMPR experiments at AstraZeneca, Macclesfield.

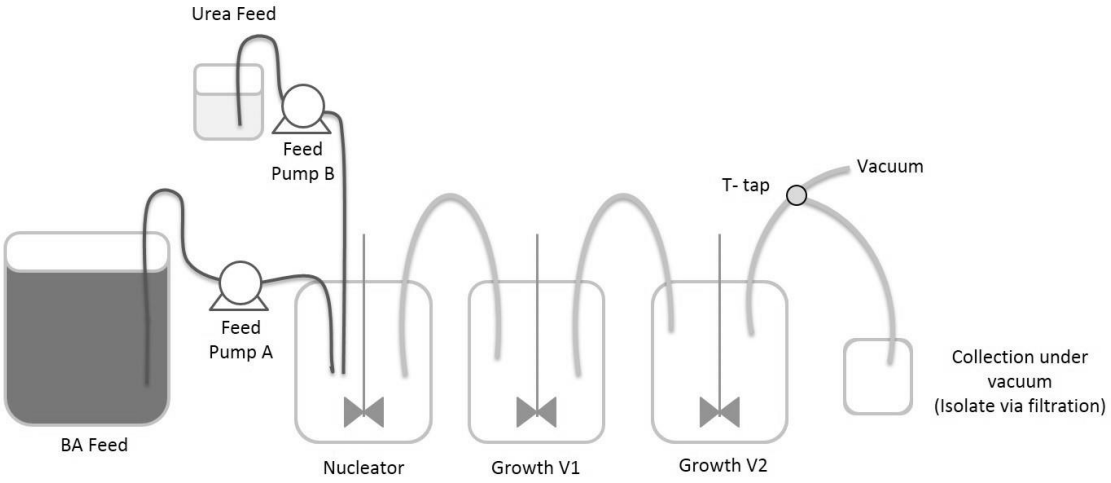

Figure 5.21 Schematic showing MSMPR set up used in experiments at AstraZeneca, Macclesfield with a separate urea and BA feed.

As per the separate configuration used at LU, two separate feed vessels were used for urea and BA (a 500 mL Duran bottle and a 2 L Duran bottle, respectively) which were pumped into the nucleator vessel using Masterflex® L/S digital peristaltic pumps fitted with a PTFE pump head and PTFE connector with Masterflex® L/S 16 norprene tubing (3.1 mm ID) (Note that the choice of pump head was not specific to the process and chosen solely due to availability of pumps).

The nucleator (Nuc), growth vessel 1 (GV1) and growth vessel 2 (GV2) (three jacketed STRs, 500 mL, 250 mL and 1 L, respectively) were fitted with a glass lids with four ground glass necks, a stainless steel three-retreat curve impeller and an overhead motor. The vessels were connected using PTFE transfer lines (5 mm ID) fitted into the lids using Quickfit® ground glass adaptors to ensure a good seal to maintain the vacuum, with the final vessel connected to the vacuum system. All three vessels were temperature regulated using separate thermofluid bath circulators.

During the experiments presented above using peristaltic transfer (section 5.2.3), the residence time in each vessel was controlled by the flow rate of suspension entering and exiting the vessel as determined by the rate of the coupled peristaltic pumps. This allowed the transfer tubes to be positioned just above the impeller where the solid suspension would have the best dispersion. However when operating with vacuum transfer, it is not possible to fine tune the suction from the vacuum to achieve the slow flow rate required for continuous MSMPR experiments. Instead, the residence time inside each vessel is governed by the position of the transfer tube opening which controls the fill level and working volume within the vessel. The opening of the transfer tube exiting each vessel was positioned at the surface of the working volume of the vessel, in order that the flow rate of the feedstock into the Nuc (controlled using peristaltic pumps) will increase the fill level at a controlled rate and regulate the transfer into the next vessel. All transfer tubes entering the vessels were positioned a few centimetres above the working volume surface for two reasons: to minimise

any splashing up the sides of the vessels, and to ensure flows were not hampered during liquid transfer; the flow rate used is not sufficient to allow liquid to flow through the liquid already in the vessel. The vacuum line operates all transfer lines simultaneously which automatically couples the flow from each vessel to the next. This eliminates the need for peristaltic pumps with a time dispense mode and the difficulties that would be faced with coupling the pumps.

All experiments used a separate urea and BA feed of 0.014 g/g $_{MeOH}$ and 0.015 g/g $_{MeOH}$, respectively. Due to the analogue nature of the vacuum produced and the fact that it has to be operated manually, the experiments were run in continuous mode with no hold period as previously used in PMSMPR experiments at LU. The flow rate though the system was dictated by the flow rates from the urea and BA feed vessels which were operated as 1.6 g min^{-1} and 10.9 g min^{-1}, respectively, which combine to give a total flow rate through the system of 12.5 g min^{-1}. The residence times for each set-up is dependent on the flow rate and volume of the crystalliser; 38 min for AZ1, AZ2 and AZ3; 51 min for AZ4 and AZ5. The temperature working volume in the vessels and the stirring speed were varied to create different crystallisation environments in an attempt to isolate UBAI preferentially (Table 5.4).

Table 5.4 Experimental conditions for UBA crystallisation using continuous MSMPR with vacuum transfer.

Expt.	Mode	Seed	Temperature (°C)			Working Vol. (mL)			Stirring (rpm)		
			Nuc.	GV1	GV2	Nuc.	GV1	GV2	Nuc.	GV1	GV2
AZ1	Conti.	N/A	20	30	20	200	200	200	250	250	250
AZ2	Conti.	N/A	20	30	20	200	200	200	250	250	250
AZ3	Conti.	N/A	20	30	N/A	400	200	N/A	250	300	N/A
AZ4	Conti.	UBAI	20	15	10	400	200	200	350	350	350
AZ5	Periodic	UBAI	20	15	10	400	200	200	350	350	350

All samples were analysed off-line using PXRD. Data were obtained using a Bruker D4 Endeavor equipped with monochromated Cu Kα radiation (λ=1.54056 Å) at 298 K. Samples were prepared on zero background silicon wafers by pressing approximately 2 mg of each sample over the wafer with a glass slide.

5.2.4.3 Results

The products from each of these runs AZ1-AZ5 (Table 5.4) were analysed using PXRD (Figure 5.23, Figure 5.25-Figure 5.28) and, for AZ1 and AZ2, by SEM (Figure 5.22, Figure 5.24).

Table 5.5 Results and observations from UBA crystallisation experiments using continuous MSMPR with vacuum transfer.

Expt.	Purpose	Observations	Product
AZ1	Test solids transfer	Blockage of transfer line from Nuc.	UBAI UBAIII
AZ2	Validation against LU set-up	Had to clear transfer lines periodically	UBAI UBAIII
AZ3	Test longer RT in Nuc. to prevent blocking	No blockage in transfer line	UBAI UBAIII
AZ4	Validation of cooling regime to obtain UBAI	No blockage in transfer line System did not produce pure UBAI as in LU experiments	UBAI UBAIII
AZ5	Compare continuous operation with periodic operation	System did not produce pure UBAI as in LU experiments Periodic transfer helped to alleviate the build-up of solids in Nuc.	UBAI UBAIII

The results from these vacuum-line MSMPR runs at AZ are summarised briefly in Table 5.5 above, showing a mixture of UBAI and UBAIII, and can be contrasted with those achieved to date in the LU peristaltic pump driven MSMPR system. It should, however, be noted that a limited number of preliminary runs were carried out using the AZ MSMPR, and the parameters for its operation are unlikely yet to be optimised.

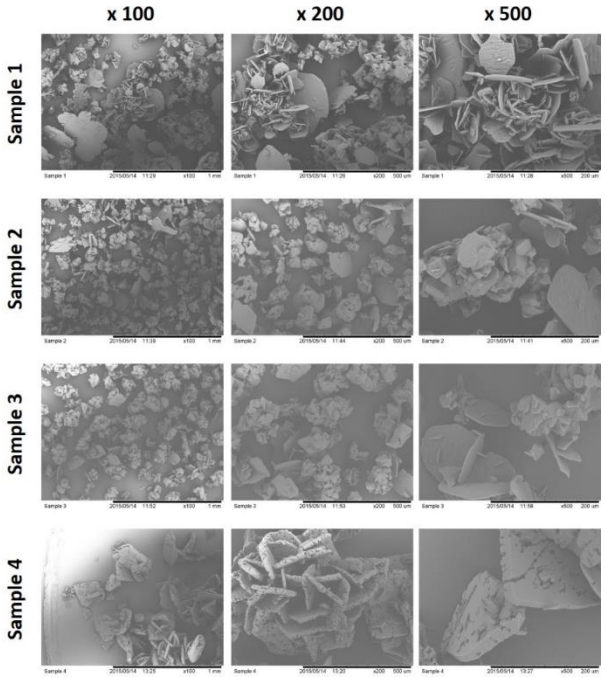

Figure 5.22 SEM images of samples from Experiment AZ1 of UBA continuous crystallisation using vacuum transfer.

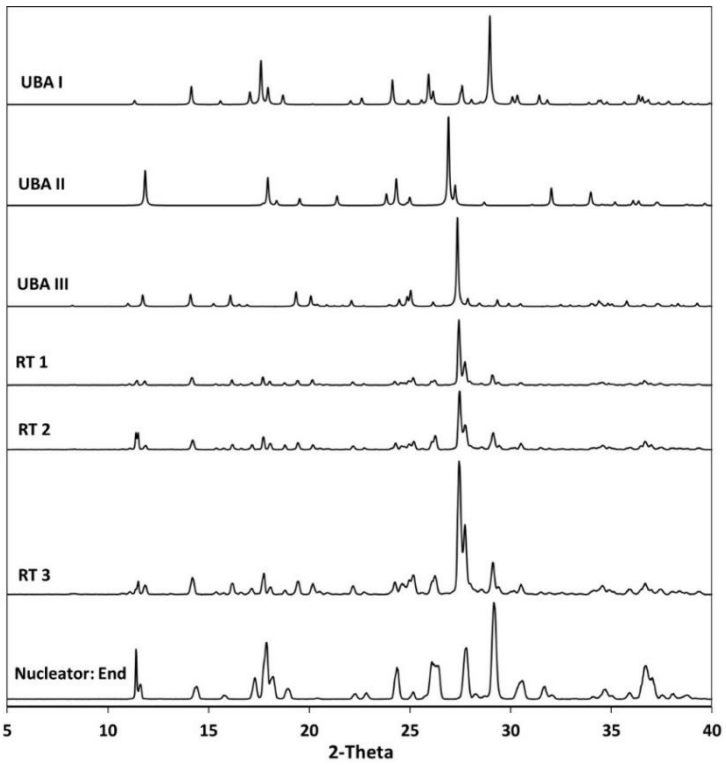

Figure 5.23 PXRD analysis of samples from Experiment AZ1 of UBA continuous crystallisation using vacuum transfer.

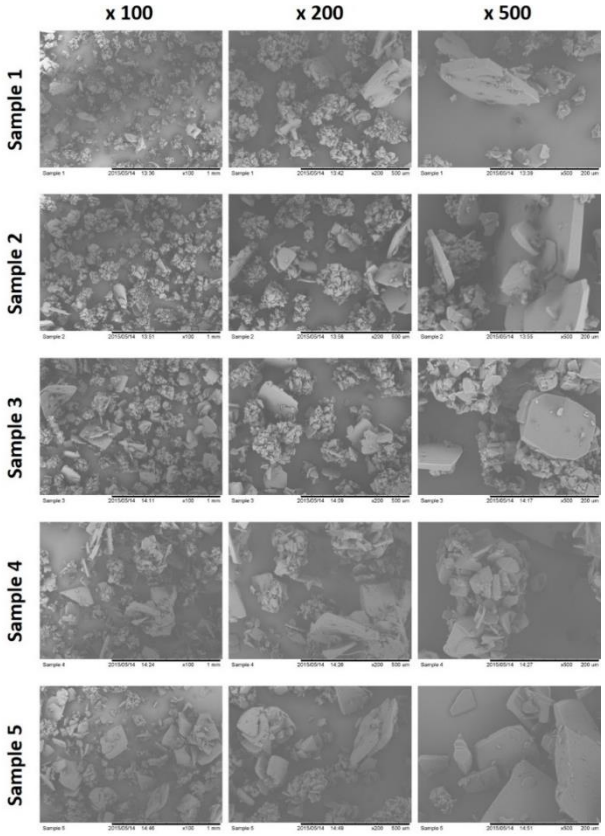

Figure 5.24 SEM images of samples from Experiment AZ2 of UBA continuous crystallisation using vacuum transfer.

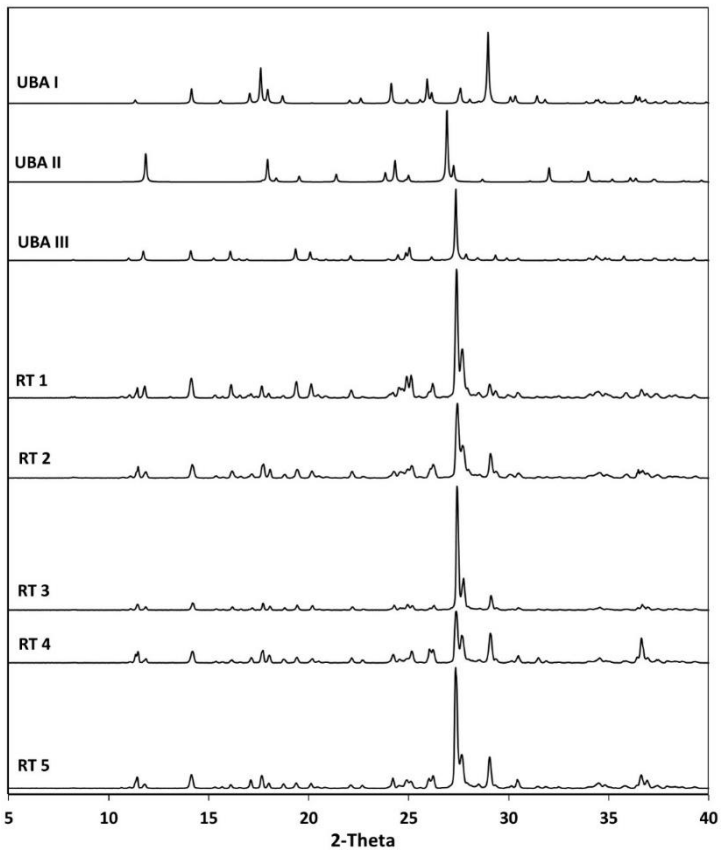

Figure 5.25 PXRD analysis of samples from Experiment AZ2 of UBA continuous crystallisation using vacuum transfer.

PXRD analysis of experiments AZ1 and AZ2 showed that throughout the experiments a mixture of UBAI and UBAIII was obtained (Figure 5.23 and Figure 5.25). During these experiment the transfer lines were temporarily removed and flushed with methanol to clear. No UBAII was present in these samples. Initially samples obtained were a mixture of UBAI and UBAIII, however by RT5 PXRD analysis indicates that UBAI is dominant. In experiments AZ1 and AZ2 issues were encountered with blockages within the transfer line between the NUC and GV1, an indicator that there is still primary nucleation occurring in the transfer lines and GV1.

In order to overcome the issues with transfer line blockages and encrustation, AZ3 was configured with only two vessels (NUC and GV1) the working volume of the NUC was doubled by altering the position of opening of the transfer line. The total RT within the crystalliser remained the same (37.8 minutes) but the RT within the NUC at 20 °C was doubled (from 12.6 minutes to 25.2 minutes) in an attempt to reduce the fouling in the transfer line to GV1. By increasing the RT the time allowed for nucleation at 20 °C was increased which restricted the nucleation process to the NUC vessel and prevented nucleation in the transfer lines and GV1.

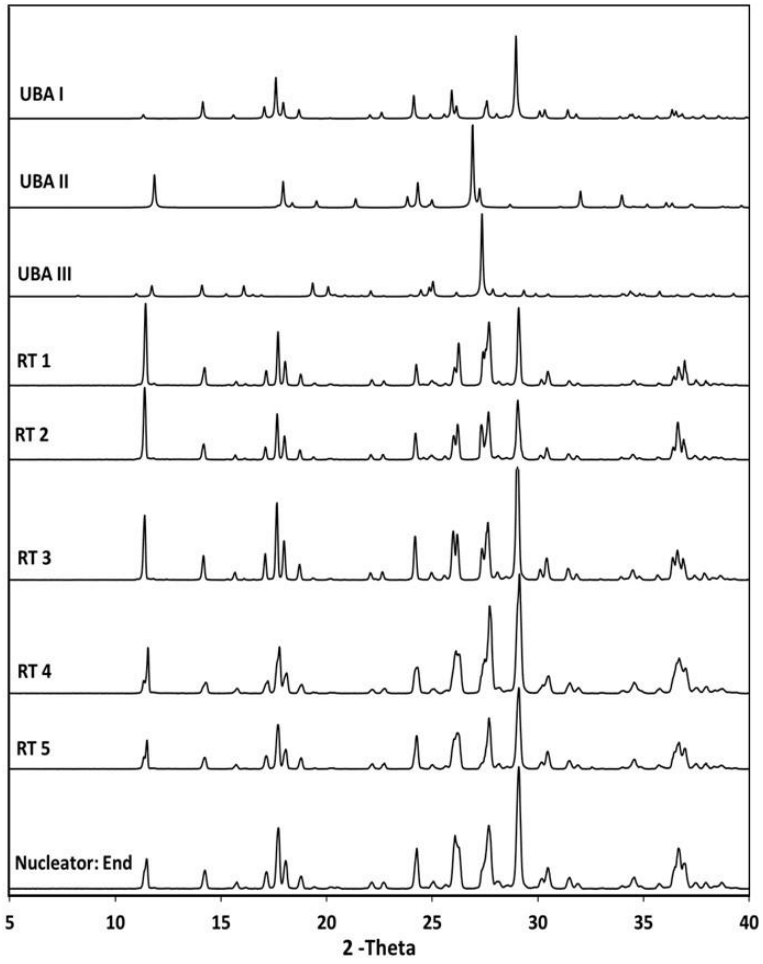

Figure 5.26 PXRD analysis of samples from Experiment AZ3 of UBA continuous crystallisation using vacuum transfer.

PXRD of samples from AZ3 initially show a mixture of UBAI and UBAIII, however by RT5 (after 189 minutes) the sample has fully transformed to UBAI. This may indicate the favourability of transformation from UBAIII to UBAI as was observed in most PMSMPR experiments at LU.

In addition to the effect upon polymorph it may prove interesting to investigate the effect increasing the working volume of the nucleator on the RTD which could be measured by monitoring the PSD. One would expect that the RTD would be broader as the likelihood of the older crystals being transferred to the next vessel before newer crystals when a larger number of crystals are present is smaller.

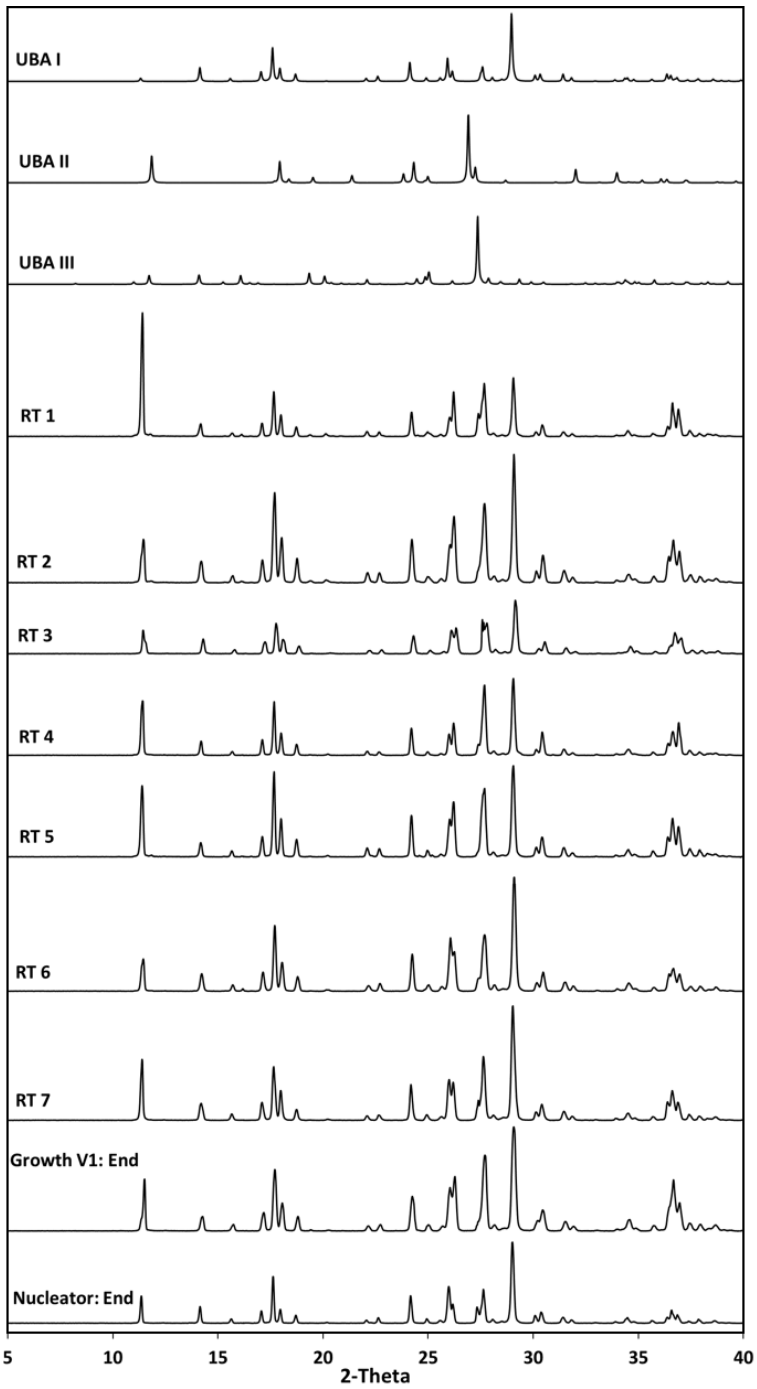

Figure 5.27 PXRD analysis of samples from Experiment AZ4 of UBA continuous crystallisation using vacuum transfer.

In experiment AZ4, UBAI seed was used and the temperature profile was reduced to mimic the profile used in experiment LU6 which obtained UBAI, however in this set up a mixture of UBAI and UBAIII was produced throughout the experiment. There are several possible reasons why solely UBAI was not produced in AZ4. Firstly, a lower concentration seed-loading (1%) was used, as was the case for AZ5, in contrast to the seeded runs at LU which used significantly higher seed loadings (10%). This step was taken to represent seed loadings used in industrial crystallisation ≤ 1%, which may not have been high enough for the level of supersaturation in the Nuc. Secondly, AZ4 utilised

continuous MSMPR operation, as opposed to the periodic operation implemented in LU6 and AZ5, although AZ5 also produced a mixture of UBAI and UBA III (Figure 5.28). While the periodic operation of AZ5 did not offer polymorph control it did reduce the propensity for build-up of solids in the Nuc. As the flow rates were much faster and the outlet of the transfer line could be positioned well below the surface of the solution. Further investigation of this will form part of the future work in developing the AZ MSMPR system.

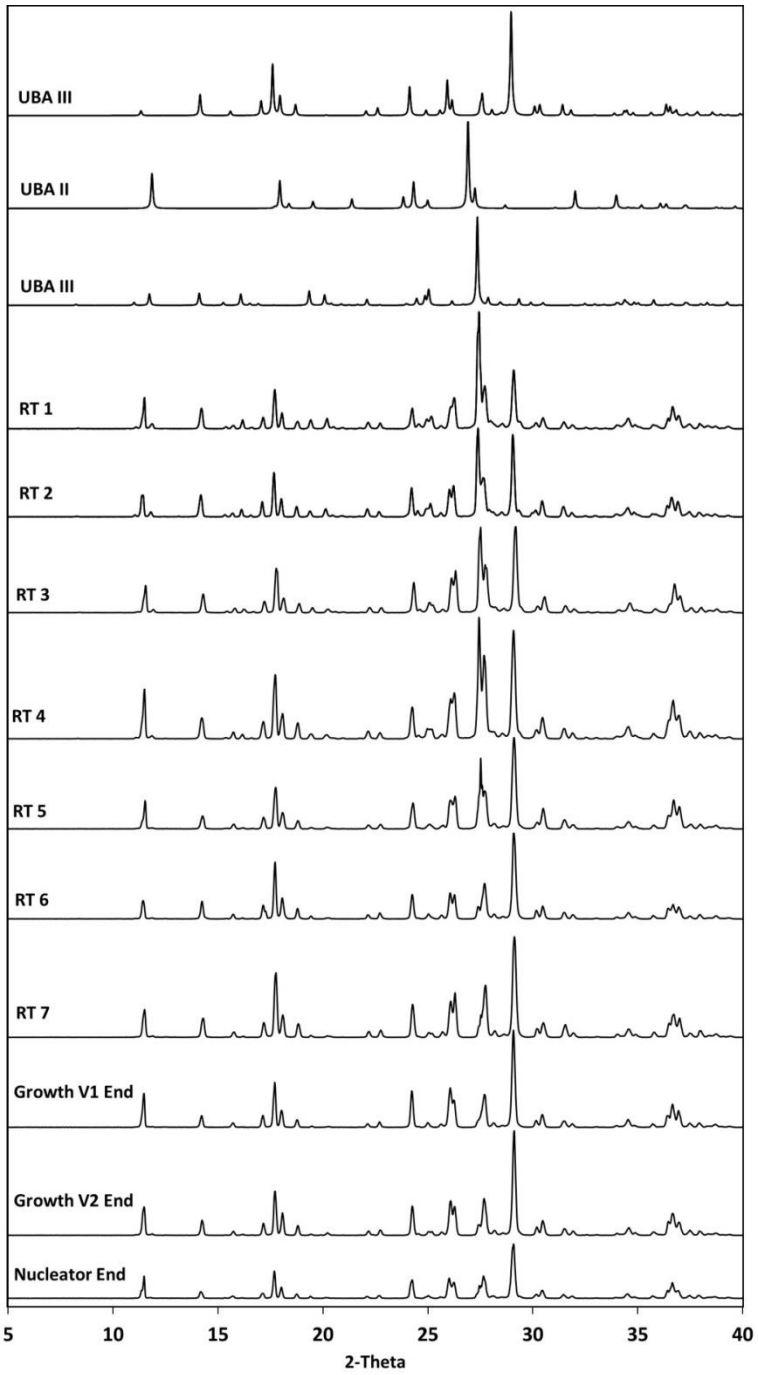

Figure 5.28 PXRD analysis of samples from Experiment AZ5 of UBA continuous crystallisation using vacuum transfer.

5.2.4.4 Conclusions

The MSMPR at AstraZeneca has been successfully commissioned and operated in a multi-component continuous crystallisation. This has involved empirical investigation of mass transfer effects, and design of transfer protocols to minimise blockages to allow complete unit operation;

- UBA has been crystallised successfully in the AZ MSMPR in five separate operational runs, with filtration and collection of the final solid products enabled; A mixture of UBAI and UBAIII was found to be produced in all experiments carried out. It has not as yet been possible to isolate individual polymorph in the MSMPR at AZ, but the process design has not been comprehensively explored as yet. One significant issue that has been identified for improvement is the loss of solvent during the vacuum transfer processes, which leads to variation in the supersaturation conditions during the process, and which should be investigated;
- No metastable UBAII has been produced in these runs in the AZ MSMPR system;
- The following difficulties were encountered using the vacuum transfer method:
    - Loss of volatile solvent to vacuum
    - Increased fouling on vessel walls at fill level
    - Reduced solids transfer due to surface position (coupled with mixing conditions)
- The use of peristaltic pumps for transfer should be investigated for the system. On a practical note, the use of dual head pumps would save on space, which is at a premium in the current location of the device.
- Transfer using pressure from nitrogen gas should also be studied as the system would be closed this should help to negate the loss of solvent which occurred when using vacuum transfer and has recently been adopted in the MSMPR set-up within CMAC at the University of Strathclyde.

5.3 Conclusions - Scaling-up Batch Cooling Crystallisation of UBA and Transfer to MSMPR

The initial conditions for batch cooling crystallisation production of the three UBA solid forms have been established by experiments in an STR at 500 ml scale. Access to UBAI and UBAIII has been shown to be dependent on the cooling rate, with slower cooling tending to favour production of UBAIII, while the more metastable UBAII proved more elusive, as might be expected. UBAII was in the end isolated in single phase form using a two-step cooling regime with linear cooling at 1 °Cmin^{-1} to 35 °C followed by very slow linear cooling (0.05 °Cmin^{-1}) to 10 °C; this was, however, not reproducible over several experiments as trace amounts of UBAI were found to be present in most of the samples. This may have been as a result of seeding from the more stable UBAI.

The order of addition of the starting materials into the crystallisation vessel was studied to investigate the effect of localised mixing conditions upon UBA polymorph selectivity in batch cooling crystallisation. It was demonstrated that by adding urea into a pre-prepared solution of BA it was possible to produce only UBAI in a reproducible way. The effect of component addition on the resulting solid product has been investigated further in the continuous MSMPR set up.

The *in-situ* PAT used in these initial UBA cooling crystallisation experiments within the STR confirmed the presence of the various UBA solid forms, but their full interpretation was hampered by later findings that these measurements suffered from the effects of fouling on the Raman probe used; the full analysis of solid forms presented here (including selectivity of solid form production) was therefore based on subsequent off-line PXRD experiments. Further investigation is required to overcome fouling on the probes and to understand if it is possible to monitor polymorphic transitions in this system (or more widely) using *in-situ* Raman spectroscopy.

The results from the work carried out in the MSMPR system at Loughborough University using peristaltic pump transfer provide evidence that the proposed PMSMPR (periodic) cascade system, with a suitably designed dissolution stage, can provide a platform for the production of the targeted polymorph (UBAI) of the model UBA co-crystal system. A range of MSMPR experiments explored the effects of various parameters on the polymorphic outcome of UBA crystallisation. The parameters investigated included

- variations in temperature profile across the MSMPR stages;
- seeding, both with UBAI and UBAIII seeds;
- periodic *vs.* continuous operation in the MSMPR;
- combined *vs.* separate urea and BA feed sources;
- the rate of addition of urea to BA when separate feed sources are employed.

Through unseeded continuous operation of MSMPR using separate urea and BA feed sources it was found to be possible to isolate UBAI as targeted. However, there were significant issues with blockages in the transfer lines due to the lower flow rates that were required to achieve this selectivity. The same conditions were subsequently investigated using periodic transfer, which also resulted in strong selectivity for UBAI (although traces of UBAIII were observed using Raman spectroscopy but not PXRD). This helped to overcome blockage of the transfer lines and as a result periodic operation was adopted for all subsequent experiments. When a combined urea and BA feed source was used instead of the separate feed approach, mixtures of UBAI and the unwanted UBAIII were produced rather than UBAI selectively. The order and rate of addition of urea to BA may influence the polymorph of UBA produced as it may influence the initial mixing dynamics, the localised saturation levels and ratio of urea and BA in the nucleator vessel directly before nucleation occurs.

Experiments were also carried out using seed crystals of UBAI and of UBAIII. These experiments were successful using UBAI seed, selectively producing UBAI product crystals. However when UBAIII seeds were used UBAIII selectivity was not achieved; this approach again resulted in a mixture of UBAI and UBAIII rather than the targeted UBAIII polymorph.

The successful isolation of pure UBAI during several of the MSMPR experiments at Loughborough using peristaltic pump transfer experiments, which in addition showed a significant reduction in product variability compared to batch operation (as discussed in sections 4.4 and 5.1), has highlighted the viability of MSMPR as a route to selective controlled continuous multi-component crystallisation. In particular the seeded experiments using periodic operation, whereby continuous operation is periodically interrupted by controlled hold periods, afforded the most control. This is most likely as a result of increased residence times for crystal growth which have helped to improve the product quality attributes and the overall yield. The periodic operation allowed the flow rate though the transfer lines to be increased and this proved particularly useful in alleviating blockage of the transfer lines which was observed in the more conventional continuous MSMPR experiments.

Less time was able to be spent at AstraZeneca optimising the vacuum transfer MSMPR system for UBA production, but in the experiments that were carried out, mixtures of UBAI and UBAIII were always obtained; it was not possible to isolate UBAII. However, this early operation of this device with a multi-component, polymorphic system shows it to have significant promise. One significant problem with operating the vacuum transfer method in continuous mode is that there is constantly a flow of air drawn over the system which causes evaporation and hence affects the level of supersaturation maintained in the crystallising solution, making it more difficult to follow the desired desupersaturation profile as the crystallisation proceeds. In addition the level of the transfer tubes had a significant impact upon the ratio of solids to solvent in the suspension transferred between vessels. Periodic operation was explored in several experiments in this MSMPR set-up and helped to improve the yield of solids transferred. However, in this case the periodic operation of vacuum transfer was controlled by hand which is not ideal for a continuous process. Further investigations are planned within AstraZeneca for this MSMPR configuration using nitrogen to pressurise the system to drive the transfer of suspension between vessels, with the aim of overcoming the issues with solvent evaporation. In addition, exploration into automated cessation of the gas flow to enable the system to be operated in the periodic nature achieved with peristaltic pump transfer at Loughborough will be undertaken in the AstraZeneca system by future CMAC placement students.

6 Flow Crystallisation of UBA

In recent years it has proved popular to scale chemical synthesis down to the micro-scale with numerous continuous reaction studies in microreactor devices (ID < 1000 μm) using either tubular or micro-well plate designs[138-141]. The key driver is process intensification[142] owing to an increased surface to volume ratio delivering better heat and mass transfer and highly controlled mixing conditions.

Microreactors have more commonly been used for chemical reaction processes rather than crystallisation due to size constraints introducing difficulties when processing solids. This has often been deemed the limiting factor for adopting continuous crystallisation using microreactor technologies although it will only cause problems if the crystals are larger than, or form agglomerates larger than, the dimensions of the tubes [138]. With this in mind several studies have shown that it is possible to create nanocrystalline materials using microreactors [143-145] and of late there has been a switch to mesoreactor crystallisation (ID > 1000 μm). Jiang *et al.* investigated crystallisation of the amino acid L-asparagine in its monohydrated form using a tubular mesocrystalliser with an ID of 2000 – 3100 μm[146] under air-liquid segmentation. Using a biphasic flow systems it is possible to create several different flow patterns including segmented flow also referred to slug flow or Taylor-flow.

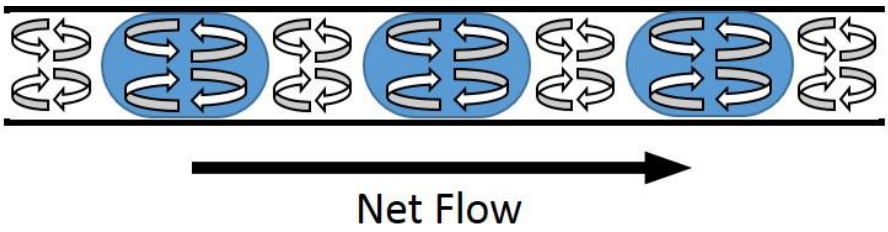

Figure 6.1 Segmented flow with internal vortex circulation as observed in segmented flow.

Due to differences in the viscosity and surface tension of each phase and the non-slip boundary between the solution and the carrier medium (either air or liquid), is created (Figure 6.1) which provides good mixing conditions within each slug and helps to prevent back-mixing in the crystalliser[142]. Overall, this ensures that each slug experiences the same crystallisation conditions, homogenising the crystallisation process.

6.1 KRAIC Tubular Flow Crystalliser

The kinetically regulated automated input crystalliser (KRAIC) (Figure 6.2) is a small scale tubular flow crystalliser designed by Dr Karen Robertson and developed within the Wilson group at the University of Bath. It comprises one or more feed vessels (round bottomed flask, 3 L), temperature controlled using a DrySyn® holder(s) (Asynt) and hotplate with thermocouple and temperature feedback control. The feed vessel(s) feed into three coils of fluorinated ethylene propylene (FEP) tubing which are connected in series. The solution enters at the bottom of each coil and leaves from the top, with the inlet of the subsequent coil positioned higher than the outlet from the previous coil, in order to minimise disruption to established fluid dynamics.

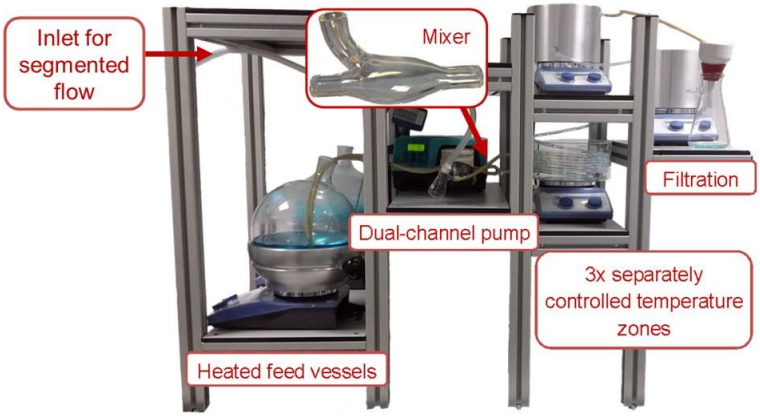

Figure 6.2 Initial set-up of KRAIC tubular flow crystalliser.

Each of the three coils are housed within three separate cylindrical DrySyn® containers, each placed on a hotplate which affords individual temperature control to each coil. To aid heat transfer and facilitate efficient temperature control the containers are filled with graphite powder or sand which packs around the FEP coils. During development experiments a glass container was used to house the first coil to allow observations on segmentation and crystal formation to be made easily.

Solution is pumped through the crystalliser using a dual channel head on a Watson Marlow 343U peristaltic pump fitted with 4.8 mm ID marprene tubing. Using a glass mixer piece (Figure 6.3), the flow from the feed vessel(s) is segmented using either a gas or liquid carrier medium to form discrete segments of crystallisation solution, referred to as slugs.

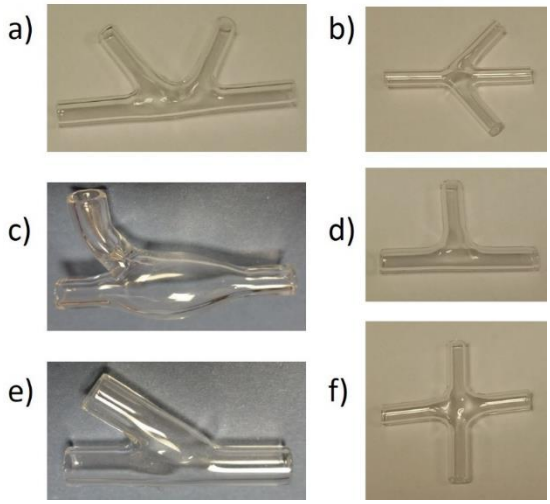

Figure 6.3 Photos of custom designed glass mixer pieces for KRAIC tubular crystalliser. a) K-piece, b) acute angled cross piece, c) impinging mixer piece, d) T-piece, e) Y-piece and f) cross piece.

When using liquid-liquid segmentation in crystallisation the wetting properties of the carrier fluid and solution must be considered, ensuring that the carrier fluid has higher surface wetting than the solution allowing the carrier fluid to coat the walls of the tube around the slug of solution. This helps to ensure that the crystallisation solution does not interact with the tube walls, reducing sedimentation and encrustation.

It is possible to combine and segment two or more feeds using one of several glass mixer pieces (Figure 6.2). This is particularly useful in the case of multi-component crystallisation. Alternatively, as part of the re-configurability of the KRAIC platform, it is possible to fit two different mixer pieces in series. Although not investigated here, this may, for example, allow two flows to be first mixed, then to subsequently segment the resultant flow (Figure 6.30).

One of the key difficulties faced in bridging the gap between small scale multi-component materials discovery and continuous crystallisation is the scale of the continuous crystallisation platforms available; for example, for the COBC experiments described later in section 6.2, the DN15 crystalliser operates at 50 mL min^{-1} and above. However, it is often not feasible to obtain such large quantities of a target material, especially when in the early stages of API development. The small scale mixing and the tubular nature of the KRAIC lends itself to the implementation of smaller scale continuous crystallisation. With a modular design it is possible to add more temperature points to access different temperature regimes and it is also easy to shorten or extend the residence time at each of the temperature points simply by adjusting the tube length.

6.1.1 Aim

The KRAIC is a custom designed crystalliser that is still in the development stages. This research aims to trial if this new apparatus is suitable for small-scale multi-component continuous crystallisation. There are two main aims of this investigation. First, to determine if co-crystallisation of UBA can be produced in the KRAIC, and if there is any influence or selectivity for the polymorphic form of UBA isolated. Secondly, the experiments carried out were among the earliest carried out on the KRAIC, and were expected to highlight operational difficulties and allow solutions to be proposed or developed to enhance the operation of this new crystallisation platform.

6.1.2 Materials

Urea (98% bio-reagent grade) was purchased from Sigma Life Science and BA (98% reagent grade) was purchased from Sigma Aldrich. All reagents were used without further purification. Laboratory reagent grade methanol purchased from Sigma Aldrich was used for all KRAIC experiments.

Several different configurations of the KRAIC were used to investigate small scale continuous crystallisation of UBA with an aim to identify the polymorphic form of UBA produced. A summary of experimental conditions are detailed in Table 6.1 below which are expanded on in the subsequent sections 6.1.3 to 6.1.6.

Table 6.1 Experimental conditions of UBA continuous crystallisation in the KRAIC.

Expt.	Temperature (°C)		Mixer Type	Segmentation media	Order of Addition	Tubing ID of coils (mm)	Net flow rate ($mLmin^{-1}$)
	sol. A	sol. B					
K1	23	55	impinging Jet	N/A	N/A	4.8	17.9
K2	23	55	impinging Jet	N/A	N/A	4.8	17.9
K3	55	N/A	Y	air	N/A	3.2	18.4
K4	55	55	K	air and PFPE	config. a (air then PFPE)	3.2	25.8
K5	55	55	K	air and PFPE	config. b (PFPE then air)	3.2	25.8

6.1.3 Non-segmented Dual Feed

In experiment K1 two solutions of UBA were prepared using a 2:1 molar ratio (urea:BA), the first solution was prepared using urea and BA concentrations of 0.009 g/g $_{MeOH}$ and 0.010 g/g $_{MeOH}$, respectively and held at 23 °C (sol. A). The second solution was prepared using urea and BA concentrations of 0.016 g/g $_{MeOH}$ and 0.018 g/g $_{MeOH}$, respectively and held at 55 °C (sol. B). Sol. A was introduced to the hot sol. B using the impinging mixer piece (Figure 6.3 c and Figure 6.4) at a combined flow rate of 17.9 mLmin^{-1} (8.9 mLmin^{-1} for each solution) and the resulting crystalline suspension was pumped along the ambient coils of FEP tubing (4.6 mm ID) to allow the solution to cool naturally over a residence time (RT) of 13.9 minutes. Upon reaching the end of the third coil the suspension was pumped directly to a Buchner funnel where the solids were isolated using vacuum filtration and analysed off-line using PXRD.

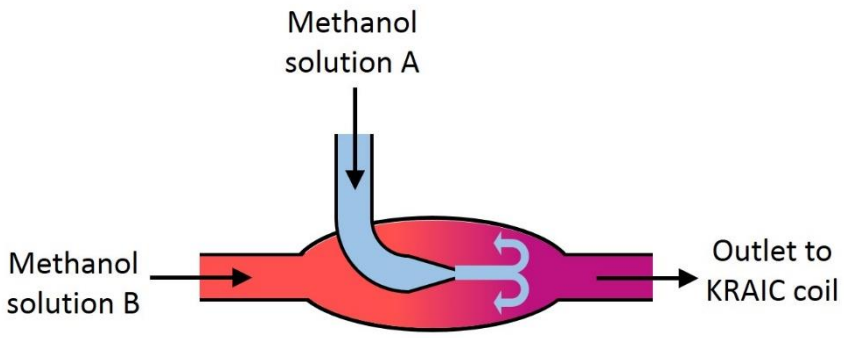

Figure 6.4 Configuration of in-put in non-segmented flow crystallisations of UBA in the KRAIC using impinging jet mixer piece.

After three minutes of operation nucleation was apparent in the first coil of the KRAIC but after ten minutes there were signs of crystals settling in the tubing. The flow rate was increased to 21.6 mLmin^{-1} (reducing RT to 11.5 minutes) in an attempt to mitigate this. The crystals were propagated through coil one and on into coils two and three. After 28 minutes significant sedimentation was observed in coil one (Figure 6.5) even at this higher flow rate. By temporarily increasing the flow rate to 25.5 mLmin^{-1} the crystals were readily moved confirming that this was an issue with sedimentation and not encrustation on the tubing walls. Segmentation is likely to help to keep the crystals suspended due to the improved mixing conditions within the segments (Figure 6.1) rather than laminar flow. The crystallisation ran for a period of around 2.5 hours, equating to 13 residence times.

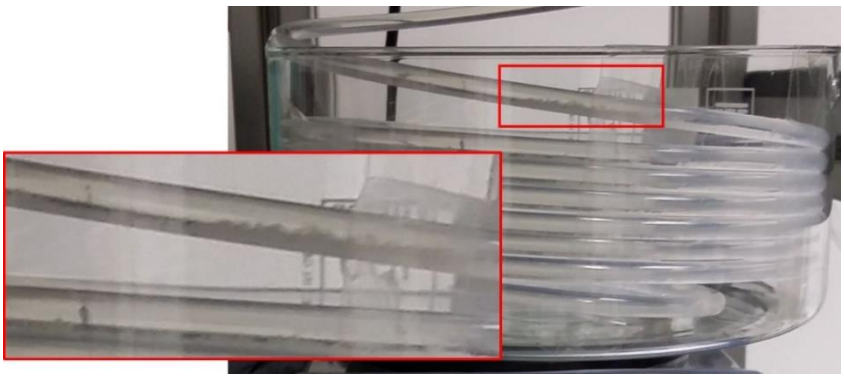

Figure 6.5 Sedimentation of UBA crystals in coil one of the KRAIC (Non-segmented UBA co-crystallisation in methanol at t= 28 minutes)

The experiment was repeated (K2) using the same crystallisation conditions including the increased flow rate (21.6 $mLmin^{-1}$) and as before crystals were visible in coil one after 3 minutes of operation with sedimentation occurring especially in the tubing between coils after 57 minutes (Figure 6.6).

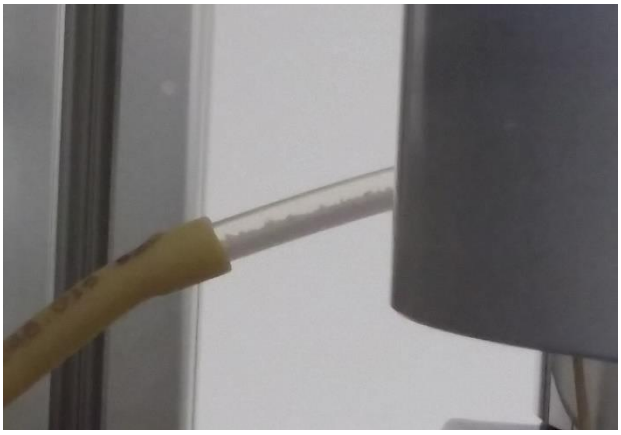

Figure 6.6 Photo of sedimentation occurring at inlet into coil two during experiment K2 at t= 57 minutes

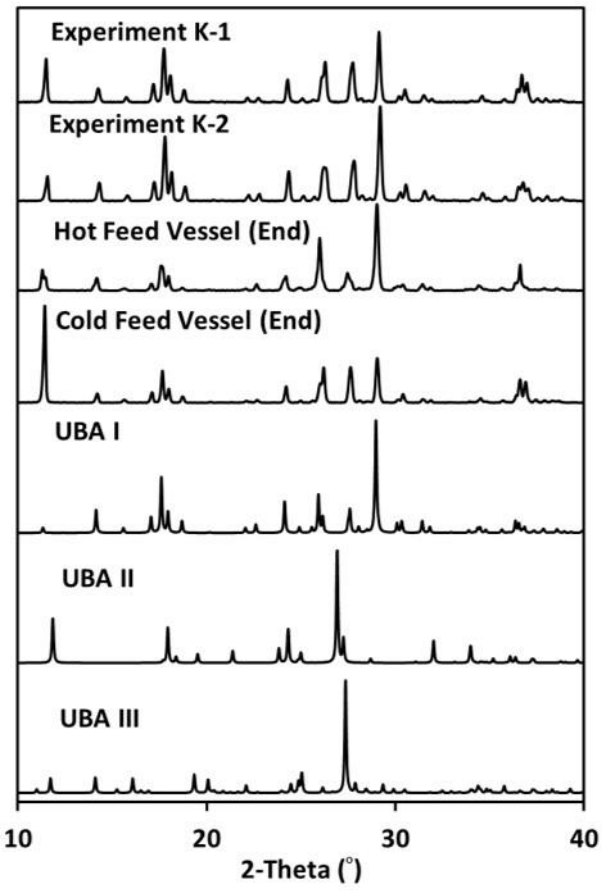

Figure 6.7 PXRD analysis of UBA samples taken from the outlet of the KRAIC in experiments K1 and K2.

Samples were collected at the end of each experiment and PXRD analysis indicted that both non-segmented UBA crystallisation experiments yielded predominantly UBAI which from previous work had been indicated to behave as the kinetic polymorph.

6.1.4 Segmented Flow Using Air

Initially the KRAIC was developed with gas segmentation to aid mixing and impart plug flow. This was trialled using an air cylinder and regulator fed into one entry of the Y-piece glass mixer whilst methanol was fed into the other entry point (Figure 6.8) and was later modified to use a peristaltic pump to input air from the atmosphere (due to irregularity of the air feed from the cylinder).

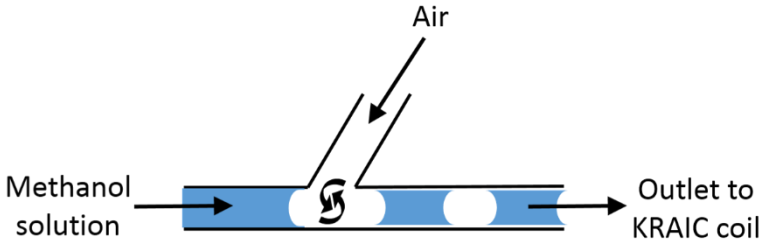

Figure 6.8 Configuration of Y-mixer piece used in experiments involving air segmentation of methanol

The methanol was dyed with methyl orange indicator to aid visualisation of the segments. Air segmentation of methanol gave uniform segmentation with sufficient surface tension and wetting properties from the methanol to prevent Ostwald ripening of the slugs (Figure 6.9).

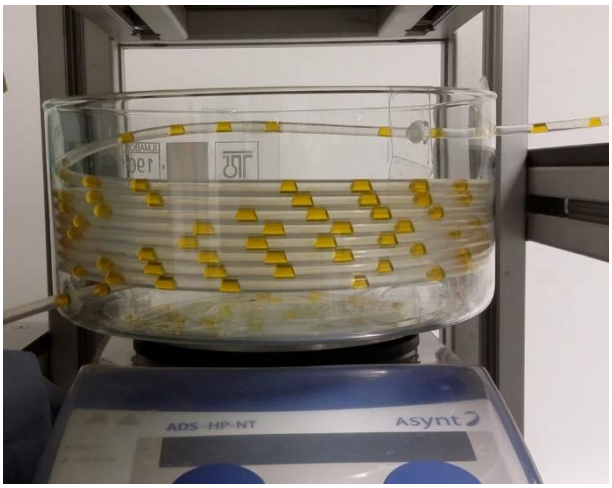

Figure 6.9 Segmentation of methanol (stained with methyl orange indicator) using air.

UBA crystallisation was also tested from methanol using air segmentation (experiment K3). A 2:1 UBA solution was prepared at 55 °C (Urea: 0.014 g/g $_{MeOH}$ and BA: 0.015 g/g $_{MeOH}$) and held at 50 °C prior to transfer to the crystalliser. 4.6 mm ID FEP tubing was used throughout the crystalliser both in solution transfer and in the coil sections. The hot UBA solution and air entered the Y-piece mixer at a flow rate of 8.9 $mLmin^{-1}$ and 9.5 $mLmin^{-1}$, respectively (in the same configuration as before, Figure 6.8). The hot segmented solution passed through the coils at a net flow rate of 18.4 $mLmin^{-1}$, passively cooling under ambient conditions over a mean RT of 13.6 minutes.

Crystallisation occurred in the first coil after 6 minutes and it was possible to observe visually tumbling of the UBA crystals within each slug, highlighting the vortex mixing. However, there were significant issues with encrustation both in the mixer piece and along the first part of coil one. The crystallisation had to be stopped after about 20 minutes due to blockage of the mixer piece due to fouling. The suspension was drained from the crystalliser and the solids were isolated using vacuum filtration and analysed using PXRD.

During this experiment and experiments carried out on other materials in the KRAIC, it became clear that the use of air segmentation causes significant encrustation and fouling problems. This is due to the fact that when the air passes through the mixer piece and tubing it causes evaporation of residual solution on the walls leaving behind crystalline material which provides prime sites for secondary nucleation. These deposits build up over time and eventually result in blockage of the crystalliser. Investigation into air segmented UBA crystallisation was thus halted and alternative segmentation media were investigated.

6.1.5 *Liquid-liquid Segmented Flow Using Perfluoropolyether (PFPE)*

Galden® SV fluid (SV70 b.p. 70 °C) is a low molecular weight perfluoropolyether (PFPE) fluid. It is immiscible with a large range of solvents, highly chemically inert and has good surface wetting with FEP which makes it a good candidate as a carrier fluid for use in the KRAIC (fitted with FEP tubing). It helps to overcome the fouling issues that occur when using air segmentation in readily precipitating systems such as crystallisation processes. Previous studies carried out in unpublished work by Robertson *et al*[*]. showed that PFPE had very good segmentation capabilities when used in aqueous systems behaving as illustrated in Figure 6.10a.

With segmentation established in aqueous systems, initial studies were therefore carried out to test the segmentation capabilities of PFPE on methanol solutions, since methanol is the solvent of choice for the proposed UBA continuous crystallisation experiments. A few milligrams of methylene blue dye were dissolved in 1 L methanol to create a coloured solution to allow the segmented methanol slugs to be distinguished from the segmentation fluid and allow insight to be gained about their size and uniformity.

The KRAIC was fitted with the Y-piece mixer (Figure 6.3 e) with the methanol inlet in-line with the outlet and the segmenting PFPE fluid entering against the net methanol flow to induce the best mixing conditions to generate segmentation (Figure 6.10 b).

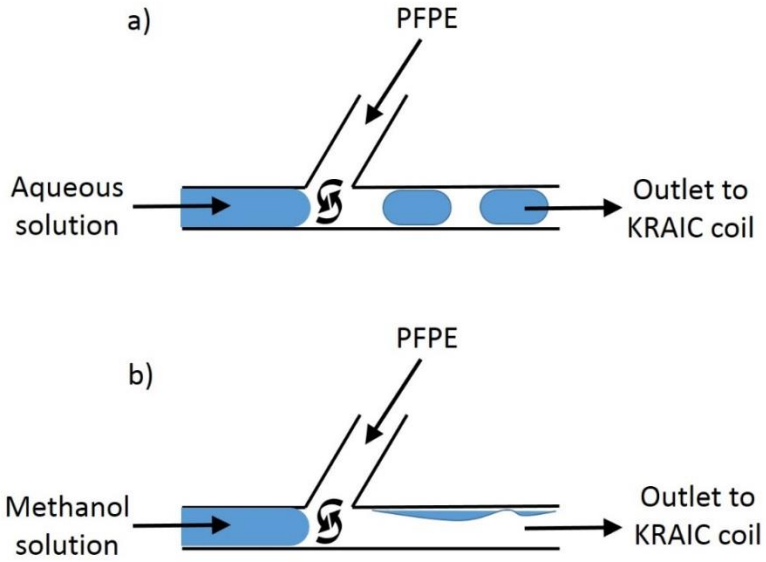

Figure 6.10 Schematic of configuration of Y-mixer piece used in the investigation into a) water segmentation with PFPE and b) methanol segmentation with PFPE.

[*] Work referenced here is currently in preparation for publication by other members of the Wilson group.

Experiments to test the segmentation of methanol using PFPE showed that the distribution of the segments was not uniform (Figure 6.11), in contrast to the uniform slugs observed during air segmentation of methanol (Figure 6.9) and with PFPE segmentation of water. Within the Y-piece mixer the methanol layered over the PFPE as a result of the lower surface tension of methanol which led to segments were of a variety of sizes. The irregularity was exacerbated through Ostwald ripening of the larger segments causing the formation of very large slugs in which there is poor vortex mixing (Figure 6.11). Merging of methanol slugs was particularly significant when moving between each of the coils due to the additional gravitational influence and resulted in methanol exiting the crystalliser preferentially over the PFPE. These experiments were repeated using IPA and ethanol solvent systems which resulted in the same outcome again due to low surface tension.

Figure 6.11 Photos of irregular segmentation of methanol (coloured with methylene blue) using PFPE as carrier fluid. The red ring highlights a large slug created by Ostwald ripening.

The decision was thus taken to discontinue further investigations using PFPE segmentation alone for methanol feed solutions, as the non-uniformity of the segments would have a significant effect on the crystallisation environment leading to irregular crystals. In order to improve this segmentation a tri-segmented approach was investigated.

6.1.6 Tri-segmented Flow Using Dual Segmentation Media: Air and PFPE

In order to regulate the non-uniform segments and layering of methanol on PFPE observed previously using solely PFPE liquid-liquid segmentation, a combination of air and PFPE segmentation was used in a tri-segmented flow set up using a K-piece mixer (Figure 6.3a). The aim of this experiment was to combine the segmentation capabilities of air with the wetting properties of PFPE; it was hoped that the former would produce uniform segments while the latter would coat the walls of the crystalliser, helping prevent fouling and reduce the risk of secondary nucleation on the walls as the segments travel along the crystalliser.

Two different configurations were investigated (experiments K4 and K5) to see whether the direction of flow and the order of segmentation with air and PFPE would (i) result in the desired improved segmented flow and (ii) have an effect upon the polymorphic outcome of UBA crystallisation.

(Figure 6.12). As for previous UBA experiments in the KRAIC, urea and BA were dissolved in methanol in a 2:1 ratio (Urea: 0.014 g/g $_{MeOH}$ and BA: 0.015 g/g $_{MeOH}$) to form a UBA feed solution which was held at 55 °C in feed vessel 1 (FV1) prior to the start of the experiment. Meanwhile PFPE was heated to 55 °C in feed vessel 2 (FV2). The UBA methanol solution and PFPE were transferred to the mixer piece using a dual head peristaltic pump (with a four–roller head) with tubing of 4.6 mm ID and 3.2 mm ID, respectively. Air flow was added using a separate peristaltic pump (with a two–roller head) fitted with 10 mm ID tubing. The UBA methanol solution entered at the straight (10.8 $mLmin^{-1}$) followed by air (9.4 $mLmin^{-1}$), which was aligned with the direction of UBA methanol flow and then the warm PFPE was introduced (5.5 $mLmin^{-1}$), directed against the flow of methanol and air (Configuration a, Figure 6.12 a). A 3.2 mm ID FEP tube was used for the length of the crystalliser instead of 4.8 mm ID tubing as used for previous experiments as this was shown to improve the liquid-liquid segmentation in other similar systems such as PFPE with acetonitrile. The net flow rate was 25.8 $mLmin^{-1}$ resulting in a 4.7 min RT. This experiment was then repeated with the order of air and PFPE addition reversed (Configuration b, Figure 6.12 b), while all other conditions were kept constant.

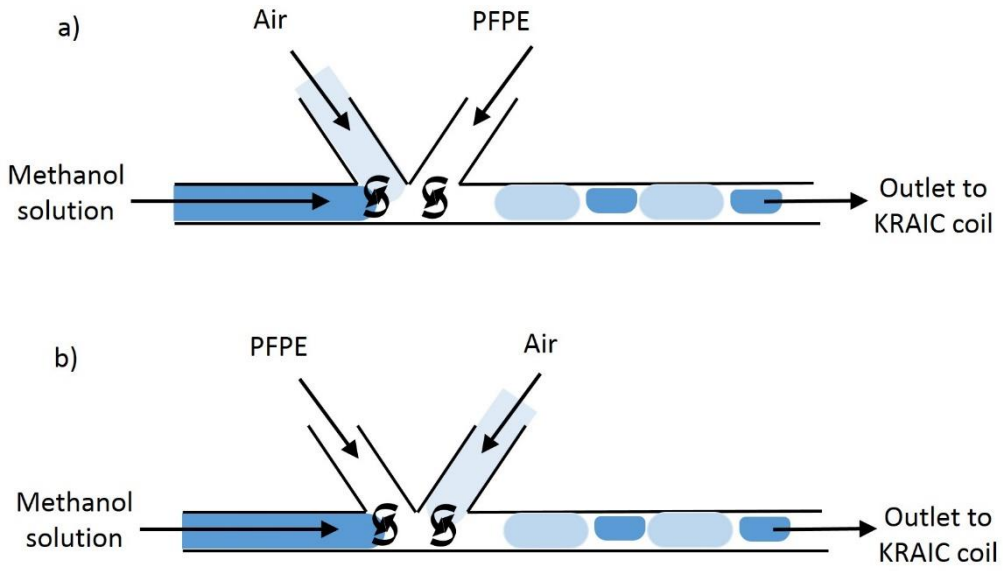

Figure 6.12 Schematic of configuration of K-mixer piece used in the investigation into segmentation of methanol with air and PFPE in two different configurations; Configuration a) air then PFPE and Configuration b) PFPE then air.

As the peristaltic pump used for air addition was fitted with a head with two pinch points large slugs of air were present periodically in the segmented flow (as shown in Figure 6.13); this could be overcome in future with either a head with more pinch points or using a gear pump.

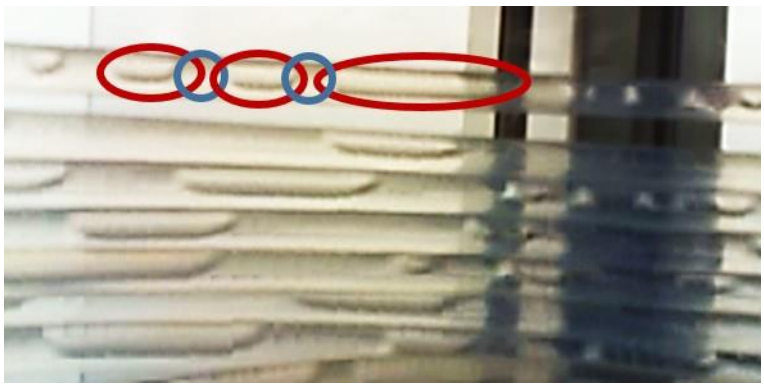

Figure 6.13 Still from a video of coil one in segmentation of UBA in methanol with air and PFPE using a K-mixer in configuration a (Experiment K4) Sections of methanol layered on PFPE are circled in blue and air segments are circled in red.

Initially there were problems encountered with back-mixing of the slugs up into the air and PFPE inlets which were alleviated by ensuring that the methanol inlet and outlet of the K-piece were horizontally level, after this adjustment the slugs appeared more regulated. Layering of methanol and PFPE were apparent in the mixer piece (Figure 6.14) and some merging of methanol segments was apparent when moving between coils, against gravity. These issues considered, it was still a significant improvement in comparison to the segmentation using air-segmentation or PFPE-segmentation alone.

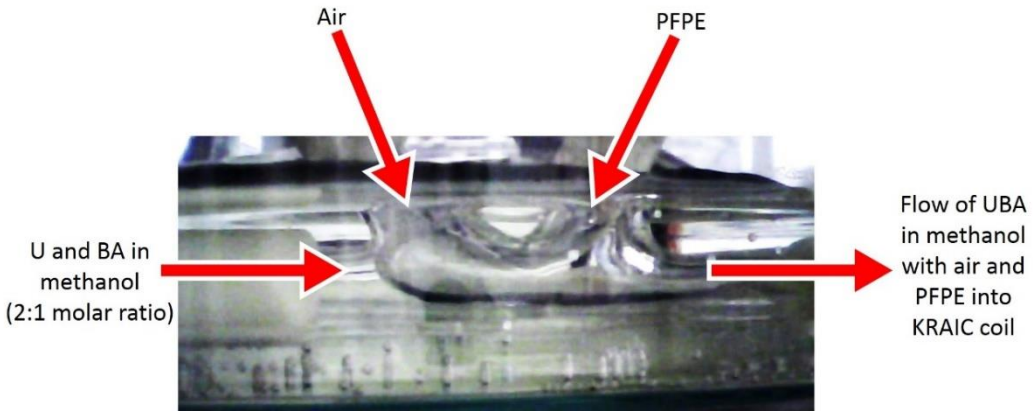

Figure 6.14 Still from a video of K-mixer in UBA tri-segmented flow experiment showing layering of methanol and PFPE in experiment K4 which leads to poor segmentation.

Crystals were first observed in coil one after 7.5 minutes and at 10.9 minutes it was possible to detect crystals exiting coil three of the crystalliser. Encrustation at the tip of the outlet of coil three was apparent after 10 minutes due to solvent evaporation. After 18 minutes fouling was present at the PFPE inlet into the K-piece. The filter paper was changed at 28 minutes (RT 1 – RT 6) and again at 46.5 minutes (RT 7 – RT 10). At 34 minutes the end of the crystalliser tube became blocked due to the continued encrustation, but the solids were easily removed with a spatula.

40 minutes into operation encrustation was observed inside the K-mixer, upon further investigation it was noted that the water bath had dropped from 50 °C to 30 °C. Attempts were made to clear the blockage by increasing the temperature of the water bath and the PFPE fluid to 55 °C, however solids continues to build up within the mixer piece (Figure 6.15).

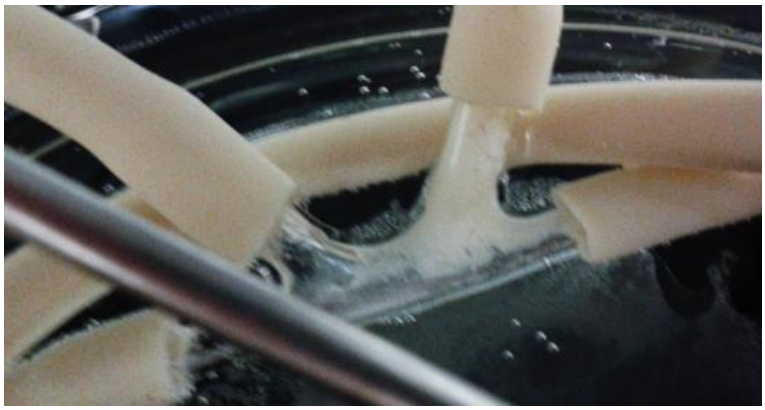

Figure 6.15 Photo of solids build-up within the K-mixer during experiment K4 after 60 minutes of operation

The samples of product from the tri-segmented experiments K4 and K5 were analysed using PXRD (Figure 6.16 and Figure 6.17). This showed that throughout both experiments using dual segmented flow a mixture of UBAI and UBAIII was produced and there is no evidence of the elusive UBAII in the samples.

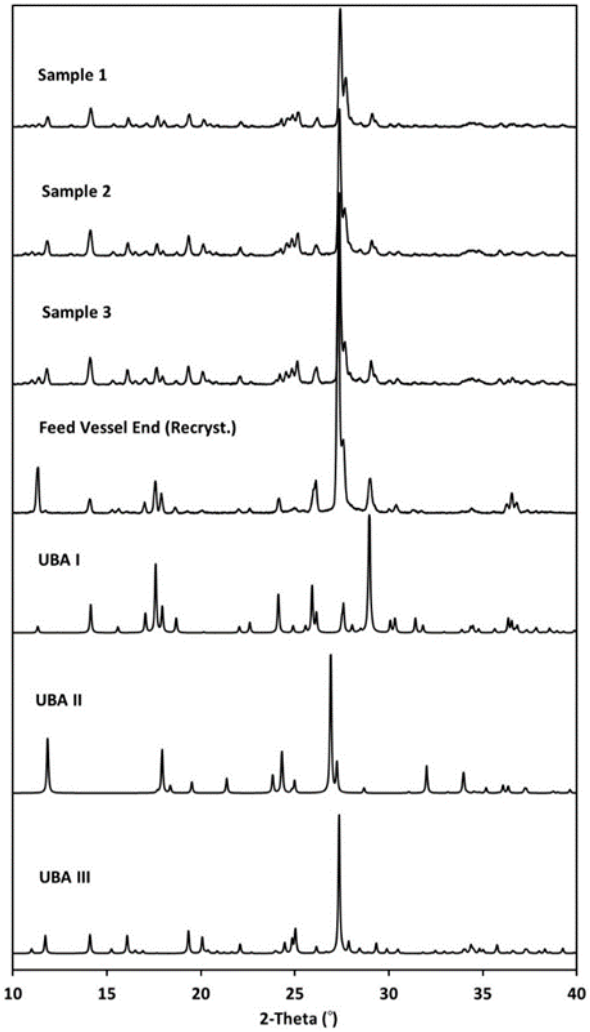

Figure 6.16 PXRD of samples from experiment K4 using tri-segmented flow with air then PFPE (configuration a)

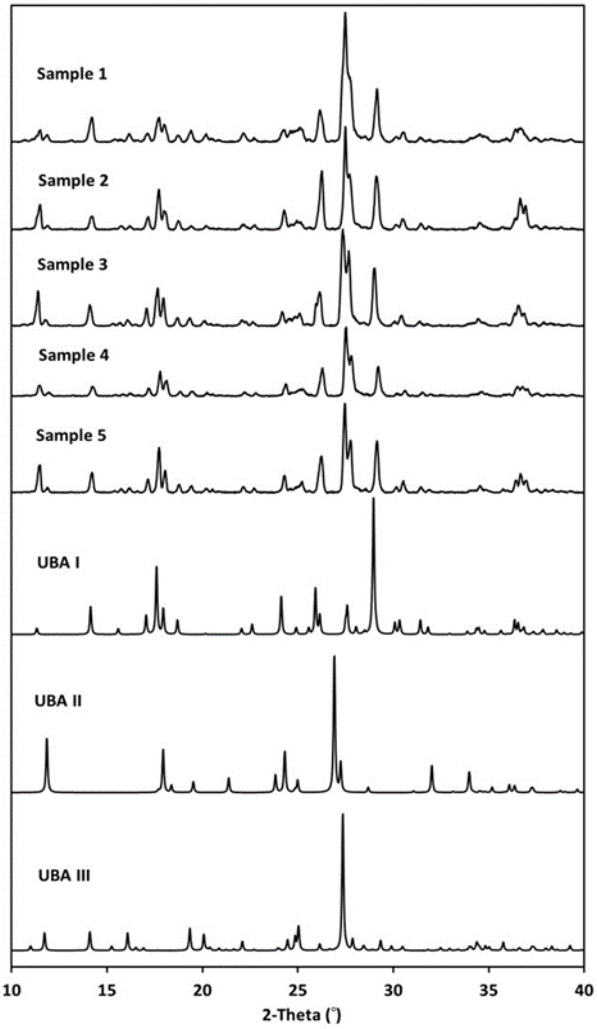

Figure 6.17 PXRD of samples from experiment K5 using tri-segmented flow with air then PFPE (configuration b)

6.1.7 Crystalliser Developments and Modifications

As UBA was one of the first systems crystallised using the custom designed KRAIC the finer details of the platform and its operation were still under development during these experiments. Several modifications were made to the KRAIC as a result of issues encountered during crystallisation of UBA and other systems.

One of the key issues encountered was fouling within the glass mixer piece as described above. Initially the mixer piece was placed upon a hot plate which was subsequently upgraded to a heated water bath (Figure 6.19 a) comprising a glass petri dish heated by a hot plate with the mixer piece clamped into place. It proved difficult to manipulate and fix the tubing in place whilst ensuring that the mixer piece was fully submersed and also level to ensure the best flow into the mixer piece (as

discovered in experiments K4 and K5). A custom designed water bath was produced which allowed the mixer piece to be fixed in place easily whilst fully submersed and level (Figure 6.18 and Figure 6.19 b)

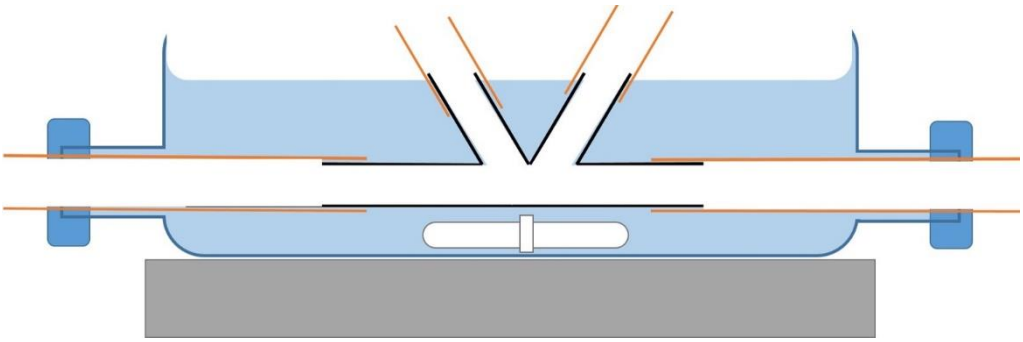

Figure 6.18 Schematic of custom water bath design to enable uniform heating of mixer piece.

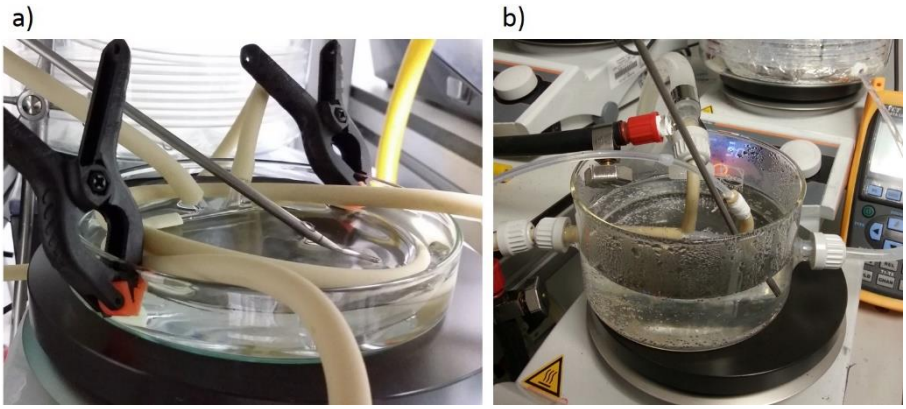

Figure 6.19 The basic water bath (a) was adapted to accommodate better the mixer piece (b).

Whilst fouling in the mixer piece was mitigated by the improved water bath design (Figure 6.18), this caused the fouling issue to be transported to the ambient transfer lines that pump the heated feed solutions between the feed vessels and the mixer piece. Although only traversing a short distance the solution often reduced in temperature causing increased supersaturation in the transfer tubes which often caused issues with fouling and blockages. On several occasions the crystallisation had to be terminated due to complete blockage. A flexible tubing jacket has been developed that attaches to custom made glass adaptors (designed in the Wilson group in collaboration with Asynt) that allow the transfer tubes to pass through the jacket and seal at either end encasing the tube in fluid heated by a bath circulator (Figure 6.20). This has proved particularly successful in mitigating fouling *en route* to the mixer piece.

Figure 6.20 Flexible tubing jacket developed to prevent fouling in transfer lines between the feed vessels and mixer piece.

6.2 Continuous Oscillatory Baffled Crystalliser (COBC)

6.2.1 The COBC and Oscillatory Flow Mixing

The COBC is much larger in scale than the KRAIC, operating at litres per hour rather than millilitres per hour. Described as a cross between an MSMPR crystalliser and a tubular net flow crystalliser, the COBC is a tubular crystalliser divided into numerous small cells by periodically spaced baffles which leave a small orifice between the cells. As liquid under oscillatory flow is passed between cells, interaction with the baffles generates eddy currents and vortex mixing is induced.

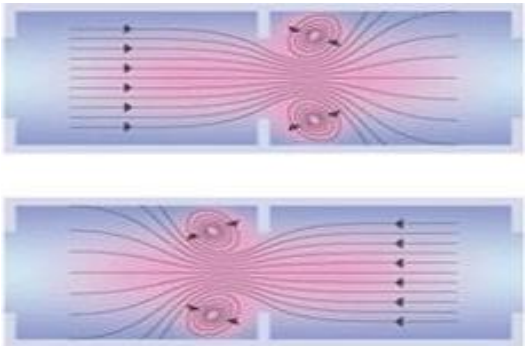

Figure 6.21 Schematic of eddy currents generated in the COBC under oscillatory flow conditions

The oscillatory conditions combined with the net flow from the peristaltic pump aim to achieve plug flow conditions.

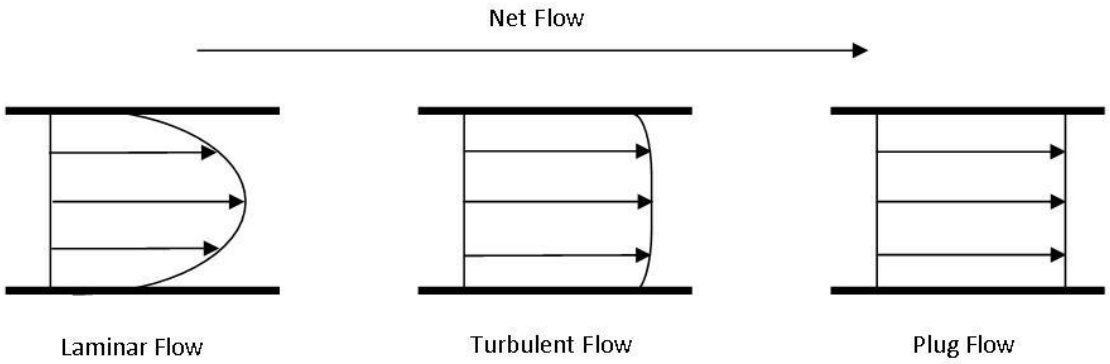

Figure 6.22 Schematic of different types of flow that can be achieved in a tubular crystalliser[147].

The oscillatory mixing within the COBC can be characterised using three dimensionless numbers; the oscillatory Reynolds number (Re_o), the net flow Reynolds number (Re_n) and the Strouhal number (St) which quantify the intensity of oscillation, the oscillatory mixing under flow and the ratio of tube diameter to oscillation amplitude, respectively[148, 149]. The level of plug flow in the system can be quantified by the velocity ratio (Ψ) which is the ratio of Re_o to Re_n. It is desirable to operate at Re_o greater than 300 to ensure a turbulent well mixed flow is achieved [150] and Ψ between 2 and 12 should give suitable plug flow in the COBC [151].

Plug flow, in which the velocity of the fluid within the crystalliser is uniform across the cross section of the tube (Figure 6.22), is desirable, particularly in a continuous system, as it helps to achieve a narrow residence time distribution (RTD), i.e. the time spent by each particle within the crystalliser, is uniform which aids control of the physical attributes of the particles including PSD and polymorphic form.

The geometry of the COBC was designed in order to operate as close to plug flow conditions as possible and is based on the principle that plug flow conditions are preferential for control over crystallisation and particle attributes in a flow system; if this is achieved, the hydrodynamics ensure that the crystallisation conditions experienced by each particle is near to identical. This feature is key to overcoming the issue of batch to batch variation and problems with scale-up in batch industrial crystallisation processes; the motivation for development of the COBC [152].

In the literature there is significant evidence of crystallisation under oscillatory mixing conditions but the majority of these studies are investigated in batch crystallisations. Two key papers document the establishment of continuous crystallisation under oscillatory flow using the COBC; crystallisation of an AstraZeneca API (collaboration with Lawton *et al.*, AstraZeneca)[152] and a multi-component crystallisation of α-lipoic acid with nicotinic acid by Zhao et al[153]. The application of oscillatory flow reactors (OFRs), including the COBC, in continuous crystallisation for the

manufacturing of pharmaceuticals and fine chemicals has also been reviewed recently by McGlone *et al*[154].

The continuous multi-component crystallisation study by Zhao *et al*.[153] involved a crystal engineering investigation with an aim to enhance the thermal stability of α-lipoic acid. Though screening with several co-former candidates three new co-crystal systems were discovered; α-lipoic acid with either nicotinic acid, isonicotinic acid or trans-cinnamide. Of these three multi-component systems the 1:1 α-lipoic acid: nicotinic acid co-crystal was found to be the most thermally stable and chosen as the candidate for transfer to continuous crystallisation. Successful crystallisation of the 1:1 α-lipoic acid: nicotinic acid co-crystal using the COBC was demonstrated under both seeded and non-seeded crystallisation conditions.

Although studies on cooling crystallisation using the COBC have been carried out previously on both multi-component materials and polymorphic materials a polymorphic multi-component system has yet to be investigated. This study on UBA documents the first polymorphic multi-component system crystallised in the COBC and highlights how mixing conditions within the COBC can be used to produce UBAI selectively.

6.2.2 Materials

Urea (98% bio-reagent grade) was purchased from Sigma Life Science and BA (98% reagent grade) from Sigma Aldrich and these reagents were used without additional purification. For all UBA crystallisation experiments in the COBC laboratory reagent grade methanol purchased from Sigma Aldrich was used.

6.2.3 Method

The DN15 COBC at UoB (Figure 6.23 and Figure 6.24) has a total volume of 2.8 L and comprises 20 jacketed glass straights and 10 unjacketed glass bends which total 16 m in length. The tubes have an ID of 15 mm and are divided into cells 27 mm in length by baffles with an orifice diameter of 7.9 mm. Prior to operation the solution flow rate was calibrated to 49 $mLmin^{-1}$ giving a mean residence time (RT) of 57.1 minutes.

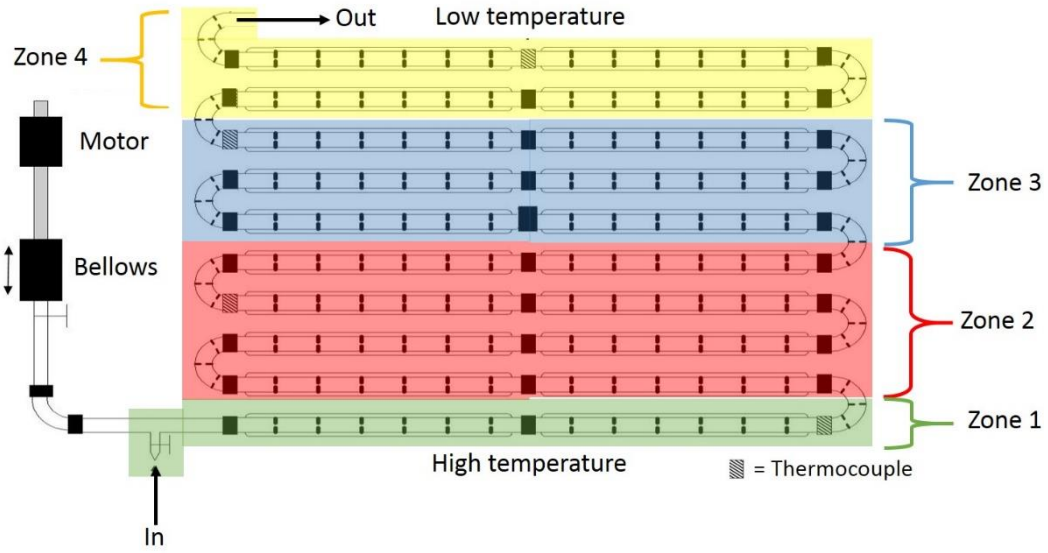

Figure 6.23 Schematic highlighting the four different temperature controlled zones of the DN15 COBC set-up at UoB, for experiments C1 and C2 (each zone is controlled by a separate bath circulator).

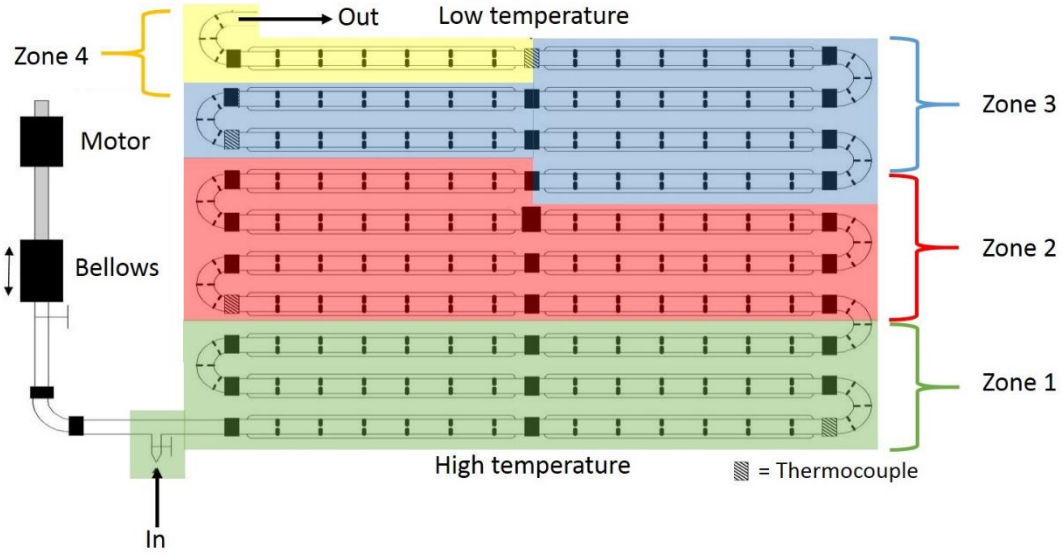

Figure 6.24 Schematic highlighting the four different temperature controlled zones of the DN15 COBC set-up at UoB, for experiment C3 (each zone is controlled by a separate bath circulator).

For each experiment 95.6 g urea and 101.4 g BA were added to 8.5 L methanol in a custom built 9 L jacketed feed vessel with an overhead four-pitched blade PTFE impeller (stirring speed 500 rpm) to form a 2:1 UBA solution. The solution was held at 55 °C until all solids were dissolved and then cooled to 50 °C. The COBC was prepared for operation by priming with the UBA methanol to purge unwanted air bubbles from the system in order to prevent oscillation dampening. The hot UBA solution was pumped from the feed vessel at 49 $mLmin^{-1}$ using a peristaltic pump with marprene tubing of 10 mm ID. The motor was set to oscillate at an amplitude of 30 mm (peak to trough) at a

frequency of 1 Hz. The suspension of crystals produced was directed into a custom vacuum filtration unit (designed in collaboration with Asynt) where the solvent was removed and the crystalline solids isolated. The filter papers were changed at time = RT and 2 RT for experiments C1 and C2 (Figure 6.23) and for experiment C3 (Figure 6.24) at time = RT, 1.5 RT, 2 RT, 2.5 RT and 3 RT.

For all three experiments the COBC was divided into four temperature controlled zones (defined in Figure 6.23 and Figure 6.24 and with temperatures summarised in Table 6.2).

Table 6.2 Experimental conditions of UBA continuous crystallisation in the COBC.

Expt.	Flow Rate ($mLmin^{-1}$)	Oscillation		Temperature (°C)				
		Amp. (mm)	Freq. (Hz)	Feed	Zone 1	Zone 2	Zone 3	Zone 4
C1	49	30	1	55	50	30	17	10
C2	49	30	1	55	50	30	17	10
C3	49	30	1	53	31	27	12	9

The temperature controlled zones were configured in such a way to give the cooling profiles detailed in Table 6.3 (experiments C1 and C2) and Table 6.4 (experiment C3). The aim in experiments C1 and C2 was to use all four heater-chillers to implement a controlled linear cooling profile around 1 $°Cmin^{-1}$ in order to mimic the cooling profile used to obtain UBAI in batch cooling crystallisation experiments.

Table 6.3 Details required to calculate the cooling rate across each temperature zone for experiments C1 and C2

Zone	Length (m)	No. of Straights	No. of Bends	Time in zone (min)	T Initial (°C)	T Final (°C)	Cooling rate ($^{o}Cmin^{-1}$)
1	1.6	2	1	5.71	55	50	0.9
2	6.4	8	4	22.84	50	30	0.9
3	4.8	6	3	17.13	30	17	0.8
4	3.2	4	2	11.42	17	10	0.6

Experiment C3 was configured in preparation for future seeding experiments. Nucleation of UBA at these concentrations was observed in batch processes at around 28 °C. (Section 5.1). Seeds of UBAI would be introduced in zone 2 after rapid cooling to 31 °C during the slow cooled period between 31 and 27 °C. The current COBC set-up at UoB is not configured to introduce a seed suspension. This experiment was carried out as a control to investigate which UBA polymorph would be produced using this profile without seeding.

Table 6.4 Details required to calculate the cooling rate across each temperature zone for experiment C3

Zone	Length (m)	No. of Straights	No. of Bends	Time in zone (min)	T Initial (°C)	T Final (°C)	Cooling rate ($°Cmin^{-1}$)
1	4.6	6	2	16.42	53	31	1.3
2	5.7	7	4	20.34	31	27	0.2
3	4.8	6	3	17.13	27	12	0.9
4	0.9	1	1	3.21	12	9	0.9

6.2.4 Results and Discussion

Experiments C1 and C2

During experiments C1 and C2 crystals were first observed (visually) in straight 11 after 15 and 18 minutes, respectively. Fouling occurred on the walls of the crystalliser after around 35 minutes and continues to build up throughout the length of the crystalliser with some masses of encrusted crystals dislodging from the walls and settling in the bends of the COBC. Experiment C1 ran for 165 minutes (approximately 2.5 residence times) before the feed solution was depleted. In experiment C2 after 150 minutes of operation the crystals had propagated back to inlet and the bellows and the experiment was halted to protect the bellows.

Experiment C3

In experiment C3 crystals could be observed visually in straight nine after just five minutes. This short induction time is due to the fact that the system was purged with UBA methanol solution. Solids started to grow on the walls of straights nine to eleven after 15 minutes. After 20 minutes there was significant fouling in straights seven to eleven. The amplitude and frequency of the oscillation was increased to 35 mm and 2 Hz temporarily in an attempt to dislodge some of the deposited material. Some of the material was removed however a significant coating of crystals was still present. It was possible to observe some crystals in straight two after 25 minutes. These crystals must be present due to back propagation, where material from the deposits on the walls has travelled backwards and seeded the solution inducing nucleation at much higher temperatures and may have been induced through the increased intensity of oscillatory conditions. Due to the vertical configuration of the COBC in all three experiments there was significant sedimentation of crystalline solids present at each of the bends with the most sedimentation occurring in bends four to seven. PXRD analysis of each sample collected every 28.5 minutes (RT/2) over approximately three RTs shows that UBAI is consistently produced throughout the crystallisation process in the COBC (Figure 6.26 samples 1 to 5).

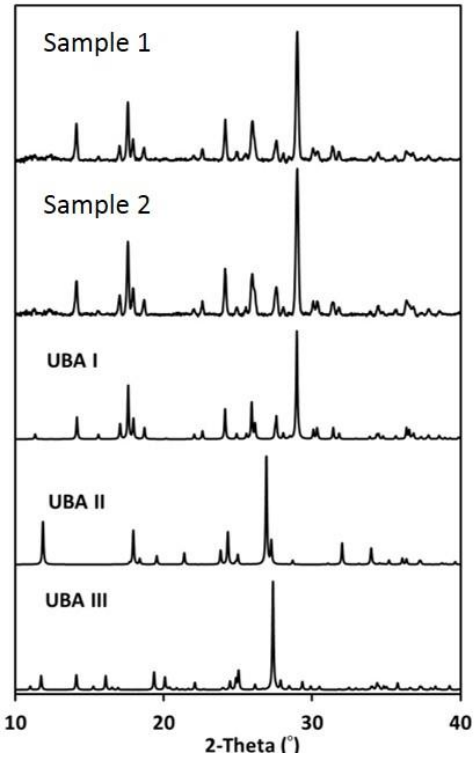

Figure 6.25 PXRD analysis of samples from crystallisation of UBA in COBC experiment C1 (sample 1 t=27 mins, sample 2 t =120 mins)

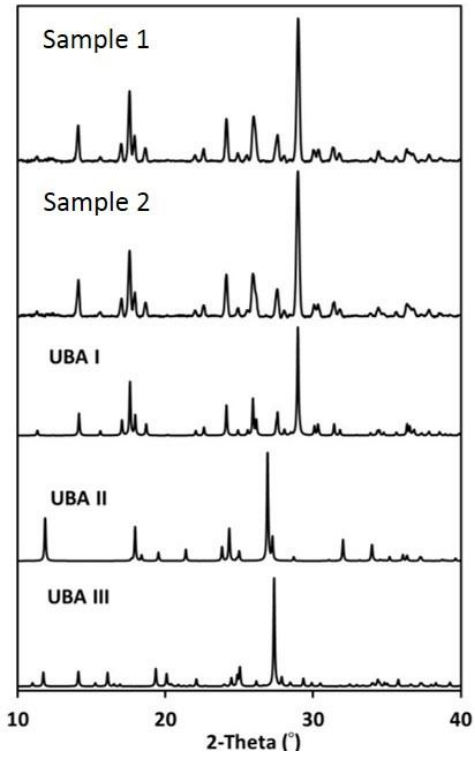

Figure 6.27 PXRD analysis of samples from crystallisation of UBA in COBC experiment C2 (sample 1 t=53 mins, sample 2 t =120 mins)

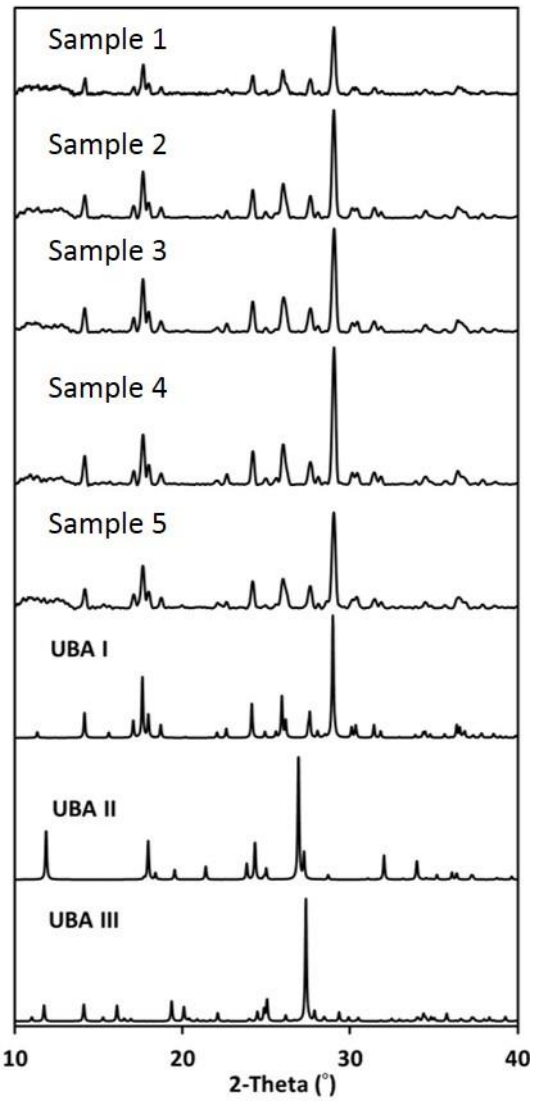

Figure 6.26 PXRD analysis of samples from crystallisation of UBA in COBC experiment C3 (sample 1 t=28.5 mins, sample 2 t =57 mins, sample 3 t= 85.5 mins, sample 4 t= 114 mins and sample 5 t= 169 mins)

The yield of UBA was between 12 and 15%. across all three experiments. This was calculated for the theoretical mass that could be achieved of U and BA in a 1:1 ratio which is the ratio of the UBA co-crystals. This is instead of using the mass of the 2:1 urea: BA ratio that is required in solution to ensure that urea is saturated enough to be available for co-crystallisation.

Using the solubility of UBAI it is possible to calculate the equilibrium concentration of UBAI in the solution when it exits the COBC at a temperature of 10 °C (0.0088 g/mL$_{MeOH}$). If this is taken into consideration then the yield of the crystallisation process is 25%.

PXRD analysis of samples taken from each experiment (Figure 6.25 to Figure 6.27) show that UBA I was produced for experiments C1 to C3 using two different cooling profiles; this is a significant finding, representing the first example of selective production of a single solid form of a polymorphic multi-component molecular systems in a continuous crystallisation platform such as the COBC.

6.3 Facilitating the Future Move to the Small Scale

During the course of the present project, CMAC researchers at the University of Bath (UoB) have been developing and commissioning a range of continuous crystallisation platforms, optimised for the assembly and manufacturing of target molecular materials at relatively small scales. These developments, led by Dr Karen Robertson and in which the author has had significant involvement, have encompassed a range of novel concepts. They have also benefitted from harnessing the best available technology solutions from both the upstream (flow chemistry) and downstream (flow processing) communities. The platforms developed operate on a range of principles, from segmented tubular flow (the KRAIC, described in chapter 6), through small scale cascade stirred tank reactors (cSTRs), to membrane-mediated continuous evaporative approaches. The platforms are being developed and commissioned with a view to deployment on a range of appropriate target materials across the CMAC consortium, forming a part of a flexible approach to providing reconfigurable and fit-for-purpose platforms for continuous crystallisation.

There is understandable focus within CMAC research on the requirement to develop continuous crystallisation processes that scale-up to larger volumes of product. For many applications, however, optimising small scale production of molecules, materials and particles – such as manufacturing of high value products – is an equally valuable challenge, and the work on new crystalliser development described here is addressing this.

6.3.1 Small Scale Cascade of Stirred Tank Reactors (cSTR)

With the focus on optimising crystallisation processes at small scale, a continuous crystalliser has been designed and constructed based on a cascade of small-volume STRs, in collaboration with Cambridge Reactor Design. Individual STR volumes are around 7-10 ml with an internal weir arrangement that harnesses gravity for transport between vessels negating the need for more pumps or a pressurised system. The UoB cSTR offers a fully reconfigurable platform with a flexible number of STRs in series, and full temperature control over each section of the device.

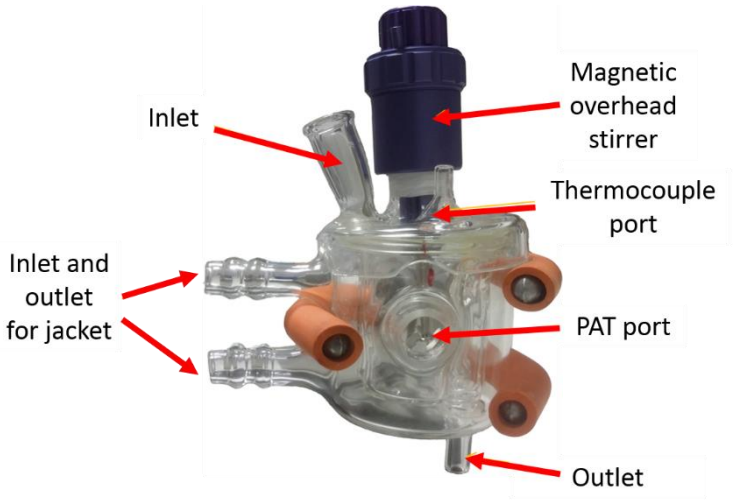

Figure 6.28 Photo of a prototype of a custom STR for the small scale cSTR set-up

6.3.2 Continuous Evaporative Crystalliser

Building upon the most common technique used for multi-component crystallisation the continuous membrane-mediated evaporative crystalliser (CMEC) aims to translate batch evaporative processes into the continuous environment. Designed within the Wilson group at UoB in collaboration with (and constructed by) ChemTrix BV (Netherlands), this crystalliser offers a small scale solution in which solvent evaporation, rather than cooling, is used as the means to induce supersaturation and control nucleation and growth. By passing the sample solution through a pair of spiral paths within the device, and mediating evaporation across a double-sided membrane in two stacked layers within the crystalliser, there is potential to achieve a high level of process control within an extremely compact crystallisation platform. The crystalliser is approximately 14 cm^3 in volume; the flow channels are 3 mm in diameter and 2 m in length, which are arranged to fit inside a compact device with a foot print of 20 cm^2. The continuous evaporative device should find particular use in cases where control of solvent behaviour is critical, including the production of solvates and hydrates, and adds a further capability within the CMAC continuous crystalliser portfolio at UoB.

The UBA system lends itself to use in the CMEC as it has been investigated using methanol solvent which has a low boiling point and as it is a small molecule system there will be good membrane

permeation. The morphology of the UBA co-crystals is block-like and there have been no issues in filtration processes during UBA experiments which indicates that it would allow solution to move freely at the membrane surface. However there have been significant issues with fouling on surfaces when investigating the UBA system and this may prove a key challenge when using UBA in the CMEC.

6.4 Conclusions – Flow Crystallisation of UBA

6.4.1 KRAIC Tubular Crystalliser

Several different crystallisation methods were tested for UBA crystallisation using the KRAIC. It was possible to selectively produce UBAI using the non-segmented flow set-up with dual UBA feed (K1 and K2). However, when a single UBA feed was used in combination with segmented flow (K3-K5) using a range of different carrier media (air, PFPE and air with PFPE) a mixture of UBAI and UBAIII was produced. As with all previous continuous crystallisation of UBA, UBAII was not present in the end product. This difference in polymorphic outcome is most likely due to the different mixing conditions experienced with the non-segmented and segmented flows. The former has laminar flow with poor mixing and a large amount of back-mixing, whereas the latter has gentle mixing under bolus flow and in an ideal system there should be no back-mixing.

In addition to this reasoning, owing to the dual UBA feed of the non-segmented flow set-up (K1 and K2) in comparison with the single feed used in segmented flow (K3-K5) the desupersaturation profiles followed are very different and are likely to have a significant effect upon the polymorphic outcome. Further investigation of crystallisation using a dual UBA feed combined with segmented flow may help to decouple the effect of the desupersaturation profile vs. mixing conditions.

The main issue encountered with fouling in the KRAIC experiments was within the glass mixer piece. This could be as a result of choice of construction material and the difference in the contact with the glass and the fluorinated ethylene propylene (FEP) tubing. It would be useful to test FEP mixers or glass mixers coated in FEP and see if these helped to reduce or prevent fouling in the mixer.

All KRAIC experiments on UBA detailed here were carried out using a peristaltic pump, however subsequent investigations on other materials have used a recently sourced gear pump. This has helped to achieve more uniform segmentation due to the nature of the constriction mode of a gear pump which reduces the amount of pulsation in comparison to a peristaltic pump. The only issue with switching to a gear pump is that the mechanism cannot function with solids present and

therefore it is imperative that the pumps are flushed out with warm solvent once the crystallisation is finished. Future experiments using UBA should be carried out using the new gear pump in order to investigate what effect this may have upon the size variation of segments, especially in the methanol system with air/PFPE segmentation.

A new air/PFPE segmentation configuration that uses a cross piece mixer (Figure 6.3 f) was recently trialled (Robertson *et al.*[*]) for a flow chemistry reaction in acetonitrile solvent, which has similar surface tension and wetting properties to methanol. Highly uniform segmentation was achieved in this experiment. This set-up will be trialled for UBA in methanol with an aim to achieve enhanced and more uniform segmentation (Figure 6.29, Figure 6.30).

This work has focused upon the application of the KRAIC for crystallisation of UBA but further development of the crystalliser is required. Surface tension and zeta potential measurements for the different liquids used could prove useful for future systems as this may lead to the discovery of more suitable carrier fluids for different purposes, taking into account fluid properties such as density and viscosity. In addition, computational fluid dynamics (CFD) simulations are being undertaken in the Bath laboratory (P.-B. Flandrin, *PhD project*). These are modelling a range of flow chemistry and flow crystallisation systems, including the KRAIC and the COBC (below). Modern CFD simulations are increasingly sophisticated and allow both carrier fluid and sample properties to be included as parameters, thus allowing for optimisation of parameters and materials for future developments of crystallisation processes in the KRAIC and other continuous crystallisers deployed in the Bath laboratory.

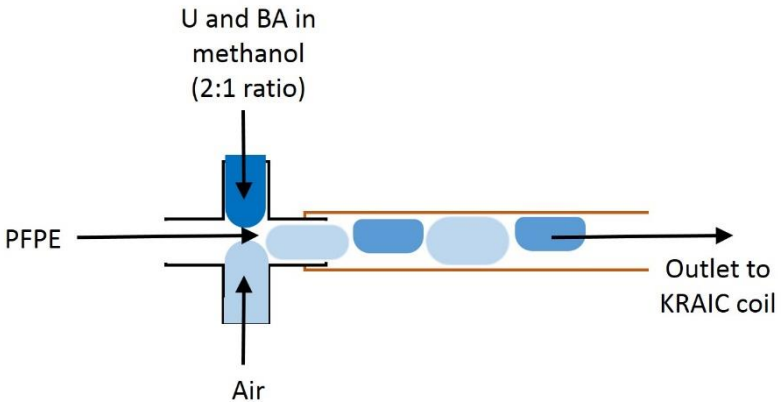

Figure 6.29 Proposed experimental set-up for UBA crystallisation using tri-segmented flow with a cross piece mixer. Note that the cross piece is viewed from a top down perspective.

[*] Work referenced here is currently in preparation for publication by other members of the Wilson group.

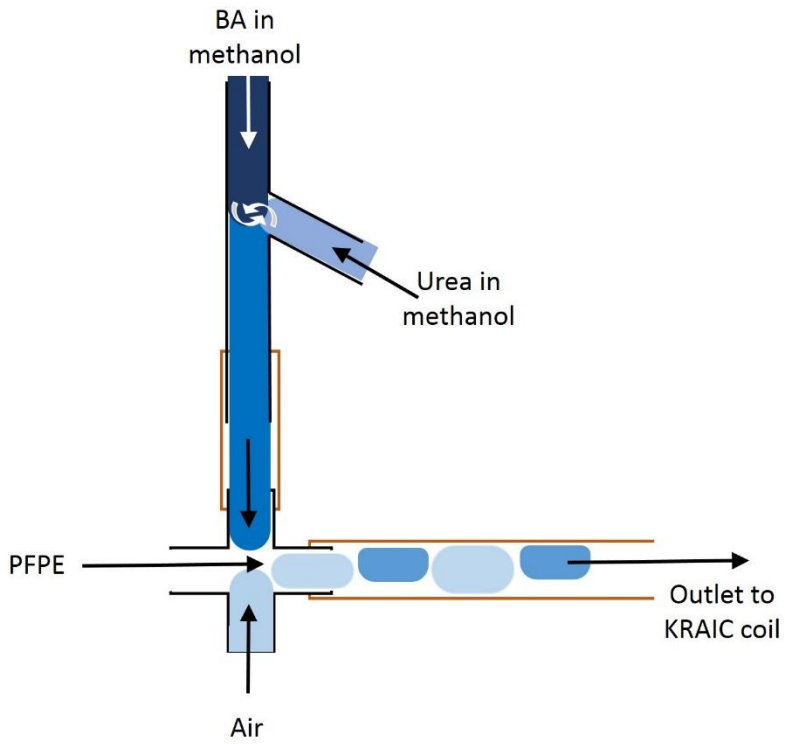

Figure 6.30 Future experiment using separate urea and BA feed through a Y-piece mixer followed by tri-segmented flow with a cross piece mixer. Note that the apparatus is drawn from a top down perspective

6.4.2 Continuous Oscillatory Baffled Crystalliser

The campaign in the COBC represents a breakthrough in establishing continuous crystallisation of multi-component molecular materials with a view to establishing a continuous platform for the production of such materials in a continuous manufacturing context. As has been noted above, the UBA system is a notable challenge for transfer to continuous. Not only is it multi-component, with introducing issues with potentially incompatible solubilities between the molecular components, etc, but it is also polymorphic in both the products (UBAI, UBAII and UBAIII) and in one of the starting constituents (BA, which can also readily form a dihydrate in addition to its polymorphism). The system was deliberately selected to pose these challenges, and it is in this context that the successes of this work can be noted.

The very fact that UBA solids are produced represents one of the first examples of a systematic exploration of continuous crystallisation production of a multi-component molecular system. In order to achieve this, cooling routes to UBA needed to be established and, crucially, transferred into the parameters selected for the continuous COBC platform.

Moreover, it has been possible to control the continuous process in the COBC so as to deliver phase pure UBAI. This is the first example of such a process delivering polymorph selectivity in a multi-component molecular system. Establishing this selectivity is particularly notable given that the thermodynamic stabilities of UBAI and UBAIII are, on all available evidence, very similar. This emphasises the high degree of control of kinetic factors that is possible in a continuous flow reactor such as the COBC. It has, however, proven challenging to obtain either UBAII or UBAIII selectively in the COBC. This is not unexpected for the highly metastable UBAII, but it should be possible to optimise the crystallisation conditions to allow the isolation of UBAIII, and work on this is ongoing.

The UBA crystallisations involved operation of the COBC for three residence times (total run time of 180 minutes), allowing the harvesting of approximately 7 g/hr of UBAI from the continuous process.

The COBC has shown selective crystallisation of UBAI of the target multi-component UBA system and represents a breakthrough in deployment of such a device and offers real potential for its exploitation in the production of multi-component solid forms. The first steps have been taken to deployed the COBC at UoB as a fully continuous crystalliser within this project, although for the process to be fully continuous much longer experimental runs are required which for the capacity of the set-up described here would require a much larger set of feed vessels.

There are also some other issues that must be addressed in further developing its use in tackling the high value target materials typically developed in the multi-component materials area. There are some restrictions upon the efficiency of the mixing within the COBC due to the fact that it uses a single motor positioned at the very beginning of the crystalliser. It is plausible that the mixing efficiency falls off as a result of increasing distance from the motor, in which case (i.e. one with smaller working volume) the mixing should be fairly consistent throughout for a shorter crystalliser, while as the crystalliser increases in length mixing will become poor (due to the dampening effect of the liquid media). As the set-up used in the experiments described here uses 20 COBC straights with a total length of 16 m, the mixing towards the end of the COBC is inconsistent with the mixing at the start of the COBC. This could be addressed by reconfiguring the COBC into a more compact arrangement; this has recently been done in the Bath laboratory, with evidence of the successful crystallisation of both succinic acid (Klapwijk *et al.*[*]) and paracetamol (Agnew *et al.*[*]) from multi-component environments. Shortening the COBC however, reduces the residence time within the crystalliser and the net flow rate needs to be kept high to maintain good mixing conditions therefore

[*] Work referenced here is currently in preparation for publication by other members of the Wilson group.

this may not be a suitable resolution particularly for systems with slow nucleation and growth kinetics.

In both the UBA runs and these subsequent COBC experiments, a second issue has become apparent, which is the large amounts of sample required for operation of the large volume DN15 COBC. These typically require around 250-500 g of material per crystallisation run, which is a large quantity for many candidate materials. Smaller diameter COBCs exist within CMAC, which may be better suited to deployment on many of the likely target materials; certainly in the earlier stages of their development where sample quantity may be limited but it is still vital to assess and develop their capacity for continuous production. Further developments of small scale crystallisers are also ongoing that help address this issue and are discussed below.

This work is has shown that is possible to selectively crystallise UBAI using the COBC with the cooling profiles and mixing conditions detailed above, further investigations are required to systematically vary the temperature profile and mixing conditions to investigate if it is possible to crystallise UBAII and UBAIII as well as UBAI.

The COBC will be modified to place feed inlet after a single heated straight to resolve issues with fouling in the unjacketed tube positioned near the bellows. This modification has been implemented in COBC configurations used within CMAC at the University of Strathclyde and has proved beneficial.

In addition the COBC is to be reconfigured to install a dual feed and seeding port in order to repeat experiment C3 with varying concentrations of seed suspension using UBAI produced *via* mechano-chemical methods (as discussed in section 4.3) and also to investigate separate addition of the urea and BA components as investigated with MSMPR experiments (section 5.2).

It has been noted throughout crystallisation of UBA that it has a tendency to foul on surfaces over long periods of time. Investigations are underway within CMAC to trial the use of different coatings on a range of materials of construction, and the potential use of heat pulses, to prevent/reduce encrustation and the UBA system will be one of the materials trialled.

6.4.3 Sample Analysis

All analysis of materials produced through flow crystallisation were carried out using off-line measurements. As PXRD is the main technique used to identify the presence of each polymorph of the UBA system it would initially be beneficial to install sampling ports throughout the COBC and

the KRAIC so that samples cold be analysed over the length of the crystalliser rather than waiting until the product is eluted from the end of the crystalliser. An aspiration aim would be to implement in-line PXRD analysis using flow through PXRD.

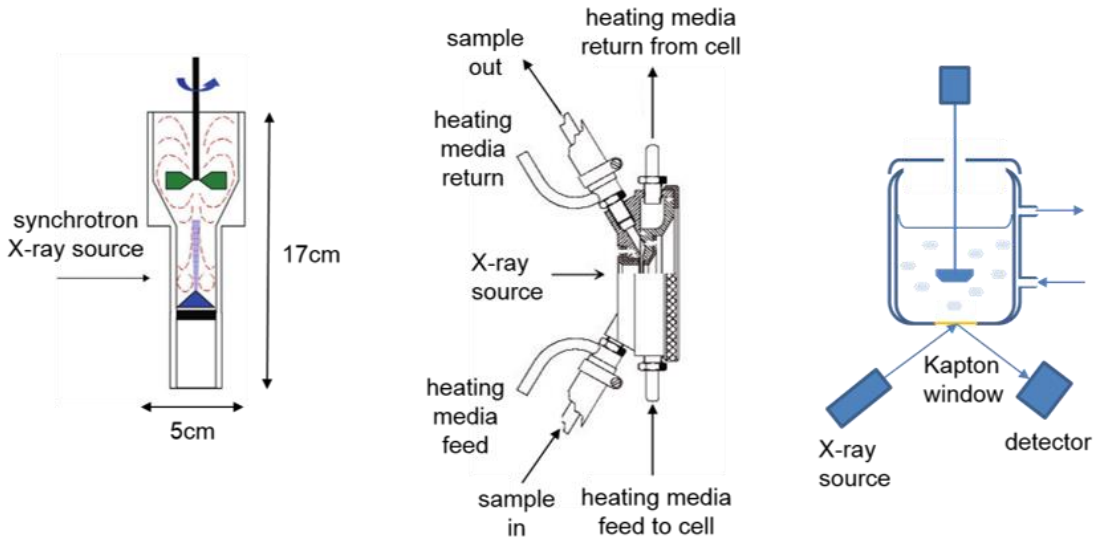

Figure 6.31 Schematic diagrams of non-commercial *in-situ* PXRD instruments as developed by Blagden *et* al.[155], Hammond *et al.*[156], and Coquerel *et al.*[157] (from left to right).

This has been partly achieved in the laboratory by various authors (Figure 6.31). In the most recent development by Coquerel[157], a slurry flow cell has been constructed, based on an STR that can be mounted on a PXRD instrument. In the experimental arrangement, the incident X-ray beam is directed towards the base of the STR which contains a Kapton window to allow the beam to penetrate into the vessel, and the crystallisation is monitored through diffraction measurements in reflectance geometry.

Building on this work on STRs, flow crystallisation systems such as the COBC or KRAIC are ideally suited to installation in an X-ray beam, and may particularly benefit from installation in more open XRD environments such as those on instruments at synchrotron radiation sources like the Diamond Light Source, Harwell, UK. The benefits here would be that, with the use of small diameter flow tubes, measurements may be possible more easily in transmission ("capillary") geometry, and the tuneable radiation at the synchrotron would open up the possibility of both wide and small angle diffraction, as well as potential spectroscopic monitoring, using the intense beams from the synchrotron source. This would build on previous work carried out by Quayle *et al.* and Hammond *et al.* in designing continuous crystallisation flow cells for deployment on synchrotron beamlines[156, 158].

7 Multi-component Materials Discovery

Running parallel to the investigations into the previously discovered multi-component system UBA, this project has also focused on new multi-component materials discovery with an aim to find candidates that may be suitable for transfer and scale up into continuous cooling crystallisation. Several new multi-component materials were discovered in a series of small scale evaporative multi-component screening experiments. Some of the complexes have been transferred into cooling crystallisation in preparation for progression on to continuous crystallisation using some small scale technologies developed at UoB (chapter 6).

7.1 Molecular Complexes of 3-deazauracil

Following on from previous studies on nucleobase derivatives, 3-deazauracil (3DU), a uracil derivative with two hydrogen bond donor groups and one hydrogen bond acceptor would be predicted to co-crystallise with a range of other small molecules. However, since the structure of this material was first determined by Low *et al.* in 1983[159], it was studied by Wilson *et al.* for around 20 years, with no polymorphism observed in the material nor any multi-component materials obtained. Portalone redetermined the structure in 2008 using more modern X-ray diffraction techniques[160].

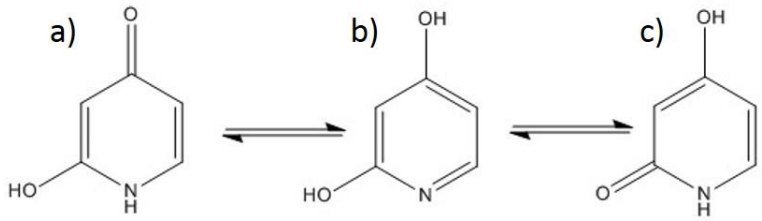

Figure 7.1 Tautomers of 3-deazauracil with potential to influence hydrogen bonding

A screening experiment in search of multi-component materials of 3DU was carried out using a range of different co-former materials (listed below), these were selected for their hydrogen donating and/or accepting groups and the compatibility of their geometries with 3DU. Crystallisations were prepared using a range of solvents and solvent mixtures (50:50 v/v) and different ratios of 3DU to co-former. Crystallisations were maintained at a range of different temperatures (Table 7.18).

Table 7.1 Experimental variables used in co-crystal screening studies of 3DU

Co-former		Ratio (3DU: co-former)	Solvent	Evaporation temperature (°C)
• 2,5-dinitrobenzoic acid • 2-nitrobenzoic acid • 3,5-dinitrobenzoic acid • 4,4'bipyridine (BP) • 5-fluorocytosine • DMAN • Fumaric acid • Isonicotinic acid • L-glutamic acid • Maleic acid	• Nicotinic acid • Oxalic acid • Oxamic acid (OXA) • Picolinic acid • Squaric aicd • Taurine • Trimesic acid (TRIM) • Urea	1:1 2:1 1:2	Water Methanol DMF IPA Ethanol Acetone	4 18 30 50

After evaporation, samples were screened for new multi-component materials using a combination of PXRD and SXRD.

Preparation of 3-deazauracil molecular complexes

As can be seen from Table 7.1 and 7.2, of the 19 co-formers tested, three of these formed molecular complexes with 3-deazauracil (3DU); these will be discussed here.

Table 7.2 Evaporative crystallisation conditions by which three 3DU multi-component complexes (3DU-TRIM, 3DU-OXA and 3DU-BP) were obtained.

Co-former	Mass of 3DU (mg)	Mass of Co-former (mg)	Molar ratio	Solvent	Vol. of solvent (mL)	Evaporation temperature (^{O}C)
TRIM	26	20	1:1	methanol/water	4	18
OXA	30	17	1:1	water		18
BP	30	20	1:1	methanol/water		4

3DU (20.8 mg, 18.8 mMol) and trimesic acid (TRIM) (39.4 mg, 18.8 mMol) were dissolved separately, each in 2 mL methanol/water solution (50:50 by volume) at room temperature. The solutions were then combined forming a 1:1 ratio of 3DU to TRIM and left to evaporate under ambient conditions. Initially a mass of white hair-like needles formed and within this there were a few small colourless blocks. These were too small and coated in too many crystallites to be used for

SXRD. The alteration of the supersaturation of the mother liquor due to the removal of solids for analysis under optical microscope promoted dissolution of the needles and growth of the colourless blocks. A colourless block was then selected from the mother liquor for SXRD.

3DU (20.8 mg, 18.8 mMol) and oxalic acid OXA (16.9 mg, 18.8 mMol) were dissolved separately in water (2 mL each) at room temperature. The solutions were combined to produce a 1:1 solution of 3DU to OXA. This was left to evaporate under ambient conditions for several days. A colourless block crystal was selected for SXRD.

3DU (13.9 mg, 12.5 mMol) and 4,4'-bipyridyl (BP) (19.5 mg, 12.5 mMol) were dissolved separately, each in 2 mL methanol/water solution (50:50 by volume) under ambient conditions. After combining the solutions to form a single 1:1 solution of 3DU:BP the vial was placed in the fridge at 4°C. A mass of pale yellow needles crystallised after 5 days from which a needle suitable for SXRD was selected.

7.1.1 Structural Analysis and Characterisation of 3-deazauracil Trimesic Acid (1:1) Monohydrate (3DU:TRIM:H_2O)

SXRD data were collected using a Rigaku R-axis/RAPID[161] single crystal diffractometer at 100 K using Mo Kα radiation (λ = 0.71073 Å). The structure was solved by charge flipping using SUPERFLIP within the WinGX v2014.1[162] package and was refined using SHELXL-2014[163].

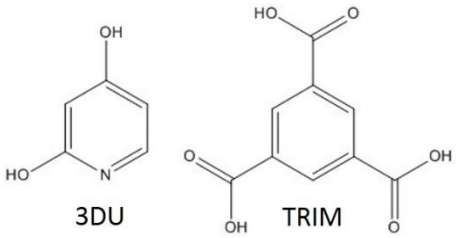

Figure 7.2 Molecular structures of 3-deazauracil (3DU) and trimesic acid (TRIM)

3DU-TRIM crystallises in the spacegroup $P2_1/c$ with two molecules of 3DU, two molecules of TRIM and two water molecules in the asymmetric unit.

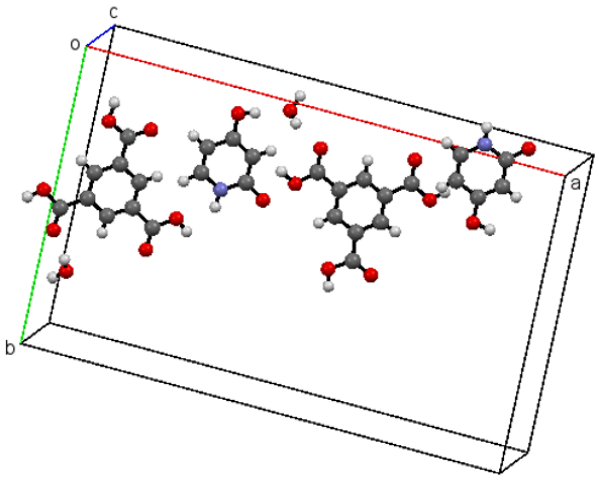

Figure 7.3 Asymmetric unit of 3DU-TRIM comprising two molecules of TRIM, two molecules of 3DU and two water molecules

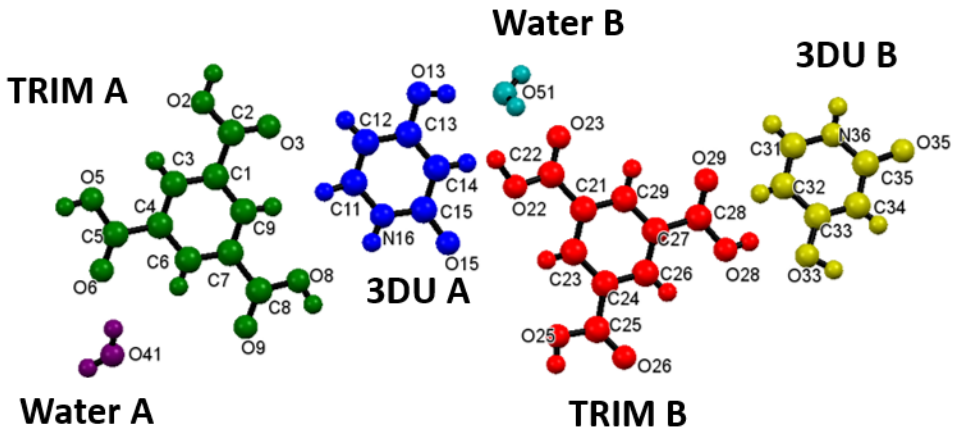

Figure 7.4 Labelling scheme of molecules within 3DU-TRIM asymmetric unit

Both molecules of 3DU adopt tautomeric configuration c (Figure 7.1) with a secondary amine, a carbonyl group situated in the *ortho* position and an alcohol situated at the *para* position.

TRIM A forms an O5-H5···O35 hydrogen bond interactions with 3DU B and 3DU B interacts with Water A an O33-H33···O41) (Figure 7.5 a and b, respectively) to create a trimer unit. Trimer units translate through the glide planes (running parallel to the a axis) to form a tape of trimer units joined through an O2-H2···O35 and an N36-H36···O3 hydrogen bond between TRIM A and 3DUB in neighbouring trimers (Figure 7.5 d and e, respectively). The TRIM A tape is further strengthened by an O-H···O hydrogen bond between TRIM A and Water A in adjacent trimers (Figure 7.5 c).

Trimers are also formed through O-H···O hydrogen bonding (Figure 7.6 f and g) between TRIM B, 3DU A and Water B and form extended TRIM B tapes which are isostructural with the TRIM A tapes except for the orientation of molecules of Water A which are oriented such as to facilitate

bifurcated C=O···HNHN hydrogen bonds between water A and TRIM B in a single tape and TRIM B tape and Water A in a neighbouring TRIM B tape (Figure 7.6 g and k).

Alternating TRIM A tapes and TRIM B tapes form extended sheets through pairs of O-H···O hydrogen bonds (Figure 7.7 l and m).

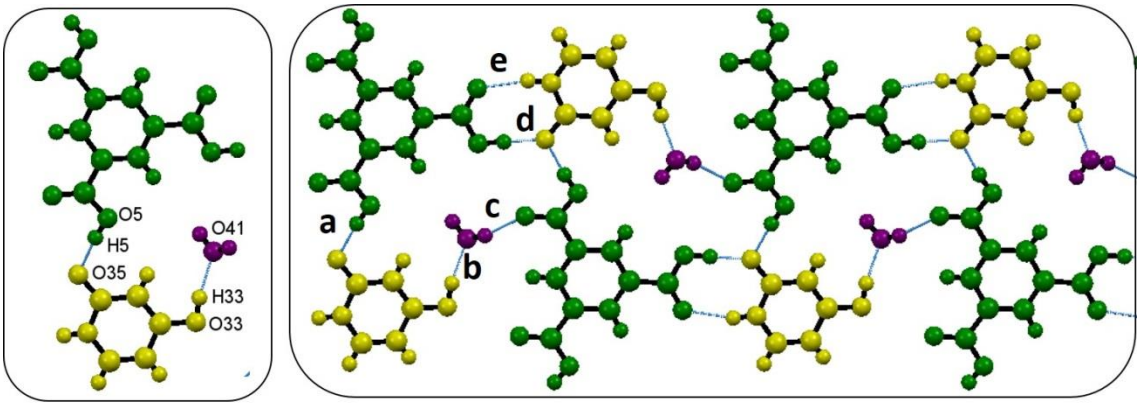

Figure 7.5 Trimer unit within TRIM-BP structure comprising, TRIM A, 3DU B and Water A (left), which interact with adjacent trimers through two O-H···O hydrogen bonds (c and d) and an N-H···O hydrogen bond (e) to form a TRIM A extended tape (right)

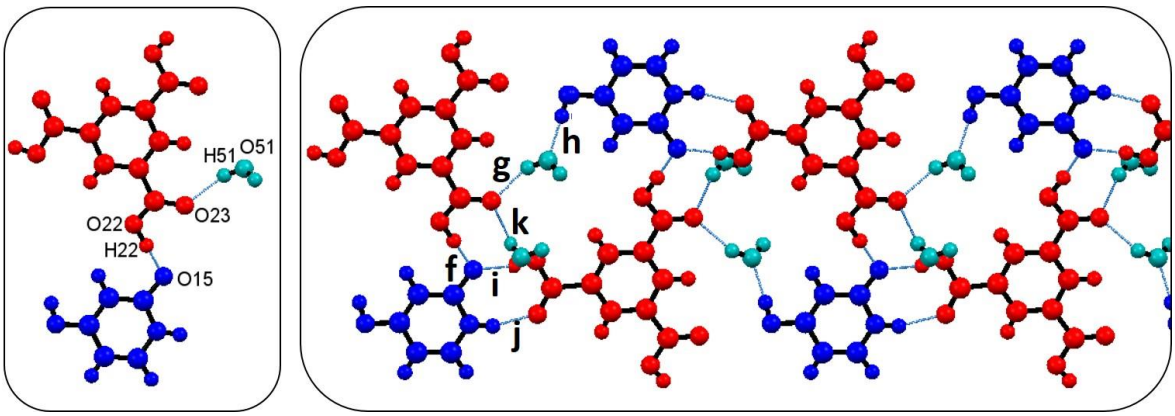

Figure 7.6 Trimer unit within TRIM-BP structure comprising, TRIM B, 3DU A and Water B (left), which interact with adjacent trimers through two O-H···O hydrogen bonds (h and i) and an N-H···O hydrogen bond (j) to form a TRIM A extended tape (right). Atom O23 forms an additional O-H···O hydrogen bond (k) to a molecule of Water B in a neighbouring TRIM A extended tape

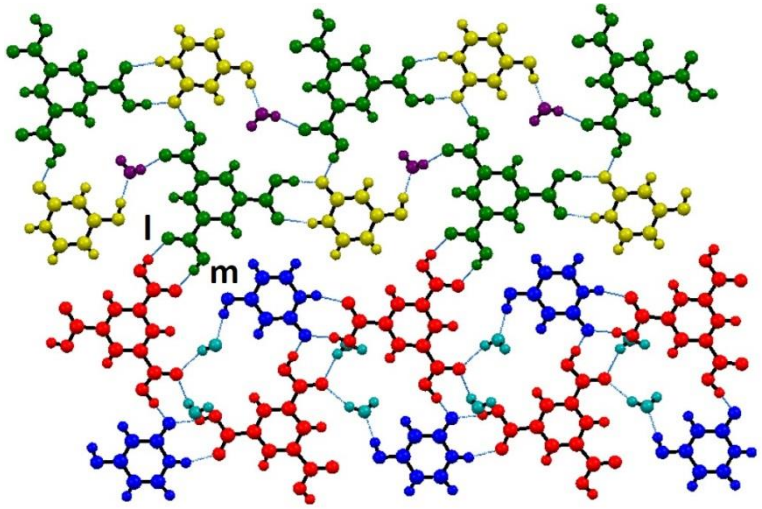

Figure 7.7 TRIM A trimer tapes (green and yellow) bond with adjacent TRIM B trimer tapes (red and blue) through pairs of O-H···O hydrogen bonds (l and m) to form an extended sheet.

Extended sheets of alternating trimer tapes are aligned parallel to the (2 0 -1) plane and stack perpendicular to this interacting through bridging hydrogen bonded water molecules and π-π interactions (Figure 7.8).

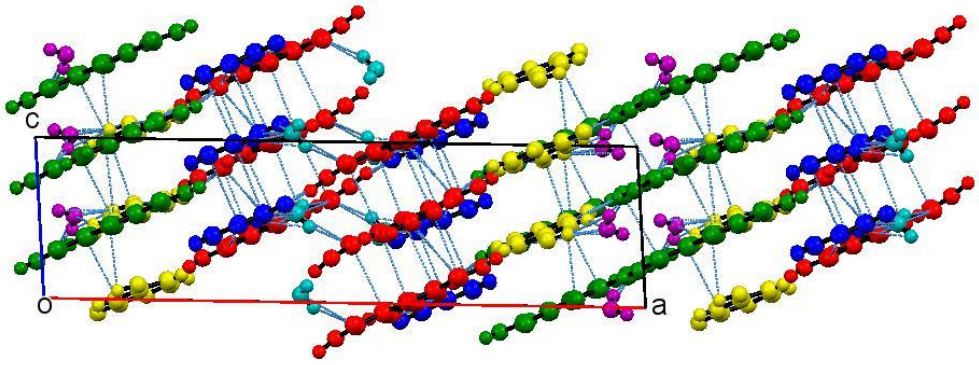

Figure 7.8 TRIM-BP structure viewed down the b-axis highlighting the layers of extended sheets aligned parallel to (2 0 -1) interacting through hydrogen bonding between channels of Water B molecules aligned parallel to the c-axis

Table 7.3 Hydrogen bond distances and angles within the 1:1 3DU-TRIM monohydrate co-crystal

D-H···A	D-H (Å)	H···A (Å)	D···A (Å)	<(DHA) (º)
O2-H2···O35 #1	1.00(7)	1.59(7)	2.595(5)	175(5)
O5-H5···O35 #2	0.91(6)	1.66(6)	2.566(5)	173(5)
O8-H8···O29 #3	0.87(5)	1.81(5)	2.667(5)	168(4)
O13-H13···O51	0.85(5)	1.84(5)	2.694(5)	179(5)
N16-H16···O26 #1	0.94(5)	1.92(5)	2.820(5)	161(4)
C14-H14···O22 #4	1.00(5)	2.63(5)	3.277(6)	122(3)
C14-H14···O51	1.00(5)	2.48(5)	3.174(6)	127(3)
O22-H22···O15 #5	1.08(7)	1.46(8)	2.533(4)	172(6)
O25-H25···O15 #1	0.90(6)	1.72(6)	2.605(5)	165(5)
O28-H28···O9 #6	0.86(4)	1.79(5)	2.640(5)	173(4)
O33-H33···O41 #7	0.94(7)	1.80(7)	2.733(7)	167(6)
N36-H36···O3 #1	0.91(5)	1.97(5)	2.854(6)	164(4)
C34-H34···O41 #7	0.89(5)	2.63(5)	3.287(8)	131(4)
O41-H22···O6	0.94(2)	1.86(3)	2.771(6)	164(8)
O51-H51···O23 #8	0.937(19)	1.95(3)	2.830(5)	155(4)
O51-H52···O23	0.942(18)	1.99(3)	2.899(5)	162(4)

Symmetry transformations used to generate equivalent atoms:

#1(-x+1, -y+1, -z), #2(x-1, -y+3/2, z-1/2), #3(-x+1, y+1/2, -z+1/2), #4(x, -y+1/2, z+1/2), #5(x, -y+1/2, z-1/2), #6(-x+1, y-1/2, -z+1/2), #7(-x+1, -y+2, -z), #8(-x+1, -y, -z)

7.1.2 Structural Analysis and Characterisation of 3-deazauracil Oxalic Acid (1:1) (3DU:OXA)

SXRD data were collected using an Agilent XCALIBUR single crystal diffractometer equipped with and Eos S2 CCD detector. The structure was solved by direct methods using SHELXS-2014[163] within the WinGX v2014.1[162] package and was refined using SHELXL-2014[163].

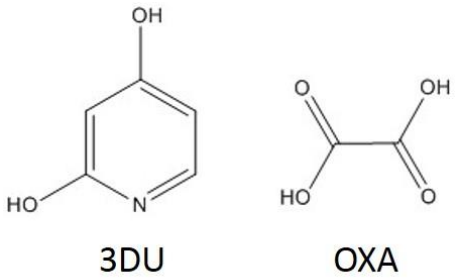

Figure 7.9 Molecular structures of 3-deazauracil (3DU) and oxalic acid (OXA)

3DU and OXA (Figure 7.9) crystallise in a 2:1 ratio to form a 3DU-OXA co-crystal where both molecular species remain neutral and the 3DU species, as in the 3DU-TRIM structure, adopts tautomeric configuration c (Figure 7.1). The asymmetric unit contains one molecule of 3DU and half a molecule of OXA which is situated on an inversion centre.

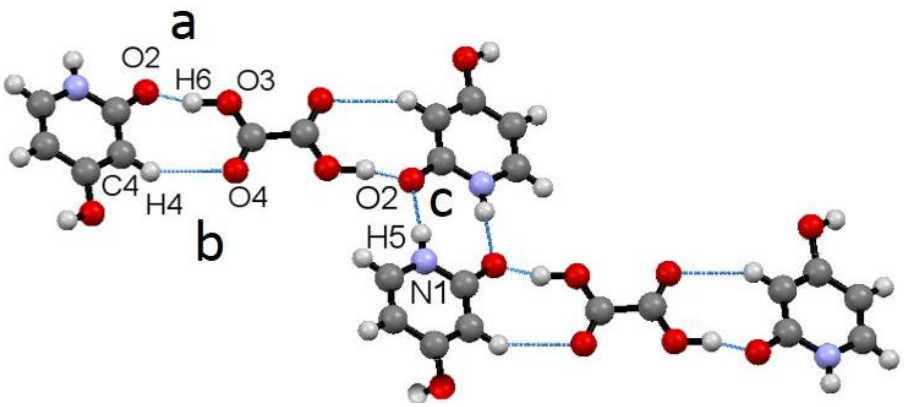

Figure 7.10 Two 3DU-OXA-3DU units, each formed through two pairs of O-H···O (a) and C-H···O (b) hydrogen bonds and bonded together through a pair of N-H···O hydrogen bonds (c)

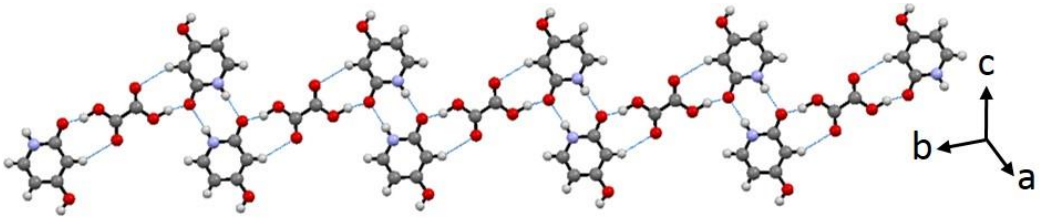

Figure 7.11 Continuous tape formed of 3DU-OXA-3DU units

A 3DU-OXA-3DU unit comprises one OXA molecule bonded to two 3DU molecules through two O2-H6···O3 hydrogen bonds between the OXA alcohol group and a carbonyl group on each 3DU molecule (Figure 7.10 a). These are stabilised by two weaker C4-H4···O4 hydrogen bonds to form two $R_2^2(8)$ motifs (which are identical due to the position on an inversion centre) (Figure 7.10 b). The 3DU-OXA-3DU units link to one another through pairs of moderate N1-H5···O2 hydrogen bonds (Figure 7.10 c) forming $R_2^2(8)$ motifs between 3DU molecules in neighbouring units which can extend to form a continuous tape. (Figure 7.11) (Hydrogen bond distances are given in Table 7.4).

Along either edge of the tape there are exposed hydrogen donating alcohol groups (3DU molecules) alternating with hydrogen bond accepting carbonyl groups (OXA molecules) which form a moderately strong O1-H3···O4 hydrogen bond with a respective carbonyl group or alcohol group on another tape. (Figure 7.12 d). It is also possible to form weaker secondary O1-H3···O3 interactions,

whose strength within the bifurcated hydrogen bond thus formed will vary with any variation in the direction of the O1-H3 alcohol group (Figure 7.12 e).

Table 7.4 Hydrogen bond distances and angles within the 2:1 3DU OXA co-crystal

Hydrogen bond	D-H (Å)	H···A (Å)	D···A (Å)	<(DHA) (º)
N1-H5···O2 #1	0.90(2)	1.91(2)	2.803(1)	174(2)
O1-H3···O4	0.89(2)	1.85(2)	2.729(1)	168(2)
O1-H3···O3 #2	0.89(2)	2.50(2)	2.968(1)	114(2)
O3-H6···O2 #3	1.08(2)	1.85(2)	2.440(1)	166(2)
C4-H4···O4 #4	0.99(2)	2.50(2)	3.388(2)	149(1)

Symmetry transformations used to generate equivalent atoms:

#1(-x, -y, -z), #2(-x+2, -y, -z+1), #3(-x+3/2, y-1/2, -z+1/2), #4 (-x+3/2, y+1/2, -z+1/2)

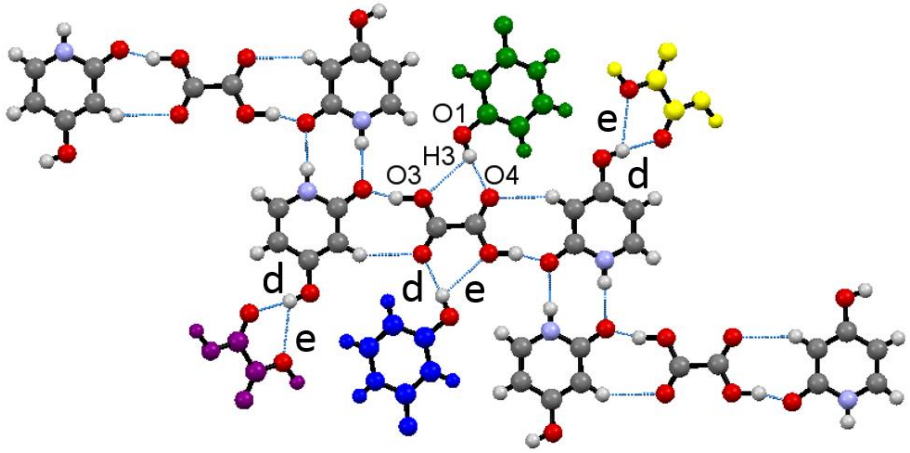

Figure 7.12 Bifurcated O-H···OO hydrogen bonding between 3DU and OXA in five neighbouring chains and through (O1-H3···O4 (d) and O1-H3···O3 (e))

As a result, each tape is bonded to four other tapes for every 3DU-OXA-3DU unit present in the tape. The extended tapes can adopt one of two orientations either parallel to the (1 1 -2) plane or parallel to the (1 -1 -2) plane (Figure 7.13). The four adjoining tapes adopt the same opposite orientation to the main tape (Figure 7.12), which is due to the conformational freedom inherent in the alcohol group of 3DU and the proximity of the 3DU molecules (3.615 Å , centroid to centroid) favour π-π stacking interactions between the 3DU molecules (Figure 7.14).

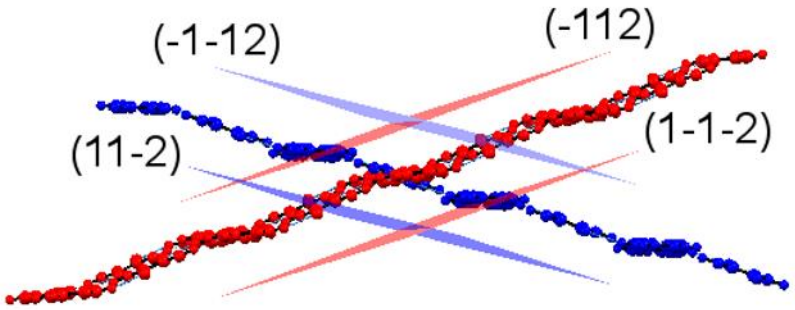

Figure 7.13 Two extended tapes in opposite orientations, parallel to either the (1 1 -2) plane or the (1 -1 -2) plane joined through bifurcated O-H···O hydrogen bonding

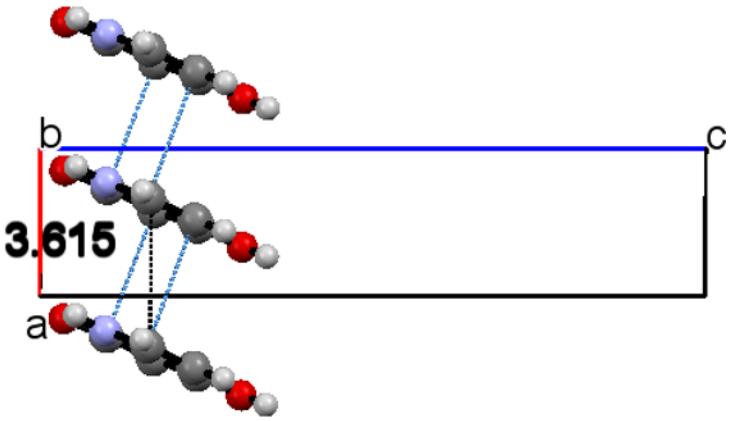

Figure 7.14 π-π stacking between 3DU molecules of extended tapes stacked parallel to the a- axis when visualised down the b axis.

7.1.3 Structural Analysis and Characterisation of 3-deazauracil 4,4'-bipyridine (2:1) Dihydrate (3DU:BP)

SXRD was carried out using a Rigaku R-axis/RAPID[161] single crystal diffractometer at 100 K using Mo Kα radiation (λ = 0.71073 Å). The structure was solved by direct methods using SHELXS-2014[163] within the WinGX v2014.1[162] package and was refined using SHELXL-2014[163].

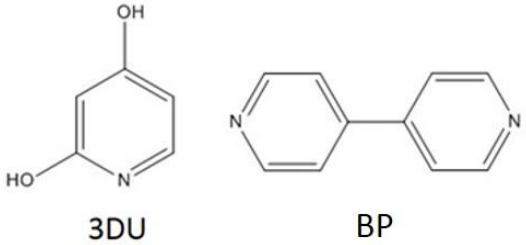

Figure 7.15 Molecular structures of 3-deazauracil (3DU) and 4,4'-bipyridine (BP)

3DU and BP (Figure 7.15) crystallise in a 2:1 ratio with an asymmetric unit comprising one molecule 3DU, half a molecule of BP and two water molecules, one of which is 50:50 disordered. Within this 2:1 dihydrated 3DU-BP co-crystal 3DU molecules related by a centre of inversion form homodimer units through two symmetry related N2-H8···O2 hydrogen bonds (2.782(4) Å). This leaves the hydroxyl groups within the 3DU homodimer available to interact with the nitrogen atoms within the BP molecule through O1-H6···N1 hydrogen bonds (2.622(5) Å) forming extended alternating chains (Figure 7.16).

These chains adopt a non-planar "zig-zag" structure (Figure 7.17) which propagates parallel to the (0 1 0) plane in the a-b direction.

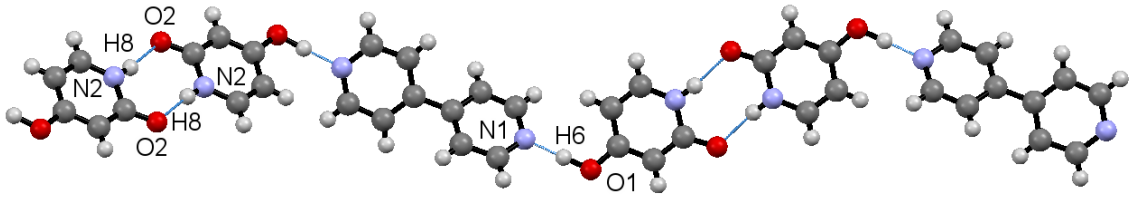

Figure 7.16 An alternating chain of 3DU homodimers and BP molecules bonded through O-H···N hydrogen bonds

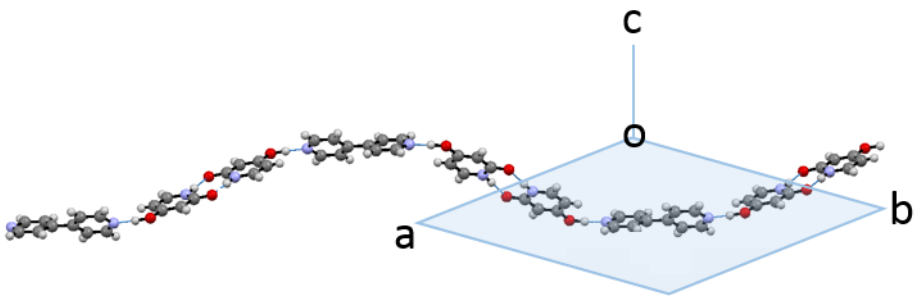

Figure 7.17 Schematic showing zig-zag shape of the alternating chains

The chains connect to form extended sheets through C1-H1···O1 hydrogen bonds and neighbouring sheets are held together through C1-H1···O1 hydrogen bonds where the atoms C1 and H1 exist in one layer and O1 resides in the adjacent layer this is possible due to the "zig-zag" nature of the chains the 3DU and BP molecules (Figure 7.18). The layers are also connected by channels of water molecules (omitted from Figure 7.18 for clarity) that run parallel to the b-axis (Figure 7.19) and π-π interactions (centroid to centroid distance of 3.779 Å) between 3DU-BP ribbons stacked parallel to the b-axis (Figure 7.20).

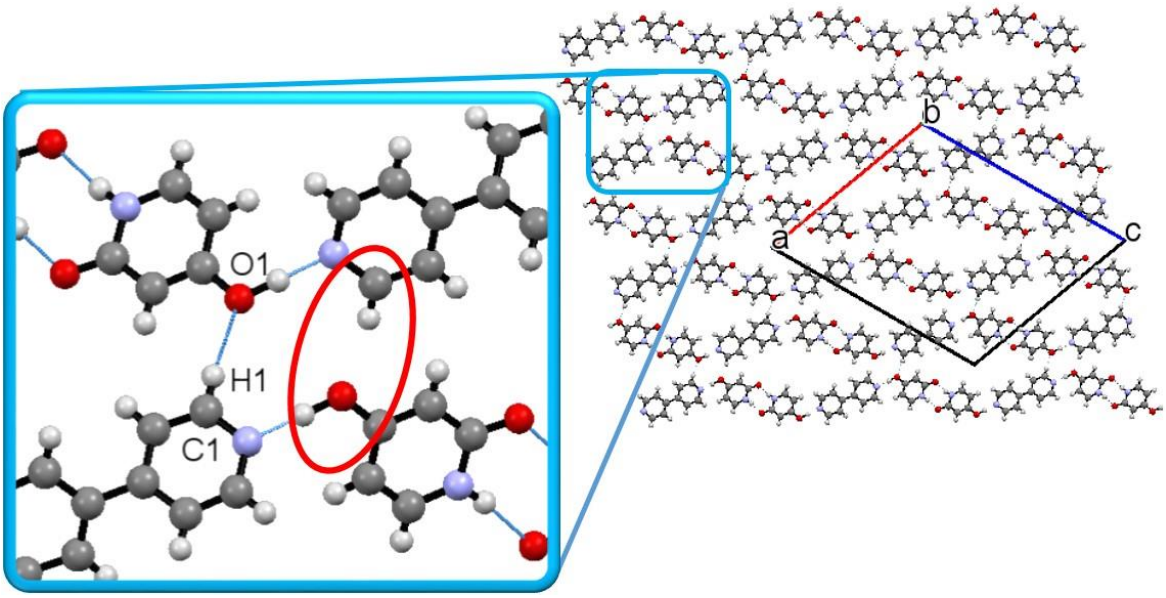

Figure 7.18 The chains connect through C1-H1···O1 hydrogen bonds to form an extended sheet. Note the atoms circled in red are also C1, H1 and O1, however due to the zig-zag nature of the chains the 3DU and BP molecules are oriented such that they form C1-H1···O1 hydrogen bonds to chains in the neighbouring layers

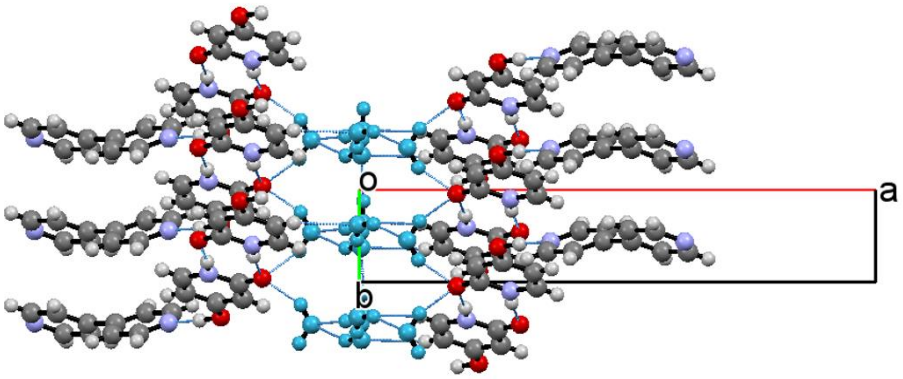

Figure 7.19 3DU-BP viewed down the c-axis showing a disordered hydrogen bonded water channel parallel to the b-axis which not only interconnects the 3DU-BP ribbons to form extended sheets but also links the neighbouring sheets together

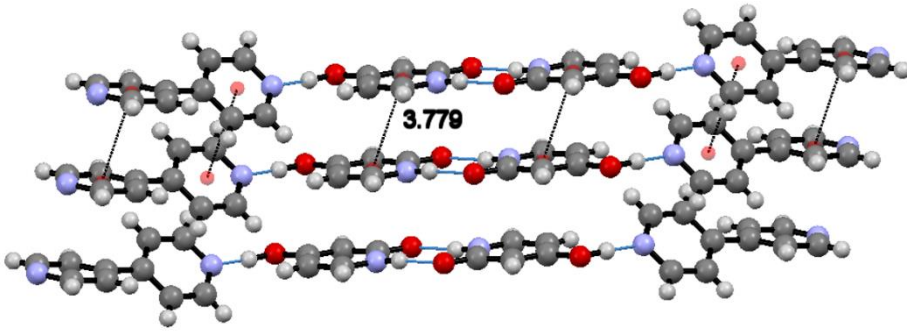

Figure 7.20 π-π interactions between 3DU-BP extended ribbons

Table 7.5 Hydrogen bond distances and angles within the 2:1 3DU-BP dihydrated co-crystal

Hydrogen bond	D-H (Å)	H···A (Å)	D···A (Å)	<(DHA) (º)
C4-H4···O3 #1	0.93	2.49	3.367(5)	157
C1-H1···O1 #2	0.93	2.45	3.344(5)	162
C5-H5···O4A #3	0.93	2.53	3.387(9)	154
O3-H11···O2 #3	0.92(2)	1.91(3)	2.767(4)	154(4)
O3-H12···O2	0.92(2)	1.92(3)	2.769(4)	152(4)
O1-H6···N1	1.08(7)	1.55(3)	2.622(5)	177(5)
O4A-H14···O3 #4	0.92(2)	1.89(3)	2.801(8)	167(10)
O4B-H13···O3 #4	0.92(2)	1.94(5)	2.822(8)	160(12)
O4B-H16···O4B #5	0.90(2)	1.98(8)	2.77(1)	146(13)
N2-H8···O2 #6	0.90(8)	1.88(8)	2.782(4)	172(7)

Symmetry transformations used to generate equivalent atoms:

#1(x-1/2, y+1/2, z), #2(-x+1/2, y-1/2, -z+1/2), #3(x, y+1, z), #4 (x-1/2, y-1/2, z), #5 (-x, -y+1, -z), #6 (-x+1/2, -y+1/2, -z)

Of the three structures discovered containing 3DU, 3DU-BP and 3DU-OXA are most similar, both containing moderate 3DU homodimer motifs creating alternating 3DU dimer – conformer ribbons and tapes, respectively. The 3DU homodimer is not present in the 3DU-TRIM structure probably owing to the three fold symmetry within the TRIM molecule rather than the two fold symmetry observed for BP and OXA molecules. The structure is additionally disrupted by the introduction of solvent water molecules.

Further investigation into the crystallisation conditions of these systems is required to ascertain if it is possible to reproduce these 3DU complexes in bulk from non-evaporative crystallisation techniques.

Table 7.6 Crystallographic data for co-crystals of 3DU with TRIM, OXA and BP

Molecular complex	**3DU-TRIM**	**3DU-OXA**	**3DU-BP**
Formula	$C_5H_5NO_2 \cdot C_9H_6O_6 \cdot H_2O$	$2C_5H_5NO_2 \cdot C_2H_2O_4$	$2C_5H_5NO_2 \cdot C_{10}H_8N_2 \cdot 4H_2O$
Molecular weight (g mol^{-1})	339.25	156.12	450.45
Temperature (K)	100	101	100
Space Group (crystal system)	$P2_1/c$ (monoclinic)	$P2_1/n$ (monoclinic)	$C2/c$ (monoclinic)
a (Å)	26.157(4)	3.6146(1)	22.557(9)
b (Å)	15.930(2)	10.6233(3)	3.779(2)
c (Å)	7.0089(8)	16.2437(4)	27.05(1)
α (°)	90.0	90.0	90.0
β (°)	93.921(7)	90.411(2)	110.580(8)
γ (°)	90.0	90.0	90.0
Volume ($Å^3$)	2913.6(7)	623.73(3)	2158.5(15)
Z	8	4	4
θ range/°	2.996-27.485	4.036-28.985	3.116-27.480
Completeness (%)	99.8	99.6	97.9
Reflections Collected	55909*	7116	9783
Independent	6672	1524	2393
Refln (obs.I> σ(I))	2642	1289	1259
R_{int}	0.2328*	0.0321	0.1052
Parameters	521	124	181
GooF on F^2	0.956	1.061	1.136
R_1 (Observed)	0.0951	0.0374	0.0810
R_1 (all)	0.2322	0.0462	0.1386
wR_2 (all)	0.2701	0.0921	0.3443

*Note that due to the needle morphology and poor quality of the 3DU-TRIM crystals it was difficult to obtain high quality data, hence the poor R_{int} of 23%. The large number of reflections collected is attributed to poor crystal quality which lead to an ambiguity in the value of the γ angle during unit cell screening and the decision was taken to collect a full sphere of data.

7.2 Molecular Complexes of 5-hydroxyuracil

Many uracil derivatives, including 5-fluorouracil[164] and 5-hydroxyuracil[165] (5OHU), have been identified and implemented as anti-cancer and antiviral agents. The uracil analogues either act as inhibitors or as substitutes for uracil in ribose nucleic acid (RNA), which disrupts the DNA

transcription process, inhibiting DNA replication and is particularly useful for cancer treatments as inhibits rapid cell division and can induce cell death[166, 167].

The structure of 5OHU (CSD ref: QARWAI) was first recorded by Copley *et al.* in 2005 in a study on crystal structure prediction of 5OHU along with 3-oxauracil, another uracil derivative used in cancer treatment.[166] The study also identified a 5OHU DMSO solvate (CSD ref: QARWEM). These are the only two structures involving 5OHU deposited in the CSD at present. No known multicomponent crystal structures of 5OHU have been recorded and to date there isn't any literature on co-crystal screening studies this coupled with status as a potential API target and favourable hydrogen bonding groups makes 5OHU a prime candidate for multi-component crystallisation.

5OHU has the potential to tautomerise (Figure 7.21) and the tautomeric form adopted can significantly change the hydrogen bonding potential of the molecule, thus affecting its characteristics for potential molecular complex formation and the solid state packing these may adopt.

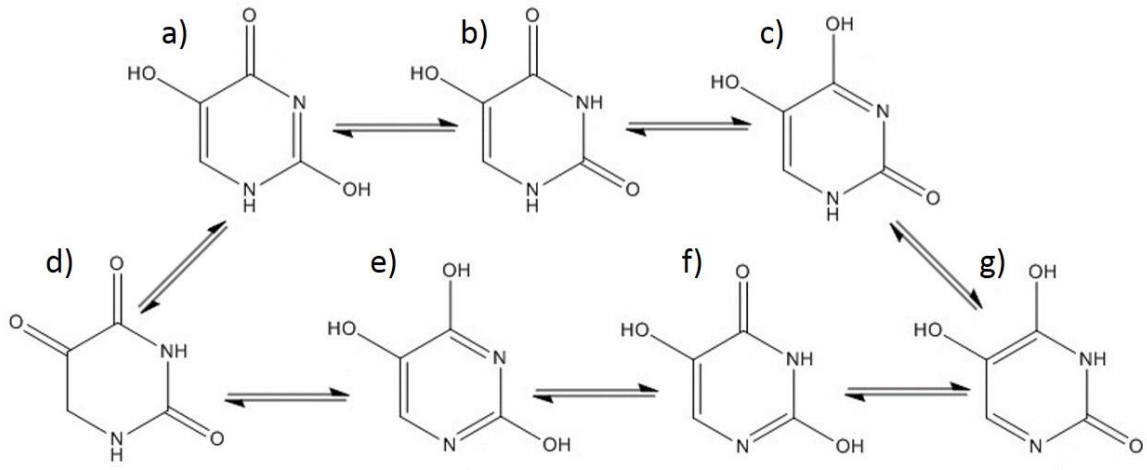

Figure 7.21 Tautomers of 5-hydroxyuracil with potential to influence hydrogen bonding

A range of different co-former materials (Table 7.7) were selected as candidates for screening for 5OHU multi-component materials. Crystallisations were prepared using several solvents, solvent combinations (50:50 by vol.) and crystallisations temperatures.

Table 7.7 Experimental variables used in co-crystal screening studies of 5OHU

Co-former		Ratio (3DU: co-former)	Solvent	Evaporation temperature (°C)
• 8-azaguanine • Vanillin Urea • Uracil • Taurine • Succinic acid • riboflavin • pyridoxine • Pyrazine carboxamide • Oxamic acid • Oxalic acid • N-methylurea	• N,N-dimethylurea • Malonic acid • Maleic acid • imidazole • Fumaric acid • cytosine • Caffeine • Benzoic acid • Benzimidazole • 4,4'-bipyridyl • 3,5-dinitrobenzoic acid • 2-aminobenzoic acid	1:1	Water Methanol Ethanol	4 18 30 40 60

Samples from the screening study were analysed using a combination of PXRD and SXRD which resulted in the discovery of a new 2:1 co-crystal of 5OHU with BP. From the 24 co-formers tested, molecular complex with 5-hydroxyuracil (5OHU) was obtained, with the co-former 4,4'-bipyridyl (BP).

The 5OHU-BP complex was grown from a 1:1 solution of 5OHU:BP formed by combining a solution of 24 mg (18.8 mMol) of 5OHU in 2 mL of water and a solution of 29.3 mg (18.8 mMol) BP in 2 mL of water, both at 40˚C. The solution was left to evaporate at 40°C for 5 days producing a mesh of off-white needle crystals formed from which a suitable single crystal was selected for SXRD.

SXRD data was collected using a Rigaku R-axis/RAPID[161] single crystal diffractometer at 100 K using Mo Kα radiation (λ = 0.71073 Å). The structure was solved by direct methods using SHELXS-2014[163] within the WinGX v2014.1[162] package and was refined using SHELXL-2014[163].

7.2.1 Structural Analysis and Characterisation of 2:1 Co-crystal of 5-hydroxyuracil with 4,4'-bipyridine

5OHU and BP (Figure 7.22) crystallise in a 2:1 ratio (5OHU:BP) which solves in the monoclinic space group C2/c with an asymmetric unit containing one molecule of 5OHU and half a molecule of BP. The 5OHU molecule exists as tautomer b (Figure 7.21) with two protonated nitrogen atoms, two carbonyl groups and an alcohol group. This is the same configuration adopted in the structure of

5OHU starting material[166]. Further structures would be required to determine if this was the most stable tautomer of 5OHU however the fact that the first structures discovered involving 5OHU are of this tautomeric configuration as are structures of other 5-substituted uracils indicates that it is a stable tautomer.

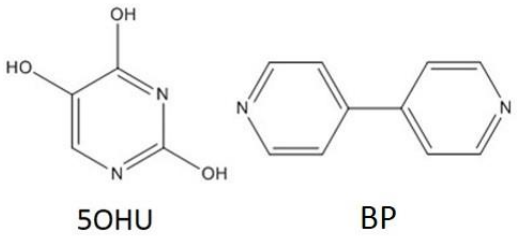

Figure 7.22 Molecular structures of 5-hydroxyuracil (5OHU) and 4,4'-bipyridine (BP)

Within the 5OHU-BP structure two molecules of 5OHU related through an inversion centre form a $R_2^2(8)$ homodimer motif through two symmetry related N1-H1···O1 hydrogen bonds (2.8295 Å) (Figure 7.23 a). The O1 atom is acts as a bifurcated H-bond acceptor as it forms an O1···H2-N2 hydrogen bond with a symmetry related neighbouring homodimer further stabilised by the second N2-H2···O1 (Figure 7.23 b). These moderately strong hydrogen bonding interactions form extended non-polar ribbon motifs (Figure 7.23 c) as observed in the crystal structure of the 5OHU starting material and in several other 5-substituted uracils including 5-ethyluracil and 5-chlorouracil[168].

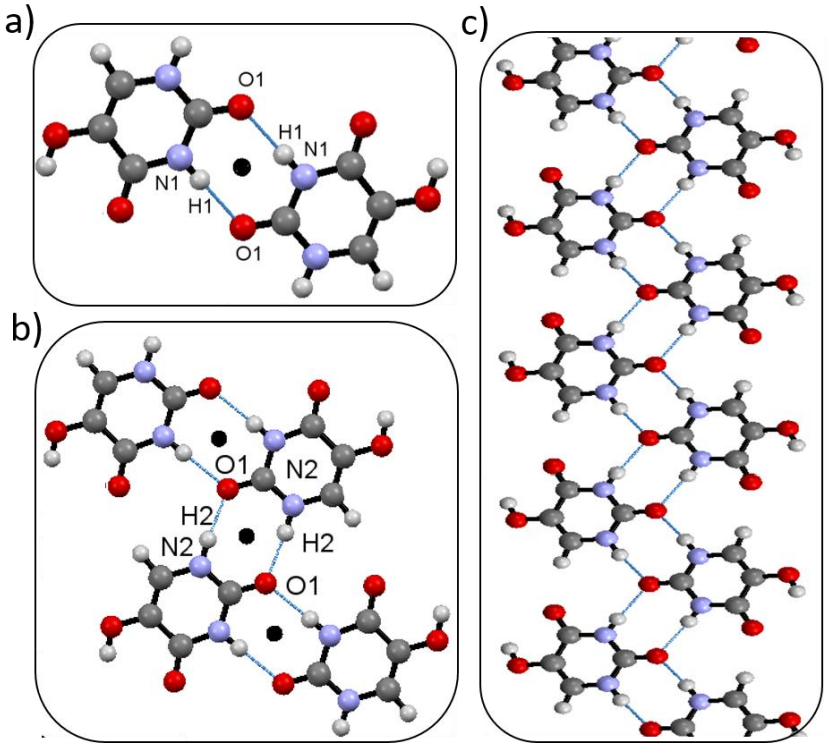

Figure 7.23 Hydrogen bonding interactions between 5OHU in the 2:1 molecular complex of 5OHU-BP. a) $R_2^2(8)$ homodimer about an inversion centre, b) linking of dimers about inversion centre through another $R_2^2(8)$ motif and c) a non-polar ribbon of 5OHU

The 5OHU ribbons are joined together through moderate O3-H4···N3 hydrogen bonds (2.785(2) Å) (supported by a weaker C5-H7···O2 hydrogen bonds) to BP linkers (Figure 7.24).

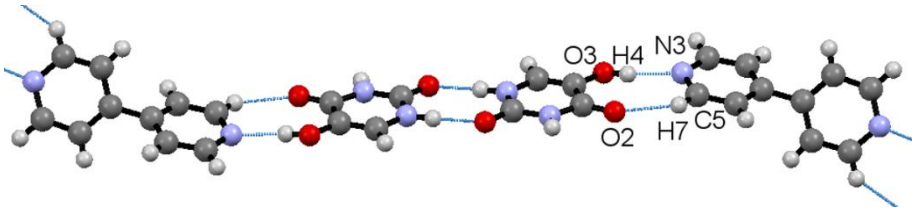

Figure 7.24 O-H···N and C-H···O hydrogen bonding linking a 5OHU dimer within an extended ribbon (that would protrude from the page) to two twisted BP molecules

The ribbons are slightly offset and staggered parallel to the b-axis with π-π interactions (3.394 – 3.632 Å) between the ribbons (Figure 7.25). The 5OHU homodimers within the ribbons alternate in orientation either parallel to the (-1 -1 6) plane or to the (-1 1 6) plane (Figure 7.26) with the BP linkers adopting an twisted configuration with the two six-membered rings positioned at 49 ° relative to one another (Figure 7.27). This results in the alternating 5OHU and BP structure observed in Figure 2.8.

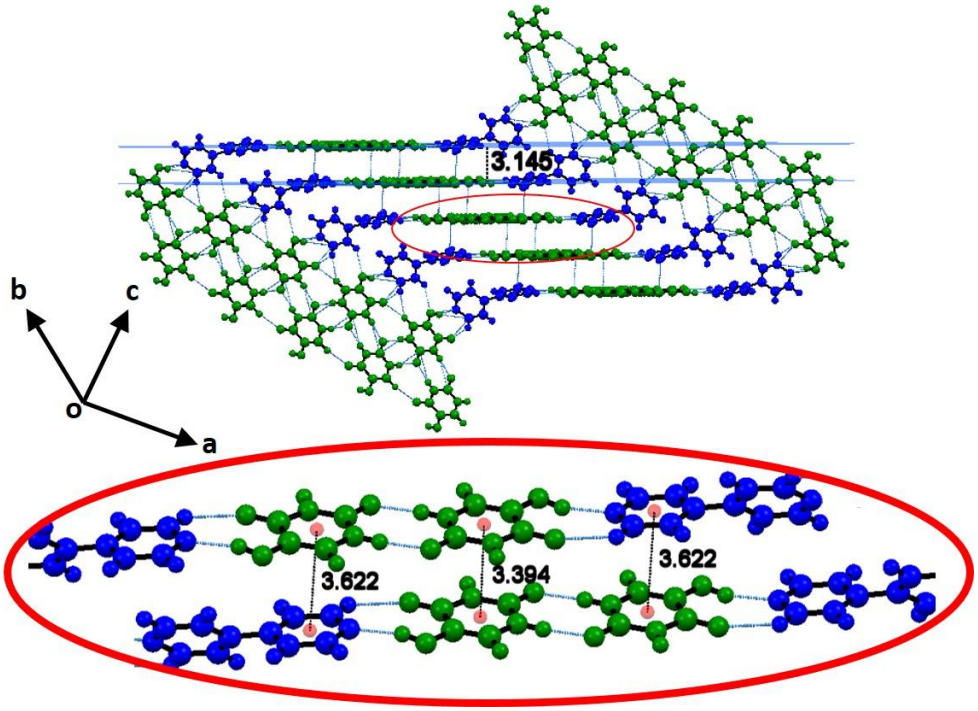

Figure 7.25 5OHU-BP and 5OHU-5OHU π-π stacking interactions between stepped layers within the 5OHU-BP crystal structure

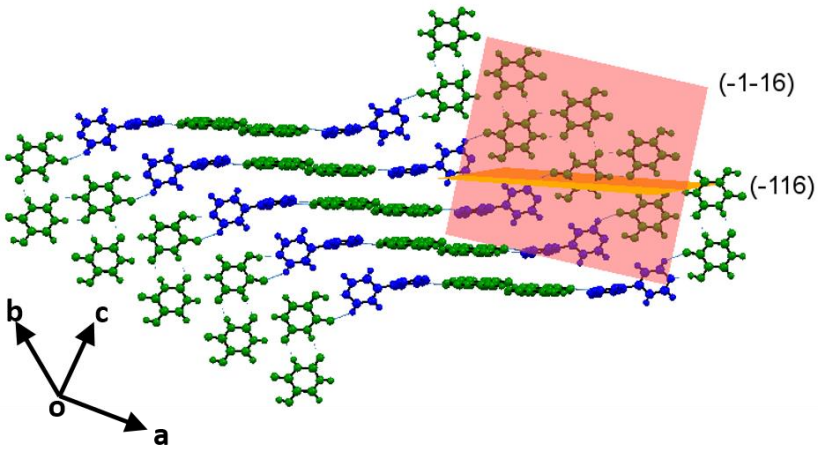

Figure 7.26 Schematic highlighting the alternating alignment of the 5OHU ribbons. Depicted here are two ribbons parallel to the (-1 -1 6) plane interconnected through BP linkers to five 5OHU ribbons orientated parallel to the (-1 1 6) plane running out of the page

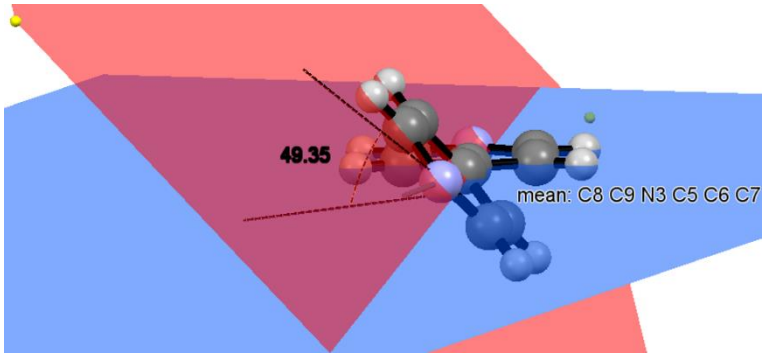

Figure 7.27 The mean planes drawn through both six-membered rings of the BP molecule (shown in red and blue) are at 49° to one another highlighting the twisted BP conformation

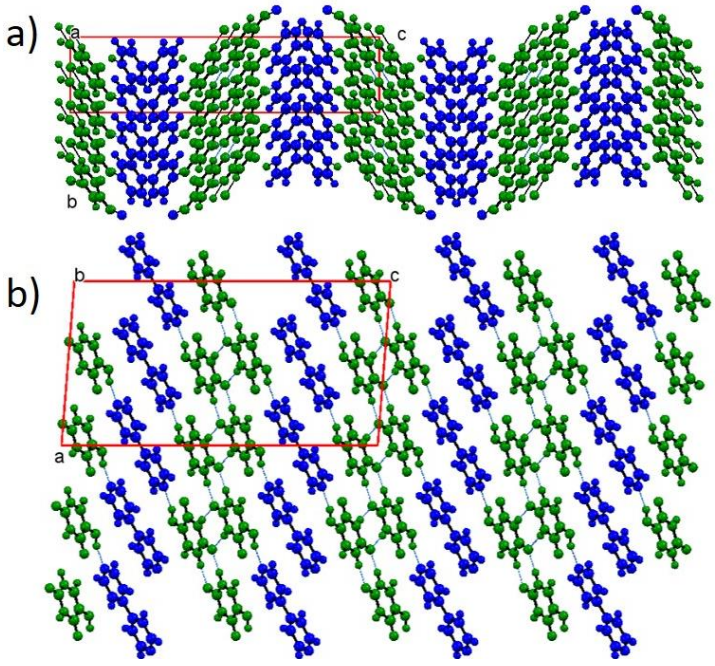

Figure 7.28 The 5OHU-BP crystal structure viewed down the a-axis (a) and the b-axis (b)

Table 7.8 Hydrogen bond distances and angles within the 2:1 5OHU BP co-crystal

D-H···A	D-H (Å)	H···A (Å)	D···A (Å)	<(DHA) (º)
N1-H1···O1 #1	0.88(2)	1.96(2)	2.830(2)	171(2)
N2-H2···O1 #2	0.96(2)	1.84(2)	2.797(2)	174(2)
O3-H4···N3	0.92(2)	1.91(2)	2.785(2)	159(2)
C2-H3···O2 #3	1.06(2)	2.43(2)	3.419(2)	154(1)
C6-H8···O3 #4	0.97(2)	2.51(2)	3.297(2)	139(1)
C5-H7···O2	0.97(2)	2.25(2)	3.050(2)	139(1)

Symmetry transformations used to generate equivalent atoms:

#1(-x+2, -y, -z+1), #2(-x+5/2, -y+1/2, -z+1), #3(x+1/2, y+1/2, z), #4(x-1/2,y-1/2,z)

Table 7.9 Crystallographic data for 2:1 co-crystal of 5OHU and BP

Compound	2:1 5OHU BP
Formula	$2C_4H_4N_2O_3 \cdot C_{10}H_8N_2$
Molecular weight / gmol^{-1}	412.37
Temperature (K)	100
Space Group (crystal system)	C 2/c (monoclinic)
a (Å)	12.4646(8)
b (Å)	5.8255(5)
c (Å)	23.976(2)
α (º)	90.0
β (º)	94.513(7)
γ (º)	90.0
Volume (*Å^3*)	1753.6(2)
Z	4
θ range (˚)	3.28-27.48
Completeness (%)	99.9
Reflections Collected	10061
Independent	1973
Refln (obs.I> σ(I))	1524
R_{int}	0.0324
Parameters	163
GooF on F^2	1.127
R_1 (Observed)	0.0370
R_1 (all)	0.0519
wR_2 (all)	0.1015

7.3 Molecular Complexes of 8-azaguanine

8-azaguanine (8AG) is a particularly insoluble yet useful aza derivative of the nucleobase guanine, which has been involved in studies for the treatment of leukaemia due to its action as a cell poison[169]poorly soluble . The aim of this study is to alter the solubility of 8-azaguanine *via* multi-component crystallisation and to transfer this process into the continuous flow environment. It was only possible to dissolve very small quantities of 8AG in water alone and only at high temperatures (90 °C). To aid dissolution of 8AG, alkaline additives were used such as sodium hydroxide and ammonium hydroxide.

Several co-formers were chosen for their compatibility with the geometry of the hydrogen bond donor and acceptor sites of 8AG (Table 7.10). Other nucleobases were the first co-formers considered. As 8AG is a derivative of guanine which forms nucleobase paring with cytosine in DNA, cytosine was selected as a potentially successful co-former. Cytosine is highly soluble in water and through co-crystallisation it was hoped that the aqueous solubility of 8AG would be improved. Where solvents other than dilute ammonium hydroxide solution were required to dissolve the co-former, the co-former and 8AG components were dissolved separately in their respective solvents and then combined in a single vial prior to evaporation at a set temperature. This ensured that the 8AG was able to dissolve completely prior to evaporation. Of the 24 co-formers screened with 8AG a molecular complex was only discovered in crystallisations involving the cytosine co-former molecule.

Table 7.10 Experimental variables used in co-crystal screening studies of 8AG

Co-former		Ratio (8AG: co-former)	Solvent	Evaporation temperature (°C)
• 2-nitrobenzoic acid • 3,4-dihydroxybenzoic acid • 3-hydroxybenzoic acid • 4-dimethylamino benzoic acid • 5-fluorocytosine • adenine • Beta-cyclodextrin • Chloranilic acid • cytosine • DL-valine • guanine	• Fumaric acid • Isonicontinc acid • L-cysteine • L-glutamic acid • L-histidine • Malic acid • Malonic acid • Nicotinic acid • Oxamic acid • Oxalic acid • Phthalic acid • Picolinic acid • Succinic acid	1:1	Water Methanol Ethanol DMSO Sodium hydroxide Ammonium hydroxide	4 18 30 40 60

Equimolar quantities of 8-azaguanine (8AG) and cytosine (Figure 7.29) were dissolved separately in water and a dilute ammonium hydroxide solution (2% ammonium hydroxide by volume), respectively, prior to mixing. Upon evaporation of the pale yellow solution at 60 °C, pale yellow crystals of block morphology were formed as well as yellow crystalline powder.

A pale yellow block shaped single crystal was selected and data were collected using a Rigaku R-axis/RAPID[161] single crystal diffractometer at 100 K using Mo Kα radiation (λ = 0.71073 Å). The structure was solved by direct methods using SHELXS-97[163] within the WinGX v1.8.05[162] package and was refined using SHELXL-97[163].

7.3.1 Structural Analysis and Characterisation of 1:1 Monohydrated Molecular Complex of 8-azaguanine with Cytosine

The components crystallise in the triclinic space group $P\bar{1}$; the unit cell parameters and crystallographic data are given in Table 7.12 and the intermolecular hydrogen bonds involved in the structure are outlined in Table 7.11, below.

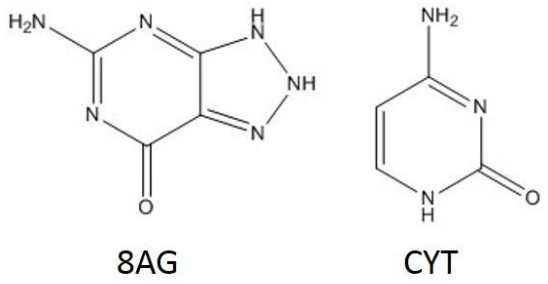

Figure 7.29. Molecular structures of 8-azaguanine (8AG) and cytosine (CYT)

A 1:1 molecular complex of 8AG and CYT (Figure 7.29) is formed with inclusion of one solvent water molecule per formula unit. Heterodimers (Figure 7.30) are formed through a pseudo Watson-Crick hydrogen bonding interaction consisting of three moderately strong hydrogen bonds, N7-H11···O2, N5-H4···N8 and N6-H6···O3 with D···A distances of 2.904(2) Å, 2.891(2) Å and 2.819(2) Å, respectively (a, b and c of Figure 7.30). A Watson-Crick hydrogen bond interaction occurs readily between the complementary nucleobases guanine and cytosine in DNA; in spite of this, there is no recorded structure of a guanine cytosine complex in the CSD to date. However, it has been possible to form a 9-ethylguanine 1-methylcytosine complex (Figure 7.31) (CSD ref. EGMCYT10)[170] in which the two components also form dimers through a pseudo Watson-Crick hydrogen bonded unit. The hydrogen bonding is similar to that found here in the 8AG-cytosine

dimer, hydrogen bond a* which, like a, is the longest of the three interactions (2.943(3) Å), c*, like c, is the shortest hydrogen bond (2.806(3) Å) and hydrogen bond b*, like b, is mid-length (2.924(3) Å).

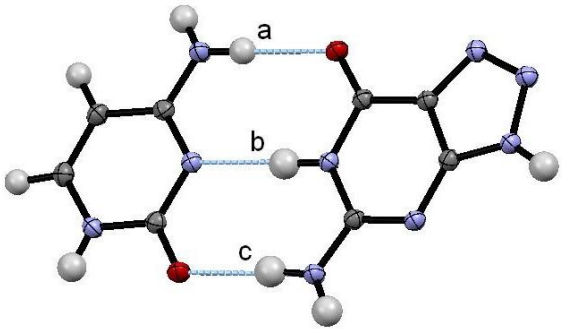

Figure 7.30. Pseudo Watson-Crick hydrogen bonding in heterodimer of 8-azaguanine and cytosine

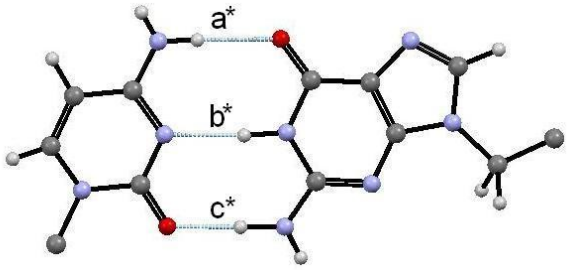

Figure 7.31. PseudoWatson-Crick hydrogen bonding in heterodimer of 9-ethylguanine 1-methylcytosine complex[170]

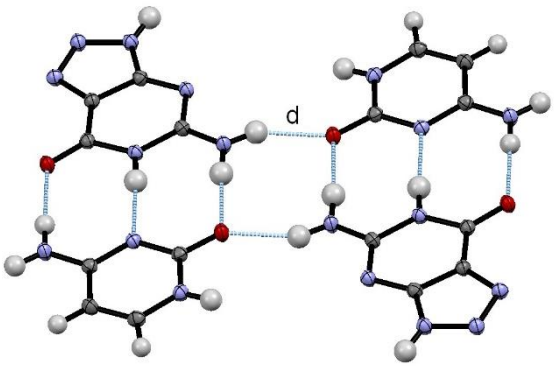

Figure 7.32. Tetramer unit formed using two equivalent N6-H5···O3 (d) hydrogen bonds in the molecular complex of 8-azaguanine cytosine monohydrate

The heterodimers interlink through two equivalent moderately strong N6-H5···O3 hydrogen bonds (2.810(2) Å) to form a planar tetramer (Figure 7.32 d), where the dimers are related *via* an inversion centre at the centre of the $R_4^2(8)$ bonding motif. Additional moderate N9-H7···O1 and O1-H2···N4 hydrogen bonds occur between the tetramer and two solvent water molecules (Figure 7.33 e and f)

forming two $R_3^3(10)$ motifs converting this to a hexamer unit. Atom O1 does not lie in plane with the tetramer; it sits approximately 0.6 Å above or below it.

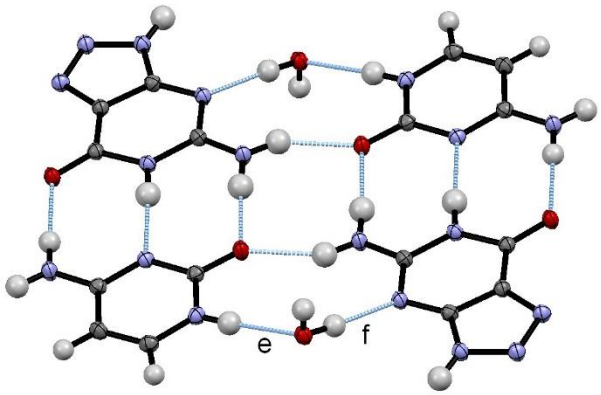

Figure 7.33. . Hexamer unit formed through N9-H7···O1 (e) and O1-H2···N4 (f) hydrogen bonds in the molecular complex of 8-azaguanine cytosine monohydrate

The hexamers arrange into an extended chain linked through moderately strong N7-H10···N1 hydrogen bonds of distance 3.065(2) Å (g, Figure 7.34).

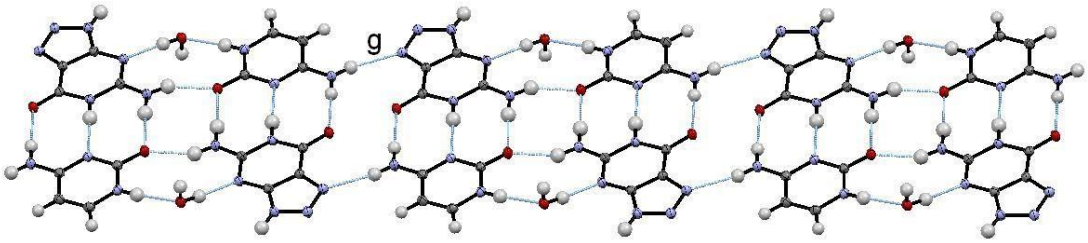

Figure 7.34. Extended chain formed from hexamers interlinked through N7-H10···N1 (g) hydrogen bonds in the molecular complex of 8-azaguanine cytosine monohydrate

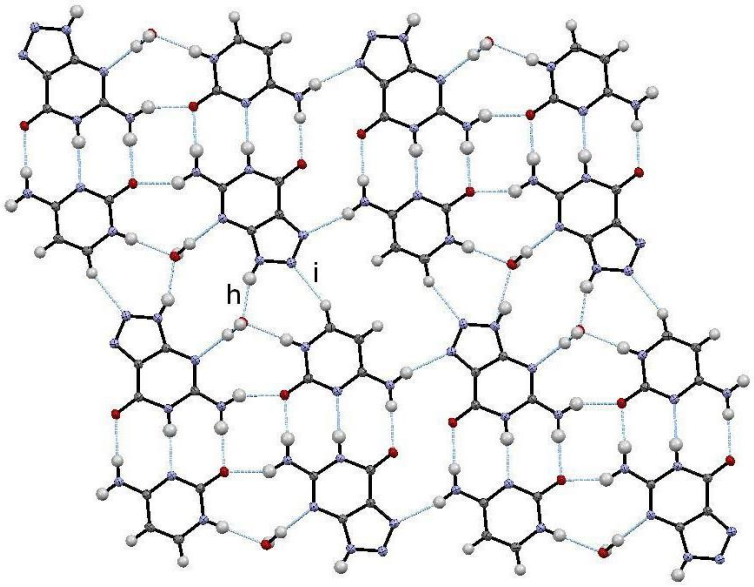

Figure 7.35.Moderate (h) and weak (i) hydrogen bonding present in extended sheet structure in the molecular complex of 8-azaguanine cytosine monohydrate

Several extended chains hydrogen bond together to form an extended sheet. Moderately strong N3-H3···O1 hydrogen bonds of 2.761(2) Å in length (h, Figure 7.35) occur between solvent water molecules from one chain and the aza ring of 8AG molecules in an adjacent chain. Additionally there are weak C7-H8···N2 hydrogen bonding interactions (3.260(2) Å) (i, Figure 7.35) present between the central nitrogen of the aza ring of one chain and a carbon in the six-membered ring of cytosine in the chain flanking this. In the structure of 8AG (CSD ref. AZGUAN01[171]) alone there is no hydrogen bonding present that involves the central nitrogen in the aza ring, but in the 8AG monohydrate structure (CSD ref. AZGUAN[169]) there is an O-H···N hydrogen bond of 2.927 Å between the central nitrogen in the aza ring and oxygen of the solvent water molecule.

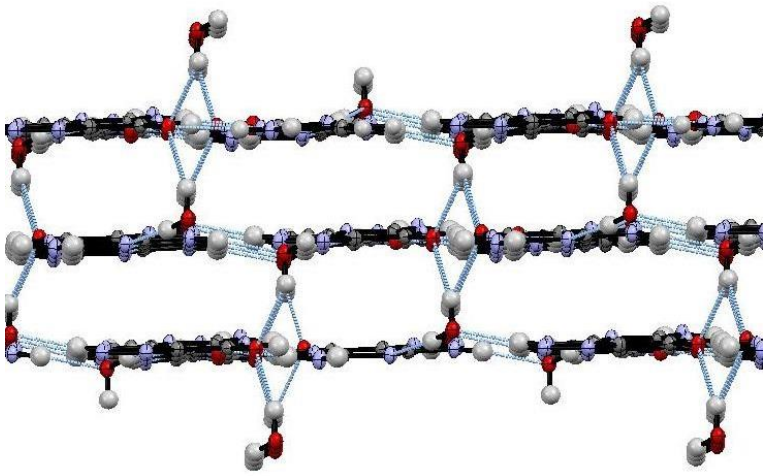

Figure 7.36. Moderate and weak hydrogen bond interactions present between adjacent extended chains in the molecular complex of 8-azaguanine cytosine monohydrate

The extended sheets stack to form a layered structure linked through DHAA bifurcated hydrogen bonds (Figure 7.36) that are present between the non-planar O1 atom of a solvent water molecule (as discussed previously) and the atoms O2 and O2' from two 8AG molecules within a neighbouring extended sheet. When three sheets are layered a $R_2^2(6)$ motif is formed, about an inversion centre, by two bifurcated hydrogen bonds (Figure 7.37). The bifurcated bonds are approximately symmetrical, D···A distances between O1 and O2 and O1 and O2' are 2.996(2) Å and 3.010(2) Å, respectively.

The 8AG molecules stack upon other 8AG molecules in neighbouring layers and are parallel to one another. They are inverted with respect to each other about an inversion centre located halfway between the planes of the rings. The same is true for cytosine molecules, i.e. like stacks onto like. π-π stacking interactions are present between the layered 8AG molecules (Figure 7.38). Between the layers A and B there are π-π stacking interactions present between the overlapping six-membered rings in each 8AG molecule at an inter-plane distance of ~3.24 Å. The five-membered aza rings of 8AG in layers B and A' also overlap giving rise to π-π stacking at an inter-plane distance of ~3.15 Å.

In the adjoining layers (B and A'), there are also additional π-π stacking interactions at an inter-planar distance of ~3.21 Å between the six-membered rings of cytosine molecules (Figure 7.39).

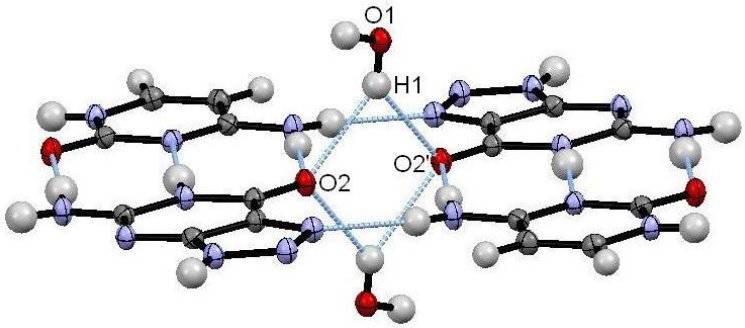

Figure 7.37. The DHAA bifurcated hydrogen bonding to water molecules in neighbouring layers in the molecular complex of 8-azaguanine cytosine monohydrate

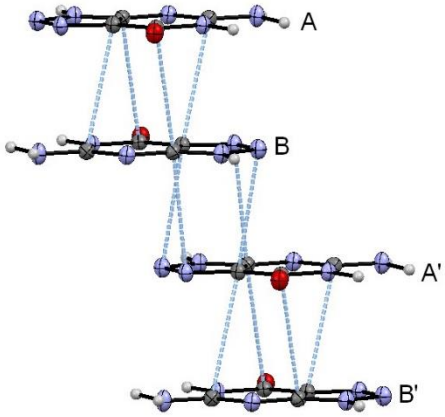

Figure 7.38. π-π stacking interactions between 8AG molecules from sheets in different layers in the molecular complex of 8-azaguanine cytosine monohydrate

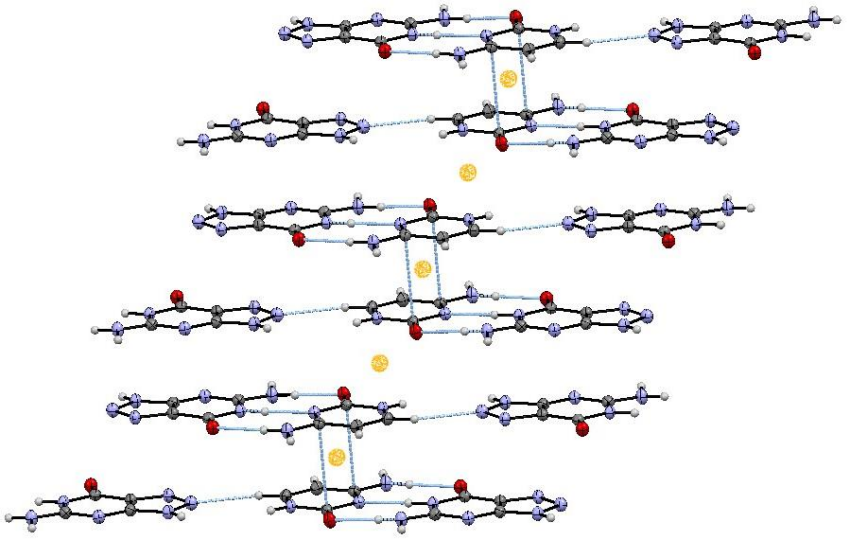

Figure 7.39. π-π stacking between cytosine molecules in adjacent sheets about an inversion centre (shown in yellow) in the molecular complex of 8-azaguanine cytosine monohydrate

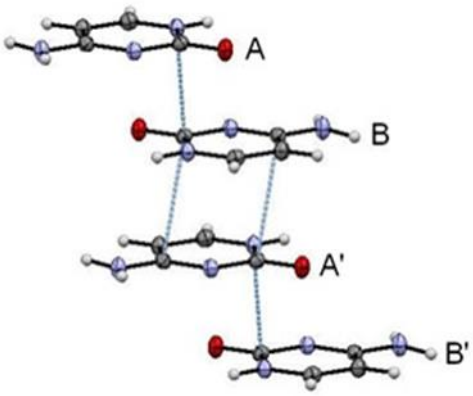

Figure 7.40 π-π stacking interactions between cytosine molecules in extended layers in the molecular complex of 8-azaguanine cytosine monohydrate

Figure 7.41 Lack of overlap between cytosine molecules in A and B (or A' and B') extended layers in the molecular complex of 8-azaguanine cytosine monohydrate

There is alternation between π-π interactions between cytosine molecules in B and A' and a lack of π-π interactions between cytosine molecules in A and B (or A' and B') (Figure 7.40). Although the inter-plane distance between cytosine molecules in A and B is 3.097 Å, which is conducive to π-π interactions, the molecules are severely offset so π overlap is poor (Figure 7.41)

Table 7.11. Hydrogen bond distances within the 1:1 8-azaguanine cytosine monohydrate molecular complex

D-H···A	D-H (Å)	H···A (Å)	D···A (Å)	<(DHA) (º)
O1-H1···O2 #1	0.86(2)	2.24(2)	3.010(2)	146(2)
O1-H1···O2 #2	0.86(2)	2.31(2)	2.996(2)	135(1)
O1-H2···N4 #3	0.93(2)	1.86(2)	2.782(2)	172(2)
N5-H4…N8	0.94(2)	1.95(2)	2.891(2)	177(2)
N7-H10···N1 #4	0.90(2)	2.18(2)	3.065(2)	169(2)
N6-H6···O3	0.92(2)	1.90(2)	2.819(2)	175(2)
N9-H7···O1 #5	0.87(2)	2.07(2)	2.934(2)	173(2)
N3-H3···O1	0.90(2)	1.90(2)	2.761(2)	159(2)
N6-H5···O3 #6	0.92(2)	1.97(2)	2.810(2)	151(2)
N7-H11···O2	0.90(2)	2.00(2)	2.904(2)	178(2)

Symmetry transformations used to generate equivalent atoms:

#1(x+1, y-1, z), #2(-x+1, -y+1, -z+1), #3(-x+1, -y, -z+1), #4(-x, -y+2, -z+1), #5(x-1, y+1, z-1), #6(x, -y+1, -z)

Table 7.12. Crystallographic data for monohydrated 1:1 8-azaguanine cytosine molecular complex

Compound	**8AG cytosine monohydrate**
Formula	$C_4H_5N_3O \cdot C_4H_4N_6O \cdot H_2O$
Crystallisation Conditions	Water with NH_3. 60 °C
Molecular weight / $gmol^{-1}$	281.26
Temperature (K)	100
Space Group	*P-1*
a (Å)	7.172(2)
b (Å)	8.779(3)
c (Å)	9.961(3)
α (º)	78.334(6)
β (º)	78.786(7)
γ (º)	66.631(6)
Volume ($Å^3$)	559.3(3)
Z	2
θ range (˚)	3.07-27.48
Completeness (%)	99.6
Reflections Collected	14108
Independent	2555
Refln (obs.I> σ(I))	2108
R_{int}	0.0299
Parameters	225
GooF on F^2	1.007
R_1 (Observed)	0.032
R_1 (all)	0.0408
wR_2 (all)	0.0914

7.4 Molecular Complexes of 5-fluorocytosine: synthesis by co-crystallisation and development of cooling crystallisation routes

7.4.1 Introduction

A substantial co-crystal screen was carried out of fluorinated nucleotide bases with a range of different carboxylic derivatives in order to investigate the effect of co-crystallisation upon solubility of the fluorinated nucleotide bases for their potential use as APIs (J. King & K. E. Wittering; J. King MChem project, University of Bath, 2013). Nucleobases are precursors for a range of APIs, especially cytosine which forms the basis of several anticancer and retroviral drugs such as Lamivudine and Cytarabine[172]. 5-flurocytosine is an antimycotic API that displays anti-fungal properties and is often used for fungal infection treatment administered in combination with amphotericin B[173].

One of the other key aims of this research was to use the anticipated co-crystal systems as an initial vehicle for moving away from the more commonplace small scale evaporative crystallisation into small scale cooling crystallisation in preparation for scale up to continuous cooling crystallisation. Two new multi-component molecular complexes of cytosine (CYT) and 5-fluorocytosine (5FCYT) with 4-chloro-3,5-dinitrobenzoic acid (4Cl35DNBA) were discovered in this study, and were selected as potential candidates for transfer to continuous cooling crystallisation. The structural and physical characterization of the new materials and preliminary experiments to transfer these systems into controlled small scale cooling crystallisation are discussed here and have been published by Wittering *et al*.[100]

In addition, a previously unreported polymorph of 4Cl35DNBA was identified through analysis of the starting material supplied by Sigma Aldrich, which emphasises the need to analyse the starting materials, as discussed for barbituric acid in section 4.1. The structural comparison to 4Cl35DNBA Form I, reported by Rehman *et al*.[174], is detailed in section 7.4.5.[100]

7.4.2 Materials

5-fluorocytosine, 98% pure was obtained from Fluorochem Ltd. (Hadfield, UK) and cytosine, 99% pure, and 4-chloro-3,5-dinitrobenzoic acid, 97% pure were both supplied by Sigma Aldrich (Gillingham, UK). All crystallisations were performed using either 99% acetone or 99.8% ethanol from Sigma Aldrich in combination with deionized water to form solvent water mixtures of different ratios.

7.4.3 A 1:1 Molecular Complex of 5-fluorocytosine and 4-chloro-3,5-dinitrobenzoic Acid

7.4.3.1 Experimental

5FC and 4Cl35DNBA (Figure 7.42) were co-crystallised in an ethanol and water solvent mix (1:1 by volume). 5FC (13.2 mg) and 4Cl35DNBA (12.9 mg) were measured into a glass vial and dissolved in the solvent solution using a combination of sonication and gentle heating. The solution was added into a single glass vial, sealed with a perforated plastic lid and left at room temperature (18–22 °C) for slow evaporative crystallisation.

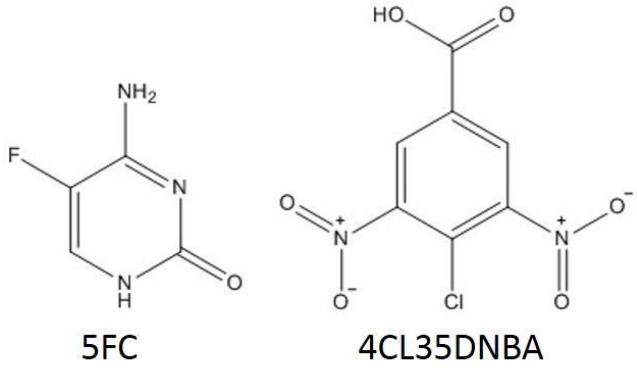

Figure 7.42 Molecular structures of 5-fluorocytosine (5FC) and 4-chloro-3,5-dinitrobenzoic acid (4Cl35DNBA)

7.4.3.2 Structural Analysis and Characterisation

The 1:1 molecular complex of 5-fluorocytosine and 4-chloro-3,5-dinitrobenzoic acid (5FC-4Cl35DNBA) is a salt with proton transfer indicated from the carboxylic acid group of 4Cl35DNBA to the lone pair of the free N2 of 5FC. Heterodimers are formed through two charge-assisted N-H···O hydrogen bonds (N···O distances 2.722(1) Å and 2.803(1) Å) (Figure 7.43 a and b, respectively). Two heterodimers related by a centre of inversion combine to form a tetramer through an additional N-H···O hydrogen bond (N···O 2.871(1) Å) as well as a C-H···F weak hydrogen bond (C···F 3.091(1) Å). Each tetramer unit forms two further hydrogen bonds to neighbouring tetramers through atoms O6 (H-bond acceptor) and N1 (H-bond donor). These connected chains pack in a zig-zag, layered arrangement along the (-1 0 1) plane.

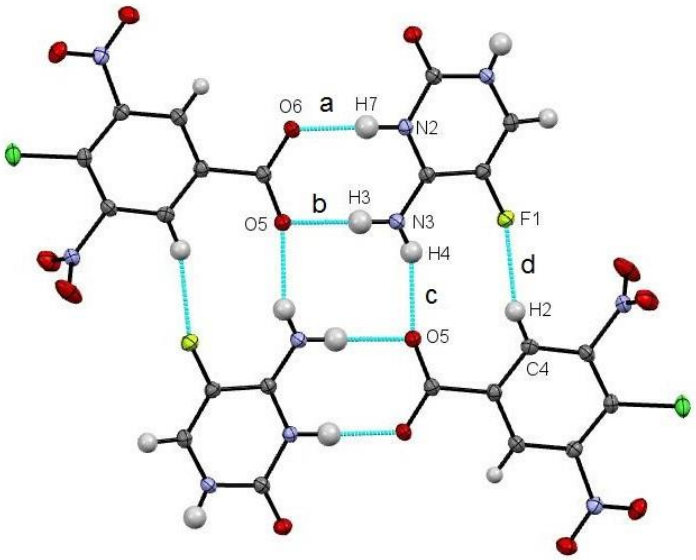

Figure 7.43 A tetramer unit of the 5FC-4Cl35DNBA molecular complex. (a) and (b) are the N-H···O hydrogen bonds forming the dimer, (c) and (d) are the N-H···O and C-H···F hydrogen bonds, respectively, that connect the two dimers together into the tetramer

Table 7.13 Hydrogen bond distances within the molecular complex of 5FC and 4Cl35DNBA

D-H···A	D-H (Å)	H···A (Å)	D···A (Å)	<(DHA) (º)
C4-H2···F1 #1	0.95(2)	2.23(2)	3.091(1)	150(1)
N1-H6···O6 #2	0.84(2)	2.07(2)	2.810(1)	147(2)
N3-H4···O5 #3	0.85(2)	2.08(2)	2.871(1)	154(2)
N3-H3···O5 #4	0.92(2)	1.88(2)	2.803(1)	177(2)
N2-H7···O6 #4	0.95(2)	1.78(2)	2.722(1)	171(2)

Symmetry transformations used to generate equivalent atoms:

#1(x, y+1, z), #2(x-1/2, -y+5/2, z-1/2), #3(x, y-1, z), #4(-x+2, -y+3, -z)

PXRD shows that when crystallisation is initiated from a solution of a 1:1 ratio or a 2:1 ratio of starting materials (5FC:4Cl35DNBA), the same 1:1 5FC-4Cl35DNBA complex is formed, which is indicated by the intense peaks at 24.4º 2θ and 27.3º 2θ in the PXRD (Figure 7.44). However, when crystallised using a 1:2 starting ratio of 5FC to 4Cl35DNBA a unique and intense PXRD peak can be seen at 26.4° 2θ. This does not correspond to the 5FC-4Cl35DNBA complex, nor is it representative of either 5FC or 4Cl35DNBA (including any known hydrates or solvates). This would infer that there is new material present, which could be a new polymorph, a new multi-component molecular complex or another solvate of the starting materials; further analysis is required to elucidate this phase.

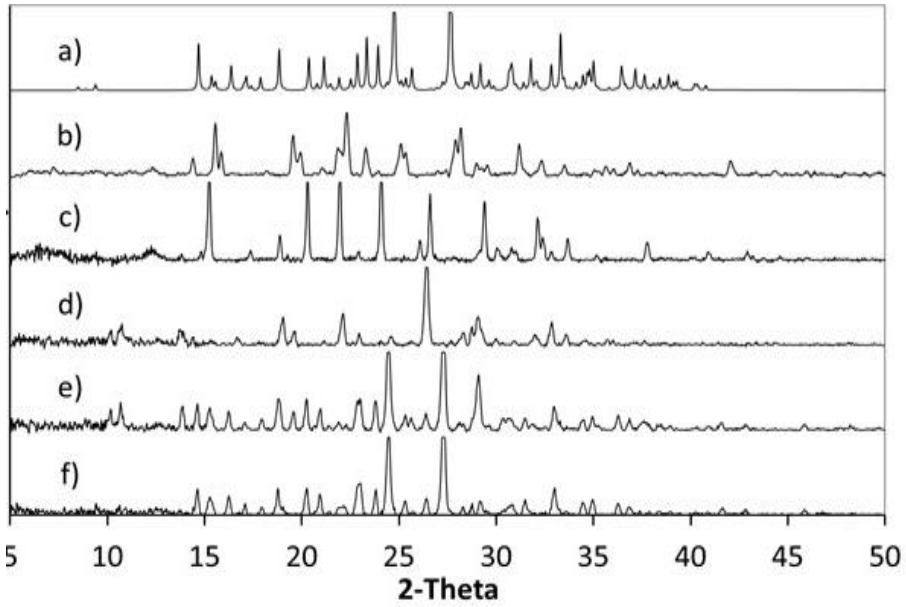

Figure 7.44 PXRD pattern generated from the single crystal determined structure of 5FC-4Cl35DNBA for comparison with PXRD patterns of (b) 4Cl35DNBA, (c) 5FC, and products of evaporative crystallisation of 5FC:4Cl35DNBA in ethanol:water (1:1 by volume) in various ratios: (d) 1:2 (e) 2:1 and (f) 1:1

DSC of a pure sample of 5FC-4Cl35DNBA arising from 1:1 evaporative crystallisation (as characterised through PXRD) shows a single endothermic event at 196.1 °C prior to decomposition (Figure 7.45a). This does not correspond to the DSC traces of the 4Cl35DNBA and 5FC starting materials. 4Cl35DNBA displays an endothermic event at 162.2 °C (Figure 7.45 b), which corresponds to its literature melting point of 159-162 °C and 5FC displays an exothermic event at 292.6 °C, which corresponds to 5FC thermal decomposition (296 °C) (Figure 7.45 c).

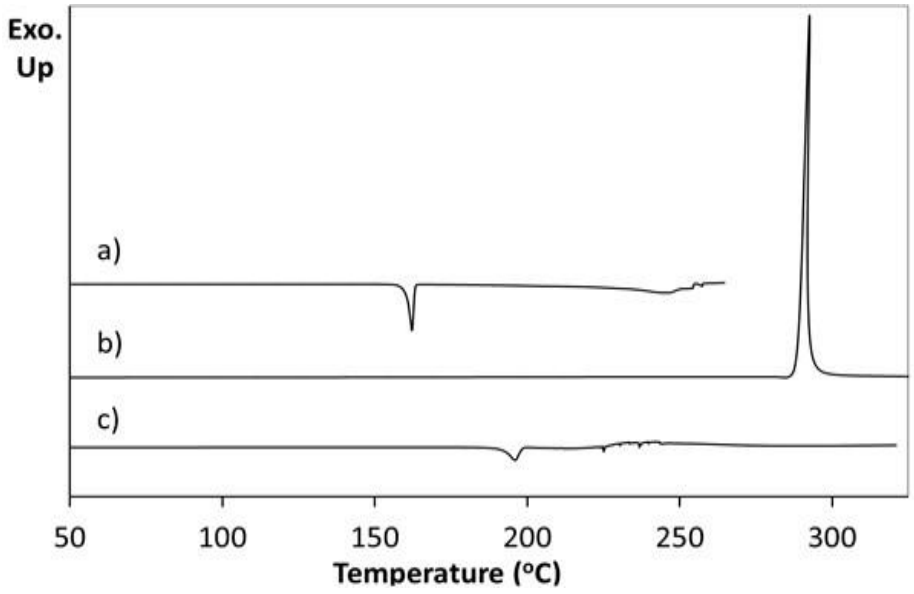

Figure 7.45 Differential scanning calorimetry of (a) 5FC-4Cl35DNBA (b) 4Cl35DNBA (c) 5FC

7.4.4 A 2:1 Monohydrated Molecular Complex of Cytosine and 4-chloro-3,5-dinitrobenzoic Acid

7.4.4.1 Experimental

CYT-4Cl35DNBA was formed from a saturated solution of the molecular components (Figure 7.46). 20 ml of acetone and water solvent solution (1:1 ratio by volume) was added to a conical flask followed by a 4:1 ratio of CYT:4Cl35DNBA until a fully saturated solution was achieved for cooling crystallisation (111.5 mg 4Cl35DNBA and 236.5 mg CYT). However, this sample immediately formed a slurry which remained in suspension. A small aliquot was transferred into a separate vial where solvent was allowed to evaporate at a constant temperature of 30 °C. After approximately 24 hours several single crystals formed. These were subsequently used for SXRD analysis. Interestingly, after 48 hours at 30 °C the rest of the slurry suspension began to re-dissolve. After 5-7 days the solvent had completely evaporated and a mixture of small, yellow needle crystals and larger plate crystals were produced.

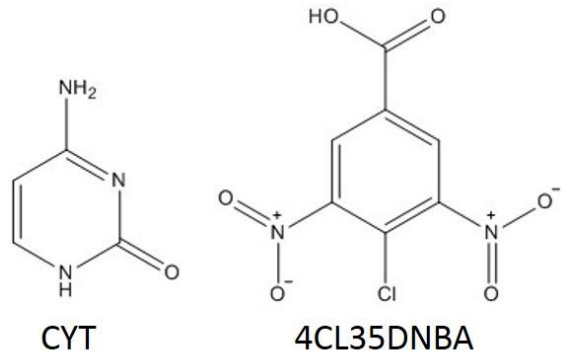

Figure 7.46 Molecular structures of cytosine (CYT) and 4-chloro-3,5-dinitrobenzoic acid (4Cl35DNBA)

7.4.4.2 Structural Analysis and Characterisation

In contrast to the 5FC-4Cl35DNBA molecular complex, CYT forms a monohydrated 2:1 complex with 4Cl35DNBA (CYT-4Cl35DNBA). The asymmetric unit contains a water molecule, a single 4Cl35DNBA molecule and two cytosine molecules (Figure 7.47). Interestingly, only one cytosine molecule remains neutral while the other accepts a proton from the carboxylic acid group of the 4Cl35DNBA molecule. De-protonation of the carboxylic acid group is indicated by the similarities in the C8-O3 and C8-O4 bond distances, at 1.230(3) Å and 1.258(3) Å, respectively.

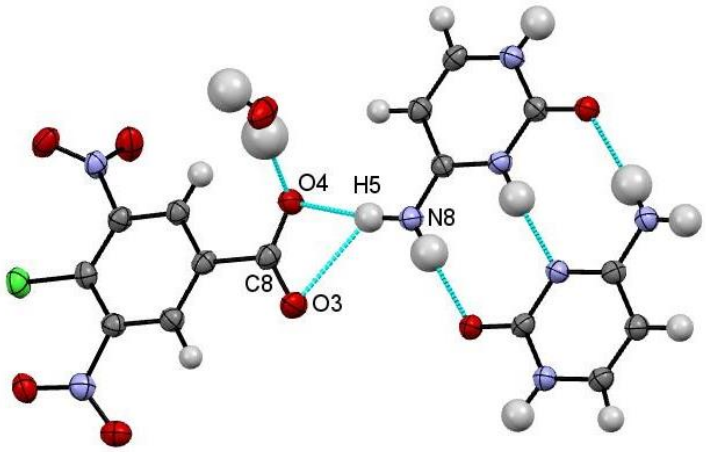

Figure 7.47 Asymmetric unit of CYT-4Cl35DNBA displaying the hydrogen bonding interactions of the deprotonated 4Cl35DNBA carboxylic acid group with the cytosine homodimer

Table 7.14 Hydrogen bond distances within the molecular complex of CYT and 4Cl35DNBA

Hydrogen Bond	D-H (Å)	H···A (Å)	D···A (Å)	<DHA (°)
N10-H3···O17 #1	0.91(3)	1.91(3)	2.806(3)	171(3)
C26-H2···O3 #2	0.95(3)	2.08(3)	3.015(3)	169(2)
C10-H8···O5 #3	0.94(3)	2.61(3)	3.527(3)	165(2)
N15-H9···O13 #4	0.98(3)	1.83(3)	2.804(3)	178(3)
N8-H5···O3 #5	0.96(3)	2.49(3)	3.186(3)	130(2)
N8-H5···O4 #5	0.96(3)	1.85(3)	2.802(3)	170(3)
N14-H12···O15 #6	0.90(3)	1.92(3)	2.793(3)	161(3)
C20-H10···O8 #4	0.97(3)	2.53(3)	3.026(3)	112(2)
N9-H4···N16 #7	0.91(3)	1.91(4)	2.820(3)	175(3)
N8-H6···O17 #7	0.90(4)	1.91(4)	2.809(3)	174(3)
N14-H13···O13 #8	0.90(4)	1.97(4)	2.865(3)	169(3)
O15-H15···O6 #9	0.87(5)	2.46(4)	3.146(3)	136(4)
O15-H15···O7 #10	0.87(5)	2.44(4)	3.055(3)	128(4)
O15-H14···O4	0.85(5)	1.93(5)	2.743(3)	161(4)

Symmetry transformations used to generate equivalent atoms:

#1(x, -y+1/2, z-1/2), #2(-x+1, y-1/2, -z+1/2), #3(x, y-1, z), #4(x, -y+1/2, z+1/2), #5(-x+1, y+1/2, -z+1/2), #6(x, y+1, z), #7(x, -y+3/2, z-1/2),#8(x, -y+3/2, z+1/2),#9(-x, -y+1, -z),#10(-x, -y, -z)

Variation in the protonation states of the two cytosine species facilitates formation of a cytosine homodimer bound through a pseudo Watson-Crick hydrogen bonding interaction consisting of three

moderately strong hydrogen bonds N8-H6···O17, N9-H4···N16 and N14-H13···O13 with D···A distances of 2.809 (3) Å, 2.820 (3) Å and 2.865 (3) Å, respectively (Figure 7.48). Three further prominent hydrogen bonds link the three components of the molecular complex. Atom H5 acts as a bifurcated hydrogen bond donor to the carboxylate ion of 4Cl35DNBA and the water molecule forms a moderate strength hydrogen bond with atom O4 of the carboxylate group. The cytosine and 4Cl35DNBA molecules lie parallel to the (1 0 -1) plane with each inversion related layer hydrogen bonded to the other through a water molecule.

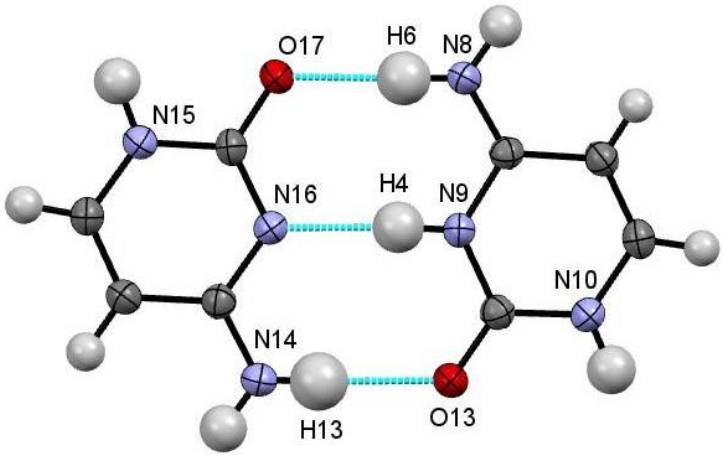

Figure 7.48 A cytosine dimer with pseudo Watson-Crick hydrogen bonding arrangement within CYT-4Cl35DNBA

The products of further evaporative crystallisations of cytosine with 4Cl35DNBA were analysed using a combination of SXRD and PXRD (Figure 7.49). This confirmed that when using a 2:1 ratio of cytosine to 4Cl35DNBA the initial stoichiometry was retained and the 2:1 molecular complex CYT-4Cl35DNBA was produced. However, when a 1:1 stoichiometry of starting materials was used a crystalline powder was formed and the resulting PXRD pattern does not correspond to any of the starting materials (including polymorphs or solvates) or to the 2:1 molecular complex; it may, therefore, represent an additional unknown complex which could be a 1:1 molecular complex of cytosine and 4Cl35DNBA or a non-hydrated molecular complex of cytosine and 4Cl35DNBA.

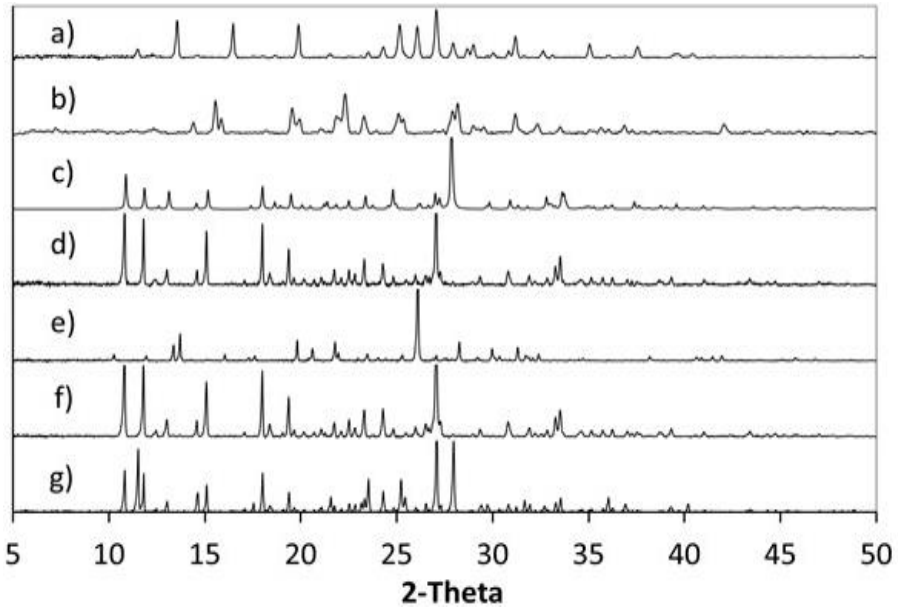

Figure 7.49 PXRD patterns of (a) cytosine, (b) 4Cl35DNBA and (c) a pattern calculated from the single crystal structure of CYT-4Cl35DNBA. These were compared with PXRD patterns of bulk products of evaporative crystallisation of cytosine and 4Cl35DNBA from different crystallisation conditions using (d) a 2:1 starting material ratio from ethanol and water, (e) a 1:1 starting material ratio from acetone and water, (f) a 2:1 starting material ratio in acetone and water and (g) supersaturated preparation from which the single crystal used for full SXRD data was obtained

The DSC trace for this form is simpler than that observed for the 2:1 CYT-4Cl35DNBA with a single endothermic event at a similar onset temperature to the second event in the 2:1 molecular complex (1:1, 192.3 °C; 2:1 184.2 °C) (Figure 7.50). The DSC trace for the 2:1 complex has an initial broad endothermic event at 95 °C which may reflect a desolvation process or a transformation into a different polymorphic or stoichiometric form.

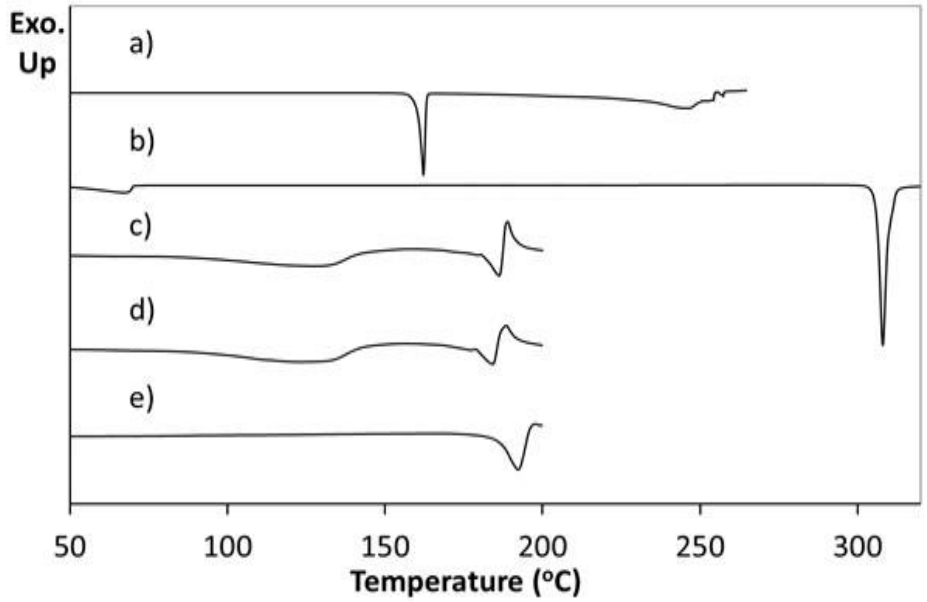

Figure 7.50 Differential scanning calorimetry of (a) 4Cl35DNBA and (b) cytosine, together with those for products of the evaporative crystallisation of cytosine and 4ClDNBA in: (c) a 2:1 starting material ratio in ethanol and water; (d) a 2:1 starting material ratio in acetone and water; (e) a 1:1 starting material ratio in acetone and water

7.4.5 A New Polymorph of 4-chloro-3,5-dinitrobenzoic Acid

7.4.5.1 Experimental

Attempts at co-crystallisation with 5FCYT and 4Cl35DNBA from ethanol and water *via* small scale evaporative crystallisation yielded single crystals of 4Cl35DNBA Form II which was shown to be a previously unreported polymorphic form of the 4Cl35DNBA starting material (Figure 7.51), as supplied by Sigma Aldrich.

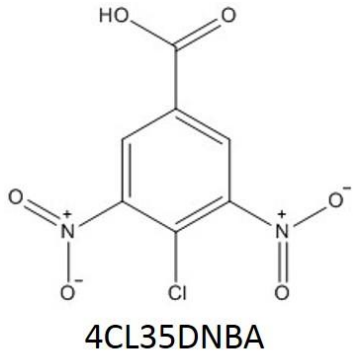

Figure 7.51 Molecular structure 4-chloro-3,5-dinitrobenzoic acid (4Cl35DNBA)

7.4.5.2 Structural Analysis and Characterisation

Further to the discovery of the two new multi-component molecular complexes discussed above, an additional polymorphic form of the starting material 4Cl35DNBA (Form II) was also characterised. The known crystal structure of 4Cl35DNBA (Form I) (Cambridge Structural Database (CSD) Refcode TIBGIV[174]) contains one molecule in the asymmetric unit and crystallises in the triclinic crystal system with space group $P\bar{1}$. The PXRD pattern of the 4Cl35DNBA starting material taken as received from Sigma Aldrich does not match the PXRD pattern generated from SXRD data of Form I (Figure 7.52).

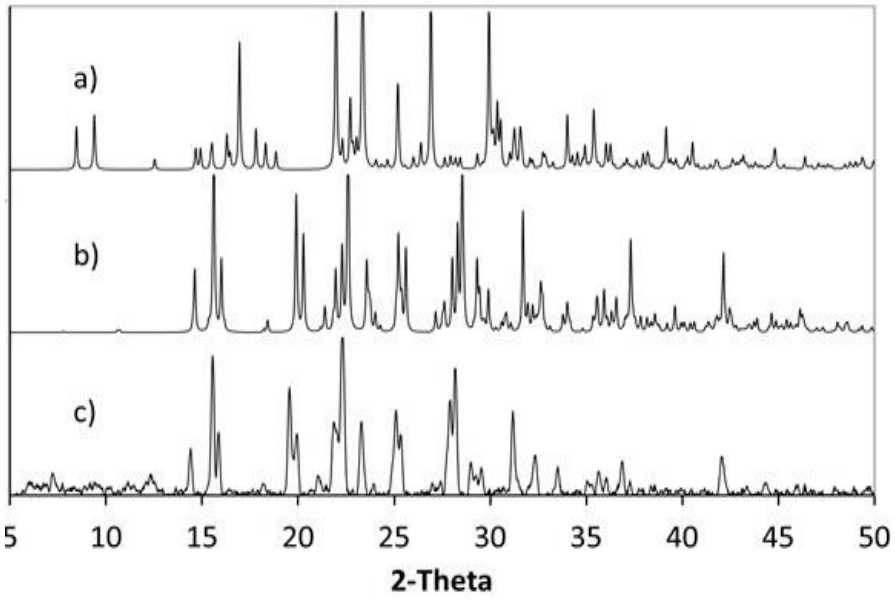

Figure 7.52 PXRD patterns of (a) 4Cl35DNBA Form I (calculated from SXRD structure) (b) 4Cl35DNBA Form II (calculated) (c) 4Cl35DNBA Form II (as supplied from Sigma Aldrich)

The asymmetric unit of Form II consists of two independent 4Cl35DNBA molecules connected through two O-H···O hydrogen bonds between the carboxylic acid moieties creating a carboxylic acid dimer motif. Form I also contains similar 4Cl35DNBA homodimer motifs; however, the homodimeric motif in Form I is planar in contrast to the twisted, non-planar dimer of Form II (Figure 7.53). In both polymorphs the homodimers pack through π-π stacking interactions to form sheets but with differing staggering of the homodimer units (Figure 7.54).

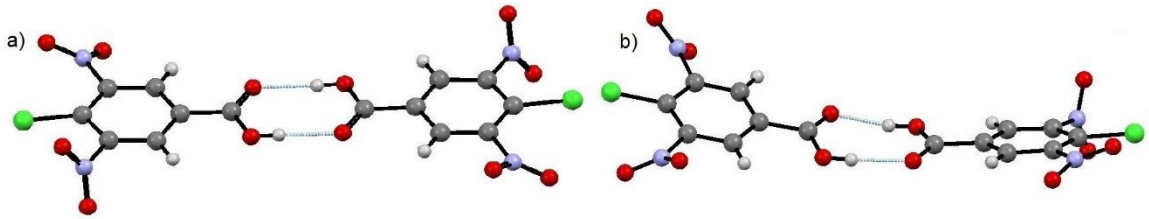

Figure 7.53 Hydrogen bonded dimer of 4Cl35DNBA in: (a) 4Cl35DNBA Form I (b) 4Cl35DNBA Form II

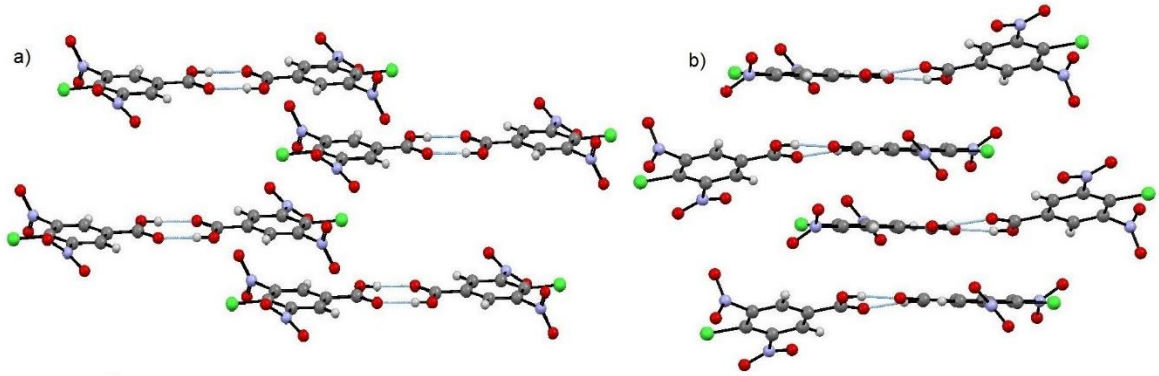

Figure 7.54 4Cl35DNBA dimers packing into layered sheets through π-π stacking interactions in: (a) **4Cl35DNBA Form I** (b) **4Cl35DNBA Form II**

Table 7.15 Hydrogen bond distances within the new polymorph of 4Cl35DNBA

D-H···A	D-H (Å)	H···A (Å)	D···A (Å)	<(DHA) (º)
O9-H6···O5 #1	0.84(2)	1.86(2)	2.695(1)	174(2)
O6-H3···O10 #1	0.84(2)	1.78(2)	2.613(1)	171(2)

Symmetry transformations used to generate equivalent atoms:

#1(-x+1, -y+1, -z)

Table 7.16 Crystallographic information on two new multi-component molecular complexes of 4Cl35DNBA and a new polymorphic form of 4Cl35DNBA

Molecular complex	5FC-4Cl35DNBA	CYT-4Cl35DNBA	4Cl35DNBA (Form II)
Formula	$[C_4H_5ON_3F]^+.$ $[C_7H_2N_2O_6Cl]^-$	$C_4H_5N_3O\cdot$ $[C_4H_6N_3O]^+$ $[C_7H_2N_2O_6Cl]^-.H_2O$	$C_7H_3ClN_2O_6$
Molecular weight ($g.mol^{-1}$)	375.7	486.8	246.6
Temperature (K)	100	100	100
Space group	$P2_1/n$	$P2_1/c$	$P2_1/n$
a (Å)	12.068(1)	14.383(3)	8.9032(4)
b (Å)	6.0558(6)	8.399(2)	8.9201(6)
c (Å)	18.857(2)	17.339(4)	22.697(2)
α (°)	90.00	90.00	90.00
β (°)	93.021(7)	110.478(8)	90.880(6)
γ (°)	90.00	90.00	90.00
Volume ($Å^3$)	1376.2(3)	1962.1(7)	1802.3(2)
Z	4	4	8
ρ (calcd)/Mg m^{-3}	1.813	1.648	1.817
θ range/°	3.2-27.5	3.0-27.5	3.2-27.5
Completeness (%)	99.9	99.9	99.8
Reflections collected	17302	24995	20452
No. of unique data [R_{int}]	3153 [0.031]	4495 [0.096]	4130 [0.029]
No. of reflections with $I>2\sigma(I)$	2918	2748	3532
GooF on F^2	1.063	1.004	1.017
Final R_1 ($I>2\ \sigma(I)$)	0.029	0.052	0.028
Final wR_2 (all data)	0.081	0.152	0.069
CCDC No.	976509	976510	976508

7.4.6 Solubility Analysis of 5FC-4Cl35DNBA

To inform and help interpret the targeted cooling crystallisation experiments, and also as a key target property in crystal engineering approaches to new solid forms, solubility analysis of 5FC-4Cl35DNBA was carried out using the Crystal16. This confirms that the molecular complex is significantly less soluble than both 5FC and 4Cl35DNBA starting materials (Figure 7.55). It proved difficult to collect a wide range of solubility data for 4Cl35DNBA using the Crystal16 due to its very

high solubility. The volume of solid required to saturate the solution at high temperatures was too great for the small 2 mL vials. Additionally, when using large volumes of solid, magnetic stirring within the vials was hindered.

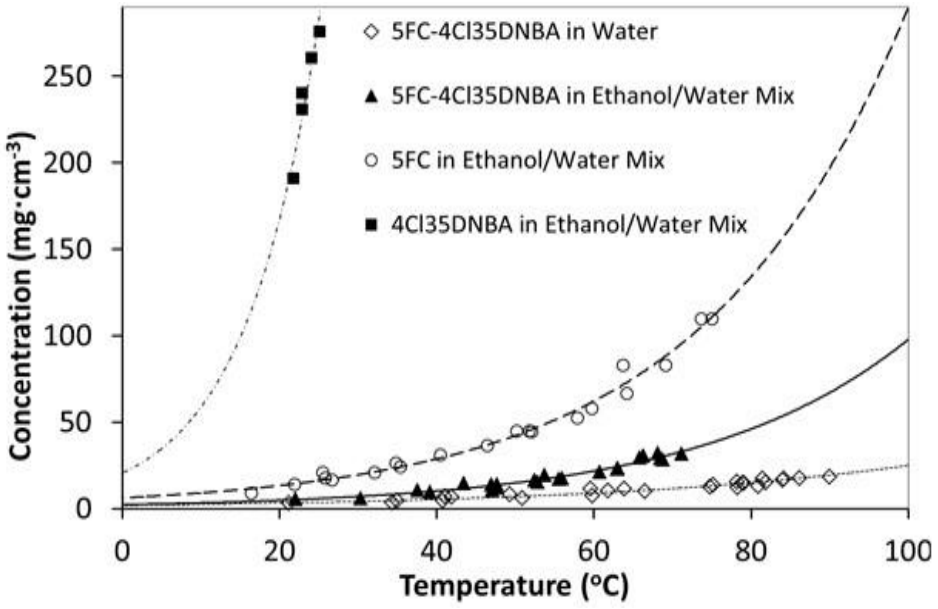

Figure 7.55 Comparison of solubility of 5FC-4Cl35DNBA co-crystal with 5FC and 4Cl35DNBA starting materials

Solubility analysis showed 4Cl35DNBA to be approximately six times more soluble in ethanol than 5FC. 5FC was more soluble in ethanol than in water and 4Cl35DNBA did not dissolve in water alone. In light of this a mixture of ethanol and water was used to help to reduce the solubility of 4Cl35DNBA. Turbidity measurements showed a 7:3 mixture of ethanol to water (by volume) to be a suitable ratio of solvents for this system.

7.4.7 Transfer to Cooling Crystallisation

Each mixture of molecular components was added to 20 ml of hot solvent solution (50 °C) until saturated. After this, the solution was left to settle whilst held at 50 °C. The top aliquot was removed using a heated syringe with micro filter and was subsequently divided into several 2.5 ml glass vials, each sealed with a cap and plastic paraffin film to minimise any possibility of evaporative crystallisation. The glass vials were then placed into a Barnstead/Stem RS12 ReactArray Reaction Block (RB) with an RS12 power supply and subjected to one of two cooling profiles generated and controlled using ReactArray Solo software Version 0.9.0.0 © 2005 Anachem Ltd. In cooling profile 1, which was used for solutions prepared with acetone, the vials were held at 50 °C for an hour followed by cooling to -5 °C at 0.2 °Cmin^{-1}. Cooling profile 2 held the vials at 65 °C for an hour prior to cooling at a rate of 0.5 °Cmin^{-1} to -5 °C. This was used for solutions prepared with ethanol. Details of the cooling crystallisations using the RB are provided in Table 7.17.

Four cooling crystallisations of 4Cl35DNBA with cytosine or 5FC were carried out with differing conditions (Table 7.17); all produced very fine, yellow needle crystals. SXRD analysis of each sample showed that several crystals in each preparation corresponded to the targeted molecular complex previously discovered through evaporative routes as described above.

Table 7.17 Cooling crystallisation experiments of CYT with 4Cl35DNBA and 5FCYT with 4Cl35DNBA using a ReactArray Reaction Block

Sample	Components	Ratio	Solvent	Cooling profile
A	CYT, 4Cl35DNBA	1:1	acetone and water	1
B	5FC, 4Cl35DNBA	1:1	acetone and water	1
C	5FC, 4Cl35DNBA	1:1	ethanol and water	2
D	5FC, 4Cl35DNBA	1:2	ethanol and water	2

PXRD analysis of sample A (Figure 7.56) confirmed that CYT-4Cl35DNBA was produced, though it is important to note that the peak intensities do vary due to preferred orientation. The bulk of samples B, C and D were confirmed to be 5FC-4Cl35DNBA (Figure 7.57).

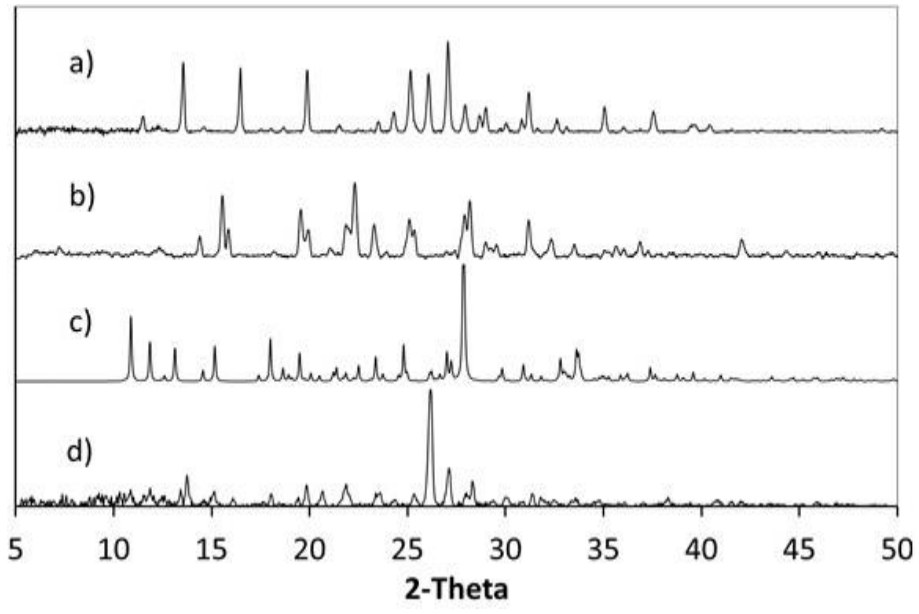

Figure 7.56 PXRD analysis of products of cooling crystallisation A (a) CYT (b) 4Cl35DNBA (c) CYT-4Cl35DNBA (d) Product A

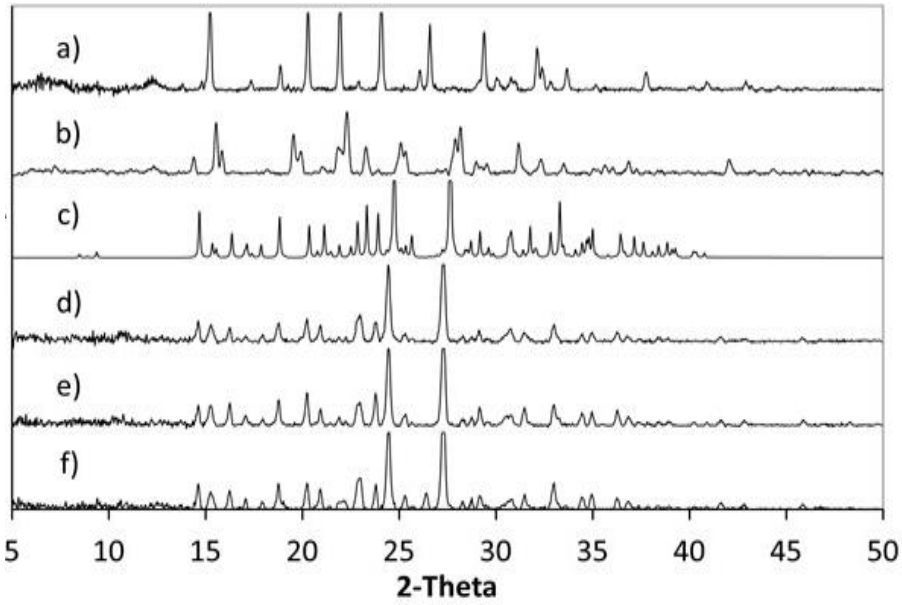

Figure 7.57 PXRD Analysis of cooling crystallisations B, C and D. (a) 5FC (b) 4Cl35DNBA (c) 5FC-4Cl35DNBA (d) Product B (e) Product C (f) Product D

The formation of 5FC-4CL35DNBA could be followed during the cooling crystallisation using turbidimetric methods using a Crystal16 apparatus (Figure 7.58). Initially the turbidity signal is noisy due to the particle size but ranges from 60% to 100% transmittance. As the temperature increases the solution becomes turbid and the transmittance drops to 0%. This increase in turbidity with an increase in temperature in the early stages of the process is perhaps counterintuitive and indicates the initial, rapid, formation of the less soluble multi-component complex (as shown by solubility measurements of the complex). As the temperature continues to increase, 5FC-4Cl35DNBA dissolves and the solution develops 100% transmittance. 5FC-4Cl35DNBA then recrystallises upon cooling and the transmittance returns to 0%. Importantly, repetition of the heating and cooling temperature ramps then follows the expected trend, showing cloud points and clear points at the same temperatures as before.

It should be noted that there are very few previous examples of the crystallisation of multi-component complexes by cooling at this scale. This relatively simple methodology thus acts as an exemplar for the intended transfer of such processes into the continuous environment, by establishing the initial cooling stage. It is also useful to note that these determinations illustrate that significant progress can be made in establishing such crystallisation processes using relatively simple analytical methods such as turbidity measurement (while acknowledging its inherent limitations), even in the absence of full process analytical technologies (PAT).

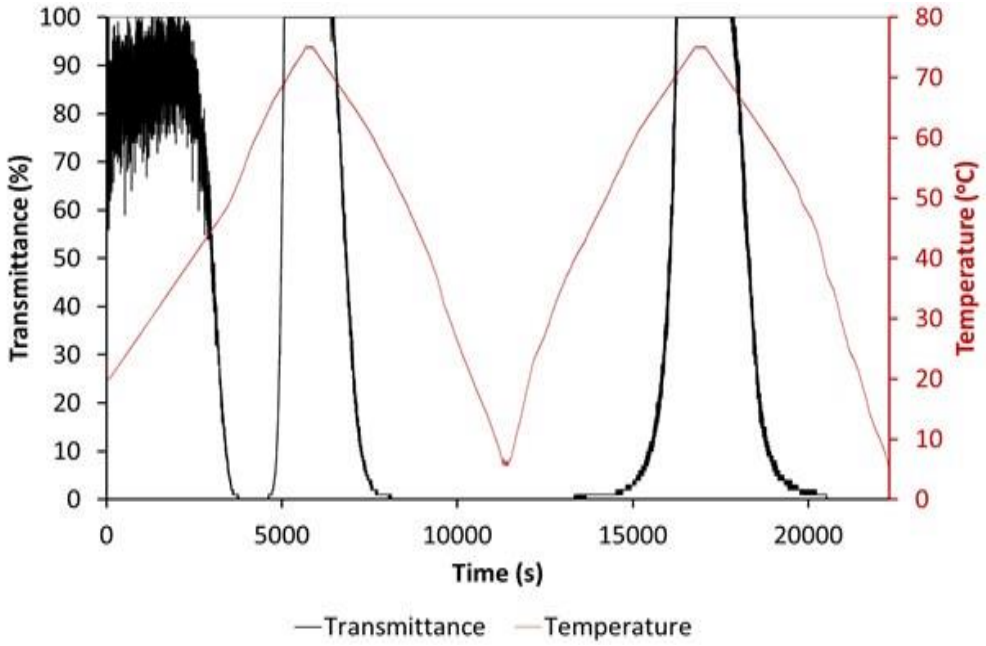

Figure 7.58 Plot of turbidity data from cooling crystallisation of 5FC with 4Cl35DNBA (1:2) in ethanol and water (7:3 by volume). The temperature regimes used are shown in red.

PXRD analysis of a range of samples from Crystal16 experiments confirm the formation of 5FC-4Cl35DNBA (Figure 7.59) as indicated by the initial precipitation shown in the turbidity data. It should be noted, however, that when a slower cooling rate of 0.5 °Cmin^{-1} was used, residual 4Cl35DNBA form II was present in the product as shown by the additional peaks in the PXRD pattern at 15.6° 2θ and 28.2° 2θ (Figure 7.59 d). While such a slow cooling rate is unlikely to be industrially relevant, for example, this element of the study was undertaken to explore the effect of cooling rate on the crystallisation products. The melt at 154.3 °C observed in DSC analysis (Figure 7.60 a) is much lower than those for the other samples, and is similar to the melting point of 4Cl35DNBA form II (162.2 °C). The other samples show endothermic events at 197.9 °C and 195.8 °C which are consistent with the 5FC-4Cl35DNBA sample produced from evaporative cooling as discussed above.

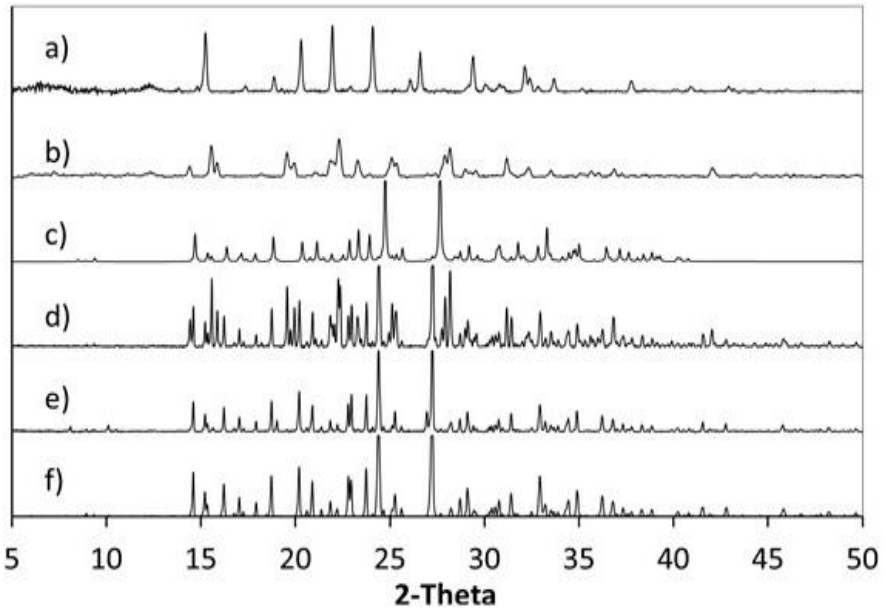

Figure 7.59 PXRD analysis of cooling crystallisations carried out using the Crystal16 apparatus: (a) 5FC (b) 4Cl35DNBA form II (c) 5FC-4Cl35DNBA. Products from 5FC and 4Cl35DNBA crystallisation in ethanol:water (7:3 by volume) in a: (d) 1:2 starting material ratio (0.5 °Cmin^{-1}), (e) 1:2 starting material ratio (2 °Cmin^{-1}) and (f) 1:1 starting material ratio (2 °Cmin^{-1})

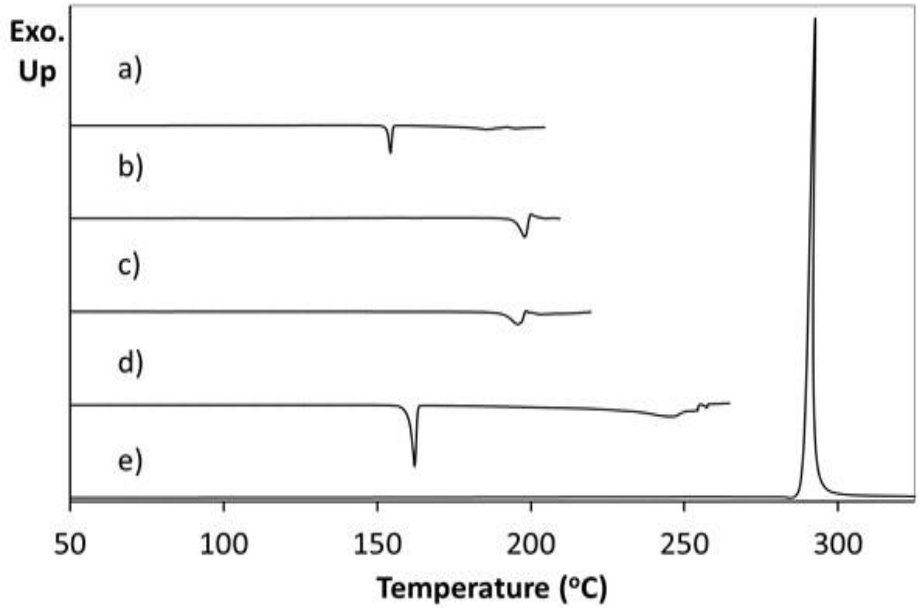

Figure 7.60 Differential scanning calorimetry of cooling crystallisations using the Crystal 16 involving 5FC-4Cl35DNBA. 5FC with 4Cl35DNBA in ethanol:water (3:7 by volume) in a: (a) 1:2 ratio (0.5 °Cmin^{-1}), (b) 1:2 ratio (2 °Cmin^{-1}) and (c) 1:1 ratio (2 °Cmin^{-1}) (d) 4Cl35DNBA (e) 5FCYT

7.4.8 Conclusions

The work presented here represents the initial attempts to develop control over cooling crystallisation of the 5FC-4Cl35DNBA multi-component system. The crystallisation products from evaporative experiments have been reproduced using small scale cooling crystallisation and attempts have been made to optimise the crystallisation conditions to enable full conversion to the co-crystal. This initial, empirical investigation has established crystallisation under cooling of the target complexes, and the dependence of yield of co-crystal as a function of cooling rate and is of immediate value to the aim of establishing a cooling regime for initial transfer into the cooling/continuous crystallisation environment.

7.4.9 Future Work

The initial empirical approach reported here should be augmented and supported by more comprehensive quantitative studies, for example using PAT exploiting different spectroscopic probes such as solution state Raman and Infrared spectroscopies, or by comprehensive dissolution studies. In particular further investigation is required to understand fully the initial association process visualised in this work by the simplest of these PAT methods, turbidity.

The Crystal16 has been used previously to map out phases for multi-component systems[175] and the overarching aim is to carry out full mapping of these systems to aid control of future crystallisation scale up for multi-component systems. This apparatus also shows potential for future insight into the crystallisation kinetics of the multi-component nucleation process through study of MSZW and crystallisation induction times[176]. Understanding, monitoring and control of the initial association step in crystallisation is a key theme within the CMAC collaboration. It provides fundamental underpinning preparation for future scale-up, in order to achieve a well-integrated and controlled cooling crystallisation process with uniform particle attributes in the continuous crystallisation environment[177]. This will be the subject on ongoing work in this area.

7.5 Multi-component Crystallisation of Fenamic Acid Derivatives: transferability of crystallisation methods and physical property enhancement

7.5.1 Introduction

This work was initially developed in preparation for a research-led undergraduate chemistry course, Frontiers of Crystallography, an idea developed and first implemented by Wilson, Parkin and Thomas in the School of Chemistry at the University of Glasgow[178]. The complexes initially produced for the structural elements of that course were subsequently characterised extensively with respect to their physical properties, structure-property relationships and the transferability of their production across crystallisation methods. The findings are reported here and have been published by Wittering *et al*[21].

Fenamic acid (FEN) along with its derivatives mefenamic acid (MEF), tolfenamic acid (TOL) and flufenamic acid (FLU) were chosen as target materials for multi-component crystallisation screening studies as a highly topical class of non-steroidal anti-inflammatory APIs (NSAIDs) with a highly polymorphic nature due to the conformational freedom at the secondary amine, present in all four molecules.

7.5.2 Materials

MEF, FLU, FEN and BP were purchased from Sigma Aldrich Chemie Gmbh (Steinheim, Germany) and TOL was purchased from TCI UK Ltd (Oxford, UK). All reagents were used without further purification. Laboratory grade solvents purchased from Sigma Aldrich were used for all crystallisations.

7.5.3 Evaporative Crystallisation

Thorough co-crystal screening studies were conducted through evaporative crystallisation methods using several different GRAS co-former molecules, solvents, ratios of fenamic acid derivative (FAD) to co-former and crystallisation temperatures (ca. 200 crystallisations; see Table 7.18).

The crystallisations were prepared using the minimal solvent required for dissolution with the aid of a sonic bath (30 °C). All combinations of API, co-former and ratio stated in Table 7.18 were tested with one or more of the solvents listed depending on solubility, so not all possible solvents were used for each combination. The maximum crystallisation temperature used was appropriate to the boiling point of the solvent used. Whilst co-crystals for all FADs with 4,4'-bipyridine have been reported

previously [179-181] these combinations have been included in this study but with a wider range of co-former / ratio / crystallisation condition permutations than previously reported. Despite this extensive study only 4,4'-bipyridine yielded co-crystals, which were found to comprise the previously reported complexes.

Table 7.18 Experimental variables used in co-crystal screening studies of FADs

FAD	Co-former	Ratio (FAD: co-former)	Solvent	Evaporation temperature (°C)
FEN	Urea[§]	1:1	Methanol	4
FLU	Oxalic acid	2:1	Isopropanol	18
MEF	Isonicotinamide	1:2	Dimethylformamide	30
TOL	Nicotinic acid[§]		Ethanol	50
	4-aminobenzoic acid		Acetone	
	2-aminobenzoic acid		Tetrahydrofuran	
	Pyridoxine[§]			
	Isonicotinic acid hydrazide[§]			
	4,4'-bipiridyl			
	2,2'-bipridyl			
	2-aminopyridine			

[§]Classified as GRAS by the Select Committee on GRAS Substances (SCOGS)

Powder X-ray diffraction was initially used to screen all samples for the presence of new co-crystals. This led to the identification of two initially unknown co-crystals which were structurally characterised using single crystal X-ray diffraction after single crystals of suitable quality were obtained through evaporative crystallisation methods; the previously reported structure of FLU-BP was also re-determined.

The following evaporative conditions were used to produce the four co-crystals characterised in this investigation:

Table 7.19 Evaporative crystallisation conditions used to obtain each FAD-BP co-crystal for structural determination using SXRD

FAD	Mass of FAD (mg)	Mass of BP (mg)	Molar ratio	Solvent	Mass of solvent (g)	Evaporation temperature (°C)
FEN	26	20	1:1	ethanol	2	18
FLU	30	17	1:1	methanol		18
MEF	30	20	1:1	IPA		4
TOL	30	18	1:1	acetone		18

7.5.4 Cooling Crystallisation

All co-crystals resulting from the evaporative screens were also produced using two different cooling procedures; a rapid cooling method and a controlled linear cooling route detailed below. The quantities of the co-crystal components were initially based on the solubility data obtained for the individual APIs in an IPA/H_2O solvent system. Although this method was successful for FEN-BP, this proved unsuccessful for FLU-BP producing a physical mixture of the individual components and very low yields of the MEF-BP and TOL-BP co-crystals. The molar ratios were therefore adjusted until the desired co-crystals could be produced reproducibly. Furthermore, in order to maximise the yield obtained for MEF-BP and TOL-BP the solvent system was changed to IPA and ethanol respectively.

Solutions of each FAD with BP were prepared using the conditions detailed in Table 7.20. After dissolution the solution was either rapidly cooled in an ice bath or subjected to a linear cooling profile of 50 °C to 5 °C at 0.05 °Cmin^{-1} using the Cambridge Reactor Design Polar Bear Plus crystalliser.

7.5.5 Mechano-chemical Crystallisation

All samples used for the solubility and stability measurements were prepared by kneading a 2:1 molar ratio of the FAD to BP with a pestle and mortar for 15 minutes with drop-wise addition of ethanol and IPA for the FEN-BP and MEF-BP co-crystals, respectively, and methanol for the FLU-BP and TOL-BP co-crystals.

Table 7.20 Experimental conditions used in rapid uncontrolled cooling crystallisation and controlled cooling crystallisation of BP with FAD

FAD	Mass of FAD (mg)	Mass of BP (mg)	Molar ratio	Solvent	Mass of solvent (g)	Cooling method
FEN	35	26	1:1	IPA/H_2O (1:1 v/v)	5	rapid uncontrolled cooling in an ice bath
FLU	50	14	2:1	IPA/H_2O (1:1 v/v)		
MEF	75	49	1:1	IPA		
TOL	150	60	3:2	Ethanol		
FEN	35	26	1:1	IPA/H_2O (1:1 v/v)	5	50 °C to 5 °C at 0.05 °Cmin^{-1} (300 rpm stirring)
FLU	50	14	2:1	IPA/H_2O (1:1 v/v)		
MEF	75	49	1:1	IPA		
TOL	150	60	3:2	Ethanol		

7.5.6 Analysis

7.5.6.1 Single Crystal X-ray Diffraction

X-ray diffraction data were recorded on an Agilent Technologies Gemini A Ultra CCD diffractometer, using monochromatic Mo-Kα radiation (λ = 0.71073 Å) at 150 K. The sample temperature was controlled using an Oxford Diffraction Cryojet apparatus and the data processed using CrysAlisPro version 1.171.36.21. The structures were solved by direct methods using SHELXS-97 and full matrix least-squares refinement was carried out using SHELXL-97. All non-hydrogen atoms were refined anisotropically and the hydrogen atoms were placed based on the Fourier difference maps. Molecular parameters for all structures were computed using the program PLATON. Crystallographic data and refinement parameters confirmed the known structures of all complexes, including the very recently reported MEF-BP and TOL-BP (Table 7.21).

Table 7.21 Crystal data and structural refinement parameters for MEF-BP, TOL-BP and FLU-BP

FAD-BP complex	MEF-BP	TOL-BP	FLU-BP
Formula unit	$2C_{15}H_{15}NO_2 \cdot C_{10}H_8N_2$	$2C_{14}H_{12}ClNO_2 \cdot C_{10}H_8N_2$	$2C_{14}H_{10}F_3NO_2 \cdot C_{10}H_8N_2$
M_r	319.37	339.79	1077.97
Crystal system	Triclinic	Monoclinic	Triclinic
Space group	$P\bar{1}$	$P2_1/c$	$P\bar{1}$
a (Å)	7.3086(3)	4.7081(2)	9.8293(4)
b (Å)	8.6692(4)	45.220(1)	10.3830(6)
c (Å)	13.6320(5)	7.9188(3)	24.991(1)
α (°)	106.135(4)	90	84.684(4)
β (°)	99.428(4)	106.896(5)	81.333(4)
γ (°)	98.758(4)	90	71.773(4)
Volume (Å^3)	800.46(6)	1613.1(1)	2392.1(2)
Z	1	2	3
Crystal size (mm^3)	0.20×0.15×0.10	0.20×0.18×0.08	0.13×0.11×0.08
ρ (calcd) (M g m^{-3})	1.325	1.399	1.497
F(000)	338	708	1110
θ Range (°)	2.89 - 29.64	3.01 - 26.37	2.80 - 25.35
Reflections collected	17917	11680	19891
No. of unique data [Rint)]	4011 [0.0444]	3267 [0.0387]	8741 [0.0545]
No. of data with $I > 2\sigma(I)$	2899	2460	4684
Final $R(I > 2\sigma(I))$	0.0485	0.0520	0.0692
Final wR_2 (all data)	0.1137	0.1053	0.2055

7.5.6.2 Powder X-ray Diffraction

PXRD patterns were collected in flat plate mode on a Bruker D8 Advance equipped with monochromated Cu-Kα radiation (λ = 1.54056 Å) in reflection geometry at 298 K.

7.5.6.3 Thermal Analysis

Differential scanning calorimetry (DSC) studies were carried out using a Thermal Advantage Q20 DSC from TA Instruments, equipped with Thermal Advantage Cooling System 90 and operated with a dry nitrogen purge gas at a flow rate of 18 cm^{3}min^{-1}. The samples were placed in sealed Tzero aluminium pans and a heating/cooling rate of 10 °Cmin^{-1} was used.

Data were collected using the software Advantage for Qseries. Complementary visual characterisation of the thermal properties of the co-crystals was carried out using a Mettler Toledo FP82 hot stage equipped with a Leica DM1000 microscope. Each crystal was subjected to a programmed temperature regime using the FP90 Central Processor. The crystals were filmed using an Infinity 2 microscopy camera.

7.5.6.4 Relative Humidity Studies

Samples of the BP co-crystals, prepared by liquid-assisted grinding, and their corresponding fenamic acid starting materials were stored under moderate (24 °C and 45% RH) and harsh (45 °C and 80% RH) humidity conditions for a four and two week period respectively. Samples were taken at regular intervals and analysed using PXRD to determine the stability of the materials under these conditions with time.

7.5.6.5 Infrared Spectroscopy

The FTIR spectra were recorded at room temperature using a Perkin Elmer FTIR Spectrometer in the range 4000-500 cm^{-1} with an ATR sampling accessory.

7.5.6.6 Solubility Measurements

Solubility studies were carried out in a mixed solvent system of IPA and water (1:1 v/v) using a CrystallinePV parallel crystalliser from Technobis Crystallization Systems BV (formerly Avantium Pharmatech BV). Comprised of eight individually controlled reactors each with a working volume of 3-8 cm^3, the CrystallinePV couples turbidity measurements with in-line particle visualisation and was used to obtain the necessary solubility information. The combination of turbidimetric data and images from in-line cameras allows determination of clear points with improved accuracy over turbidity measurements alone. Vials were cycled through temperature ranges from 20 °C to 75 °C using a heating rate of 0.5 $°Cmin^{-1}$ and stirring at 800 rpm using standard (4 mm) magnetic stirrer bars. Data were analysed using CrystalClear software. It should be noted that this solvent system is generally regarded as acceptable for deployment in crystallisation processes within the pharmaceutical.

7.5.7 Results and Discussion

7.5.7.1 Solid state Structure

The two initially unknown co-crystals produced in the evaporative crystallisations (TOL-BP & MEF-BP) were structurally characterised using single crystal X-ray diffraction on single crystals of suitable quality; the previously reported structure of FLU-BP was also re-determined, as the previous determination was of relatively low quality. It should be noted that while this work was in progress,

Surov *et al.*[179] in parallel synthesised and determined the X-ray crystal structures of TOL-BP and MEF-BP co-crystals. The two recently reported co-crystals, as well as the previously reported complexes FEN-BP and FLU-BP, were prepared through evaporative methods) and also by cooling methods and by liquid-assisted grinding, see below). As noted above, a range of other GRAS co-formers were explored; however no new pharmaceutically relevant co-crystals were prepared. The scarcity of co-crystals of FADs is due to both the strong carboxylic acid homodimer synthon that is dominant within the numerous polymorphs of the FADs, and the ability for the molecules to adopt several stable conformations of their own. The strength of these interactions within these systems results in the evident preferential formation of polymorphs over co-crystals.

The crystal structures of MEF-BP and TOL-BP (both form as 2:1 API:BP complexes)[179] contain the common acid-pyridine hydrogen bonded heterosynthon and intramolecular N-H···O hydrogen bond (Figure 7.61, Table 7.22) that has been seen previously in the other co-crystals of FADs with BP[180, 181].The contents of the asymmetric units of MEF-BP and TOL-BP, however, comprise one API molecule and half a BP molecule which is in contrast to the previously reported 2:1 co-crystals of FLU-BP and FEN-BP that have three and two API molecules in the asymmetric unit, respectively. The dihedral angles relating the mean planes of the phenyl rings for each API molecule in the FLU-BP and FEN-BP structures are considerably different, ranging from 49 to 70° for FEN-BP and from 41 to 47° for FLU-BP. The MEF-BP co-crystal displays the largest angle between the mean planes of the phenyl rings of 79.05(4)°.

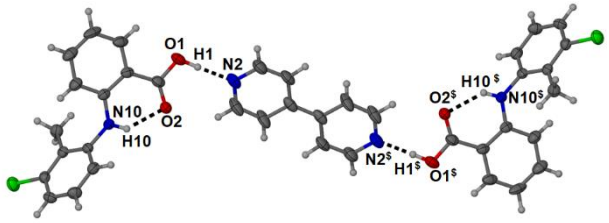

Figure 7.61 The inter- and intramolecular hydrogen bonds of TOL-BP as a representative diagram for the two crystal structures discussed here.

Table 7.22 Geometrical parameters for the significant hydrogen bonds of MEF-BP and TOL-BP

FAD-BP Co-crystal	Hydrogen bond	*d*(H···A)/Å	*d*(D-H···A)/Å	∠(D-H···A)/°
MEF-BP	O1-H1···N2[a]	1.72(2)	2.682(2)	178(2)
	N10-H10···O2	1.94(2)	2.656(1)	137(2)
TOL-BP	O1-H1···N2[b]	1.75(4)	2.674(4)	176(3)
	N10-H10···O2	1.99(2)	2.659(3)	138(2)
	C14-H14···Cl18[c]	2.81(2)	3.634(2)	146(2)

[a]x, 1+y, z; [b]1+x, y, z; [c]-1+x, ½-y, -1/2+z

The overall packing arrangements of MEF-BP and TOL-BP are significantly different from one another. The bipyridine molecule of MEF-BP lies co-planar with the benzoic acid group of mefenamic acid. These co-planar sections are positioned along the (2 -1 1) planes. The semi-perpendicular dimethyl phenyl rings form π-π interactions with their inversion-related counterparts (Figure 7.62) and two weak C-H···O interactions further stabilise the co-crystal and lock the conformation of MEF. The 4,4'-bipyridine molecule of TOL-BP is not co-planar to the benzoic acid group of tolfenamic acid (27(2)° angle between the mean planes; Figure 7.63) which results in extended, twisted TOL-BP-TOL trimer units. The chlorine atoms form weak hydrogen bonds to a phenyl C-atom (C-H···Cl, 3.634(2) Å, 146(2)°). Further detailed structural descriptions and comparisons for MEF-BP, TOL-BP and other previously published fenamates with 4,4-bipyridine have been highlighted in the Surov *et al.* paper.

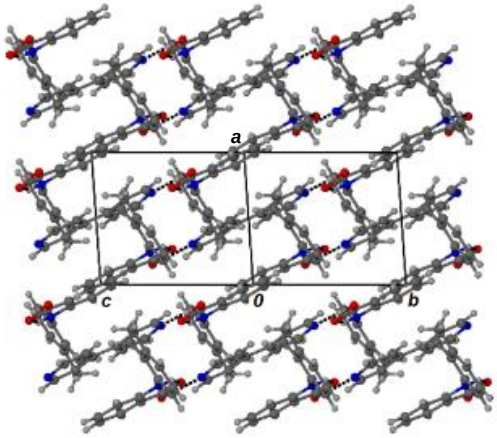

Figure 7.62 The packing arrangement of the MEF-BP co-crystal as viewed along (0 1 1)

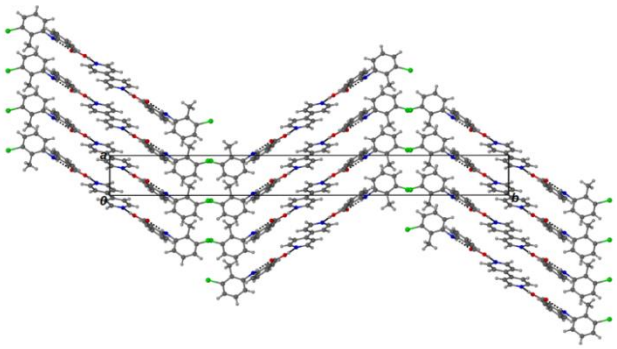

Figure 7.63 A packing diagram of TOL-BP as viewed down the c-axis illustrating the non-planar relationship between the API and 4,4'-bipyridine molecules

Table 7.23 Melting points of the various polymorphs of mefenamic, tolfenamic and flufenamic acid as well as their co-crystals with 4,4'-bipyridine. All temperatures are reported in °C

Polymorph	Mefenamic acid	Tolfenamic acid	Flufenamic acid
I	-†	213.10[5]	134.5[6]
II	229[4]	213.52[5]	129.6[6]
III	-‡	214.09[5]	127.4[6]
IV	-	206.78[5]	123.9[6]
V	-	215.17[5]	124.9[6]
VI	-	-	124.2[6]
VII	-	-	120.7[6]
FAD-BP Complex	163	156	128

† Converts to form II upon heating
‡Converts to form I at ambient temperature and form II upon heating

7.5.7.2 Cooling crystallisation

All samples obtained from the rapid cooling and controlled cooling crystallisations were analysed using PXRD (Figure 7.64) and show that all four co-crystals can be reproducibly prepared on this scale. Interestingly, both the rapid cooling profile and the controlled cooling profile (0.05 $^{\circ}$Cmin^{-1}) give the same crystalline form. This may be an indication of the favourability and stability of these FAD-BP co-crystals.

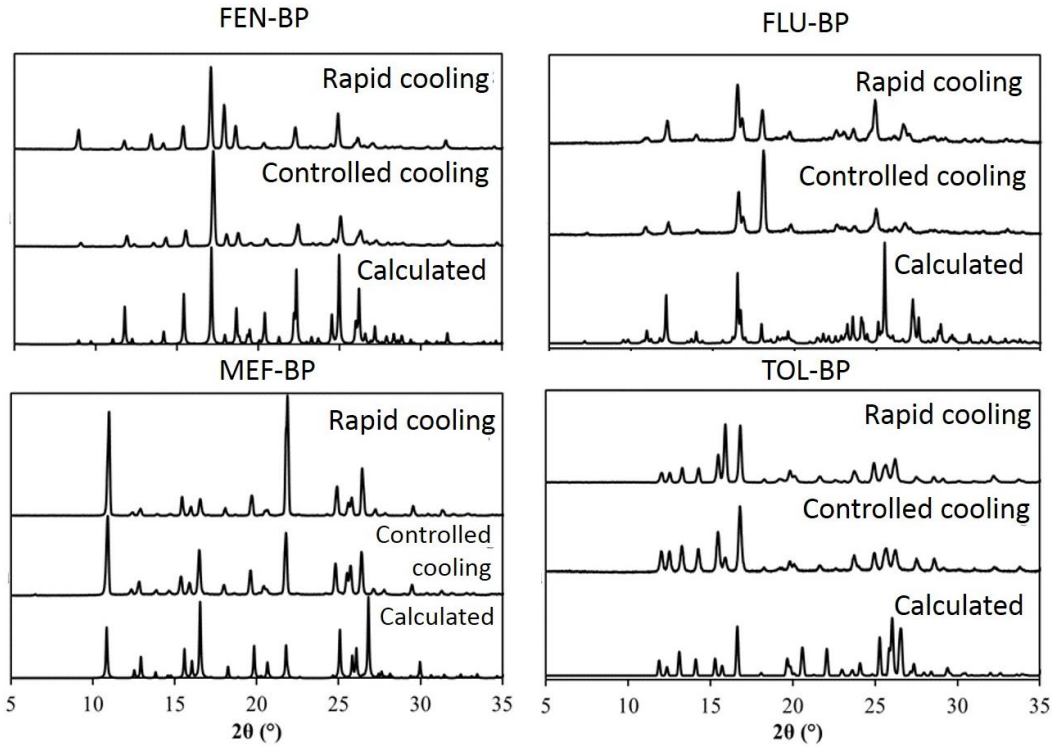

Figure 7.64 Comparison of PXRD patterns of products from cooling crystallisation of FADs with BP with patterns calculated from the respective FAD-BP single crystal data

7.5.7.3 Mechano-chemical Crystallisation

PXRD was used to confirm that the solid forms of the kneaded samples were also the same as those obtained from the slow evaporation method (Figure 7.65).

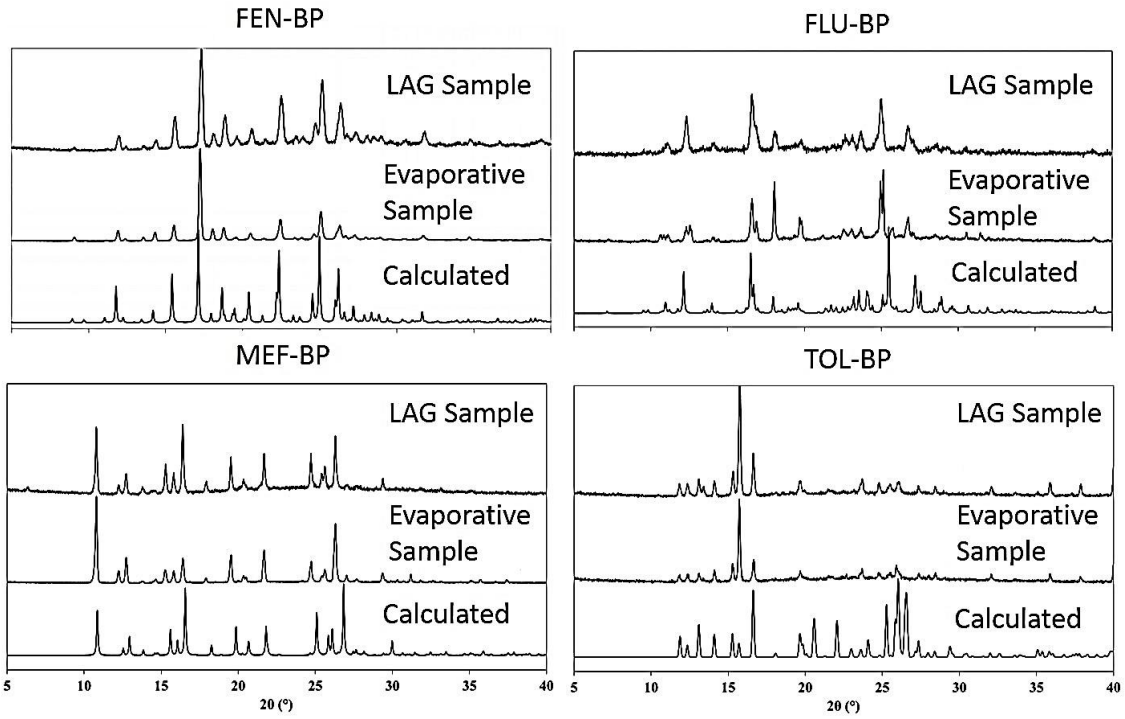

Figure 7.65 PXRD analysis of FAD-BP co-crystals produced from LAG and small scale evaporative crystallisation for comparison with patterns calculated from SXRD data

7.5.7.4 Solubility Analysis

The solubilities of all four co-crystals and their corresponding API starting materials have been determined and compared. When evaluating the solubility of the raw starting materials, FLU is found to be more soluble than the other FADs (5 mg g^{-1} at 25 °C) while MEF and TOL have very low solubilities in the IPA and water solvent system used. The new co-crystals of each FAD also follow this trend with the FLU-BP complex possessing the highest solubility.

Figure 7.66 shows the determined solubilities for each of the four target materials, and the comparison with that for their corresponding BP co-crystal. These results show that the solubility of the co-crystals is comparable to that of the parent APIs. It is important to note that these values only take into account the mass of the API within the co-crystal, allowing direct comparison with the solubility of the pure API.

As an additional contribution towards the full description of solubility trends amongst the fenamic acid series and their BP co-crystals, rapid cooling of a saturated solution of TOL was undertaken,

yielding yellow needles of TOL form II were produced in sufficient quantity to allow the solubility of this polymorphic form to be determined in addition to that of TOL form I (Figure 7.66, bottom right).

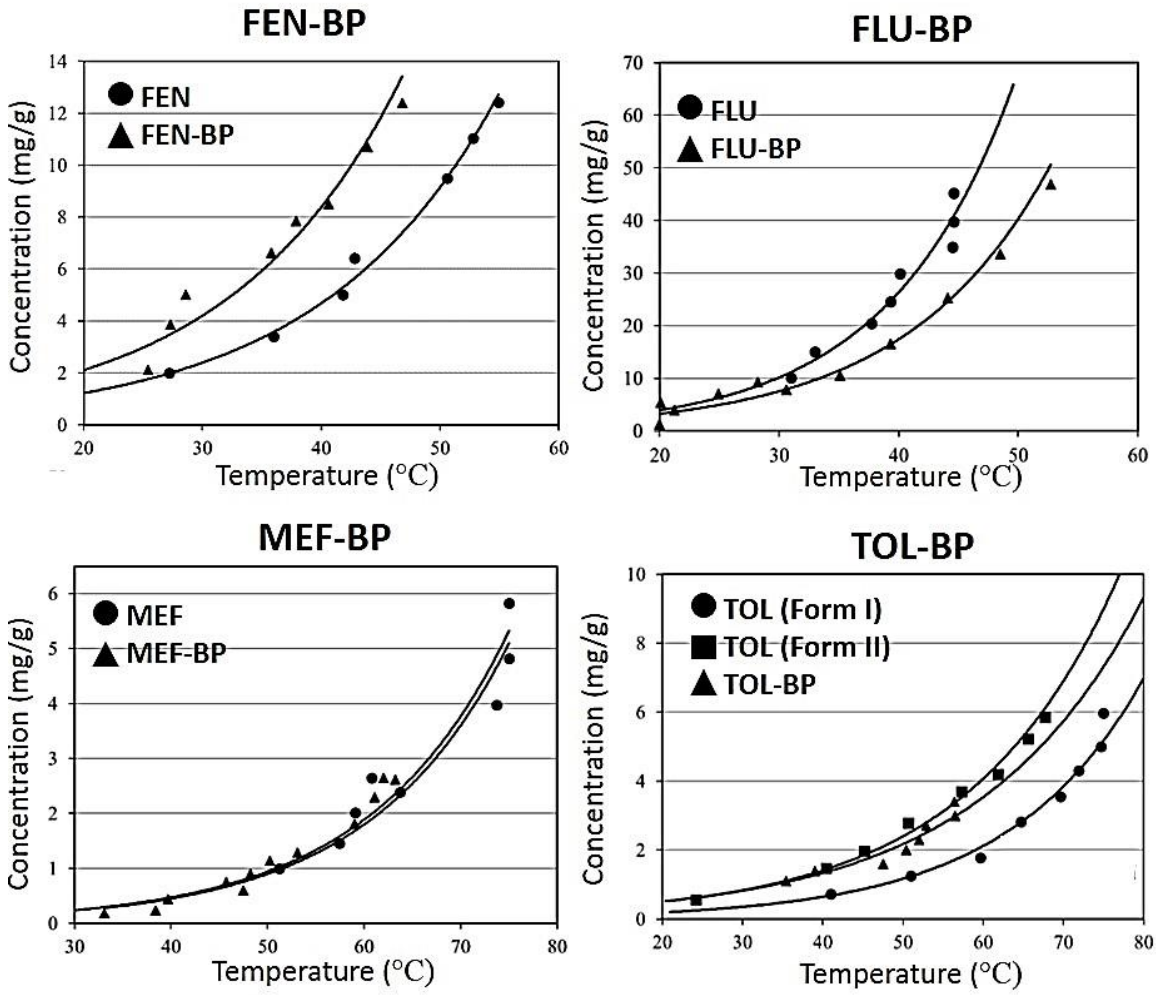

Figure 7.66 Comparison of solubility of the FAD-BP co-crystal with the solubility of the respective FAD. (Note all solubilities for FAD-BP take into account the mass of the FAD component only)

7.5.7.5 Thermal Analysis

A heat-cool cycle was carried out using DSC for each of the co-crystals and their corresponding APIs (Figure 7.67). Hot-stage microscopy (HSM) was also used to visualise the thermal event of melting for the co-crystals and to observe any other obvious phase changes upon heating or cooling (Figure 7.67).

The DSC trace of FEN shows a single endothermic peak at 186 °C upon heating and two exothermic peaks at 116 and 106 °C upon cooling. FLU also displays one endothermic peak at 135 °C which

corresponds to the melting point of the most stable polymorphic form of flufenamic acid. Both FEN and FLU decompose upon heating and thus the recrystallisation peaks seen for FEN could be assigned to decomposition products. The co-crystals of FEN and FLU with BP melt at lower temperatures (146 and 128 °C) than their free acids and recrystallise upon cooling at 116 and 107 °C respectively (Figure 7.67).

The DSC trace of MEF shows an endothermic peak at 170 °C which corresponds to an enantiotropic phase transition of form I to form II[182-184]. This is followed by another endothermic peak at 231 °C which represents the melting point of MEF form II. Upon cooling an exothermic peak is observed at 135 °C which could be attributed to the recrystallisation of form I, which is stable at lower temperatures.[182] The DSC traces for TOL form I and form II both show a sharp endotherm at 213 °C which agrees with previously reported results.[185] Upon cooling, an exothermic peak is observed at 135 °C for form I and 150 °C for form II.

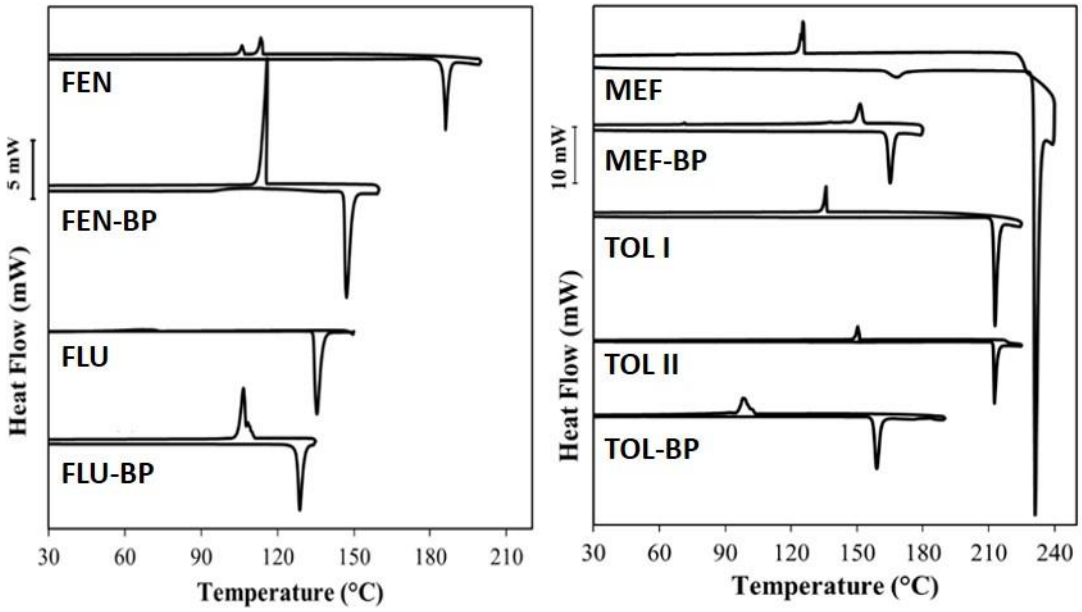

Figure 7.67 Comparison of DSC of the FAD-BP co-crystals with DSC of the respective FAD

The DSC profiles of MEF-BP and TOL-BP display endothermic peaks at 163 and 156 °C upon heating and exothermic recrystallisation peaks at 151 and 98 °C upon cooling (Figure 7.67). In contrast to the DSC profile for FEN-BP and FLU-BP, where it can convincingly be stated that the co-crystals recrystallise upon cooling (owing to similar enthalpy changes for the endotherm and exotherm); the asymmetric and smaller exotherms for the other two co-crystals suggests a more complex thermal event than a simple recrystallisation of the co-crystal.

As many of the polymorphs of the FADs differ only in a slight conformational change they have very similar melting points; the MEF form I to form II enantiotropic transition is an exception to this statement. It is common for phase transitions to be seen in DSC traces of polymorphic pharmaceuticals and it is therefore significant that in the DSC traces of these co-crystals there are no additional endothermic or exothermic peaks prior to melting that can be associated with a typical phase transition.

Furthermore, no polymorphs of the co-crystals were observed during the extensive co-crystal screen; this suggests locking of the conformational freedom on formation of the co-crystal structures has resulted in a reduction in the propensity for polymorphism in these FADs.

The melting points of all of the co-crystals are significantly lower than those of their corresponding API, with the largest difference of *ca.* 66 °C between the melting point of the MEF-BP co-crystal and that of polymorphic form II of MEF (Table 7.23).

7.5.7.6 Relative Humidity Stability

A number of APIs are known to interconvert between polymorphic forms as well as anhydrous and monohydrate forms under relatively mild humidity conditions. This can cause serious issues with production, storage and transport of pharmaceutical products, and it has been shown that co-crystal formation of APIs can reduce or eliminate the possibility of these undesirable transformations.[70, 73, 186, 187] The co-crystals of the FADs studied here, along with the API starting materials, were thus investigated under moderate humidity storage conditions (24 °C and 45% RH) and 'stress' humidity storage conditions (45 °C and 80% RH) over a period of four and two weeks, respectively.

PXRD patterns were recorded at various intervals and remained unchanged showing no indication of either new products being formed (possible hydrates) or dissociation of the co-crystals into their individual components (Figure 7.68 and Figure 7.69). These types of transformations normally occur at the higher humidity conditions (>75% RH) and have been found to be dependent on the aqueous solubility of the two components.[187, 188]

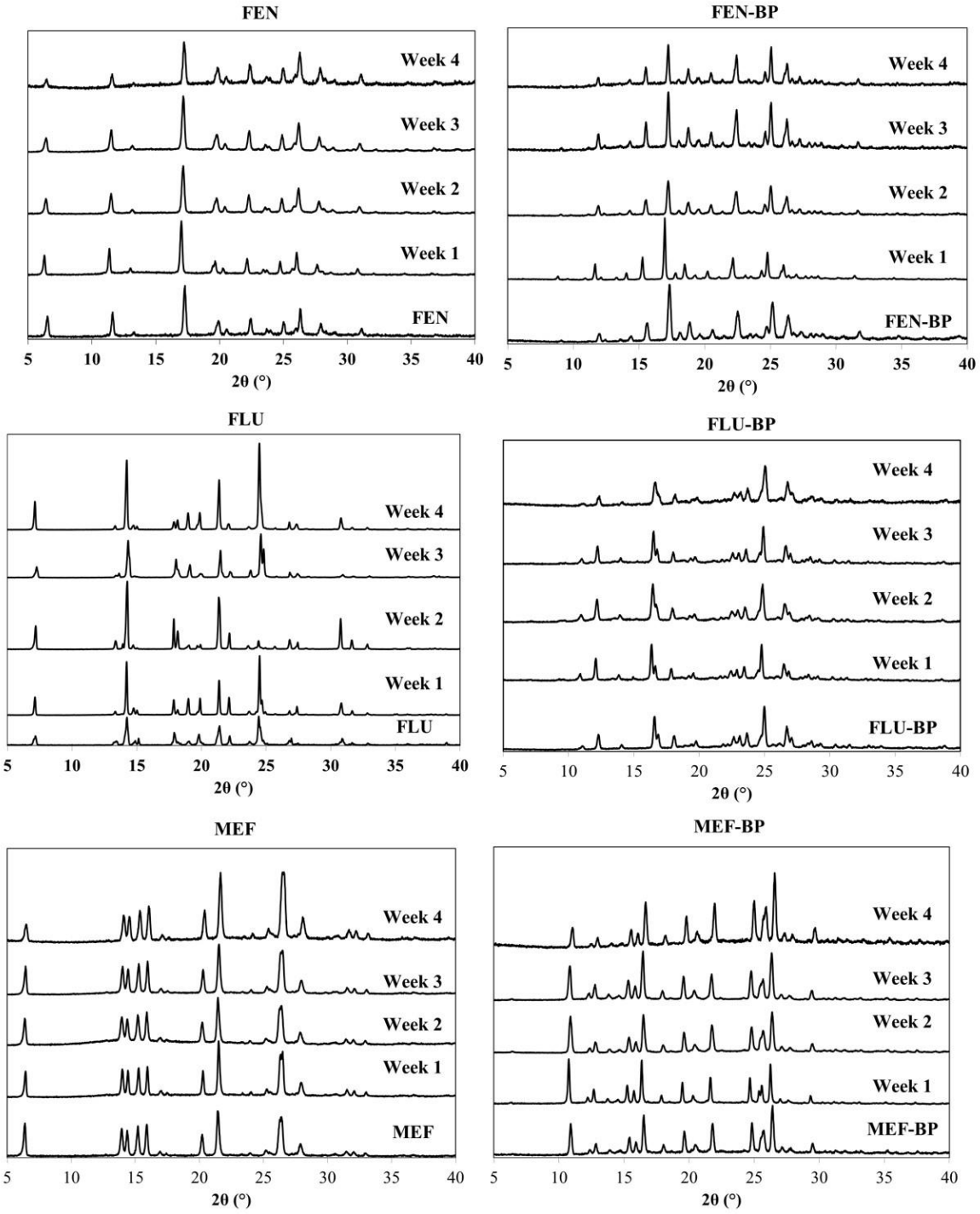

Figure 7.68 PXRD patterns showing the stability of FEN and the FADs, FLU and MEF and their respective FAD-BP co- crystals, FEN-BP, FLU-BP and MEF-BP under moderate humidity conditions (24 °C and 45% RH)

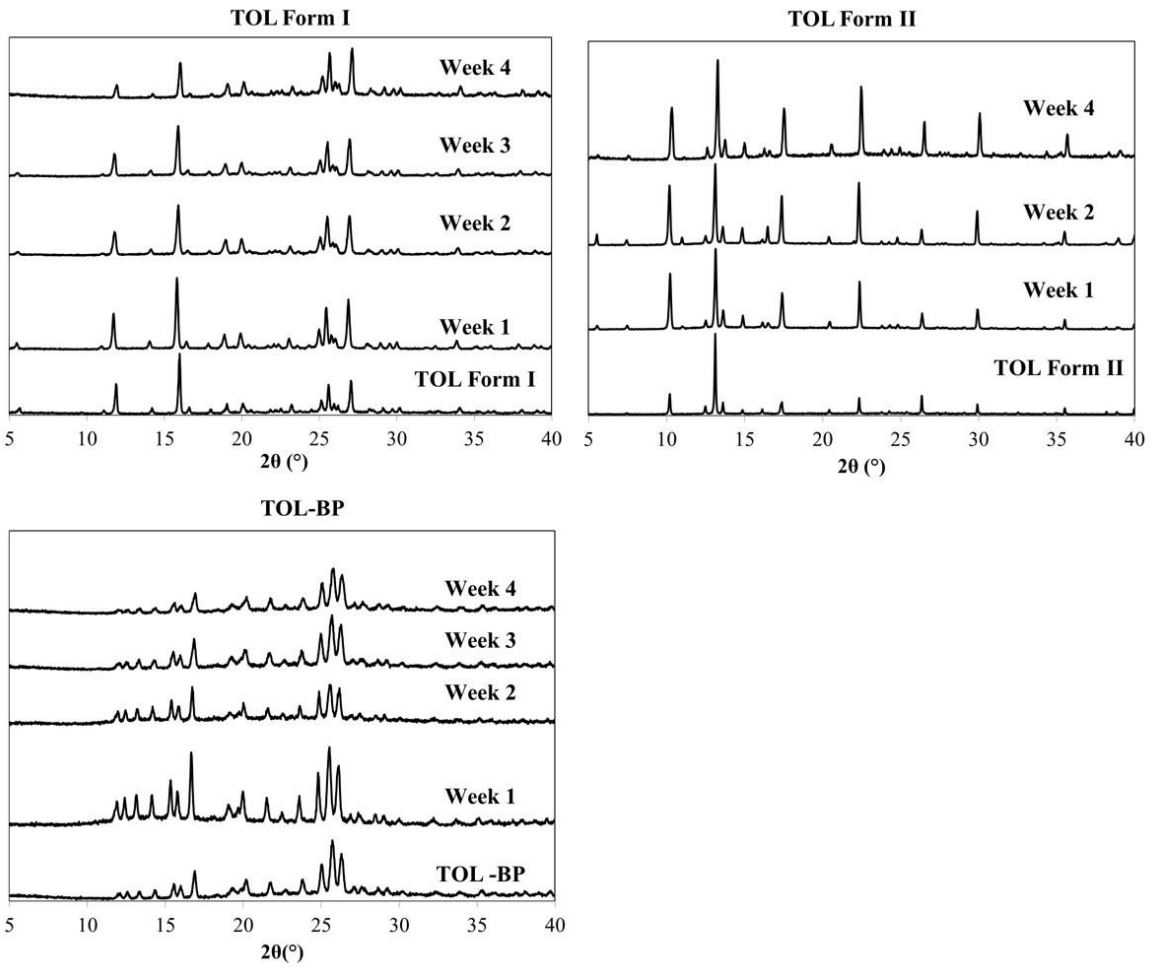

Figure 7.69 PXRD patterns showing the stability of the FAD TOL (Form I and Form II) and its respective TOL-BP co- crystal under moderate humidity conditions (24 °C and 45% RH)

7.5.7.7 IR spectroscopy

Fourier Transform infrared spectroscopy was used to study the conformational and structural changes of the important functional groups involved in the hydrogen bonds. In the free acids, the carboxylic acid groups form standard $R_2^2(8)$ dimers (Figure 7.71 a). In contrast, the co-crystals contain *pyridine*-acid supramolecular synthons and thus the carbonyl groups are not directly involved in the intermolecular hydrogen bonds and instead form a stronger intramolecular hydrogen bond with the secondary amine of the fenamic acids (Figure 7.71 b).

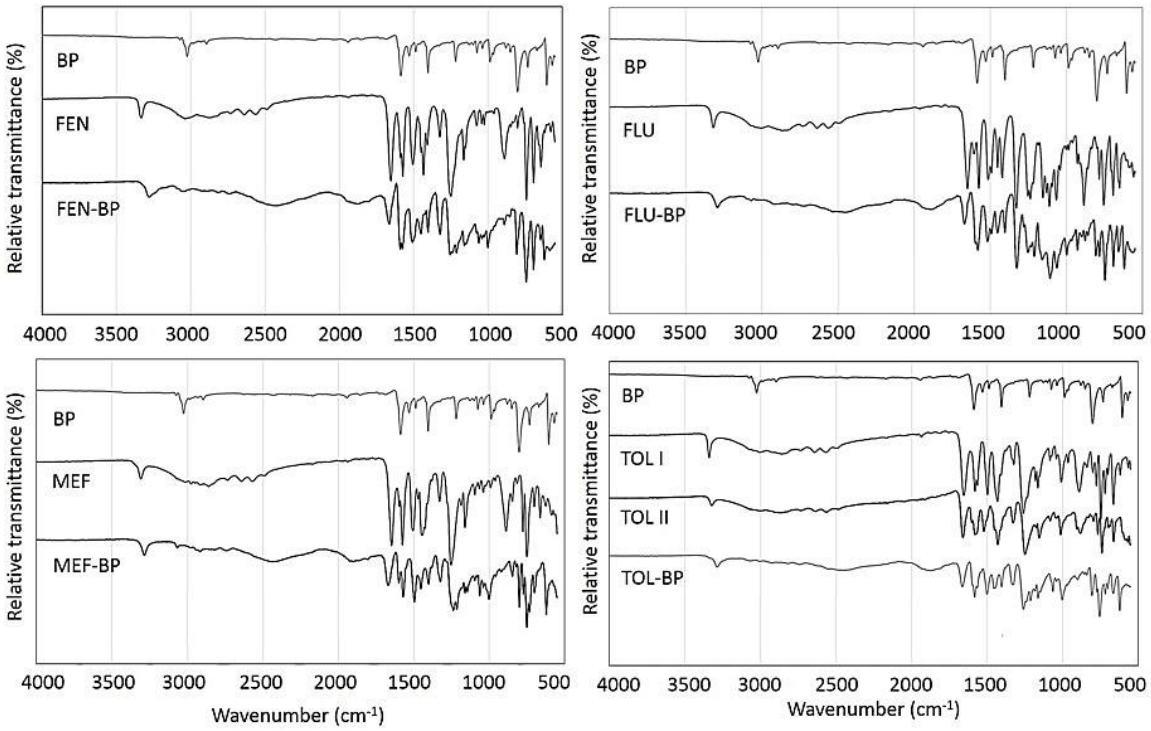

Figure 7.70 FTIR spectra of the starting materials and FAD-BP co-crystals

Detailed FTIR studies have been conducted on MEF form I and form II. It has been shown that form I, which contains the intramolecular hydrogen bond has an N-H stretching mode that occurs at a lower frequency (3311-3312 cm^{-1}) than form II (3346-3347 cm^{-1}) in which the intramolecular hydrogen bond no longer exists.[189] In all our results we see a redshift for the N-H stretching mode upon co-crystal formation indicating a strengthening of the intramolecular hydrogen bond. The C=O stretching mode undergoes a blueshift upon co-crystal formation, which is further supported by a decrease in the carbonyl bond length (Table 7.24). The dimeric hydrogen-bonded units that are commonly seen for the stable polymorphs of the FADs have carbonyl stretching modes that occur at marginally lower frequencies than the co-crystals due to the increased C=O bond length which is due to a slight pull from the hydrogen bond acceptor. The large shifts (between 10 and 53 cm^{-1}) observed for the relevant stretching modes within these systems confirms the formation of co-crystals.

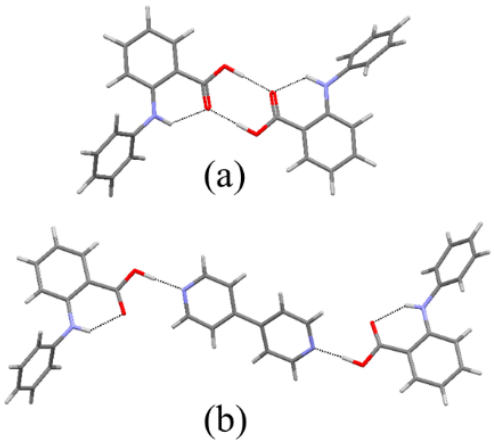

Figure 7.71 Hydrogen bonding synthons present in a) pure FADs and b) co-crystals

Table 7.24 Comparison of stretching frequencies and bond lengths of key functional groups in the FAD starting materials and the respective FAD-BP co-crystals.

Vibration frequency (cm^{-1})	FEN	FEN-BP	FLU	FLU-BP	MEF	MEF-BP	TOL (I)/(II)	TOL-BP
N-H stretch	3334	3286	3320	3293	3308	3285	3339/3322	3286
C=O stretch	1653	1666	1651	1671	1647	1670	1654/1659	1664
C=O bond length (Å)	1.233	1.214	1.234	1.220	1.232	1.219	1.234/1.241	1.221

7.5.8 Conclusions

This work reports the co-crystal screening of a series of FADs. A total of four co-crystals were discovered from these screens, two of which have been previously known and two discovered in parallel in this work and in a recent report.[179] These four co-crystals of fenamic acid, flufenamic acid, mefenamic acid and tolfenamic acid with the co-former 4,4'-bipyridine have been crystallised reproducibly here by a range of methods and characterised in terms of their thermal behaviour along with the determination of their key physical properties. The determination of these solid-form molecular structures and their physicochemical analysis add to the library of previously reported co-crystals discovered *en route* to enhancing important solid-state properties, such as thermal stability and solubility, of these NSAIDs.

In the pharmaceutical industry it is vitally important for APIs to display long term solid form stability. This is of particular note for polymorphic APIs, such as the fenamate family studied here, where phase transitions can occur due to heat and pressure changes, especially during secondary processing. It has been shown in this study that co-crystallisation enables these polymorphic transformations to be minimised, which is illustrated through the thermal investigations on four of the FADs and their respective co-crystals. DSC measurements demonstrated that while the melting points of the co-crystals were lowered with respect to the APIs, the four fenamate co-crystals displayed no evidence of thermally induced phase transitions in contrast to the parent APIs. Although the APIs in this study are co-crystallised with the non-GRAS co-former 4,4'-bipyridine, it serves as a proof of concept model for future investigations into inhibition of polymorphism in APIs as solid form stability and selectivity has been achieved under the experimental conditions investigated here.

The stability of the reported co-crystals provides a robustness with respect to the crystallisation method used for their production. A variety of crystallisation methods, including rapid and controlled cooling, evaporative and grinding crystallisations, have all produced the desired co-crystals, in a single polymorphic form and reproducibly. This is of the utmost importance for large-scale production where available techniques and environmental control can be variable.

It is of particular value that co-crystallisation has been achieved through cooling methods as this is the most commonly used technique in industrial crystallisation at present. Additionally, co-crystallisation through liquid-assisted grinding, which has been demonstrated in this investigation, can be translated to a screw extrusion process on an industrial scale.[72] This offers environmental benefits through a significant or complete reduction in solvent use[76] and thus minimises the risk of potentially toxic residual solvent remaining in the end product.[75, 190]

Turbidimetric measurements have provided solubility data of the APIs and their 4,4'-bipyridine co-crystals over a temperature range of 25-70 °C in an IPA/water solvent system. Characterising the solubility of starting materials and products is an early step in designing any cooling crystallisation process and is fundamental to the optimisation of scale-up to industrial crystallisation volumes. The data presented will be beneficial to the design and optimisation of future cooling crystallisation processes comprising these materials.

8 Conclusions and Future Work

8.1 Conclusions

This work has presented a range of studies relevant to the development of continuous crystallisation methods for the manufacture of multi-component molecular complexes. Traditionally, investigations of this class of materials has focused on structure, with the approach of crystal engineering being used to predict and generate new complexes based on an understanding of intermolecular interactions. There has also been increasing awareness of the importance of property determination, particularly in terms of physical properties that are potentially useful for applications, including solubility, melting point. In studies of new or recently discovered molecular complexes here, reported in Chapter 7, the importance and relevance of full property determination has been emphasised, most notably in the series of fenamic acid complexes, where a comprehensive characterisation programme has been carried out. Moreover, it has become increasingly apparent that the understanding of the relevant physical properties – most obviously solubility – is a critical factor in the design of potential crystallisation processes; this aspect is revisited in the future work section below (section 8.1).

This point illustrates one of the conundrums in the design of crystallisation processes, in that it is vital to determine a range of physical properties, notably solubility, before a crystallisation regime can be set up that will lead to the production of the very material whose properties need to be determined. This is most pronounced in the present case for the elusive form of urea barbituric acid (see below), where significant effort was required to isolate sufficient quantities of UBAII even to allow a basic solubility profile to be obtained. Resolving this conundrum relies on iterative approaches to materials production, property measurement and process design.

In order to put the potential for crystallisation for manufacture of fine chemical and pharmaceutical products at the core of the study, it is important to demonstrate that particular multi-component materials can be produced by a range of crystallisation methods, and to investigate the scalability of these. To this end, significant investigations have been reported on the robustness of formation of a particular molecular complex, including the selectivity for solid-form (polymorph) in a number of the complexes studied. The crystallisation methods investigated have ranged from evaporative crystallisation (the traditional way in which such materials are initially synthesised), through to cooling, slurrying and mechano-crystallisation (grinding) methods. A range of systems have been shown to be transferable across two or more of these techniques, vital in understanding the relationship of solid form production to crystallisation method.

While some limited scale-up studies have been carried out here on new or recently discovered molecular complexes, the bulk of the thesis focuses on the previously known polymorphic multi-component systems urea barbituric acid, in which the full range of translational studies towards full continuous crystallisation have been undertaken, from evaporative discovery, through cooling and scale-up, to delivery of products using a range of continuous crystallisation platforms. The findings of these investigations are summarised briefly below.

The initial crystallisation and properties of the various UBA polymorphs (forms I, II and III, with UBAII being metastable) have been reported in Chapter 4. The systematic evaporative co-crystallisations carried out on the UBA system have shown that it is possible to produce each of the UBA polymorphs; importantly, the work presented here has examined the products in bulk, rather than simply as single crystals extracted from the solid product. This is vital in assessing phase purity of the resulting products. It was found that the more stable pair of polymorphs (UBAI and UBAIII) are produced under a range of conditions, while the metastable polymorph UBAII is only produced in one of the trials carried out; this is in keeping with its metastable nature, and its known status as an elusive solid. UBAI and UBAIII are found frequently to co-exist, and in all cases PXRD analysis shows that the final product includes residual starting material. The mechano-crystallisation experiments give access exclusively to UBAI, and in liquid-assisted grinding experiments using stoichiometric quantities of urea and barbituric acid, and the solvents methanol, ethanol or water, UBAI is formed as the sole product; this selectivity was not obtained in evaporative approaches. This facile and selective method to isolate UBAI offers a route to UBAI seed production for further selective crystallisation experiments.

A design of experiments (DOE) approach was used to investigate the effects of the various parameters on the product generated; these confirmed that in the experimental space investigated UBAI was the dominant polymorph, with UBAII clearly elusive

The importance of the provenance of starting materials was also investigated with one supplier being shown to supply a different polymorphic form of barbituric acid to the others, a factor that can significantly affect the design and implementation of crystallisation processes.

In Chapter 5, the initial conditions for cooling crystallisation production of the UBA solid forms were established, including their scaling to larger (500 mL) volumes. Access to UBAI and UBAIII are dependent on the cooling rate, with slower cooling tending to favour production of UBAIII, while the more metastable UBAII is once again more elusive and was only isolated in a single experiment using a two-step cooling profile (1 °Cmin^{-1} to 35 °C followed by 0.05 °Cmin^{-1} to 10 °C) and was produced with traces of UBAI. The method of adding urea into a pre-prepared solution of BA was

shown to produce only UBAI solid product, offering a further route towards polymorph selectivity. The in-situ PAT used in these initial experiments within the STR confirmed the presence of the various UBA solid forms, but their full interpretation was hampered by the effects of fouling on the Raman probe used, and the conclusions were based on off-line PXRD experiments.

These cooling conditions were then used to design a range of campaigns for UBA production in the mixed-suspension, mixed-product-removal (MSMPR) system at Loughborough University, in collaboration with the research groups of Professors C.D. Rielly and Z. Nagy. These experiments showed the potential of periodic operation of such an MSMPR system, with a suitably designed dissolution stage, to provide a platform for the consistent production of the desired polymorphic form of the model UBA co-crystal system, decreasing product variability significantly compared to batch operation.

The MSMPR work was then taken to a related but distinct system at AstraZeneca, Macclesfield, with the system there differing most significantly in using vacuum transfer of material rather than the peristaltic pump arrangement at Loughborough. Although less time was spent on campaigns in the AZ MSMPR system, in the experiments that were carried out, mixtures of UBAI and UBAIII were always obtained, and it was not possible to isolate UBAII. This device clearly has promise, even in the challenging multi-component, polymorphic system examined here. If the significant problem that the continuous vacuum transfer process causes evaporation and makes it more difficult to follow the desired supersaturation curves as the crystallisation proceeds, can be overcome, then this system has much promise for the future.

Continuous production runs on the UBA system were also carried out in a range of crystallisers in the Bath Continuous Crystallisation Laboratory (BCCL) at the University of Bath, and are described in Chapter 6. The platforms used were the KRAIC segmented flow device and the NiTech DN15 Continuous Oscillatory Baffled Crystalliser (COBC). With the inherent reconfigurability of the KRAIC, in particular, a wide range of options for segmentation, flow rates, materials transport, etc, were investigated.

In the KRAIC, it was found possible to produce UBAI selectively using the non-segmented flow set-up with a dual UBA feed. However, when a single UBA feed was used in combination with segmented flow, using a range of different carrier media (air, PFPE and air with PFPE), a mixture of UBAI and UBAIII was produced. As with all previous continuous crystallisations of UBA, UBAII was not present in the end product. This difference in polymorphic outcome is most likely due to the different mixing conditions experienced with the non-segmented and segmented flows, together with the different de-supersaturation profiles followed in the two feed set-ups. Further investigation of

crystallisation using a dual UBA feed combined with segmented flow may help to decouple the effect of the de-supersaturation profile *vs.* the mixing conditions.

For the COBC studies of UBA, a range of different operating parameter were used, producing consistently good quality single phase UBAI product throughout the crystallisation processes. This was achieved over relatively extended periods of operation (typically 180 minutes, three residence times). The campaign carried out in the COBC represents a key breakthrough in establishing continuous crystallisation of multi-component molecular materials with a view to establishing a continuous platform for the production of such materials in a continuous manufacturing context. Achieving this for a multi-component system with starting components of substantially different solubility characteristics, and being able to produce a single form selectivity even though UBAI and UBAIII appear to be very close energetically, is a significant result. This emphasises the high degree of control of kinetic factors that is possible in a continuous flow reactor such as the COBC, holding much promise for the use of continuous crystallisation in this context.

It has, however, proven challenging to obtain either UBAII or UBAIII selectively in the COBC. This is not unexpected for the highly metastable UBAII, but it should be possible to optimise the crystallisation conditions to allow the isolation of UBAIII, and work on this is ongoing.

The COBC has been shown to deliver selective crystallisation of UBAI of the target multi-component UBA system and represents a breakthrough in deployment of such a device and offers real potential for its exploitation in the production of multi-component solid forms. The first steps have been taken to deploy the COBC at UoB as a fully continuous crystalliser within this project, although for the process to be fully continuous much longer experimental runs are required which for the capacity of the set-up described here would require a much larger set of feed vessels.

The range of crystallisations carried out during this project has produced a range of information about the polymorphic nature of UBA and the relationship between polymorphs. It has been possible to isolate successfully all three polymorphs. UBAI, which is the most prevalent polymorph, can be crystallised reproducibly via cooling and can also be obtained from mechanical co-crystallisation. However, it has proved more challenging to isolate UBAIII reproducibly and it is still extremely difficult to isolate the elusive polymorph UBAII.

8.2 Future Work

In order to progress this initial establishment of the continuous crystallisation of multi-component molecular complexes, the following developments are clear next steps.

It will be important to establish a full UBA multi-component phase diagram. While an obvious tool for designing effective processes to assemble multi-component systems and to control the production of particular solid forms, such full phase diagram investigations remain relatively rare. However, with advances in instrumentation, most phase diagrams should be accessible for relatively rapid determination. In carrying out this phase diagram determination, it will also be possible to identify appropriate anti-solvents that can be used to control precipitation of the product materials and enhance yield. The yield of the UBA cooling crystallisation process is currently very low by industrial standards (maximum of 60%) as the solubility in methanol does not vary significantly with temperature. Other solvent systems such as ethanol, IPA and mixtures with water should be investigated. It would also be interesting to explore anti-solvent addition as a final step to the crystallisation process. Current industrial processes frequently use a non-polar solvent such as hexane as anti-solvent in the final stages of a cooling crystallisation process, to enhance yield; this method could be investigated systematically. The use of an appropriate anti-solvent may also offer more access to the metastable UBA form II.

The possible use of water as a solvent or co-solvent in UBA continuous crystallisation is severely hindered by the tendency of the barbituric acid starting material to form BA hydrate. It would be interesting to investigate if there is a threshold for the presence of water in the crystallisation solvent or can a temperature profile be developed that when adhered to would prevent formation of the BA hydrate. It would also be of interest to investigate the effect of impurities in the BA starting materials and how these affect the polymorph of UBA adopted.

The periodic MSMPR system at Loughborough has been shown to be an effective platform for production of UBA solid forms, with some evidence of selectivity. Use of this device with other polymorphic multi-component systems should be investigated. In addition, a more systematic investigation of the contrasting performance of peristaltic pump *vs.* vacuum transfer of materials in the Loughborough and AZ MSMPR systems should be undertaken, in order to develop the latter further towards operation with solid form selectivity. In addition, the option for both continuous and periodic operation of the small scale cSTR being developed in BCCL should be pursued in parallel, offering a different transfer mechanism (using gravity), together with the significant scaling involved (down-scaling from 500 mL to 7 mL STR vessels)

This work is has shown that is possible to selectively crystallise UBAI using the COBC with the sets of cooling profiles and mixing conditions described in Chapter 6. Further investigations should target the crystallisation of UBAII and UBAIII in the COBC, by varying systematically the temperature profile and mixing conditions. In terms of hardware, the COBC will be modified to place the feed inlet after a single heated straight to resolve issues with fouling in the unjacketed tube positioned near the bellows, a modification implemented in COBC configurations used within CMAC; the COBC will also be reconfigured to install a dual feed and seeding port in order to repeat experiment C3 with varying concentrations of seed suspension using mechano-chemically produced UBA I seeds, and to investigate separate addition of the urea and BA components as investigated with MSMPR experiments.

All analyses of materials produced from the COBC were carried out using off-line measurements. As PXRD is the main technique used to identify the presence of each polymorph in the UBA system it would initially be beneficial to install sampling ports so that samples could be analysed over the length of the crystalliser in situ. An aspirational aim would be to implement in-line PXRD analysis using flow-through PXRD, either in the laboratory or at a synchrotron source such as Diamond Light Source. Routine use of full quantitative phase analysis using PXRD would be of real benefit in assessing selectivity and yield; the techniques for doing so are standard, and include the ability to analyse multi-phase samples. The methods adopted can be based either on comparison with rigorous internal standards, Rietveld refinement, or on a combination of these with cluster analysis programs such as PolySNAP.

The main issue encountered with fouling in the KRAIC experiments was within the glass mixer piece; to resolve this FEP mixers or glass mixers coated in FEP should be tested. All KRAIC experiments on UBA were carried out using a peristaltic pump, however subsequent investigations on other materials have used a recently sourced gear pump. This has helped to achieve more uniform segmentation due to the nature of the constriction mode of a gear pump which reduces the amount of pulsation in comparison to a peristaltic pump. Future experiments using UBA should be carried out using the gear pump in order to investigate what effect this may have upon the size variation of segments, especially in the methanol system with air/PFPE segmentation. New air/PFPE segmentation configurations are also still under development in BCCL, which should be trialled for UBA in methanol with an aim to achieve enhanced and more uniform segmentation. More generally, further development of the novel KRAIC crystalliser should also be pursued, as outlined in section 6.1.7, using both experimental and computational approaches. Work is being developed on CFD (Computational Fluid dynamics) within the Wilson group. Within CMAC significant efforts have been made in characterization of the COBC using CFD, but the Bath effort complements this by

focusing upon modelling the KRAIC in order to gain additional information to support the understanding gained through *ex silico* experimental work.

The UBA system should also be examined in the continuous membrane-mediated evaporative crystalliser (CMEC) in BCCL. The conditions under which UBA continuous crystallisation has been realised are well suited to implementation in the CMEC as it uses methanol solvent which has a low boiling point and as a small molecule system will have good membrane permeation. Filtration during UBA experiments have caused no issues, indicating that it would allow solution to move freely at the membrane surface, though surface fouling seen in the UBA system could cause difficulties.

In terms of the next targets for translation of multi-component systems into the continuous crystallisation environment, these might include thiobarbituric acid urea co-crystals, beginning with a systematic investigation of the polymorphic behaviour of this multi-component molecular complex system. It would also be relevant to look into the transfer into the KRAIC or other continuous platform of the 5FCYT-4Cl35DNBA co-crystal system, for which batch cooling crystallisation parameters have been obtained (Section 7.4).

There has been evidence in the MSMPR studies on UBA that seeding may be used to preferentially produce UBA form I and UBA form III. The seed loading for this is crucial. High seed loading (10%) has been shown to direct the formation of UBA I and UBA III, however a seed loading more representative of those used in industry (around 1%) have shown little effect. UBA II is more elusive and there has not been enough material generated to use this as seed. Further investigation into seeding using each of the different polymorphs may prove useful. Seeding has yet to be implemented in the small scale continuous crystallisation apparatus at Bath and will form the basis of a future PhD project for which UBA will be a key candidate.

8.3 Publications

The following papers have been published to date from the work presented in this thesis:

"From evaporative to cooling crystallisation: an initial co-crystallisation study of cytosine and its fluorinated derivative with 4-chloro-3,5-dinitrobenzoic acid."

K. Wittering, J. King, L. H. Thomas and C. C. Wilson (2014). *Crystals*, **4**, 123-140 [DOI: 10.3390/cryst4020123].

"Crystallisation and physicochemical property characterisation of conformationally-locked co-crystals of fenamic acid derivatives"

K. E. Wittering, L. R. Agnew, A. R. Klapwijk, K. Robertson, A. J. P. Cousen D. L. Cruickshank and C.C. Wilson (2015). *CrystEngComm*, **17**, 3610-3618 [DOI: 10.1039/C5CE00297D].

"Towards continuous crystallization of a polymorphic multi-component molecular system"

K. A. Powell, G. Bartolini, K. E. Wittering, A. N. Saleemi, C. C. Wilson, C. D. Rielly, and Z. K. Nagy (2015). *Cryst Growth Design*, **15**, 4821-4836 [DOI: 10.1021/acs.cgd.5b00599]

In addition, the following was published from related work:

"Absorbate-induced piezochromic response in a porous molecular crystal."

C. H. Hendon, K. E. Wittering, T-H. Chen, W. Kaveevivitchai, I. Popov, D. L. Cruickshank, K. T. Butler, C. C. Wilson, O. S. Miljanic & A. Walsh (2015). *Nano Letters*, **15**, 2149-2154 [DOI: 10.1021/acs.nanolett.5b00144].

References

1. M. Gryl, A. Krawczuk and K. Stadnicka, *Acta Crystallographica Section B-Structural Science*, 2008, **64**, 623-632.
2. G. M. Schmidt, *Pure Appl. Chem.*, 1971, **27**, 647-678.
3. G. R. Desiraju, *Crystal Engineering The Design of Organic Solids*, Elsevier, Amsterdam, 1989.
4. C. B. Aakeroy and N. Schultheiss, Assembly of Molecular Solids via Non-covalent Interactions in *Making Crystals by Design*, eds. D. Braga and F. Grepioni, WILEY-VCH Verlag GmbH & Co., Weinheim, 2007, 209-240.
5. D. V. Soldatov and I. S. Terekhova, *Journal of Structural Chemistry*, 2005, **46**, S1-S8.
6. C. B. Aakeroy, N. R. Champness and C. Janiak, *Crystengcomm*, 2010, **12**, 22-43.
7. G. R. Desiraju, *Journal of Chemical Sciences*, 2010, **122**, 667-675.
8. K. Molcanov and B. Kojic-Prodic, *Crystengcomm*, 2010, **12**, 925-939.
9. C. B. Aakeroy, S. Forbes and J. Desper, *Journal of the American Chemical Society*, 2009, **131**, 17048–17049.
10. L. H. Thomas, C. Wales, L. Zhao and C. C. Wilson, *Crystal Growth & Design*, 2011, **11**, 1450–1452.
11. A. D. Bond, *Crystengcomm*, 2007, **9**, 833-834.
12. G. R. Desiraju, *CrystEngComm*, 2003, **5**, 466-467.
13. R. Hilfiker, F. Blatter and M. v. Raumer, Relevance of Solid-state Properties for Pharmaceutical Products in *Polymorphism*, Wiley-VCH Verlag GmbH & Co. KGaA, 2006, 1-19.
14. D. Giron, *Journal of Thermal Analysis and Calorimetry*, 2001, **64**, 37-60.
15. P. W. Cains, Classical Methods of Preparation of Polymorphs and Alternative Solid Forms in *Polymorphism in Pharmaceutical Solids*, *2nd edn.*, CRC Press, 2009, 76-138.
16. A. D. Bond, *Current Opinion in Solid State & Materials Science*, 2009, **13**, 91-97.
17. D. Braga and J. Bernstein, Crystal Polymorphism: Challenges at the Crosroads of Science and Technology in *Making Crystals by Design*, eds. D. Braga and F. Grepioni, WILEY-VCH Verlag GmbH & Co., Weinheim, 2007, 293-314.
18. S. P. F. Miller, A. S. Raw and L. X. Yu, Scientific Considerations of Pharmaceutical Solid Polymorphism in Regulatory Applications in *Polymorphism*, Wiley-VCH Verlag GmbH & Co. KGaA, 2006, 385-403.
19. L. A. Yu, *Accounts of Chemical Research*, 2010, **43**, 1257-1266.
20. L. Yu, *Journal of Physical Chemistry A*, 2002, **106**, 544-550.
21. K. E. Wittering, L. R. Agnew, A. R. Klapwijk, K. Robertson, A. J. P. Cousen, D. L. Cruickshank and C. C. Wilson, *CrystEngComm*, 2015, **17**, 3610-3618.
22. A. J. Cruz-Cabeza and J. Bernstein, *Chem. Rev.*, 2014, **114**, 2170.
23. W. McCrone, *Polymorphism In Physics and chemistry of the organic solid state*, Wiley Interscience, 1965.
24. J. Bernstein, *Polymorphism in Molecular Crystals*, Oxford University Press Inc., New York, 2002.
25. S. Byrn, D. Curtin and I. Paul, *J.Am.Chem.Soc*, 1972, **94**, 890-898.

26. S. Lohani and D. J. W. Grant, in *Polymorphism*, Wiley-VCH Verlag GmbH & Co. KGaA, 2006, pp. 21-42.

27. N. Variankaval, A. S. Cote and M. F. Doherty, *Aiche Journal*, 2008, **54**, 1682-1688.

28. W. Kaialy, H. Larhrib, M. Ticehurst and A. Nokhodchi, *Crystal Growth & Design*, 2012, **12**, 3006–3017.

29. N. Blagden, M. de Matas, P. T. Gavan and P. York, *Advanced Drug Delivery Reviews*, 2007, **59**, 617-630.

30. J. F. Remenar, S. L. Morissette, M. L. Peterson, B. Moulton, J. M. MacPhee, H. R. Guzman and O. Almarsson, *Journal of the American Chemical Society*, 2003, **125**, 8456-8457.

31. D. I. A. Millar, H. E. Maynard-Casely, D. R. Allan, A. S. Cumming, A. R. Lennie, A. J. Mackay, I. D. H. Oswald, C. C. Tang and C. R. Pulham, *Crystengcomm*, 2012, **14**, 3742-3749.

32. B. B. Koleva, T. Kolev, R. W. Seidel, H. Mayer-Figge, M. Spiteller and W. S. Sheldrick, *Journal of Physical Chemistry A*, 2008, **112**, 2899-2905.

33. A. R. Millward and O. M. Yaghi, *Journal of the American Chemical Society*, 2005, **127**, 17998–17999.

34. P. A. Kollman and L. C. Allen, *Chemical Reviews*, 1972, **72**, 283-303.

35. P. Linus, *The Nature of the Chemical Bond*, Cornwell Univerisy Press, 1993.

36. G. A. Jeffrey, *An introduction to hydrogen bonding*, Oxford University Press, Oxford, 1997.

37. M. D. Joesten, *Journal of Chemical Education*, 1982, **59**, 362-366.

38. A. D. Burrows, Crystal engineering using multiple hydrogen bonds in *Supramolecular Assembly Via Hydrogen Bonds I*, Springer-Verlag Berlin, Berlin, 2004, vol. 108, pp. 55-95.

39. T. Steiner, *Angewandte Chemie-International Edition*, 2002, **41**, 48-76.

40. E. Arunan, G. R. Desiraju, R. A. Klein, J. Sadlej, S. Scheiner, I. Alkorta, D. C. Clary, R. H. Crabtree, J. J. Dannenberg, P. Hobza, H. G. Kjaergaard, A. C. Legon, B. Mennucci and D. J. Nesbitt, *Pure and Applied Chemistry*, 2010, **83**, 1637-1641.

41. A. D. McNaught and A. Wilkinson, *IUPAC. Compendium of Chemical Terminology*, 2nd edn., Blackwell Scientific Publications, Oxford, 1997.

42. P. Atkins and J. de Paula, *Elements of Physical Chemsitry*, 4th edn., Oxford University Press, Oxford, 2005.

43. P. Mignon, S. Loverix, J. Steyaert and P. Geerlings, *Nucleic Acids Research*, 2005, **33**, 1779-1789.

44. C. A. Hunter and J. K. M. Sanders, *Journal of the American Chemical Society*, 1990, **112**, 5525–5534.

45. M. L. Waters, *Current Opinion in Chemical Biology*, 2002, **6**, 736-741.

46. J. W. Mullin, *Crystallization*, 3rd edn., Reed Educational and Professional Publishing Ltd., 1997.

47. Y. Sonoda, F. Hirayama, H. Arima, Y. Yamaguchi, W. Saenger and K. Uekama, *Chemical Communications*, 2006, 517-519.

48. J. R. Luft, J. R. Wolfley and E. H. Snell, *Crystal Growth & Design*, 2011, **11**, 651-663.

49. R. Davey and J. Garside, *From Molecules to Crystallizers An Introduction to Crystallization*, Oxford University Press Inc., New York, 2000.

50. N. S. Tavare, *Industrial Crystallization Process Simulation Analysis and Design*, Plenum Press, New York, 1995.

51. L. Cronin, P. J. Kitson and C. C. Wilson, Process Understanding – Crystallization in *Process Understanding: For Scale-Up and Manufacture of Active Ingredients*, ed. I. Houson, Wiley-VCH Verlag GmbH &Co. KGaA, Weinheim, 2011.

52. P. G. Vekilov, *Crystal Growth & Design*, 2010, **10**, 5007-5019.

53. J. Anwar, S. Khan and L. Lindfors, *Angewandte Chemie International Edition*, 2015, not yet assigned.

54. D. Erdemir, A. Y. Lee and A. S. Myerson, *Acc Chem Res*, 2009, **42**, 621-629.

55. A. Myerson, *Handbook of Industrial Crystallization*, 2nd edn. Butterworth-Heinemann, 2002.

56. K. R. Seddon and M. J. Zaworotko, *Crystal Engineering The Design and Application of Functional Solids*, Springer-Verlag, Netherlands, 1999.

57. N. Lin and X. Y. Liu, *Chemical Society Reviews*, 2015, **44**, 7881-7915.

58. T. Vetter, M. Iggland, D. R. Ochsenbein, F. S. Hänseler and M. Mazzotti, *Crystal Growth & Design*, 2013, **13**, 4890-4905.

59. A. Kabalnov, *Journal of Dispersion Science and Technology*, 2001, **22**, 1-12.

60. N. Kubota, *Journal of Crystal Growth*, 2008, **310**, 4647-4651.

61. C. Lindenberg, M. Krattli, J. Cornel, M. Mazzotti and J. Brozio, *Crystal Growth & Design*, 2009, **9**, 1124-1136.

62. E. Kougoulos, I. Marziano and P. R. Miller, *Journal of Crystal Growth*, 2010, **312**, 3509-3520.

63. N. Nonoyama, K. Hanaki and Y. Yabuki, *Organic Process Research & Development*, 2006, **10**, 727-732.

64. W. Beckmann, *Journal of Crystal Growth*, 1999, **198–199, Part 2**, 1307-1314.

65. N. Kaneniwa, M. Otsuka and T. Hayashi, *Chemical and pharmaceutical bulletin*, 1985, **33**, 3447-3455.

66. C. P. M. Roelands, S. Jiang, M. Kitamura, J. H. ter Horst, H. J. M. Kramer and P. J. Jansens, *Crystal Growth & Design*, 2006, **6**, 955-963.

67. J. Cervenka, K. Hussain and A. W. Aabye, Patent: Continuous crystallization process of iodinated phenyl derivatives, WO 2006-NO289, 2006.

68. Z. K. Nagy, M. Fujiwara and R. D. Braatz, *Journal of Process Control*, 2008, **18**, 856-864.

69. A. Delori, T. Friscic and W. Jones, *CrystEngComm*, 2012, **14**, 2350-2362.

70. T. Friščić, A. V. Trask, W. Jones and W. D. S. Motherwell, *Angewandte Chemie*, 2006, **118**, 7708-7712.

71. M. R. Caira, L. R. Nassimbeni and A. F. Wildervanck, *Journal of the Chemical Society, Perkin Transactions 2*, 1995, 2213-2216.

72. C. Medina, D. Daurio, K. Nagapudi and F. Alvarez-Nunez, *Journal of Pharmaceutical Sciences*, 2010, **99**, 1693-1696.

73. A. V. Trask, W. D. S. Motherwell and W. Jones, *Crystal Growth & Design*, 2005, **5**, 1013-1021.

74. A. Bak, A. Gore, E. Yanez, M. Stanton, S. Tufekcic, R. Syed, A. Akrami, M. Rose, S. Surapaneni, T. Bostick, A. King, S. Neervannan, D. Ostovic and A. Koparkar, *Journal of Pharmaceutical Sciences*, 2008, **97**, 3942-3956.

75. H. G. Moradiya, M. T. Islam, S. Halsey, M. Maniruzzaman, B. Z. Chowdhry, M. J. Snowden and D. Douroumis, *CrystEngComm*, 2014, **16**, 3573-3583.

76. S. L. James, C. J. Adams, C. Bolm, D. Braga, P. Collier, T. Friščić, F. Grepioni, K. D. M. Harris, G. Hyett, W. Jones, A. Krebs, J. Mack, L. Maini, A. G. Orpen, I. P. Parkin, W. C. Shearouse, J. W. Steed and D. C. Waddell, *Chemical Society Reviews*, 2012, **41**, 413-447.

77. A. V. Trask, W. S. Motherwell and W. Jones, *Chemical communications*, 2004, 890-891.

78. J. Nyvlt, *Industrial Crystallisation: The Present State of the Art*, Verlag Chemie, Weinheim, 1978.

79. J. L. Quon, H. Zhang, A. Alvarez, J. Evans, A. S. Myerson and B. L. Trout, *Crystal Growth & Design*, 2012, **12**, 3036−3044.

80. A-T. Nguyen, Y. L. Joo and W-S. Kim, *Crystal Growth & Design*, 2012, **12**, 2780-2788.

81. S. Teychene and B. Biscans, *Crystal Growth & Design*, 2011, **11**, 4810-4818.

82. R. J. P. Eder, S. Radl, E. Schmitt, S. Innerhofer, M. Maier, H. Gruber-Woelfler and J. G. Khinast, *Crystal Growth & Design*, 2010, **10**, 2247-2257.

83. W. Massa, *Crystal Structure Determination*, 2nd edn., Springer-Verlag, 2004.

84. A. J. Blake, W. Clegg, R. O. Gould and P. Main, *Crystal structure analysis : principles and practice*, 2nd edn., Oxford University Press, Oxford, 2001.

85. P. Ewald, *50 Years of X-ray Diffraction*, N. V. A. Oosthoek's Uitgeversmaatshappij, Utrecht, 1962.

86. C. G. Darwin, *Phillosopical Magazine*, 1914, **27**, 315-333.

87. W. Clegg and Zeneca Pharmaceuticals., *Crystal structure determination*, Oxford University Press, Oxford, 1998.

88. V. Elser, *Acta Crystallographica Section A*, 2003, **59**, 201-209.

89. G. Oszlányi and A. Sütő, *Acta Crystallographica Section A*, 2008, **64**, 123-134.

90. L. Palatinus and G. Chapuis, *Journal of Applied Crystallography*, 2007, **40**, 786-790.

91. R. Dinnebier and S. Billinge, *Powder Diffraction Theory and Practice*, The Royal Society of Chemistry, Cambridge, 2008.

92. S. Bhattacharya, H. G. Brittain and R. Suryanarayanan, Thermoanalytical and crystallographic methods in *Polymorphism in Pharmaceutical Solids*, 2nd edn., ed. H. G. Brittain, Taylor and Francis, 2009, vol. 95, 318-346.

93. R. C. Mackenzie, Nomenclature in Thermal analysis in *Treatise on Analytical Chemistry*, eds. P. J. Elving and I. M. Kolthoff, John Wiley & Sons, New York, 1983, vol. 12, 1-16.

94. G. R. Heal, Thermogravimetry and Derivative Thermogravimetry in *Principles of Thermal Analysis and Calorimetry*, The Royal Society of Chemistry, 2002, 10-54.

95. 19th WHO Model List of Essential Medicines, WHO, 2015, http://www.who.int/selection_medicines/committees/expert/20/EML_2015_FINAL_amended_AUG2015.pdf, (accessed 09/09/2015, 2015).

96. N. Zencirci, E. Gstrein, C. Langes and U. J. Griesser, *Thermochimica Acta*, 2009, **485**, 33-42.

97. J. A. Zerkowski, C. T. Seto, D. A. Wierda and G. M. Whitesides, *Journal of the American Chemical Society*, 1990, **112**, 9025-9026.

98. J. A. Zerkowski, J. C. MacDonald and G. M. Whitesides, *Chemistry of Materials*, 1994, **6**, 1250-1257.

99. J. A. Zerkowski and G. M. Whitesides, *Journal of the American Chemical Society*, 1994, **116**, 4298-4304.

100. K. Wittering, J. King, L. Thomas and C. Wilson, *Crystals*, 2014, **4**, 123-140.

101. J. E. Worsham, H. A. Levy and S. W. Peterson, *Acta Crystallographica*, 1957, **10**, 319-323.

102. A. Olejniczak, K. Ostrowska and A. Katrusiak, *The Journal of Physical Chemistry C*, 2009, **113**, 15761-15767.

103. F. J. Lamelas, Z. A. Dreger and Y. M. Gupta, *The Journal of Physical Chemistry B*, 2005, **109**, 8206-8215.

104. W. Bolton, *Acta Crystallographica*, 1963, **16**, 166-173.

105. T. C. Lewis, D. A. Tocher and S. L. Price, *Crystal Growth & Design*, 2004, **4**, 979-987.

106. D. Braga, M. Cadoni, F. Grepioni, L. Maini and K. Rubini, *CrystEngComm*, 2006, **8**, 756-763.

107. M. U. Schmidt, J. Brüning, J. Glinnemann, M. W. Hützler, P. Mörschel, S. N. Ivashevskaya, J. van de Streek, D. Braga, L. Maini, M. R. Chierotti and R. Gobetto, *Angewandte Chemie International Edition*, 2011, **50**, 7924-7926.

108. M. R. Chierotti, R. Gobetto, L. Pellegrino, L. Milone and P. Venturello, *Crystal Growth & Design*, 2008, **8**, 1454-1457.

109. A. R. Al-Karaghouli, B. Abdul-Wahab, E. Ajaj and S. Al-Asaff, *Acta Crystallographica Section B*, 1977, **33**, 1655-1660.

110. G. A. Jeffrey, S. Ghose and J. O. Warwicker, *Acta Crystallographica*, 1961, **14**, 881-887.

111. M. V. Roux, C. Foces-Foces and R. Notario, *Pure and Applied Chemistry*, 2009, **81**, 1857-1870.

112. G. S. Nichol and W. Clegg, *Acta Crystallographica Section B*, 2005, **61**, 464-472.

113. L. Eriksson, E. Johansson, N. Kettaneh-Wold, C. Wikström and S. Wold, *Design of Experiments Principles and Applications*, 3rd edn., MKS Umetrics AB, 2008.

114. G. Barr, W. Dong and C. J. Gilmore, *Journal of Applied Crystallography*, 2009, **42**, 965-974.

115. A. Kitaigorodskii, *Acta Crystallographica*, 1965, **18**, 585-590.

116. P. T. Galek, L. Fabian, W. S. Motherwell, F. H. Allen and N. Feeder, *Acta Crystallographica Section B: Structural Science*, 2007, **63**, 768-782.

117. P. T. Galek, F. H. Allen, L. Fábián and N. Feeder, *CrystEngComm*, 2009, **11**, 2634-2639.

118. P. T. Galek, L. Fábián and F. H. Allen, *CrystEngComm*, 2010, **12**, 2091-2099.

119. J. D. H. Donnay and D. Harker, *American Mineralogist*, 1937, **22**, 446-467.

120. S. P. Thompson, J. E. Parker, J. Potter, T. P. Hill, A. Birt, T. M. Cobb, F. Yuan and C. C. Tang, *Review of Scientific Instruments*, 2009, **80**, 075107.

121. M. Laszcz, K. Trzcinska, A. Witkowska, E. Lipiec-Abramska and W. J. Szczepek, *CrystEngComm*, 2015, **17**, 2346-2352.

122. M. Horvat, E. Meštrović, A. Danilovski and D. Q. M. Craig, *International Journal of Pharmaceutics*, 2005, **294**, 1-10.

123. *The Rigaku Journal*, 2003, **20**, 30-32.

124. P. M. Schaber, J. Colson, S. Higgins, D. Thielen, B. Anspach and J. Brauer, *Thermochimica acta*, 2004, **424**, 131-142.

125. K. A. Powell, A. N. Saleemi, C. D. Rielly and Z. K. Nagy, *Chemical Engineering and Processing: Process Intensification*, 2015, **97**, 195-212.

126. K. A. Berglund, Analysis and measurement of crystallization utilizing the population balance in *Handbook of Industrial Crystallization*, 2nd edn., ed. A. S. Myerson, Butterworth-Heinemann, Woburn, 2002, 101-113.

127. D. Randolph Alan and A. Larson Maurice, *Journal*, 1988.

128. P. H. Karpinski and J. S. Wey, Precipitation processes in *Handbook of Industrial Crystallization*, 2nd edn., ed. A. S. Myerson, Butterworth-Heinemann, Woburn, 2002, 141-160.

129. S. Ferguson, G. Morris, H. Hao, M. Barrett and B. Glennon, *Chemical Engineering Science*, 2013, **104**, 44-54.

130. T-T. C. Lai, J. Cornevin, S. Ferguson, N. Li, B. L. Trout and A. S. Myerson, *Crystal Growth & Design*, 2015, **15**, 3374-3382.

131. G. Power, G. Hou, V. K. Kamaraju, G. Morris, Y. Zhao and B. Glennon, *Chemical Engineering Science*, 2015, **133**, 125-139.

132. H. Zhang, J. Quon, A. J. Alvarez, J. Evans, A. S. Myerson and B. Trout, *Organic Process Research & Development*, 2012, **16**, 915-924.

133. R. Peña and Z. K. Nagy, *Crystal Growth & Design*, 2015, **15**, 4225–4236.

134. Y. Yang and Z. K. Nagy, *Industrial & Engineering Chemistry Research*, 2015, **54**, 5673-5682.

135. A. D. Randolph and M. A. Larson, *AIChE Journal*, 1962, **8**, 639-645.

136. M. Barrett, M. McNamara, H. Hao, P. Barrett and B. Glennon, *Chemical Engineering Research and Design*, 2010, **88**, 1108-1119.

137. M. R. Abu Bakar, Process analytical technology based approaches for the monitoring and control of size and polymorphic form in pharmaceutical crystallisation processes, PhD Thesis, Loughborough University, 2010.

138. K. S. Elvira, X. C. i Solvas, R. C. R. Wootton and A. J. deMello, *Nat Chem*, 2013, **5**, 905-915.

139. J. R. Burns and C. Ramshaw, *Lab on a Chip*, 2001, **1**, 10-15.

140. S. Zhang, N. Ferté, N. Candoni and S. Veesler, *Organic Process Research & Development*, (Web): April 17, 2015, DOI: 10.1021/acs.oprd.5b00122.

141. D. Lombardi and P. S. Dittrich, *Expert Opinion on Drug Discovery*, 2010, **5**, 1081-1094.

142. P. Sobieszuk, J. Aubin and R. Pohorecki, *Chemical Engineering & Technology*, 2012, **35**, 1346-1358.

143. R. D. Dombrowski, J. D. Litster, N. J. Wagner and Y. He, *Chemical Engineering Science*, 2007, **62**, 4802-4810.

144. M. Faustini, J. Kim, G.-Y. Jeong, J. Y. Kim, H. R. Moon, W.-S. Ahn and D.-P. Kim, *Journal of the American Chemical Society*, 2013, **135**, 14619-14626.

145. K.-J. Kim, R. P. Oleksak, E. B. Hostetler, D. A. Peterson, P. Chandran, D. M. Schut, B. K. Paul, G. S. Herman and C.-H. Chang, *Crystal Growth & Design*, 2014, **14**, 5349-5355.

146. M. Jiang, Z. Zhu, E. Jimenez, C. D. Papageorgiou, J. Waetzig, A. Hardy, M. Langston and R. D. Braatz, *Crystal Growth & Design*, 2014, **14**, 851-860.

147. X.-W. Ni, CMAC Doctoral Training Centre Lecture titled Oscillatory Baffled Reactors and Crystallisers, Heriot-Watt Univerity, Edinburgh, December 2012.

148. X. Ni, M. R. Mackley, A. P. Harvey, P. Stonestreet, M. H. I. Baird and N. V. R. Rao, *Chemical Engineering Research & Design*, 2003, **81**, 373-383.

149. X. Ni, H. Jian and A. Fitch, *Chemical Engineering Research & Design*, 2003, **81**, 842-853.

150. T. Howes, M. R. Mackley and E. P. L. Roberts, *Chemical Engineering Science*, 1991, **46**, 1669-1677.

151. P. Stonestreet and P. M. J. Van der Veeken, *Chemical Engineering Research & Design*, 1999, **77**, 671-684.

152. S. Lawton, G. Steele, P. Shering, L. H. Zhao, I. Laird and X. W. Ni, *Organic Process Research & Development*, 2009, **13**, 1357-1363.

153. L. Zhao, V. Raval, N. E. B. Briggs, R. M. Bhardwaj, T. McGlone, I. D. H. Oswald and A. J. Florence, *CrystEngComm*, 2014, **16**, 5769-5780.

154. T. McGlone, N. E. B. Briggs, C. A. Clark, C. J. Brown, J. Sefcik and A. J. Florence, *Organic Process Research & Development*, 2015, **19**, 1186-1202.

155. N. Blagden, R. Davey, M. Song, M. Quayle, S. Clark, D. Taylor and A. Nield, *Crystal Growth & Design*, 2003, **3**, 197-201.

156. R. B. Hammond, X. Lai, K. J. Roberts, A. Thomas and G. White, *Crystal Growth & Design*, 2004, **4**, 943-948.

157. G. Coquerel, A. Lafontaine and M. Sanselme, Method of measuring scattering of x-rays, its applications and implementation device, 2012, WO2012136921.

158. M. J. Quayle, R. J. Davey, A. J. McDermott, G. J. T. Tiddy, D. T. Clarke and G. R. Jones, *Physical Chemistry Chemical Physics*, 2002, **4**, 416-418.

159. J. N. Low and C. C. Wilson, *Acta Crystallographica Section C*, 1983, **39**, 1688-1690.

160. G. Portalone, *Acta Crystallographica Section E*, 2008, **64**, o1107-o1108.

161. CrystalClear: An Integrated Program for the Collection and Processing of Area Detector Data, Rigaku, © 1997-2011.

162. L. J. Farrugia, *J. Appl. Cryst.*, 1999, **32**, 837-838.

163. G. M. Sheldrick, *Acta Cryst.* , 2008, **A64**, 112-122.

164. J. M. Carethers, E. J. Smith, C. A. Behling, L. Nguyen, A. Tajima, R. T. Doctolero, B. L. Cabrera, A. Goel, C. A. Arnold, K. Miyai and C. R. Boland, *Gastroenterology*, 2004, **126**, 394-401.

165. M. Saarma, A. Merrits, M. Karelson, Antisense oligonucleotides with hydroxy- and/or mercapto-modified bases as antiviral agents, WO2009060122 A3.

166. R. C. B. Copley, L. S. Deprez, T. C. Lewis and S. L. Price, *CrystEngComm*, 2005, **7**, 421-428.

167. L. Hokmabady, H. Raissi and A. Khanmohammadi, *Structural Chemistry*, 2015, 1-18.

168. S. A. Barnett, A. T. Hulme, N. Issa, T. C. Lewis, L. S. Price, D. A. Tocher and S. L. Price, *New Journal of Chemistry*, 2008, **32**, 1761-1775.

169. W. M. Macintyre, P. Singh and M. S. Werkema, *Biophysical journal*, 1965, **5**, 697-713.

170. E. J. Obrien, *Acta Crystallographica*, 1967, **23**, 91-106.

171. J. Sletten, E. Sletten and L. H. Jensen, *Acta Crystallographica Section B*, 1968, **24**, 1692-1698.

172. P. M. Bhatt, Y. Azim, T. S. Thakur and G. R. Desiraju, *Crystal Growth & Design*, 2009, **9**, 951-957.

173. A. Vermes, H. J. Guchelaar and J. Dankert, *Journal of Antimicrobial Chemotherapy*, 2000, **46**, 171-179.

174. Aziz-ur-Rehman, M. Helliwell, S. Ali and S. Shahzadi, *Acta Crystallographica Section E*, 2007, **63**, o1743-o1744.

175. M. Habgood, M. A. Deij, J. Mazurek, S. L. Price and J. H. ter Horst, *Crystal Growth & Design*, 2010, **10**, 903-912.

176. S. A. Kulkarni, S. S. Kadam, H. Meekes, A. I. Stankiewicz and J. H. ter Horst, *Crystal Growth & Design*, 2013, **13**, 2435-2440.

177. J. H. ter Horst, *Chemical Engineering & Technology*, 2012, **35**, 965-965.

178. C. C. Wilson, A. Parkin and L. H. Thomas, *Journal of Chemical Education*, 2012, **89**, 34-37.

179. A. O. Surov, A. A. Simagina, N. G. Manin, L. G. Kuzmina, A. V. Churakov and G. L. Perlovich, *Crystal Growth & Design*, 2015, **15**, 228-238.

180. S. Kumaresan, P. G. Seethalakshmi, P. Kumaradhas and B. Devipriya, *Journal of Molecular Structure*, 2013, **1032**, 169-175.

181. S. Aitipamula, A. B. H. Wong, P. S. Chow and R. B. H. Tan, *CrystEngComm*, 2014, **16**, 5793.

182. S. SeethaLekshmi and T. N. G. Row, *Crystal Growth & Design*, 2012, **12**, 4283-4289.

183. S. Romero, B. Escalera and P. Bustamante, *International Journal of Pharmaceutics*, 1999, **178**, 193-202.

184. T. Umeda, N. Ohnishi, T. Yokoyama, T. Kuroda, Y. Kita, K. Kuroda, E. Tatsumi and Y. Matsuda, *Chem Pharm Bull (Tokyo)*, 1985, **33**, 2073-2078.

185. V. López-Mejías, J. W. Kampf and A. J. Matzger, *J. Am. Chem. Soc.*, 2009, **131**, 4554-4555.

186. N. J. Babu, P. Sanphui and A. Nangia, *Chemistry – An Asian Journal*, 2012, **7**, 2274-2285.

187. M. D. Eddleston, R. Thakuria, B. J. Aldous and W. Jones, *Journal of Pharmaceutical Sciences*, 2014, **103**, 2859-2864.

188. F. Kato, M. Otsuka and Y. Matsuda, *International Journal of Pharmaceutics*, 2006, **321**, 18-26.

189. R. K. Gilpin and W. Zhou, *Vibrational Spectroscopy*, 2005, **37**, 53-59.

190. A. Y. Lee, D. Erdemir and A. S. Myerson, *Annual Review of Chemical and Biomolecular Engineering*, 2011, **2**, 259-280.